Dynamical electron-phonon interaction in novel quantum materials from first principles

Girotto, Nina

University of Zagreb
Faculty of Science
Department of Physics

Nina Girotto

Dynamical electron-phonon interaction in novel quantum materials from first principles

DOCTORAL DISSERTATION

Zagreb, 2024

University of Zagreb
Faculty of Science
Department of Physics

Nina Girotto

Dynamical electron-phonon interaction in novel quantum materials from first principles

DOCTORAL DISSERTATION

Supervisor:
dr. sc. Dino Novko

Zagreb, 2024

Sveučilište u Zagrebu
Prirodoslovno-matematički fakultet
Fizički odsjek

Nina Girotto

Dinamička elektron-fonon interakcija u novim kvantnim materijalima iz prvih principa

DOKTORSKI RAD

Mentor:
dr. sc. Dino Novko

Zagreb, 2024

Acknowledgements

Najviše se zahvaljujem mentoru, Dinu Novku. Toliko mi je bilo dobro da bih ja do penzije mogla biti vaša doktorandica. Znam da ništa što tu napišem neće biti dovoljno da se zahvalim za ovih 4-5 godina, ali ipak bih voljela reći da iskreno mislim da ste vi najbolji mentor koji postoji. Sve vaše znanstvene ideje, sve konferencije i škole na kojima sam bila i vaše sveukupno vodstvo su stvarno bili prevrijedni i hvala vam na tome.

Hvala Ivoru na jako jako puno toga. Hvala na jako puno pomoći oko superračunala i svih skripti za raznorazne programe. Veliki dio ovog doktorata je napravljen uz tvoju pomoć!

Luka, možda se ne čini tako, ali ovo je sve teorijska podloga za stroj za teleportaciju. Volim te jako! A ako i ti mene voliš, pročitati ćeš cijelu ovu divotu.

Jako se puno zahvaljujem i mami i papetu. Jako ste mi puno pomogli svojim savjetima, podrškom i napravili od mene ovo što jesam. Nadam se da ću ja svojoj djeci moći dati koliko ste i vi meni! Mama, samo da provjerim, hoću li ja postati doktor prije tebe ili...? A pape, ti nisi doktor, jel da?

Hvala i mojim sekanima, volim ja vas (ali vam to neću nikad priznat). I nonotu i noni, između ostaloga, hvala na beskonačnom izvoru keksa.

Hvala Anama za super društvo u uredu i malo ženske podrške!

I thank Matthieu for the Overleaf document!

Financial support from the Croatian Science Foundation (Grant no. UIP-2019-04-6869) is gratefully acknowledged.

Abstract

With the aim of elucidating various experimental results in several relevant novel materials, this thesis delves into clarifying the role of dynamical electron-phonon coupling. Using first-principles theory as a basis for our calculations, we often go beyond these methods and complement them with many-body perturbation theory. The main aim of this work is to provide a thorough overview of the far-reaching consequences of resorting to the static approximation of electron-lattice interaction when using *ab-initio* methods. After setting an in depth theoretical basis, this thesis deals with three topics.

Firstly, we show a variety of novel bulk and two-dimensional materials all exhibiting remarkable nonadiabatic effects in their phonon spectra. Apart from the expected long-wavelength nonadiabatic effects, we found sizable nonadiabatic Kohn anomalies away from the Brillouin zone center for materials with strong intervalley electron-phonon scatterings. With our thorough theoretical calculations we reveal important consequences that the dynamical electron-phonon coupling has on estimating the superconducting and transport properties. With significant modifications of the electron-phonon coupling across the Brillouin zone, the dynamical phonon anomalies alter the superconducting transition temperature compared to the adiabatic result and rescale the low-temperature and low-frequency regime of the scattering time $1/\tau_{op}(\omega, T)$ from about T^3 to about T^2, resembling the Fermi liquid result for electron-electron scattering.

Secondly, we focus on temperature-dependent Raman experiments done on graphene and Weyl semimetals and simulate the dynamical phonon self-energy contributions beyond the first-order perturbation theory. Contrary to the common belief, we reveal a prevailing electron-phonon coupling contribution to the linewidths of their strongly-coupled phonons and manage to provide convincing justifications of experimental observations.

Finally, we discuss the out-of equilibrium phenomena, as achieved in ultrafast pump-probe experiments. We simulate the time-resolved modifications in the phonon spectra and electron-phonon

properties, taking place due to a photoexcited electron distribution in graphene and molybdenum disulphide (MoS_2). A significant contribution of this work lies in the methodology we use, because nonequilibrium simulations of dynamical electron-phonon coupling are out of reach for the current *ab-initio* methods. In graphene, we find several important photo-induced effects. We reveal photo-induced phonon gain and we resolve the debate about whether photoexcitation enhances electron-phonon coupling matrix elements or if the observed effects stem from the modified phase space and provide evidence to support the latter option. In MoS_2, due to its multivalley band structure, time-dependent Boltzmann equations reveal a characteristic manner of electron relaxation. The corresponding time dynamics of phonons shows time-dependent anisotropic phonon softenings, dynamical Kohn anomalies, and strengthening of electron-phonon coupling.

Keywords: electron-phonon coupling, *ab-initio* methods, Kohn anomaly, phonon self-energy, linewidth, nonadiabaticity

Prošireni sažetak

Glavni cilj ovog doktorskog rada je provesti temeljito istraživanje uloge dinamičkog elektron-fonon vezanja (eng. electron-phonon coupling, EPC) u kvazi-2D materijalima iz prvih principa. Glavno pitanje kojim se bavi je pitanje utjecaja i posljedica dinamičkog EPC-a na fonone u uvjetima ravnoteže i izvan nje. EPC je odgovorno za objašnjenje mnoštva zanimljivih fizikalnih fenomena, kao što su transport nosioca naboja, termalni transport te konvencionalna supravodljivost, dok istovremeno postoji velika praznina između novih eksperimentalnih spoznaja i pripadnih teorijskih uvida u mikroskopske procese. Za mnoge praktične primjene, zanimljiv je koncept upravljanja svojstvima i faznim prijelazima materijala. Posebno su zanimljivi 2D materijali kojima je lako manipulirati dopiranjem, fotopobuđenjem ili tlakom, a veliki dio informacija o svojstvima pohranjen je u fononskom spektru. Stoga, od velike je važnosti produbiti razumijevanje dinamičke elektron-fonon interakcije koja je nedostupna u okvirima raspoloživih računa iz prvih principa, a može uvelike mijenjati adijabatski predviđena svojstva fonona.

Istraživanje se oslanja na teoriju funkcionala gustoće (eng. density functional theory - DFT) i nadopunjuje se odgovarajućim teoretskim dodacima koji nisu a priori uzeti u obzir pri izračunima iz prvih principa. DFT se do sada pokazala snažnim alatom za izračun EPC-a iz prvih principa. Svrha ovog istraživanja je unaprijeđivanje te metode, zbog čega kombiniramo DFT s perturbativnom teorijom mnoštva čestica (eng. MBPT), programima za izračun anharmoničkih efekata i Boltzmannovim transportnim jednadžbama (vidi Poglavlja 2, 3, 4).

DFT se oslanja na adijabatsku aproksimaciju, zbog čega se prva tema opisana u Poglavlju 5 ovog doktorskog istraživanja bavi neadijabatskom korekcijom fononskog spektra raznih 2D i 3D materijala. To na ključan način doprinosi razumijevanju dinamičkih efekata EPC-a te njihovih dalekosežnih implikacija na supravodljiva i transportna svojstva u raznim materijalima. Mi predlažemo način korekcije fononskih spektara i EPC-a te pokazujemo njene posljedice na izračun supravodljivih i transportnih svojstava. Pokazali smo da u 8 promatranih sustava dinamičke korekcije ublažavaju

statički dobivene Kohn anomalije u fononskom spektru i zauzvrat drastično smanjuju jačinu EPC-a.

Povrh dinamičkih efekata, DFT ne uračunava efekte iznad prvog reda u MBPT prilikom izračuna vlastite energije fonona. Ova disertacija u Poglavlju 6 pokazuje da viši redovi MBPT-a, donose velike anharmoničke doprinose posredovane elektronima. Takvo istraživanje pomaže u razumijevanju temperaturno ovisnih Raman spektara sustava s jakom elektron-fonon interakcijom. Pokazuje se da u grafenu i Weyl semimetalima, usprkos drugačijem uvjerenju zajednice, EPC predstavlja značajni mehanizam temperaturne promjene fononskih frekvencija i širine fononskih linija.

Fotopobuđenjem mogu se inducirati nove zanimljive faze u materijalu, što je od velikog značaja za primjenu, a uvelike neistraženo. Mi prezentiramo dvije nove metode za simulaciju neravnotežnih distribucija elektrona te njihovih posljedica na dinamiku fonona, elektrona i EPC-a u Poglavlju 7. U fotoinduciranom grafenu, simulirali smo neravnotežnu distribuciju nosioca u nekoliko različitih faza termalizacije i izračunali dinamičku spektralnu funkciju fonona. Otkrili smo otvrđivanje fonona i općenito proširenje fononskih linija uslijed vezanja na elektrone izvan ravnoteže. Izračuni EPC-a u fotopobuđenom MoS_2 otkrili su tranzijentne fononske anomalije te proširenje fononskih linija za vrijeme termalizacije elektrona. Ovakva istraživanja koja objedinjuju vremensku evoluciju neravnotežne raspodjele nosioca te renormalizaciju fonona koja je time inducirana su bitna jer je napravljen korak k samosuglasnom opisu EPC-a u netermalnim uvjetima. Takav pristup je prigodan za proučavanje ultrabrzih fenomena gdje dinamička renormalizacija fonona igra važnu ulogu. To istraživanje pruža temelj za proučavanje sustava gdje se fotopobuđenjem mogu inducirati fazni prijelazi ili uređena stanja.

U ovoj disertaciji navodi se nekoliko teorijskih metoda koje upotpunjavaju nedostatke izračuna iz prvih principa i koje se mogu primijeniti na široki spektar materijala i fizikalnih problema. Disertacija je usko povezana s eksperimentalnim radom, dok se tehnološka primjena ovakvih istraživanja proteže od nalaženja optimalnih materijala za razne uređaje pa sve do krojenja njihovih željenih svojstava i primjene u raznim granama industrije.

Ključne riječi: elektron-fonon vezanje, metode iz prvih principa, Kohn anomalija, vlastita energija fonona, širina linije, neadijabatski efekti.

Contents

1 Introduction **1**
- 1.1 Manifestations of electron-phonon interaction . . . 1
- 1.2 Thesis outline . . . 5

2 Theoretical methods **7**
- 2.1 The Born-Oppenheimer approximation . . . 7
- 2.2 Electrons . . . 10
  - 2.2.1 Density functional theory . . . 10
- 2.3 Phonons . . . 15
  - 2.3.1 Harmonic approximation . . . 16
  - 2.3.2 Density functional perturbation theory . . . 17
- 2.4 Electron-phonon coupling . . . 21
  - 2.4.1 *Ab-initio* approach . . . 22
  - 2.4.2 Wannier functions . . . 23

3 Software **25**
- 3.1 Quantum ESPRESSO . . . 25
- 3.2 Wannier90 . . . 26
- 3.3 EPW . . . 26

4 Phonon renormalization **27**
- 4.1 Dynamical effects in the electron-phonon coupling . . . 27
  - 4.1.1 Electron and phonon self-energies . . . 27
  - 4.1.2 *Ab-initio* phonon renormalization . . . 30
  - 4.1.3 Intraband phonon self-energy beyond the first-order term . . . 33

5 Dynamical renormalization in novel materials **46**
- 5.1 Adiabatic or nonadiabatic? . . . 46
- 5.2 Eliashberg spectral function . . . 48
- 5.3 Selected materials . . . 49
  - 5.3.1 Computational details . . . 50

5.4 Results . . . 52
5.5 Conclusion . . . 61

6 Temperature-dependent Raman spectra **63**
6.1 Raman features of graphene . . . 63
6.2 Electron-mediated anharmonicity . . . 65
6.2.1 Conventional anharmonicity . . . 68
6.3 Computational details . . . 71
6.3.1 Electron-phonon contribution . . . 71
6.3.2 Anharmonic contribution . . . 71
6.4 Results . . . 73
6.4.1 Out-of-equilibrium conditions . . . 76
6.5 Raman features of Weyl semimetals . . . 78
6.5.1 Basic properties of TaAs and TaP . . . 79
6.5.2 Temperature-dependent properties of TaAs and TaP . . . 81
6.6 Conclusion . . . 87

7 Electron-phonon coupling in photoexcited systems **89**
7.1 Photoexcitation . . . 89
7.2 Graphene . . . 91
7.2.1 Photo-excited carrier distribution in graphene . . . 91
7.2.2 Phonon renormalization . . . 92
7.2.3 cDFPT details . . . 98
7.2.4 Photo-induced static effects in the phonon spectrum . . . 100
7.2.5 Photo-induced dynamical effects in the phonon spectrum . . . 102
7.3 Molybdenum disulphide . . . 110
7.3.1 Theory . . . 111
7.3.2 Computational details . . . 116
7.3.3 Results and discussion . . . 117
7.4 Conclusion . . . 124

8 Thesis summary and outlook **126**

Curriculum vitae **128**

References **130**

Chapter 1

Introduction

1.1 Manifestations of electron-phonon interaction

With the aim of understanding the properties of solids, most textbooks usually start from the free electron model. The fact that a solid viewed as a gas of free electrons is a viable model is quite surprising. This simple yet counter-intuitive model successfully manages to account for a range of metallic properties. In the free electron model, the interaction between the ions and electrons, as well as between electrons themselves, are ignored. Still, it assumes that some scattering mechanism exists, introducing the concept of relaxation time and it treats the electrons quantum-mechanically through the Pauli exclusion principle. This elementary model of a quantum gas of electrons with a parabolic dispersion, which scatter from time to time, captures some phenomena related to heat and electrical transport since the two are based upon free electrons [1, 2]. For example, the Wiedemann–Franz law, which asserts that the ratio between the thermal conductivity contributed by electrons and the electrical conductivity of a metal is directly proportional to the temperature. Another qualitative prediction of the free electron model is the temperature dependence of the electronic contribution to the heat capacity. Good quantitative results following from the free electron model, are the electrical conductivity, as well as the Seebeck coefficient for alkali metals, which describes the thermoelectric effect relating the flow of current and a temperature gradient.

A direct extension of the free electron model is obtained by an addition of a periodic perturbation arising from the ions frozen in their positions, constituting a nearly free electron model. The electrons are again viewed as moving freely, but now through a crystal lattice. The Schrödinger equation containing a periodic potential is solvable via Bloch's theorem, which introduces the notion of

electronic band structure and manages to explain the presence of bandgaps and variations in electron density at different energy levels, unlike the free electron model.

As long as one does not investigate the source of electronic collisions, the simplified model of immobile ions can justify a variety of metallic equilibrium and transport properties. However, the lattice is not a rigid, fixed array, since every ion possesses thermal energy and vibrates around its equilibrium position. The lattice, therefore, also participates in both the thermal and electric transport. The moving lattice also explains how the solids melt and how a solid reacts to any probing method that interacts with its ions, such as infrared light, X-rays, or neutrons. Moreover, lattice vibrations are an important origin of electronic scattering in metals and can radically change how the electrons interact. Many physical insights into phonons can be gained using a classical model for the lattice, where the ions are interconnected by springs and oscillate harmonically ignoring the existence of electrons.

However, the movement of the ions affects the electron gas around them via electrostatic forces, and vice versa. Electron-phonon coupling (EPC) is a fundamental concept in condensed matter physics that describes the interaction between electrons and lattice vibrations [3]. The significance of EPC spans from fundamental properties in metals and semiconductors to cutting-edge applications.

Signatures of EPC can be visible both in the phonon and electron band structures and, generally, both are renormalized and a linewidth is introduced in their spectra [4]. Consequently, due to EPC, energy gaps in semiconductors renormalize as well [5]. Photoemission spectroscopy (i.e., angle resolved photoemission spectroscopy - ARPES) in metals can reveal strong EPC in the electronic band structure in the form of large band dispersion modulation at the scale of phonon energy near the Fermi surface (i.e., the so-called kinks) [6]. If, on the other hand, the system is a low-doped insulator, sub-bands can be formed below the conduction band minimum, due to polaronic distortions of lattice [7–9].

In this thesis, the main focus will be the EPC effects on the phonons. In the phonon band structure, Kohn anomalies can be observed as a result of EPC [10]. Kohn anomalies are kink-like modulations of the phonon dispersion at particular momentum, which arise if a certain phonon coupled to electrons is also able to excite an electron from below to above the Fermi sea. Kohn anomalies generally mark the strongly-coupled mode, which softens due to EPC. Since their appearance in reciprocal space mirrors the Fermi surface, their shape and the magnitude of the softening is largely determined by the available phase space for electronic transitions and, therefore, by doping and temperature [see Fig. 1.1(a)]. However, the simple picture of an electron scattering from one part of the Fermi surface

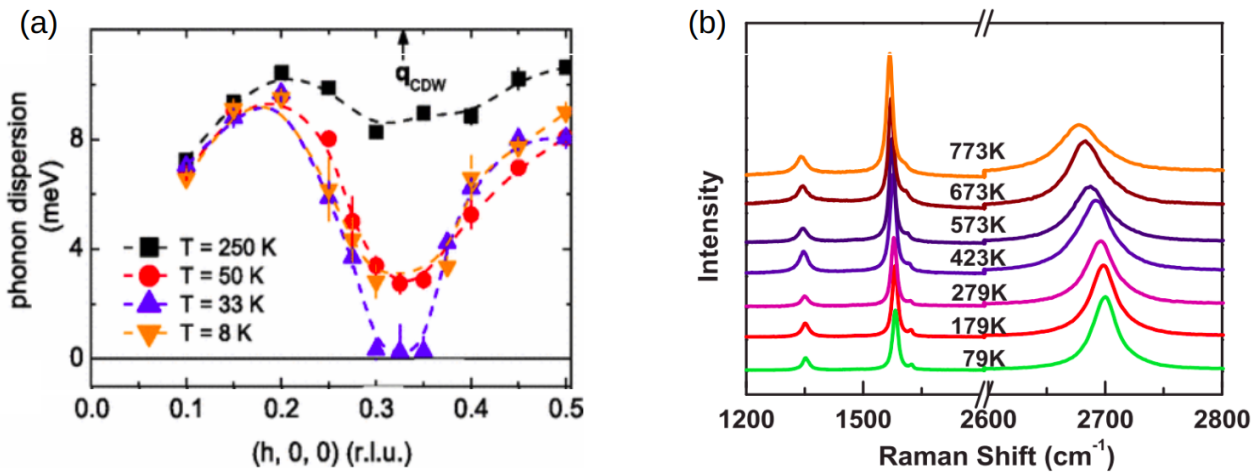

Figure 1.1: (a) A soft phonon in 2H-$NbSe_2$ measured with IXS (from Ref. [17]). (b) Temperature-dependent Raman spectrum of graphene. A strongly-coupled G peak is at the frequency of about 1600 cm^{-1}, and it shows a considerable frequency and linewidth modulation as a function of temperature (from Ref. [18]).

to the other, due to its interaction with a phonon, hides certain complexities. Namely, an electron involved is a *quasiparticle*, dragging a cloud of mutually interacting electron-hole and phonon excitations. Eventually, it turns out that a phonon indirectly interacts with all other phonons in the system, revealing its anharmonicity. The result of an experimental measurement is an interplay of the mentioned electron-phonon and phonon-phonon interactions and it is not easy to disentangle them. The most familiar phonon probe is probably Raman scattering, where incoming excitation light either gains or looses energy during its interaction with the electron-phonon system. Since photons have negligible momentum and momentum remains a conserved quantity, Raman probe is usually measuring only zero-momentum, or Brillouin zone-center phonons (at least in the first-order Raman process). Graphene is an example of a system where a Kohn anomaly is present in the Brillouin zone center (Γ point) [11, 12], and the frequency and linewidth of that mode heavily depend on temperature and doping [13–16] [see Fig. 1.1(a)]. Whether a Kohn anomaly is hidden at some finite wave vector, probes such as inelastic x-ray scattering (IXS) or electron energy loss spectroscopy can be of service [see Fig. 1.1(a)]. Strongly-coupled phonon modes with a finite momentum are involved and considered important for various physical phenomena, such as formation of the charge density waves (CDWs), phonon-limited mobility, and phonon-assisted absorption. Solar cell make use of this latter feature, for instance when light changes its momentum in interaction with the silicon, making it highly efficient under direct sunlight.

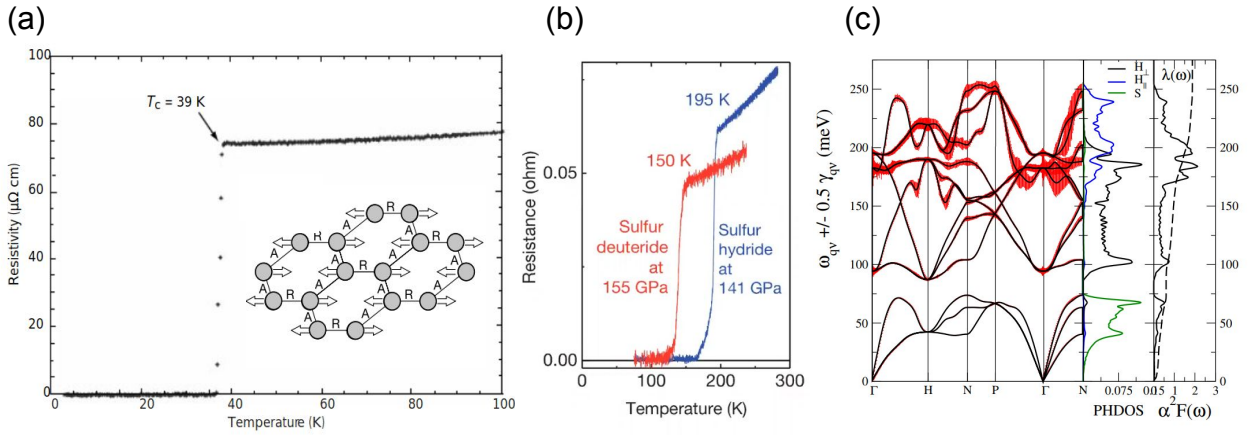

Figure 1.2: Examples of the resistivity drop as a sign of the superconductivity onset in (a) MgB_2 (experiment from Ref. [19] and mode from Ref. [20]) and (b) sulfur- deuteride and hydride achieved under high pressure (from Ref. [21]). In panel (c) is the phonon dispersion and EPC properties (phonon density of states, Eliashberg function, EPC strength λ) for hydrogen sulfide under high pressure (from Ref. [22]).

Possibly the most interesting consequence of EPC is superconductivity [23]. Certain materials can conduct electric current with zero resistance and expel magnetic fields when cooled below a critical temperature. The first proposed theory behind it, implies an attractive interaction between two electrons mediated by phonons. Namely, at low temperatures, two electrons with opposite spins can effectively overcome their mutual electrostatic repulsion and form pairs due to the attractive electron-phonon interaction. These pairs of electrons are known as Cooper pairs. This state is separated by an energy gap which is larger than the available thermal energy, preventing electrons from scattering and leading to zero electrical resistance. Fig. 1.2(a) demonstrates the resistivity drop due to superconductivity in magnesium diboride (MgB_2) at 40 K, together with the phonon mode responsible for the strong coupling to electrons [19, 20]. Another remarkable recent example of superconductivity is discovered at high temperature and pressure in hydrogen based materials [see Fig. 1.2(b)]. Even at such extreme conditions, EPC still remains the driving mechanism of superconductivity [see Fig. 1.2(c)].

Superconductivity is not only interesting from the fundamental aspect, but also in terms of technological applications. Nowadays, in order to facilitate the technological applications an interesting and attractive ideas of inducing and controlling phase transitions, such as superconductivity, are being thoroughly explored. Especially intriguing are the laser-induced ultrafast phenomena, because under non-equilibrium conditions, systems can exhibit novel properties, sometimes unreachable

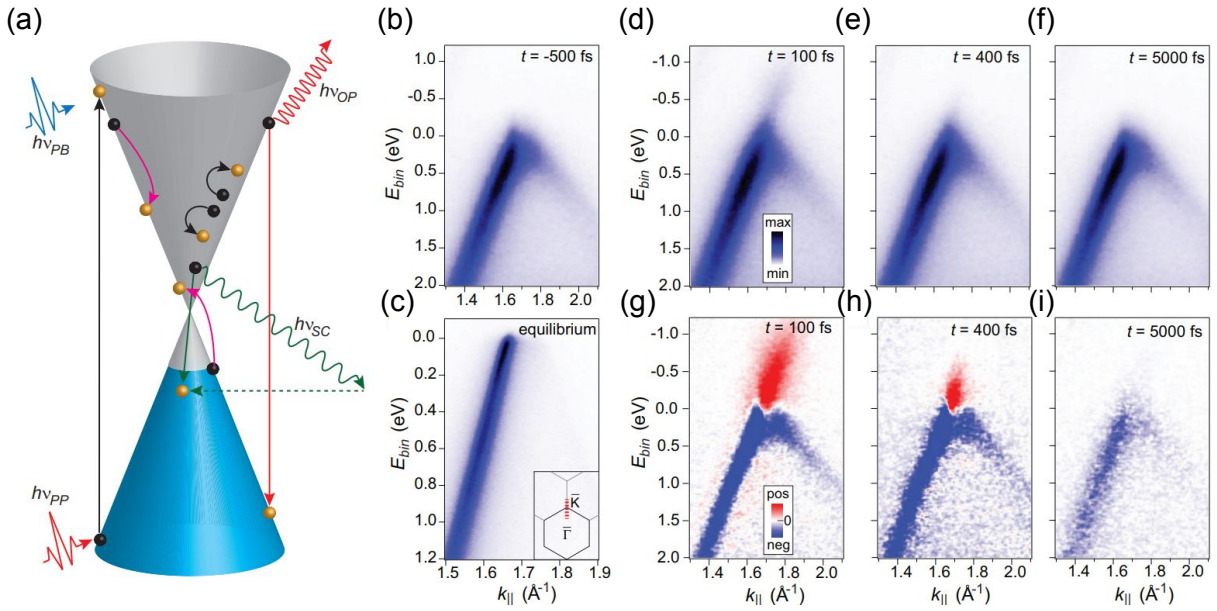

Figure 1.3: (a) Schematics of a pump ($\hbar\nu_{PP}$)-probe ($\hbar\nu_{PB}$) experiment inside graphene Dirac cone. Electrons (black spheres) thermalize via optical and acoustic phonon emission (red and green wiggled lines respectively). Dirac cone in equilibrium measured by (b) ARPES and (c) synchrotron radiation. In panels (d)-(f) is the photo-emission intensity around the Dirac cone for a few time instants after the pump pulse application. (g)-(i) The corresponding difference spectra with respect to the one before the pump pulse. Figure is from Ref. [24].

in equilibrium [25, 26]. After an initial short laser pulse drives the system out of equilibrium and promotes electrons to excited states, the system returns to equilibrium through a series of relaxation steps, in which EPC plays an important role [see Fig. 1.3]. For instance, hot electrons are transferring their excess energy to phonons via electron-phonon scatterings, which is considered to be the main mechanism for electron thermalization on the picosecond timescale. In photo-excited non-equilibrium systems EPC is not only important for carrier population thermalization, but is also at the center of other ultrafast processes crucial for controllable manipulation of phases, such as light-induced coherent phonons, structural phase transitions, ferroelectricity, and ferromagnetism [27–29]

1.2 Thesis outline

Knowing the far-reaching consequences of EPC, no wonder it has been thoroughly studied and has continued to captivate the interest of scientists. Calculations of EPC from first principles

were developed with density functional perturbation theory (DFPT), around a decade after density functional theory (DFT). Even though extremely complex and computationally expensive, there has been remarkable advancement in the field of EPC calculations in the last twenty years, enabling realistic and powerful calculations, with a high accuracy and predictive power.

In this thesis we are presenting new findings on the dynamical electron-phonon interactions in various layered and two-dimensional materials, making use of DFT and DFPT. Despite the immense progress, *ab-initio* EPC calculations still rely on some approximations, such as the adiabatic approximation [30] and being aware of that shortcoming, we are complementing *ab-initio* techniques with the many-body perturbation theory (MBPT). In this thesis, three major topics related to the dynamical EPC will be covered, respectively shedding new light on the EPC related transport phenomena, the role of EPC in the temperature-dependent Raman properties and out-of equilibrium pump-probe experiments.

In order to understand the basis of first-principles calculations, its building blocks are introduced in Chapter 2 and the software used extensively throughout this thesis is presented in Chapter 3. Growing evidence of the inadequacy of the adiabatic approximation [31–46] serves as a motivation to delve into various aspects of the dynamical phonon renormalization presented in Chapter 4. Its importance and strength in many novel two-dimensional materials is presented in Chapter 5, where its profound consequences on transport properties are examined. The rest of the thesis is done within the scope of the dynamical renormalization. In Chapter 6 we go beyond the simple first-order dynamical renormalization and simulate the temperature-dependent Raman spectra of graphene and Weyl semimetals by taking into account the effects of electron-mediated anharmonicity. This thesis puts forward these latter effects as an unavoidable ingredient when simulating the EPC contributions to the temperature-dependent spectral features of strongly-coupled phonons [34, 47]. The last topic of this thesis, Chapter 7, considers the EPC in photo-excited systems. It reveals the mechanisms of hot-carrier cooling via strongly-coupled phonons, and how they affect photo-induced phonon renormalizations in graphene and single-layer MoS_2.

Chapter 2

Theoretical methods

The theoretical approach to many-body systems is a challenging and fundamental problem in quantum mechanics, especially in the context of condensed matter physics. In many-body systems, the behavior of each constituent particle (electron, nucleus, etc.) is strongly influenced by the presence of all other particles, leading to complex interactions that are difficult to treat exactly. In this chapter, we delve into the theoretical methods to calculate electron band structure, phonon dispersion and the interaction between electrons and phonons. The main emphasis is put on first-principles methods, as they are the main tools used in this thesis.

2.1 The Born-Oppenheimer approximation

The usual approach is to start from a general static problem of N_e electrons moving in the Coulomb field produced by N_n nuclei. The Hamiltonian which describes the system has the following form

$$\hat{H} = \hat{T}_n + \hat{T}_e + \hat{V}_n + \hat{V}_e + \hat{V}_{en}. \tag{2.1}$$

The first two terms represent the kinetic energy of the nuclei

$$\hat{T}_n = \sum_{k=1}^{N_n} \frac{(\hat{p}_k^n)^2}{2M_k^n} \tag{2.2}$$

and electrons

$$\hat{T}_e = \sum_{k=1}^{N_e} \frac{(\hat{p}_k^e)^2}{2m_e}. \tag{2.3}$$

$\hat{p}$ denotes the momentum of the k-th nuclei or electron, depending on the superscript, while m denotes their mass. The next three terms in the Hamiltonian are the potential terms describing the interaction between nuclei

$$\hat{V}_n = \frac{1}{2} \sum_{l \neq k=1}^{N_n} \frac{Z_k e Z_l e}{|\mathbf{r}_k^n - \mathbf{r}_l^n|} \tag{2.4}$$

between the electrons

$$\hat{V}_e = \frac{1}{2} \sum_{l \neq k=1}^{N_e} \frac{e^2}{|\mathbf{r}_k^e - \mathbf{r}_l^e|} \tag{2.5}$$

and their mutual interaction

$$\hat{V}_{en} = -\sum_{k=1}^{N_n} \sum_{l=1}^{N_e} \frac{Z_k e^2}{|\mathbf{r}_k^n - \mathbf{r}_l^e|}. \tag{2.6}$$

The potential

$$-\sum_{k=1}^{N_n} \frac{Z_k e}{|\mathbf{r}_k^n - \mathbf{r}_l^e|} \tag{2.7}$$

that one electron feels due to a nuclear ensemble, will later be referred to as the external potential V^{ext}. In its most general form, the Schrödinger equation gives a description of a system evolving in time

$$i\frac{\partial}{\partial t} |\Psi(t)\rangle = \hat{H} |\Psi(t)\rangle , \tag{2.8}$$

where $\langle \mathbf{r}_k^n; \mathbf{r}_l^e | \, |\Psi(t)\rangle = \Psi(\mathbf{R}, t)$ is the many-body wavefunction which depends on the set of coordinates of all the electrons and nuclei in the system $\mathbf{R}$. Since we defined a time-independent Hamiltonian, solving a Schrödinger equation amounts to finding the eigenfunctions and eigenenergies which diagonalize the Hamiltonian

$$\hat{H} |\Psi\rangle = E |\Psi\rangle . \tag{2.9}$$

In practice, the Schrödinger equation is not usually straightforwardly solved, due to a large number of degrees of freedom and the complexity they bring. Instead, almost certainly one needs to resort to a convenient approximation, for example the Born-Oppenheimer approximation (BOA) [48]. The BOA allows us to separate the motion of electrons and nuclei into distinct independent degrees of freedom, simplifying the quantum mechanical treatment of the system. The main idea behind the BOA is rooted in the vast difference in mass between electrons and nuclei. Since electrons are

much lighter than nuclei, they respond to changes in the system potential energy (e.g., due to atomic configurations) much faster than the nuclei do. This characteristic timescale separation allows us to make the key assumption that the electronic motion instantaneously adjusts to any changes in the nuclear positions, effectively decoupling the electronic and nuclear degrees of freedom. Under this assumption, the total wavefunction can be written as a product of nuclear and electronic parts $\sum_\alpha \chi(\mathbf{r}_k^n)\psi_\alpha^{\mathbf{r}_k^n}(\mathbf{r}_l^e)$. The nuclear term $\chi(\mathbf{r}_k^n)$ depends only on a set of positions of the nuclei. The wavefunction of the electron subsystem parametrically depends on the positions of the nuclei because the electronic energy is influenced by the arrangement of the positively charged nuclei in the system, in addition to the dependence on the electron positions. The electronic part forms a complete set of orthogonal wavefunctions in **r** space. If we focus on the electronic part, we can suppose we know the solution to this part of the equation:

$$[\hat{T}_e(\mathbf{r}_l^e) + \hat{V}_e(\mathbf{r}_l^e) + \hat{V}^{ext}(\mathbf{r}_k^n;\mathbf{r}_l^e)]\psi_\alpha^{\mathbf{r}_k^n}(\mathbf{r}_l^e) = E_\alpha(\mathbf{r}_k^n)\psi_\alpha^{\mathbf{r}_k^n}(\mathbf{r}_l^e). \tag{2.10}$$

Multiplying both sides of the static Schrödinger equation from the left with $\left[\psi_\beta^{\mathbf{r}_k^n}(\mathbf{r}_l^e)\right]^*$ and integrating over all the electronic coordinates, we obtain

$$\sum_k \left[-\frac{\hbar^2}{2M_k}\nabla^2_{\mathbf{r}_k^n} + \hat{V}_n(\mathbf{r}_k^n) + E_\beta(\mathbf{r}_k^n) + \Delta\right]\chi(\mathbf{r}_k^n) = E\chi(\mathbf{r}_k^n) \tag{2.11}$$

where the symbol Δ stands for the two remaining terms deriving from the action of the ∇^2 operator upon the electronic part of the wavefunction:

$$\Delta = -\frac{\hbar^2}{2M_k}\sum_\alpha \int d\mathbf{r}_l^e \left[\left(\psi_\beta^{\mathbf{r}_k^n}(\mathbf{r}_l^e)\right)^* \nabla^2_{\mathbf{r}_k^n}\psi_\alpha^{\mathbf{r}_k^n}(\mathbf{r}_l^e)\chi(\mathbf{r}_k^n) + 2\left(\psi_\beta^{\mathbf{r}_k^n}(\mathbf{r}_l^e)\right)^* \nabla_{\mathbf{r}_k^n}\psi_\alpha^{\mathbf{r}_k^n}(\mathbf{r}_l^e)\nabla_{\mathbf{r}_k^n}\chi(\mathbf{r}_k^n)\right]. \tag{2.12}$$

In the adiabatic BOA, the Δ term is neglected. Both terms in Δ describe electron transitions invoked by the movement of the nuclei. However, under the assumption of the instantaneous adjustment of electrons to the new positions of the nuclei, we neglect these terms and obtain two separate equations - one for the electronic and one for the ionic degrees of freedom. The energy $E_\alpha(\mathbf{r}_k^n)$ enters the equation for the nuclei as an effective potential. The work presented in this thesis goes beyond the BOA, with a thorough exploration of the dynamical limit to the EPC.

2.2 Electrons

The discussion about how to solve the many-body problem within BOA naturally starts with electrons. They are responsible for the majority of the crystal properties and in many cases these can be, at least qualitatively, explained within the noninteracting electron picture. Even though the ionic and electronic degrees of freedom are effectively decoupled with introducing BOA, the problem at hand is still not easily solvable, since the number of electrons in a finite system is very large. A groundbreaking and versatile theoretical approach that has revolutionized the field of condensed matter physics, materials science, and quantum chemistry is DFT. Instead of working with the large number of degrees of freedom and obtaining the many-body electron wavefunction, DFT deals with the more tractable problem of obtaining the electron density.

2.2.1 Density functional theory

DFT provides a robust framework for calculating the electronic structure of materials. DFT relies upon Hohenberg-Kohn theorems introduced in 1964, which provide a rigorous basis for the method. The two theorems, which are proven in the original articles [49, 50] state that

- The ground state total energy, wavefunction and the external potential are all unique functionals of the ground state density of electrons $n_0(\mathbf{r})$. The first theorem implies that all the essential information about the ground state electronic structure is encoded in the electron density and that the external potential acts as a functional of the density.

- The ground state density of electrons $n_0(\mathbf{r})$ minimizes the energy functional $E[n_0(\mathbf{r})]$. The energy functional consists of two terms, the external potential $V^{ext}[n_0(\mathbf{r})]$ and a system-independent part which contains all the information about the electron-electron interactions and kinetic energy - the *universal functional* $F[n_0(\mathbf{r})]$ both of which are functionals of the electronic density.

The second theorem guarantees the existence of a unique *universal functional* $F[n_0(\mathbf{r})]$ that, when minimized with respect to the electron density, will give the exact ground-state energy of the system. However, the explicit form of the *universal functional* $F[n_0(\mathbf{r})]$ is generally not known and remains a challenging problem in DFT.

The external potential functional can be written in terms of the density

$$V^{ext}[n(\mathbf{r})] = \int d\mathbf{r} V^{ext}(\mathbf{r}) n(\mathbf{r}), \tag{2.13}$$

but the kinetic term and the electron-electron interaction do not have an exact formulation in terms of the density. Therefore the real problem now amounts to finding a good approximation for $F[n_0(\mathbf{r})]$.

Kohn - Sham equations

W. Kohn and L. J. Sham proposed a groundbreaking approach [50] to solve the many-body Schrödinger equation by using DFT. This approach is known as the Kohn-Sham DFT, and it has become the cornerstone of modern electronic structure calculations. The Kohn-Sham DFT method overcomes the challenges of directly solving the many-body Schrödinger equation for interacting electrons by mapping the problem to a system of non-interacting electrons in an effective potential. The key idea behind the Kohn-Sham DFT is to introduce a set of fictitious non-interacting electrons that experience an effective potential that reproduces the same ground state electron density as the real interacting system. An immediate advantage of using a noninteracting system is that the kinetic energy term is known.

The Schrödinger equation of a Kohn-Sham noninteracting fictitious electron reads

$$\left[-\frac{1}{2}\nabla^2 + \hat{V}_{\mathrm{SCF}}\right] \psi_i^{KS}(\mathbf{r}) = \varepsilon_i \psi_i^{KS}(\mathbf{r}). \tag{2.14}$$

The first term in the Kohn-Sham Hamiltonian is the kinetic energy and the second term is an effective potential which acts on a single electron. It is determined in a way that the ground state density of the auxiliary system coincides with the exact one. The potential term is self-consistent (SCF) in a way that it is specified by the density of electrons obtained as a solution of the Kohn-Sham problem. The potential term consists of the Coulomb interaction in the Hartree approximation, external potential and of the exchange-correlation part which essentially incorporates all the missing electronic energy not included in the non-interacting kinetic and electrostatic terms. The density can be obtained as

$$n(\mathbf{r}) = \sum_i^{N_e} |\psi_i^{KS}(\mathbf{r})|^2. \tag{2.15}$$

The energy functional of the electronic density in the Kohn-Sham formalism looks like

$$E[n] = -\frac{1}{2}\sum_{i}^{N_e}\int d\mathbf{r}\psi_i^*(\mathbf{r})\nabla^2\psi_i(\mathbf{r}) + \frac{1}{2}\int d\mathbf{r}\int d\mathbf{r}'\frac{n(\mathbf{r})n(\mathbf{r}')}{|\mathbf{r}-\mathbf{r}'|} + \int d\mathbf{r}V^{ext}n(\mathbf{r}) + E_{xc}[n]. \quad (2.16)$$

The first term is the kinetic energy of a non-interacting electron gas with density $n(\mathbf{r})$. The energy functional is minimized by the ground state density under the requirement of the particle number conservation. If we use ε_i from the right hand side of Eq. (2.14) as the Lagrange parameter, the minimization procedure leads us back to Eq. (2.14) but with

$$\hat{V}_{\mathrm{SCF}}[n] = \frac{1}{2}\int d\mathbf{r}'\frac{n(\mathbf{r}')}{|\mathbf{r}-\mathbf{r}'|} + V^{ext}(\mathbf{r}) + \frac{\delta E_{xc}}{\delta n(\mathbf{r})}. \quad (2.17)$$

In DFT, if the form of the SCF potential is known, a self-consistent loop is established by calculating the wavefunctions and density from the potential, and then updating the potential and calculating them again. The procedure is repeated until the changes in subsequent SCF loops are smaller than some desired energy threshold.

Exchange-correlation functional

The exchange-correlation functional is generally unknown and DFT relies upon finding a good assumption for it. The simplest approximations are the so-called semi-local exchange-correlation functionals, since these functionals only locally depend on the electronic charge density and its gradient. In the local density approximation (LDA), the exchange-correlation functional is approximated point by point in real space by the exchange-correlation energy of the homogeneous electron gas having density $n(\mathbf{r})$ [50]. It is the oldest and the most popular exchange-correlation functional. LDA assumes a linear dependence on the density and it can be written as the integral

$$E_{XC}^{LDA} = \int d\mathbf{r}n(\mathbf{r})\varepsilon_{XC}^{Hom.}(n(\mathbf{r})), \quad (2.18)$$

where $\varepsilon_{XC}^{Hom.}(n(\mathbf{r}))$ is the exchange-correlation energy density of an interacting homogeneous electron gas. It can be decomposed as a sum of an exchange and correlation parts. The exchange part is calculated as the average Hartree-Fock exchange energy per electron in a homogeneous electron gas

and is known analitically as

$$\varepsilon_X^{Hom.}(n(\mathbf{r})) = -\frac{3}{4}\left(\frac{3n(\mathbf{r})}{\pi}\right)^{\frac{1}{3}}, \tag{2.19}$$

where the homogeneous electron density is substituted by a position-dependent one. The correlation term is obtained from a fit to Monte Carlo data. The LDA tends to overestimate the correlation energy, especially in systems with varying electron densities. The parametrization by Perdew and Zunger addresses this issue by introducing a more sophisticated treatment of the correlation energy by posing a set of conditions it must satisfy [51]. The Perdew-Zunger functional incorporates the correct behavior of the correlation energy in the uniform electron gas limit and in the high-density limit. A more elaborate approximation of the exchange-correlation functional considers not only the density, but also its gradient to be the functional variables. The generalized gradient approximation (GGA) to the exchange-correlation functional reads as

$$E_{XC}^{GGA} = \int d\mathbf{r} n(\mathbf{r}) \varepsilon_{XC}(n(\mathbf{r}), \nabla n(\mathbf{r})). \tag{2.20}$$

The additional information about the spatial variation of the electron density allows for a more refined description of exchange and correlation effects, especially in regions with varying electron densities. The Perdew-Burke-Ernzerhof parametrization [52] is commonly used, as is also the case for this thesis.

Pseudopotentials

A wavefunction describing a valence electron at first glance should be plane-wave-like interstitially, while close to the ion cores it should oscillate rapidly in order for the valence electrons to have a higher kinetic energy than the core electrons localized around lattice sites. The orthogonalized plane-wave method incorporates these requests by constructing wavefunctions as plane waves orthogonal to the core levels. The orthogonalized plane wave is defined as

$$\psi_{\mathbf{k}}^{OPW}(\mathbf{r}) = \frac{1}{\sqrt{\mathcal{N}}} e^{i\mathbf{kr}} + \sum_c b_c \psi_{\mathbf{k}}^c(\mathbf{r}) \tag{2.21}$$

here superscript 'c' denotes a core state wavefunction. Factor $\frac{1}{\sqrt{\mathcal{N}}}$ is the normalizatio factor, which can be obtained as a product of the number of unit cells $N^{uc} = N_1 \cdot N_2 \cdot N_3$ of the system and the volume of one unit cell $V^{uc} = |\mathbf{a_1} \times \mathbf{a_2} \cdot \mathbf{a_3}|$ if $\mathbf{a}_i$ are the primitive translation vectors. The sum is

performed over all core levels with Bloch wavevector $\mathbf{k}$, while the constants b_c are determined from the orthogonality requirement of $\psi_{\mathbf{k}}^{OPW}(\mathbf{r})$ to every core level. Therefore, we can write

$$b_c = -\int d\mathbf{r}\psi_{\mathbf{k}}^{c*}(\mathbf{r})e^{i\mathbf{kr}}. \tag{2.22}$$

The actual valence electronic state is a linear combination of the orthogonalized plane waves

$$\Psi_{\mathbf{k}}(\mathbf{r}) = \sum_{\mathbf{K}} c_{\mathbf{K}}\psi_{\mathbf{K}+\mathbf{k}}^{OPW}(\mathbf{r}), \tag{2.23}$$

where the sum is over all reciprocal lattice vectors $\mathbf{K}$. This approach is the best way to reduce the actual problem of an electron in a periodic potential to an effectively nearly free electron calculation, by introducing pseudopotentials. An extension of the orthogonalized plane wave method is the pseudopotential method. The main idea behind a pseudopotential method is to combine the core level states and a nuclear potential to form an effective potential. The expression (2.23) represents a solution to the Schrödinger equation

$$\hat{H}\Psi_{\mathbf{k}}(\mathbf{r}) = \varepsilon_{\mathbf{k}}\Psi_{\mathbf{k}}(\mathbf{r}). \tag{2.24}$$

If now a plane wave part from Eq. (2.23) is separated and labeled $\Psi_{\mathbf{k}}^{PW}(\mathbf{r})$, we have

$$\hat{H}\Psi_{\mathbf{k}}^{PW}(\mathbf{r}) + \hat{H}\sum_c b_c\psi_{\mathbf{k}}^c(\mathbf{r}) = \varepsilon_{\mathbf{k}}\Psi_{\mathbf{k}}^{PW}(\mathbf{r}) + \varepsilon_{\mathbf{k}}\sum_c b_c\psi_{\mathbf{k}}^c(\mathbf{r}). \tag{2.25}$$

The cumbersome terms can be buried in an effective potential, leading to the Schrödinger equation

$$\left[\hat{H}_0 + \hat{V}_{PP}\right]\Psi_{\mathbf{k}}^{PW}(\mathbf{r}) = \varepsilon_{\mathbf{k}}\Psi_{\mathbf{k}}^{PW}(\mathbf{r}), \tag{2.26}$$

where $\hat{H}_0$ refers to the Hamiltonian of a noninteracting system with a self-consistent potential V_{SCF}, and $\hat{V}_{PP}$ includes an external potential and a nuclear potential screened by the core electrons

$$\hat{V}_{PP}\Psi_{\mathbf{k}}^{PW}(\mathbf{r}) = \hat{V}\Psi_{\mathbf{k}}^{PW}(\mathbf{r}') + \sum_c(\varepsilon_{\mathbf{k}} - \varepsilon_{\mathbf{k}}^c)\int d\mathbf{r}'\psi_{\mathbf{k}}^{c*}(\mathbf{r}')\Psi_{\mathbf{k}}^{PW}(\mathbf{r}')\psi_{\mathbf{k}}^c(\mathbf{r}), \tag{2.27}$$

where the last part is essentially a projector onto the core states, acting in this case on $\Psi_{\mathbf{k}}^{PW}(\mathbf{r})$. The core states energy is denoted by $\varepsilon_{\mathbf{k}}^c$. We are left with an effective Schrödinger equation (2.26) satisfied by the smooth part of the Bloch function. A small number of plane waves is sufficient for

a good approximation and in every DFT code the desired cut-off value can be chosen. From the definition of a pseudopotential Eq. (2.27), it is obvious that the pseudopotential is nonlocal. Its act on a wavefunction is not just a multiplication by some function of $\mathbf{r}$. Also, it depends on the energy of the valence state $\varepsilon_{\mathbf{k}}$ that we wish to calculate. There are actually many other ways to define $\hat{V}_{PP}$ in a way that the valence eigenvalues of the crystal Hamiltonian correspond to the eigenvalues obtained in Eq. (2.26). In the calculations presented in this thesis, we use norm-conserving pseudopotentials. They have no $\varepsilon_{\mathbf{k}}$ dependence and they are constructed in a way to satisfy a set of criteria for the matching of pseudopotential and all-electron eigenvalues and wavefunctions. It is also desirable that they are as smooth as possible, so that their reciprocal-space representation decays as quickly as possible.

2.3 Phonons

Transport phenomena, in which heat or electricity are carried through some structure due to the influence of a temperature or electric field gradient, are not easily interpreted if we restrict our selves to individual particle models. Therefore, when calculating specific heats, one must replace the Einstein model with the Debye model. The fundamental difference between the two models is that the Einstein model considers each atom to vibrate like a simple harmonic oscillator, while the Debye model considers a distribution of energy among the normal vibration modes of the entire crystal, i.e., its collective excitations. The duality of waves and particles is the dominant concept of modern physics and therefore with these elastic excitations in the solid, we can associate its particle aspect. The quantized units of energy of the lattice vibration field are called phonons and the lattice is then viewed as a gas of phonons which act as bosons. This entire thesis is concerned with these particles, their spectra and interactions.

As announced, phonons play a key role in heat transport properties, resistivity, they mediate the attractive interaction between electrons leading to superconductivity, and they play a crucial role in structural phase transitions. According to the BOA, phonons can be described in a rather simple way. Another approximation, which actually makes the concept of phonons meaningful is the harmonic approximation.

2.3.1 Harmonic approximation

By employing the BOA, we consent to viewing the energy of the electron system as depending on the time-independent positions of the nuclei. In turn, the energy of the electrons together with the Coulomb potential between the nuclei, enter the equation for the nuclei as an effective potential, reformulating Eq. (2.11)

$$\sum_k \left[-\frac{\hbar^2}{2M_k} \nabla^2_{\mathbf{r}^n_k} + \hat{V}_n(\mathbf{r}^n_k) + E_\beta(\mathbf{r}^n_k) \right] \chi(\mathbf{r}^n_k) = \sum_k \left[T^n_{\mathbf{k}} + E_{eff}(\mathbf{r}^n_k) \right] \chi(\mathbf{r}^n_k). \tag{2.28}$$

This effective potential can be expanded in a Taylor series as a function of atomic displacements from the equilibrium $u(\mathbf{r}^n_k)$

$$\begin{aligned} \sum_k E_{eff}(\mathbf{r}^n_k) = E_{eff}\big|_{u=0} + \sum_{k,i} \left. \frac{\partial E_{eff}}{\partial u(r^n_{k,i})} \right|_{u=0} u(r^n_{k,i}) + \\ \frac{1}{2} \sum_{k,i,k',j} \left. \frac{\partial^2 E_{eff}}{\partial u(r^n_{k,i}) \partial u(r^n_{k',j})} \right|_{u=0} u(r^n_{k,i}) u(r^n_{k',j}) + \dots \end{aligned} \tag{2.29}$$

where the three Cartesian directions are implied in the sums by *i,j* indices. If we ignore the first constant term, realize that the second term vanishes due to the energy minimum in the equilibrium and consider only terms up to second order, we are left with the quadratic term. The double derivative describes how the force acting on one atom in one direction changes if another atom is displaced in the other direction and it defines an interatomic force constants matrix

$$C^{i,j}_{k,k'}(\mathbf{r}^n_k) = \frac{\partial^2 E_{eff}}{\partial u(r^n_{k,i}) \partial u(r^n_{k',j})}. \tag{2.30}$$

This matrix is symmetric and positive definite because the nuclei vibrate around their equilibrium position in the Born-Oppenheimer energy landscape. A Fourier transform from real space to momentum space, i.e.,

$$C^{i,j}_{k,k'}(\mathbf{q}) = \sum_{\mathbf{r}^n_k} e^{i\mathbf{q}\mathbf{r}^n_k} C^{i,j}_{k,k'}(\mathbf{r}^n_k), \tag{2.31}$$

divided by the square of the atomic masses, constitutes the dynamical matrix $D_{\mathbf{q}}$, whose eigenvalues are phonon frequencies squared and eigenvectors are the phonon displacements. The dimension of the dynamical matrix is $3N$, where N is the number of atoms in the unit cell. The $3N$ solutions, or

normal modes are labeled by the index ν. In the nonadiabatic (NA) regime, we would have to deal with time-dependent atomic displacements $u(\mathbf{r}_k^n, t)$. The Fourier transform of the time-dependent interatomic force constants to the ($\mathbf{q}$,ω) domain, i.e.,

$$C_{k,k'}^{i,j}(\mathbf{q},t) = \sum_{\mathbf{r}_k^n} e^{i\mathbf{q}\mathbf{r}_k^n - i\omega t} C_{k,k'}^{i,j}(\mathbf{r}_k^n, t), \tag{2.32}$$

would then make the eigenvalue problem of the dynamical matrix self-consistent in the following way

$$\left[\mathrm{Re}(D_{\mathbf{q}}(\omega_{\mathbf{q}\nu})) - \omega_{\mathbf{q}\nu}^2\right] \mathbf{e}_{\mathbf{q}\nu} = 0, \tag{2.33}$$

where $\omega_{\mathbf{q}\nu}$ are the eigenvalues with ν labeling the phonon branches and $\mathbf{e}_{\mathbf{q}\nu}$ are the eigenvectors. The dynamical matrix would have also an imaginary part introduced due to the time dependence of the atomic positions. Its imaginary part refers to the phonon lifetimes or linewidths

$$\gamma_{\mathbf{q}\nu} = 2 \sum_{k,k',i,j} \mathbf{e}_{\mathbf{q}\nu}^{i,k} \frac{\mathrm{Im}(D_{\mathbf{q}}^{i,j,k,k'})}{\omega_{\mathbf{q}\nu}} \mathbf{e}_{\mathbf{q}\nu}^{j,k'}. \tag{2.34}$$

In other words, the phonon frequencies obtain a certain width, unlike the adiabatic frequencies which are infinitely sharp.

2.3.2 Density functional perturbation theory

In order to calculate the phonon spectrum from first principles, one needs to obtain the second derivative of the energy functional with respect to the atomic displacements [30]. A theorem which will come in handy is the Hellmann-Feynman theorem. It states that for a general Hamiltonian $\hat{H}$ depending on a set of parameters λ_i, and which has eigenvalues E and eigenvectors ψ the derivative of E with respect to some λ can be calculated as

$$\partial_\lambda E = \langle \psi | \, \partial_\lambda \hat{H} \, | \psi \rangle . \tag{2.35}$$

The expression for the ground-state electron density functional Eq. (2.16) contains a system-independent universal functional, the external potential of an electron within an ensemble of nuclei and the Coulomb repulsion term of the nuclei. Since the atomic positions are parameters in the electronic Hamiltonian of the system, the application of the Hellmann-Feynman theorem on the

functional E leads to

$$\nabla_{u(\mathbf{r}_k^n)} E_k[n] = \int d\mathbf{r} \nabla_{u(\mathbf{r}_k^n)} V_{\mathrm{SCF}}(\mathbf{r}_k^n) n(\mathbf{r}) + \nabla_{u(\mathbf{r}_k^n)} \hat{V}_n. \tag{2.36}$$

Another application of the Hellmann-Feynman theorem yields the interatomic force constants

$$\begin{aligned} C_{k,k'}^{i,j}(\mathbf{r}_k^n) &= \frac{\partial^2 E_k}{\partial u(r_{k,i}^n) \partial u(r_{k',j}^n)} \\ &= \int d\mathbf{r} \frac{\partial V_{\mathrm{SCF}}(\mathbf{r}_k^n)}{\partial u(r_{k,i}^n)} \frac{\partial n(\mathbf{r}_k^n)}{\partial u(r_{k',j}^n)} + \int d\mathbf{r} \frac{\partial^2 V_{\mathrm{SCF}}(\mathbf{r}_k^n)}{\partial u(r_{k,i}^n) \partial u(r_{k',j}^n)} n(\mathbf{r}) + \frac{\partial^2 \hat{V}_n}{\partial u(r_{k,i}^n) \partial u(r_{k',j}^n)}. \end{aligned} \tag{2.37}$$

Once the ground-state density and its first derivative are known, we can straightforwardly calculate the phonon spectrum. The main task of DFT is to obtain the ground state density. What leads us to the DFPT whose main task is to obtain the response of that density to ionic displacements. In DFT calculations for metallic systems, a smearing function is introduced $\tilde{\delta}(x)$ as well as its integral - the corresponding smoothed step function $\tilde{\theta}(x)$. In all the calculations in this thesis, we use a Fermi-Dirac smoothed step function $f(\varepsilon)|_\mu^T = 1/(1+e^{\frac{\varepsilon-\mu}{k_B T}})$ and its derivative as a smearing function

$$\tilde{\delta}(\varepsilon) = -\frac{1}{2k_B T} \frac{1}{1+\cosh\left(\varepsilon/k_B T\right)}.$$

k_B is the Boltzmann constant and μ is the chemical potential. The smearing width is then given by the temperature. The expression for the electron density response is given by

$$\partial n(\mathbf{r}) = \sum_{n,m} \frac{\tilde{\theta}(\varepsilon_n) - \tilde{\theta}(\varepsilon_m)}{\varepsilon_n - \varepsilon_m} \Psi_n^*(\mathbf{r}) \Psi_m(\mathbf{r}) \left\langle \Psi_m(\mathbf{r}) \right| \partial V_{\mathrm{SCF}} \left| \Psi_n(\mathbf{r}) \right\rangle, \tag{2.38}$$

where the dependence of $\mathbf{r}$ on all the indices is omitted for simplicity. The wavefunctions $\Psi_{n,m}$ and energies $\varepsilon_{n,m}$ refer to the Kohn-Sham wavefunctions and energies, and indices n and m are composite indices for the band and momentum. The electron density response and the change of the SCF potential also depend on the phonon momentum $\mathbf{q}$, the displaced atom index and the direction of its displacement, which are all omitted here as well. Next, the following abbreviation is introduced:

$$\partial \Psi_n(\mathbf{r}) = \sum_m \frac{\tilde{\theta}(\varepsilon_n) - \tilde{\theta}(\varepsilon_m)}{\varepsilon_n - \varepsilon_m} \tilde{\theta}(\varepsilon_m, \varepsilon_n) \Psi_m(\mathbf{r}) \left\langle \Psi_m(\mathbf{r}) \right| \partial V_{\mathrm{SCF}} \left| \Psi_n(\mathbf{r}) \right\rangle. \tag{2.39}$$

$\tilde{\theta}(\varepsilon_m, \varepsilon_n)$ is defined as $1/(1+e^{\frac{\varepsilon_n-\varepsilon_m}{k_BT}})$. The partial derivative of the potential ∂V_{SCF} with respect to the ionic displacement is given by [see Eq. (2.17)]

$$\partial V_{\text{SCF}} = \int \frac{\partial n(\mathbf{r}')}{|\mathbf{r}-\mathbf{r}'|} d\mathbf{r}' + \partial V^{ext} + \left.\frac{\delta E_{xc}[n]}{\delta n(\mathbf{r})}\right|_{n_0} \partial n(\mathbf{r}). \tag{2.40}$$

Equations (2.38) and (2.40) need to be solved self-consistently. In order to avoid the summation over the unoccupied states, in DFPT the actual equation being solved is [30]:

$$(H_{KS} + Q - \varepsilon_n)\,|\partial\Psi_n\rangle = -(f(\varepsilon_n)|_\mu^T - P_n)\partial V_{\text{SCF}}\,|\Psi_n\rangle \tag{2.41}$$

where

$$Q = \sum_m \alpha_m\,|\psi_m\rangle\,\langle\psi_m|$$

$$P_n = \sum_m \beta_{n,m}\,|\psi_m\rangle\,\langle\psi_m|$$

and

$$\beta_{n,m} = f(\varepsilon_n)|_\mu^T f(\varepsilon_m)|_{\varepsilon_n}^T + f(\varepsilon_m)|_\mu^T f(\varepsilon_n)|_{\varepsilon_m}^T + \alpha_m \frac{f(\varepsilon_n)|_\mu^T - f(\varepsilon_m)|_\mu^T}{\varepsilon_n - \varepsilon_m} f(\varepsilon_n)|_{\varepsilon_m}^T.$$

The parameters α_m are present in order to avoid zero eigenvalues of the matrix on the left-hand side of the equation $(H_{KS}+Q-\varepsilon_n)$. This happens if the denominator in $\partial\Psi_n$ is close to zero. To avoid that, the α_m are set to zero for unoccupied states and to some constant value for all partially occupied states. This way, we need no information about the totally unoccupied states because for those, the Kohn-Sham wavefunction perurbation vanishes. Note that the Fermi-Dirac distribution function never reaches zero, which would make all the states partially occupied, but in actual calculations, we neglect its value after some energy. Phonon frequencies obtained in DFPT are statically screened by the Kohn-Sham electrons because the derivation of DFPT relies on the BOA. The interatomic force constants are static, without the time dependence, or when Fourier transformed, without the ω dependence. With all these we end up with the set of self-consistent equations (Sternheimer equations) describing the electron density response to a time-independent perturbation and phonons with infinite lifetime.

Constrained DFPT

The Kohn-Sham states near the Fermi level are the ones which are under the most influence of phonons, electron-phonon scattering, as well as electronic correlations, while the high-energy states are less involved and can be treated as a background screening. Moreover, at temperatures where the low-temperature phenomena are active, the energy states far from the Fermi surface are either totally empty or totally occupied. The idea behind the constrained DFPT (cDFPT) is to identify these active states' subset, exclude them when doing the DFPT calculation and then treat them in a different fashion [53,54]. Important advantage of this approach is that it provides a full momentum-dependent picture of phonon renormalization due to constrained photo-excited electron distribution [53,55–59]. The cDFPT method can be used in order to describe filling of the excited states, i.e., in photoexcited and out-of-equilibrium systems in general. This method is in that case equivalent to the Δ SCF method, and using DFT and DFPT for such purposes is fully justified [60,61].

In the cDFPT, the original Sternheimer equation is modified in a way that

$$\beta_{n,m} = f(\varepsilon_n)|_\mu^T f(\varepsilon_m)|_{\varepsilon_n}^T + f(\varepsilon_m)|_\mu^T f(\varepsilon_n)|_{\varepsilon_m}^T + \alpha_m \frac{f(\varepsilon_n)|_\mu^T - f(\varepsilon_m)|_\mu^T}{\varepsilon_n - \varepsilon_m} f(\varepsilon_n)|_{\varepsilon_m}^T.$$

only if both indices *n,m* refer to the states outside the active subspace. If they do not, then

$$\beta_{n,m} = f(\varepsilon_n)|_\mu^T$$

what makes the r.h.s. of the Sternheimer equation vanish (2.41). The obtained phonons are partially screened as well as the EPC matrix elements, because the intra-active subspace excitation processes are excluded.

In a similar manner, cDFT and cDFPT can be used to simulate an arbitrary carrier distribution, under the condition that the number of carriers is conserved. It represents a powerful method to investigate the impact such nonequilibrium distribution may have on the dynamics of the phonon degrees of freedom.

cDFT and cDFPT techniques are closely related to the concept of "downfolding" [62–64], where the full problem is mapped to an *ab-initio* low-energy effective system with a significantly reduced number of degrees of freedom [65].

2.4 Electron-phonon coupling

In the previous section, the EPC term was treated as a perturbation to obtain the phonon frequencies. In fact, within the BOA, electron and phonon degrees of freedom are separated under the assumption of a large difference between their energy scales. Namely, the electrons are considered to instantaneously adjust to the positions of the vibrating nuclei. The electron-phonon interaction therefore has no dynamical effects. In order to derive the electron-phonon Hamiltonian, we start from the electronic Hamiltonian in the BOA Eq. (2.10) which parametrically depends on the atomic positions. If we expand it in the Taylor series as a function of atomic displacements up to the first order, we obtain

$$\hat{T}_e(\mathbf{r}_l^e) + \hat{V}_e(\mathbf{r}_l^e) + \hat{V}^{ext}(\mathbf{r}_k^n;\mathbf{r}_l^e)\big|_{u=0} + \sum_{k,i} \left.\frac{\partial \hat{V}^{ext}}{\partial u(r_{k,i}^n)}\right|_{u=0} u(r_{k,i}^n). \tag{2.42}$$

The last term describes how the electrons feel the change of the nuclear position, and we recognize it as the EPC term. To proceed, we exchange the vector position of the k-th nuclei $\mathbf{r}_k^n$ by the Bravais lattice vector $\mathbf{R}$. The phonon eigenvectors $e_{\mathbf{q}\nu}$ and a Fourier transform establish the connection between a collective phononic eigendisplacement with magnitude $u_{\mathbf{q}\nu}$ and the real-space Cartesian displacements $u_{\mathbf{R}i}$ of the atoms:

$$u_{\mathbf{R}i} = \sum_{\mathbf{q}} u_{\mathbf{q}i} e^{-i\mathbf{q}\mathbf{R}} \tag{2.43}$$

$$u_{\mathbf{q}i} = \sum_{\mathbf{R}} u_{\mathbf{R}i} e^{i\mathbf{q}\mathbf{R}} \tag{2.44}$$

$$u_{\mathbf{q}i} = \frac{1}{\sqrt{NM_i}} \sum_{\nu} u_{\mathbf{q}\nu} e_{\mathbf{q}i\nu} \tag{2.45}$$

$$u_{\mathbf{q}\nu} = \sum_{i} \sqrt{NM_i}\, u_{\mathbf{q}i} e^*_{\mathbf{q}i\nu}. \tag{2.46}$$

We can then rewrite the EPC term from Eq. (2.42) in reciprocal space as

$$\sum_{\mathbf{R}i} \left.\frac{\partial \hat{V}^{ext}}{\partial u_{\mathbf{R}i}}\right|_{u=0} u_{\mathbf{R}i} = \sum_{\mathbf{q}i} \left.\frac{\partial \hat{V}^{ext}}{\partial u_{\mathbf{q}i}}\right|_{u=0} u_{\mathbf{q}i}. \tag{2.47}$$

The index 'i' runs over the Cartesian directions of all basis atoms. Explicitly, the matrix elements of this term in second quantization can be expressed as

$$\sum_{\mathbf{q}i\mathbf{k}mn} \langle \mathbf{k}+\mathbf{q}m| \frac{\partial \hat{V}^{ext}}{\partial u_{\mathbf{q}i}} |\mathbf{k}n\rangle \, u_{\mathbf{q}i} \hat{c}^{\dagger}_{\mathbf{k}+\mathbf{q}m} \hat{c}_{\mathbf{k}n}, \tag{2.48}$$

Phonon field can be defined in terms of phonon creation and annihilation operators as

$$\hat{u}_{\nu\mathbf{q}} = \sqrt{\frac{1}{2M_i\omega_{\nu\mathbf{q}}}} (\hat{b}_{\nu\mathbf{q}} + \hat{b}^{\dagger}_{\nu-\mathbf{q}}). \tag{2.49}$$

Finally, we reach a familiar expression for the electron-phonon Hamiltonian

$$\hat{H}_{el-ph} = \sum_{\mathbf{k}\mathbf{q}\nu mn} g_{\nu}\left(\mathbf{k}n, \mathbf{k}+\mathbf{q}m\right) \hat{c}^{\dagger}_{\mathbf{k}+\mathbf{q}m} \hat{c}_{\mathbf{k}n} (\hat{b}_{\mathbf{q}\nu} + \hat{b}^{\dagger}_{-\mathbf{q}_{\nu}}) \tag{2.50}$$

where the electron-phonon matrix elements are $g_{\nu}\left(\mathbf{k}n, \mathbf{k}+\mathbf{q}m\right)$. The latter contain the derivative of the electron-phonon interaction term with respect to the phonon displacements and are inversely proportional to the phonon frequency

$$g_{\nu}\left(\mathbf{k}n, \mathbf{k}+\mathbf{q}m\right) = \sum_i \sqrt{\frac{1}{2NM_i\omega_{\nu\mathbf{q}}}} e_{\mathbf{q}i\nu} \langle \mathbf{k}+\mathbf{q}m| \frac{\partial \hat{V}^{ext}}{\partial u_{\mathbf{q}i}} |\mathbf{k}n\rangle . \tag{2.51}$$

2.4.1 *Ab-initio* approach

In order to calculate phonons with DFPT, the perturbation of the self-consistent potential term needs to be calculated when solving the Sternheimer set of equations. It is the key ingredient required for calculating the interatomic force constants. Therefore, a DFPT calculation readily yields the electron-phonon matrix elements since all the ingredients are known. However, we must not forget that DFPT relies on the adiabatic BOA. The *ab-initio* electron-phonon matrix elements are statically screened

$$g^{\mathrm{DFPT}}_{\nu}\left(\mathbf{k}n, \mathbf{k}+\mathbf{q}m\right) = \sum_i \sqrt{\frac{1}{2NM_i\omega_{\nu\mathbf{q}}}} e_{\mathbf{q}i\nu}\omega_{\nu\mathbf{q}} \langle \mathbf{k}+\mathbf{q}m| \frac{\partial \hat{V}_{\mathrm{SCF}}}{\partial u_{\mathbf{q}i}} |\mathbf{k}n\rangle . \tag{2.52}$$

When solving Eq. (2.41) for each state, we obtain the induced density in Eq. (2.38). The new induced density then constructs the variations of the terms in the SCF potential. These induced potentials yield a screened perturbation $\partial \hat{V}_{\mathrm{SCF}}$ and the cycle is repeated until self-consistency is achieved.

2.4.2 Wannier functions

The end goal when doing electron-phonon calculations are not the electron-phonon matrix elements, but rather some other quantities which contain the matrix elements as a weighing factor. For example, when calculating the lifetime of a certain phonon mode ν with a wavevector $\mathbf{q}$, one needs to sum the EPC matrix elements and other EPC quantities across the whole Brillouin zone in $\mathbf{k}$ space. Summations of this type are very frequent in EPC calculations, but unfortunately, in order to converge them, one needs to sum over a very dense $\mathbf{k}$ mesh ($\sim 10^6$). Since it is computational highly demanding to perform DFT and DFPT calculations on that many $\mathbf{k}$ points, Wannier interpolation was developed in order to make the electron-phonon calculations affordable. Instead of using the standard description of electrons in solids as delocalized Bloch waves, an alternative is to introduce Wannier functions [66]. Wannier functions are linear combinations of localized orbitals and are defined as arbitrary unitary transformations of the Bloch states $\Psi_{m\mathbf{k}}$

$$w_{\mathbf{R}n} = \sum_{\mathbf{k}m} U_{mn\mathbf{k}} \Psi_{m\mathbf{k}}(\mathbf{r}) e^{i\mathbf{kr}}. \tag{2.53}$$

The localization of Wannier functions is not obvious, but a very simplified argument would be that if we let $\mathbf{r} \to \infty$, the periodic part of the Bloch function is the same as if $\mathbf{r} \to 0$, while the phase factor in Eq. (2.53) contains very rapid oscillations which cancel each other out. The unitary matrix $U_{mn\mathbf{k}}$ is arbitrary, which gives considerable freedom when constructing Wannier functions. It is present in order to restore the smoothness in $\mathbf{k}$ space. Namely, if we start from a set of Hamiltonian eigenstates that are not smooth in $\mathbf{k}$, and introduce unitary rotations $U_{mn\mathbf{k}}$ that remove these discontinuities in a way that $\nabla\Psi_{m\mathbf{k}}$ is well defined, then Eq. (2.53) should yield well-localized Wannier functions. The smoothness of the reciprocal-space object, dictates the localization of the resulting real-space object, and vice versa. A simple and yet efficient method to construct a set of well-localized Wannier functions is by projection. A finite set of localized orbitals z_n in the unit cell is projected onto the Bloch manifold for each $\mathbf{k}$ vector

$$|\Phi_{n\mathbf{k}}\rangle = \sum_m |\Psi_{m\mathbf{k}}\rangle \langle \Psi_{m\mathbf{k}}|z_n\rangle . \tag{2.54}$$

For the procedure, one needs a matrix of inner products $A^{mn}_{\mathbf{k}} = \langle \Psi_{m\mathbf{k}}|z_n\rangle$. States $|\Phi_{n\mathbf{k}}\rangle$ obtained this way are not orthonormal, which is why the overlap matrix $S^{mn}_{\mathbf{k}} = \langle \Phi_{m\mathbf{k}}|\Phi_{n\mathbf{k}}\rangle$ is computed and used in

order to construct an orthonormal Bloch-like basis set

$$|\tilde{\Phi}_{n\mathbf{k}}\rangle = \sum_m \frac{|\Phi_{m\mathbf{k}}\rangle}{\sqrt{S^{mn}_{\mathbf{k}}}}. \tag{2.55}$$

These wavefunctions are smooth in $\mathbf{k}$ and are unitary transformations of the original $|\Phi_{n\mathbf{k}}\rangle$. When they are inserted in Eq. (2.53), well-localized wavefunctions can be obtained.

However, generally another approach is widely used nowadays. An approach developed by Marzari and Vanderbilt [67] in which localization is enforced by introducing a well-defined localization criterion. With the localization functional

$$\Omega = \sum_n \left[\langle 0n| r^2 |0n\rangle - \langle w_{\mathbf{0}n}| r |w_{\mathbf{0}n}\rangle^2 \right] = \sum_n \left[\langle r^2 \rangle_n - \bar{\mathbf{r}}_n^2 \right], \tag{2.56}$$

the sum of the quadratic spreads of the wavefunctions in the home unit cell around their centers is measured. Maximally localized wavefunctions (MLWFs) are then obtained by minimizing the Ω functional with respect to the $U_{mn\mathbf{k}}$. This is an iterative procedure, where an initial set of localized orbitals is given, projected onto the Bloch orbitals, which then enter Eq. (2.53). The resulting Wannier functions are then used to calculate the localization functional with Eq. (2.56). The $U_{mn\mathbf{k}}$ are iteratively refined until the localization functional is minimized.

MLWFs are constructed to be as localized as possible in real space while still faithfully representing the electronic structure. This localization ensures that each Wannier function is primarily centered around a particular atomic site or region. As a result, MLWFs can capture the essential physics of the system, without considering very long-range interactions, enabling calculations on a very dense momentum grids. In comparison with orthogonalized atomic orbitals, very compact models can be made with MLWFs, but the resulting functions are less intuitive than simple orbitals with a clear interpretation.

Chapter 3

Software

In this Chapter, we explicitly present the *ab-initio* codes that were used in this thesis.

3.1 Quantum ESPRESSO

Quantum ESPRESSO (QE) is a suite for first-principles electronic-structure calculations and materials modeling [68–70]. It is an open-source project with a broad user group worldwide. It is based on DFT, plane wave basis sets, and pseudopotentials.

The self-consistent Kohn-Sham equations are solved with the PWscf package. It performs calculations such as ground-state energy and one-electron (Kohn-Sham) orbitals, atomic forces, stresses and it can be used for structural optimization. It has many other functionalities, such as calculations of molecular dynamics on the Born-Oppenheimer surface, macroscopic polarization (and orbital magnetization) via Berry Phases and various forms of finite electric fields, but those are outside of the scope of this thesis. QE source codes will in this thesis be modified with the aim of implementing cDFT.

Phonon calculations are done with DFPT with the PHonon package for linear-response calculations. The codes available in the PHonon package can perform calculations of phonon frequencies and eigenvectors at a generic wave vector, effective charges and dielectric tensors, electron-phonon interaction coefficients for metals and interatomic force constants in real space. In this thesis, we often modify the codes in the PHonon package responsible for the calculation of static screening in order to implement cDFPT.

3.2 WANNIER90

WANNIER90 is a program which calculates the MLWFs and uses them as a basis set when representing the electronic structure from *ab-initio* data [71]. WANNIER90 is a part of QE. For the calculations of MLWFs which are not separated from the rest of the bands with an energy gap, a disentanglement procedure needs to be used [72]. This procedure requires us to define two energy windows. The larger 'outer' window contains all the bands one wants to Wannierize, and inside of the larger window the Ω functional minimization is performed. Inside the 'inner' window, the obtained Wannier functions exactly reproduce the Kohn-Sham energy bands. The inner window is therefore usually chosen around the Fermi level.

3.3 EPW

Electron Phonon Wannier (EPW) is an open-source community code for *ab-initio* calculations of electron-phonon interactions using DFPT and MLWFs [73–75]. It is a part of QE. EPW can calculate electron-phonon interaction self-energies, electron-phonon spectral functions, and total as well as mode-resolved electron-phonon coupling strengths. In this thesis, the functionalities of the EPW code which are used the most extensively are the calculation of the Eliashberg electron-phonon spectral functions and the total electron-phonon coupling strength, phonon linewidths and phonon spectral functions. The publicly available codes performing these calculations were modified during the making of this thesis, in order to enable the calculations of the various dynamical aspects of EPC.

Chapter 4

Phonon renormalization

4.1 Dynamical effects in the electron-phonon coupling

In metals, low-energy electrons are responsible for screening the phonons coupled to them. Typically the screening reduces phonon frequency, because the positively charged ions experience the electrostatic forces with less intensity due to a neutralizing background created by the electrons. Strong screening can lead to Kohn anomalies or even charge density waves and structural phase transitions [76]. On the other hand, EPC can also strongly affect the electrons and create interesting features in their band structure, as mentioned in Chapter 1. In this section, we will try to understand how the electron-phonon interaction affects both the phonons and electrons simultaneously. In the following we show how this perplexing self-consistency problem can be resolved for practical calculations within the DFT framework.

4.1.1 Electron and phonon self-energies

The interacting electron and phonon propagators satisfy their corresponding Dyson equations [2],

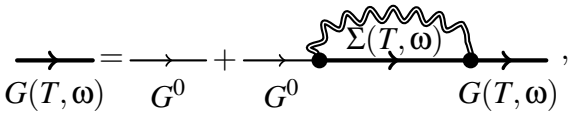

(4.1)

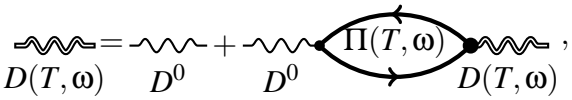

(4.2)

which mirror the self-consistency of the underlying problem. The electron (phonon) propagators are denoted by G (D), while the bare noninteracting propagators are G^0 (D^0). The black dots represent the EPC matrix elements, with the larger one being the dynamically screened one and the smaller one the bare vertex. The two expressions are symmetric and depict the process of the bare propagator being screened by the EPC. The diagrammatic Dyson equation can be rewritten in the Matsubara finite temperature formalism for the electron Green's function as

$$G_n(\mathbf{k}, ip_j) = G_n^0(\mathbf{k}, ip_j) + G_n^0(\mathbf{k}, ip_j)\Sigma_n(\mathbf{k}, ip_j)G_n(\mathbf{k}, ip_j) \tag{4.3}$$

and similarly for the interacting phonon propagator

$$D_\nu(\mathbf{q}, i\omega_j) = D_\nu^0(\mathbf{q}, i\omega_j) + D_\nu^0(\mathbf{q}, i\omega_j)\Pi_\nu(\mathbf{q}, i\omega_j)D_\nu(\mathbf{q}, i\omega_j). \tag{4.4}$$

These Dyson equations state that the exact interacting electron and phonon propagators can be obtained just by calculating the electron-phonon electron $\Sigma_n(\mathbf{k}, i\omega_j)$ and phonon $\Pi_\nu(\mathbf{q}, i\omega_j)$ self-energy terms. The finite temperature dependence is implied in the definition of the Matsubara fermion $p_j = (2j+1)\pi k_B T$ and boson frequencies $\omega_j = 2j\pi k_B T$. The bare propagators describe the propagation of noninteracting electrons or phonons. They have poles at the locations of the bare electron energies $\varepsilon_{\mathbf{k},n}$ or phonon frequencies $\omega_{\mathbf{q},\nu}$ written as

$$G_n^0(\mathbf{k}, ip_j) = \frac{1}{ip_j - \varepsilon_{\mathbf{k},n}} \tag{4.5}$$

$$D_\nu^0(\mathbf{q}, i\omega_j) = \frac{2\omega_{\mathbf{q},\nu}}{(i\omega_j)^2 - (\omega_{\mathbf{q},\nu})^2}. \tag{4.6}$$

Expressions (4.5) and (4.6) can be substituted in the Dyson equations leading to

$$G_n(\mathbf{k}, ip_j) = \frac{1}{ip_j - \varepsilon_{\mathbf{k},n} - \Sigma_n(\mathbf{k}, ip_j)} \tag{4.7}$$

$$D_\nu(\mathbf{q}, i\omega_j) = \frac{2\omega_{\mathbf{q},\nu}}{(i\omega_j)^2 - (\omega_{\mathbf{q},\nu})^2 - 2\omega_{\mathbf{q},\nu}\Pi_\nu(\mathbf{q}, i\omega_j)}. \tag{4.8}$$

The expressions for the dressed propagators Eqs. (4.8) and (4.7) and the bare ones Eqs. (4.6) and (4.5) resemble each other. The differences between the two can be described by the two effects induced by the electron-phonon self-energies:

1. the bare electron (phonon) energy spectrum is shifted by the real part of the electron-phonon induced electron (phonon) self-energy

2. the electron (phonon) energy spectrum is broadened by the imaginary part of the electron-phonon induced electron (phonon) self-energy.

Since all measurable properties are actually retarded correlation functions, the goal is almost always to calculate retarded propagators. These can be obtained by analytical continuation of the Matsubara frequencies in the upper complex plane, i.e., $ip_j \to E + i\delta$ and $i\omega_j \to \omega + i\delta$.
In order to reach the expressions for the electron and phonon self-energy, we return to the Feynman diagrams (4.1) and (4.2). The expression for the electron self-energy from the diagram is

$$\Sigma_n(\mathbf{k}, ip_j) = \frac{1}{\beta}\sum_{m\mathbf{q}\nu}\sum_{i\omega_j}\left[\tilde{g}^{nm}_{\nu}\left(\mathbf{k},\mathbf{k}+\mathbf{q}\right)\right]^* \tilde{g}^{nm}_{\nu}\left(\mathbf{k},\mathbf{k}+\mathbf{q}\right) \times D_{\nu}(\mathbf{q}, i\omega_j) G_m(\mathbf{k}+\mathbf{q}, ip_j + i\omega_j) \tag{4.9}$$

and for the phonon self-energy

$$\Pi_{\nu}(\mathbf{q}, i\omega_j) = \frac{1}{\beta}\sum_{nm\mathbf{k}}\sum_{ip_j}\left[g^{nm}_{\nu}\left(\mathbf{k},\mathbf{k}+\mathbf{q}\right)\right]^* \tilde{g}^{nm}_{\nu}\left(\mathbf{k},\mathbf{k}+\mathbf{q}\right) \times G_n(\mathbf{k}, ip_j) G_m(\mathbf{k}+\mathbf{q}, ip_j + i\omega_j) \tag{4.10}$$

where g ($\tilde{g}$) is the bare (screened) EPC vertex defined with Eq. (2.51) [Eq. (2.52)]. Even though the screened vertex is dynamically screened, we omit writing its frequency dependence because it is the usual practice. From now on, we will write the dependence of EPC matrix elements on $(\mathbf{k}, \mathbf{k}+\mathbf{q})$ as $(\mathbf{k}, \mathbf{q})$. These are the full self-energy expressions and far too complicated to be calculated from first principles. The entangling self-consistency is reflected in the fact that in order to calculate the self-energy, an exact interacting propagator is required, for which the self-energy needs to be known. For practical *ab-initio* calculations, we need to start somewhere and break this cycle. A significant simplification can be made if one evaluates the self-energy expressions only in the first order, where the dressed propagator are replaced by their bare counterparts. Diagrammatically, this amounts to reducing the Dyson equations to

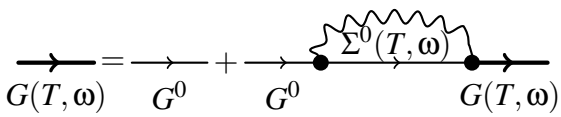

(4.11)

for the electron and

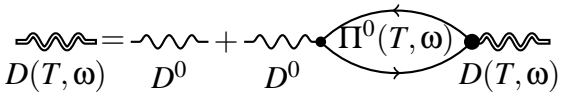

(4.12)

for the phonon self-energy. Further connection with the first-principles DFPT calculations is done by employing the BOA [4, 30, 77]. The phonon self-energy is therefore not only calculated in the first order, but DFPT calculations also reduces the first-order phonon self-energy to its static limit [4]. A separate EPC calculation with EPW needs to be performed in order to obtain the dynamical first-order self-energies.

In this thesis, the main focus will be on the phonon self-energy, its first principles calculations with DFPT and EPW, and their improvements and analysis with theoretical and computational adjustments. Regarding the theoretical corrections that are performed within this thesis, we will now introduce the dynamical renormalization of phonons and extension of the phonon self-energy calculation up to all orders of the perturbation theory.

4.1.2 *Ab-initio* phonon renormalization

In DFPT, an electronic contribution to the interatomic force constants is evaluated as a static, first-order expression of the phonon self-energy in Eq. (4.10) [30]. As announced, the self-energy which renormalizes the bare phonons in DFPT can be obtained by taking the bare electron propagators instead of full propagators in Eq. (4.10)

$$\Pi^0_\nu(\mathbf{q}, i\omega_j) = \frac{1}{\beta}\sum_{nm\mathbf{k}}\sum_{ip_j}\left[g^{nm}_\nu\left(\mathbf{k},\mathbf{q}\right)\right]^* \tilde{g}^{nm}_\nu\left(\mathbf{k},\mathbf{q}\right) \times G^0_n(\mathbf{k}, ip_j) G^0_m(\mathbf{k}+\mathbf{q}, ip_j + i\omega_j). \tag{4.13}$$

Plugging in the expressions for the bare propagators, one obtains

$$\Pi^0_\nu(\mathbf{q}, i\omega_j) = \frac{1}{\beta}\sum_{nm\mathbf{k}}\sum_{ip_j}\left[g^{nm}_\nu\left(\mathbf{k},\mathbf{q}\right)\right]^* \tilde{g}^{nm}_\nu\left(\mathbf{k},\mathbf{q}\right) \frac{1}{ip_j - \varepsilon_{\mathbf{k},n}} \frac{1}{ip_j + i\omega_j - \varepsilon_{\mathbf{k}+\mathbf{q},m}}. \tag{4.14}$$

Summation over the Matsubara frequencies p_j is performed by solving a complex integral

$$\oint \frac{1}{z - \varepsilon_{\mathbf{k},n}} \frac{1}{z + i\omega_j - \varepsilon_{\mathbf{k}+\mathbf{q},m}} \frac{1}{e^{\beta z}+1} dz = 2\pi i \sum \text{Res} \tag{4.15}$$

along an infinitely large circumference $z = \mathrm{R}e^{i\phi}$, $\mathrm{R}\to\infty$. Since the integral vanishes, it is enough to calculate the sum of residua. The contributions to the sum are listed below

$$z_1 = \varepsilon_{\mathbf{k},n}: \qquad \frac{1}{\varepsilon_{\mathbf{k},n} + i\omega_j - \varepsilon_{\mathbf{k}+\mathbf{q},m}} \frac{1}{e^{\beta\varepsilon_{\mathbf{k},n}}+1} = \frac{f(\varepsilon_{\mathbf{k},n})}{\varepsilon_{\mathbf{k},n} + i\omega_j - \varepsilon_{\mathbf{k}+\mathbf{q},m}} \tag{4.16}$$

$$z_2 = -i\omega_j + \varepsilon_{\mathbf{k}+\mathbf{q},m}: \qquad \frac{1}{-i\omega_j + \varepsilon_{\mathbf{k}+\mathbf{q},m} - \varepsilon_{\mathbf{k},n}} \cdot \frac{1}{e^{-i\beta\omega_j + \beta\varepsilon_{\mathbf{k}+\mathbf{q},m}}+1} = -\frac{f(\varepsilon_{\mathbf{k}+\mathbf{q},m})}{\varepsilon_{\mathbf{k}+\mathbf{q},m} - i\omega_j - \varepsilon_{\mathbf{k}}}$$

$$z_3 = \frac{i\pi(2n+1)}{\beta}: \qquad \frac{1}{ip_n - \varepsilon_{\mathbf{k},n}} \frac{1}{ip_n + i\omega_j - \varepsilon_{\mathbf{k}+\mathbf{q},m}} \frac{1}{\beta}. \tag{4.17}$$

The Fermi-Dirac distribution $1/(e^{\beta\varepsilon}+1)$ is denoted by $f(\varepsilon)$. Adding back the EPC matrix elements, we notice that the last residuum is the desired quantity. Phonon self-energy is, therefore, equal to the sum of the first two residua:

$$\Pi^0_\nu(\mathbf{q}, i\omega_j) = \sum_{nm\mathbf{k}} \left[g^{nm}_\nu(\mathbf{k},\mathbf{q})\right]^* \tilde{g}^{nm}_\nu(\mathbf{k},\mathbf{q}) \frac{f(\varepsilon_{\mathbf{k},n}) - f(\varepsilon_{\mathbf{k}+\mathbf{q},m})}{\varepsilon_{\mathbf{k},n} + i\omega_j - \varepsilon_{\mathbf{k}+\mathbf{q},m}}. \tag{4.18}$$

Performing an analytical continuation to the upper complex plane with $i\omega_j = \omega + i\eta$, where η is an infinitesimal parametar $\eta \to 0^+$ results in the standard expression for the first-order phonon self-energy:

$$\Pi^0_\nu(\mathbf{q}, \omega) = \sum_{nm\mathbf{k}} \left[g^{nm}_\nu(\mathbf{k},\mathbf{q})\right]^* \tilde{g}^{nm}_\nu(\mathbf{k},\mathbf{q}) \frac{f(\varepsilon_{\mathbf{k},n}) - f(\varepsilon_{\mathbf{k}+\mathbf{q},m})}{\varepsilon_{\mathbf{k},n} - \varepsilon_{\mathbf{k}+\mathbf{q},m} + \omega + i\eta}. \tag{4.19}$$

In order to get a static contribution as in DFPT, one needs to set $\omega = 0$. Formally, this implies that the phonons from DFPT are statically screened, because the full wealth of information hidden in the dynamical dielectric function which screens the vertices, is replaced by its static counterpart [78]. Another important thing to note is that EPC calculations based on DFPT are dealing with both vertices screened, because the bare vertex is inaccessible in DFPT. Luckily, even though the usual many-body expression for the phonon self-energy contains only one screened vertex [4, 79], it was recently shown that the double-screened equation used in the work throughout this thesis is the most

accurate when combined with DFT due to error cancellation to first order [77, 80]. It leads to the expression

$$\Pi^0_\nu(\mathbf{q}) = \sum_{nm\mathbf{k}} \left|\tilde{g}^{nm}_\nu\left(\mathbf{k},\mathbf{q}\right)\right|^2 \frac{f(\varepsilon_{\mathbf{k},n}) - f(\varepsilon_{\mathbf{k}+\mathbf{q},m})}{\varepsilon_{\mathbf{k},n} - \varepsilon_{\mathbf{k}+\mathbf{q},m}}. \tag{4.20}$$

The adiabatic DFPT phonon propagator, can therefore be written as

$$D_\nu(\mathbf{q},\omega) = \frac{2\omega_{\mathbf{q},\nu}}{\omega^2 - \omega^2_{\mathbf{q}\nu} - 2\omega_{\mathbf{q}\nu}\Pi^0_\nu(\mathbf{q})} \tag{4.21}$$

and it consists of a series of delta functions centered at the adiabatic DFPT phonon frequencies

$$\omega^{\mathrm{A}}_{\mathbf{q}\nu} = \sqrt{(\omega_{\mathbf{q}\nu})^2 + 2\omega_{\mathbf{q}\nu}\Pi^0_\nu(\mathbf{q})},$$

where $\omega_{\mathbf{q}\nu}$ are the bare frequencies, when electron-electron interactions are not included. Phonons calculated in DFPT are adiabatic modes with infinite lifetime and have no physical spectral width in phonon density of states (DOS). The main issue with calculating the dynamical phonon self-energy and thereby obtaining the EPC induced phonon linewidth, is its convergence. The summation in Eq. (4.19) needs to be performed over very dense grids of $\mathbf{k}$ and $\mathbf{q}$ vectors, what became feasible with the implementation of the Wannier interpolation in the EPC calculation, or in the EPW code.

Since the starting point of EPC calculations in this thesis is DFPT, the phonon frequencies which enter the EPC calculation with EPW, are already renormalized by the static part of the phonon self-energy. When performing an EPC calculation, one needs to calculate separately the dynamical [Eq. (4.19)] phonon self-energy using dense $\mathbf{k}$- and $\mathbf{q}$-grids and the static part [Eq. (4.20)] using the same grid and electronic temperature as used in the DFPT calculation. In this way, one can exactly subtract the static contribution that the adiabatic frequencies already contain and add the full dynamical self-energy at any desired temperature, calculated with arbitrarily dense grids. The phonon self-energy object, obtained in this way, will here be called the NA phonon self-energy [4]

$$\Pi^{\mathrm{NA}}_\nu(\mathbf{q},\omega) = \Pi^0_\nu(\mathbf{q},\omega) - \Pi^0_\nu(\mathbf{q}). \tag{4.22}$$

Explicitly, the real and imaginary parts of the dynamical phonon self-energy are

$$\mathrm{Re}\left[\Pi^0_\nu(\mathbf{q},\omega)\right] = \sum_{nm\mathbf{k}} \left|\tilde{g}^{nm}_\nu\left(\mathbf{k},\mathbf{q}\right)\right|^2 (\varepsilon_{\mathbf{k},n} - \varepsilon_{\mathbf{k}+\mathbf{q},m} + \omega) \frac{f(\varepsilon_{\mathbf{k},n}) - f(\varepsilon_{\mathbf{k}+\mathbf{q},m})}{(\varepsilon_{\mathbf{k},n} - \varepsilon_{\mathbf{k}+\mathbf{q},m} + \omega)^2 + \eta^2}, \tag{4.23}$$

$$\mathrm{Im}\left[\Pi^0_\nu(\mathbf{q},\omega)\right] = -\eta \sum_{nm\mathbf{k}} \left|\tilde{g}^{nm}_\nu\left(\mathbf{k},\mathbf{q}\right)\right|^2 \frac{f(\varepsilon_{\mathbf{k},n}) - f(\varepsilon_{\mathbf{k}+\mathbf{q},m})}{(\varepsilon_{\mathbf{k},n} - \varepsilon_{\mathbf{k}+\mathbf{q},m} + \omega)^2 + \eta^2}. \tag{4.24}$$

The NA (or dynamic) phonons propagator is now

$$D_\nu(\mathbf{q},\omega) = \frac{2\omega^{\mathrm{A}}_{\mathbf{q}\nu}}{\omega^2 - (\omega^{\mathrm{A}}_{\mathbf{q}\nu})^2 - 2\omega^{\mathrm{A}}_{\mathbf{q}\nu}\Pi^{\mathrm{NA}}_\nu(\mathbf{q},\omega)}. \tag{4.25}$$

It now corresponds to a sum of Lorentzians centered at

$$\omega \approx \omega^{\mathrm{A}}_{\mathbf{q}\nu} + \mathrm{Re}\left[\left(\Pi^{\mathrm{NA}}_\nu(\mathbf{q},\omega)\right)\right]$$

with a width

$$\gamma_{\mathbf{q}\nu} = -2\mathrm{Im}\left[\Pi^{\mathrm{NA}}_\nu(\mathbf{q},\omega)\right].$$

Usually, for the calculations of the NA frequency shift and the corresponding linewidth, we use the on-shell approximation $\Pi^0_\nu(\mathbf{q},\omega) \to \Pi^0_\nu(\mathbf{q},\omega_{\mathbf{q}\nu})$. For the calculations of the phonon spectral function

$$B_\nu(\mathbf{q},\omega) = -\frac{1}{\pi}\mathrm{Im}\left[\frac{2\omega^{\mathrm{A}}_{\mathbf{q}\nu}}{\omega^2 - (\omega^{\mathrm{A}}_{\mathbf{q}\nu})^2 - 2\omega^{\mathrm{A}}_{\mathbf{q}\nu}\Pi^{\mathrm{NA}}_\nu(\mathbf{q},\omega)}\right]. \tag{4.26}$$

we do not resort to the on-shell approximation.

With this tool we are able to simulate more realistic phonon spectra having both EPC-induced frequency shifts and broadenings. Next we show how to go beyond the standard first-order self-energy contribution and introduce higher-order electron-phonon scattering events.

4.1.3 Intraband phonon self-energy beyond the first-order term

Even though *ab-initio* calculations allow for the first-order phonon self-energy calculations, the bare electron and hole propagators, which constitute a phonon self-energy bubble can also be interacting. This is already implicitly shown diagrammatically in the phonon Dyson equation (4.2), with the *dressed* instead of the bare propagators constituting the self-energy diagram. Here we will examine a special limit, where instead of having free electron-hole pairs interacting with phonons, we include the effects of electron (or hole)-phonon interaction within these single-particle *dressed* propagators.

First, a derivation of the first-order electron self-energy will be provided, in order to later draw an analogy with the more complex electron-hole self-energy. The finite temperature expression for

the electron self-energy can be obtained using the Matsubara formalism. The first-order electron self-energy is [2]

$$\Sigma(\mathbf{p},E) = i\sum_{\nu\mathbf{q}}\int_{-\infty}^{\infty}\frac{d\omega}{2\pi}|g_\nu(\mathbf{p},\mathbf{q})|^2 D^0(\mathbf{q},\omega)G^0(\mathbf{p}-\mathbf{q},E-\omega), \tag{4.27}$$

where the band indices are omitted. To calculate this sum, it is convenient to define a complex integral

$$\oint \frac{2\omega_{\mathbf{q}\nu}}{-z^2+\omega_{\mathbf{q}\nu}^2}\frac{1}{ip_n+z-\varepsilon_{\mathbf{p}+\mathbf{q}}}\frac{1}{e^{\beta z}-1}dz = 2\pi i\sum Res \tag{4.28}$$

over a large closed loop. The left hand side of this equation vanishes, what becomes obvious if we integrate along an infinitely large circle $z = Re^{i\phi}$, R$\to\infty$. Sum of residua can be calculated as

$$\begin{aligned}
z_1 = \omega_{\mathbf{q}\nu}: &\\
&\frac{1}{ip_n+\omega_{\mathbf{q}\nu}-\varepsilon_{\mathbf{p}+\mathbf{q}}}\cdot\frac{1}{e^{\beta\omega_{\mathbf{q}\nu}}-1} = \frac{f^B(\omega_{\mathbf{q}\nu})}{ip_n+\omega_{\mathbf{q}\nu}-\varepsilon_{\mathbf{p}+\mathbf{q}}}\\
z_2 = -\omega_{\mathbf{q}\nu}: &\\
&\frac{1}{ip_n-\omega_{\mathbf{q}\nu}-\varepsilon_{\mathbf{p}+\mathbf{q}}}\cdot\frac{1}{e^{-\beta\omega_{\mathbf{q}\nu}}-1} = \frac{f^B(\omega_{\mathbf{q}\nu})+1}{ip_n-\omega_{\mathbf{q}\nu}-\varepsilon_{\mathbf{p}+\mathbf{q}}}\\
z_3 = -ip_n+\varepsilon_{\mathbf{p}+\mathbf{q}}: &\\
&\frac{2\omega_{\mathbf{q}\nu}}{\omega_{\mathbf{q}\nu}^2-(ip_n-\varepsilon_{\mathbf{p}+\mathbf{q}})^2}\cdot\frac{1}{e^{\beta(\varepsilon_{\mathbf{p}+\mathbf{q}}-ip_n)}-1} = -\frac{2\omega_{\mathbf{q}\nu}}{\omega_{\mathbf{q}\nu}^2-(ip_n-\varepsilon_{\mathbf{p}+\mathbf{q}})^2}f(\varepsilon_{\mathbf{p}+\mathbf{q}})\\
z_4 = \frac{i2\pi n}{\beta}: &\\
&\frac{2\omega_{\mathbf{q}\nu}}{\omega_{\mathbf{q}\nu}^2-(i\omega_n)^2}\cdot\frac{1}{ip_n+i\omega_n-\varepsilon_{\mathbf{p}+\mathbf{q}}}\frac{1}{\beta}
\end{aligned} \tag{4.29}$$

The Bose-Einstein distribution $1/(e^{\beta\varepsilon}-1)$ is denoted by $f^B(\varepsilon)$. The last residuum is equal to the electron self-energy

$$\begin{aligned}
\Sigma(\mathbf{p},ip_n) = &\sum_{\mathbf{q}\nu}|g_\nu(\mathbf{p},\mathbf{q})|^2\\
&\times\left(\frac{f^B(\omega_{\mathbf{q}\nu})+f(\varepsilon_{\mathbf{p}+\mathbf{q}})}{ip_n+\omega_{\mathbf{q}\nu}-\varepsilon_{\mathbf{p}+\mathbf{q}}}+\frac{f^B(\omega_{\mathbf{q}\nu})+1-f(\varepsilon_{\mathbf{p}+\mathbf{q}})}{ip_n-\omega_{\mathbf{q}\nu}-\varepsilon_{\mathbf{p}+\mathbf{q}}}\right).
\end{aligned} \tag{4.30}$$

Analytical continuation $ip_n \to \omega + i\eta$ leads to a retarded electron self-energy

$$\Sigma(\mathbf{p},\omega) = \sum_{\mathbf{q}\nu} |g_\nu(\mathbf{p},\mathbf{q})|^2 \tag{4.31}$$

$$\times \left(\frac{f^B(\omega_{\mathbf{q}\nu}) + f(\varepsilon_{\mathbf{p}+\mathbf{q}})}{\omega + i\eta + \omega_{\mathbf{q}\nu} - \varepsilon_{\mathbf{p}+\mathbf{q}}} + \frac{f^B(\omega_{\mathbf{q}\nu}) + 1 - f(\varepsilon_{\mathbf{p}+\mathbf{q}})}{\omega + i\eta - \omega_{\mathbf{q}\nu} - \varepsilon_{\mathbf{p}+\mathbf{q}}} \right).$$

The first-order electron self-energy is available in EPW, but here we aim to go a step further and calculate the electron self-energy with renormalized electron and phonon propagators

$$\Sigma(\mathbf{k}, ip_k) = -\frac{1}{\beta} \sum_{\mathbf{q}\nu j} \int_{-\infty}^{\infty} \frac{d\omega}{2\pi} |g_\nu(\mathbf{k},\mathbf{q})|^2 D_\nu(\mathbf{q}, i\omega_j) G(\mathbf{k}-\mathbf{q}, ip_k - i\omega_j). \tag{4.32}$$

The phonon spectral function can be used to introduce the spectral representation of the phonon propagator

$$D_\nu(\mathbf{q}, i\omega_j) = \int_0^\infty B_\nu(\mathbf{q},\Omega) \left[\frac{1}{i\omega_j - \Omega} - \frac{1}{i\omega_j + \Omega} \right]. \tag{4.33}$$

Another quantity that will appear due to the product of the EPC vertex and the spectral representation of the phonon propagator in Eq. (4.32) is the electron-phonon spectral function. It can be defined as

$$\alpha^2F(\mathbf{k},\mathbf{q},\Omega) = N_0 |g_\nu(\mathbf{k},\mathbf{k}+\mathbf{q})|^2 B_\nu(\mathbf{q},\Omega), \tag{4.34}$$

where N_0 denotes the bare DOS, $N(\varepsilon)$, at the Fermi level. It is usually called the Eliashberg spectral function and it is frequently found averaged over the Fermi surface

$$\alpha^2F(\Omega) = \frac{1}{N_0^2} \sum_{\mathbf{kq}} \alpha^2F(\mathbf{k},\mathbf{q},\Omega) \delta(\varepsilon_{\mathbf{k}} - \varepsilon_F) \delta(\varepsilon_{\mathbf{k}+\mathbf{q}} - \varepsilon_F). \tag{4.35}$$

Plugging Eqs. (4.34) and (4.33) into Eq. (4.32), the expression for the electron self-energy becomes

$$\Sigma(\mathbf{k}, ip_k) = \frac{1}{\beta} \sum_{\mathbf{q}j} \int_0^\infty d\Omega \frac{\alpha^2F(\mathbf{k},\mathbf{q},\Omega)}{N_0} \left(\frac{2\Omega}{\omega_j^2 + \Omega^2} \right) G(\mathbf{k}-\mathbf{q}, ip_k - i\omega_j). \tag{4.36}$$

Using a Fermi surface harmonics formalism, the angular and energy part of the $\mathbf{k}$ dependence can be separated [81]. Focusing on the energy part can be viewed as averaging over the Fermi surface, and

it leaves us with

$$\Sigma(ip_k) = \frac{1}{\beta}\sum_{\mathbf{q}j}\int_{-\infty}^{\infty} d\varepsilon \frac{\tilde{N}(\varepsilon)}{N_0}\int_0^{\infty} d\Omega \alpha^2 F(\Omega)\left(\frac{2\Omega}{\omega_j^2+\Omega^2}\right) G(\varepsilon, ip_k - i\omega_j). \tag{4.37}$$

After a Matsubara frequency summation and an analytical continuation to the upper complex plane, the imaginary part of the electron self-energy is [82]

$$\mathrm{Im}\Sigma(\varepsilon) = -\pi\int_0^{\infty} d\Omega \alpha^2 F(\Omega)\left\{\frac{\tilde{N}(\varepsilon-\Omega)}{N_0}[f_B(\Omega)+1+f(\varepsilon-\Omega)] + \frac{\tilde{N}(\varepsilon+\Omega)}{N_0}[f_B(\Omega)+f(\varepsilon+\Omega)]\right\}. \tag{4.38}$$

An important thing to notice is that instead of taking into account only the bare DOS, the quasi-particle DOS is calculated

$$\tilde{N}(\varepsilon) = \int d\mathbf{k} A(\varepsilon, \mathbf{k}). \tag{4.39}$$

It is done self-consistently from the set of equations for the electron spectral function

$$A(\varepsilon, \mathbf{k}) = \frac{\mathrm{Im}\Sigma(\varepsilon)}{[\varepsilon - \varepsilon_{\mathbf{k}} - \mathrm{Re}\Sigma(\varepsilon) + \mu]^2 + [\mathrm{Im}\Sigma(\varepsilon)]^2}. \tag{4.40}$$

Along with the quasiparticle DOS $\tilde{N}(\varepsilon)$ and spectral function $A(\varepsilon, \mathbf{k})$, in the self-consistent calculation one also needs to include the chemical potential temperature shift $\mu(T)$. The chemical potential needs to be obtained from a renormalized DOS, by imposing conservation of carriers with the temperature change. Namely, if at a very low temperature, with the energies ε measured from the Fermi level, the system contains a certain number of carriers n_0, then as temperature increases, the chemical potential needs to be adjusted in order to host the same number of electrons

$$n_0 = \int_{-\infty}^{\infty} d\varepsilon \tilde{N}(\varepsilon) f(\varepsilon, T \to 0) = \int_{-\infty}^{\infty} d\varepsilon \tilde{N}(\varepsilon + \delta\mu(T)) f(\varepsilon, T). \tag{4.41}$$

The object we are searching for is the electron-hole self-energy, a two-particle property. However, the derived one-particle features will be its building blocks.

The electron-hole pair self-energy $M_{nm}(\mathbf{k}, i\zeta_j)$ is defined through the Bethe-Salpeter equation for the electron-hole pair propagator $Z_{nm}(\mathbf{k}, i\zeta_j)$ with the electron-phonon interaction:

$$Z_{nm}(\mathbf{k}, i\zeta_j) = Z^0_{nm}(\mathbf{k}, i\zeta_j) + Z^0_{nm}(\mathbf{k}, i\zeta_j) M_{nm}(\mathbf{k}, i\zeta_j) Z_{nm}(\mathbf{k}, i\zeta_j), \tag{4.42}$$

where each object should have four band indices [83], but for clarity, we condensed them into two. In terms of Feynman diagrams, the Eq. (4.42) can be written as

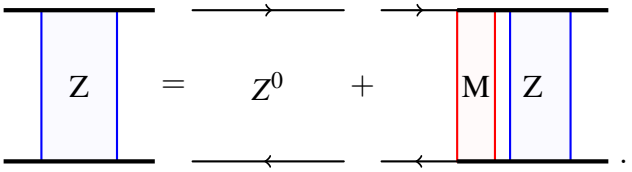

(4.43)

Scatterings of electron-hole pairs on phonons include the summation of diagrams that differ topologically (i.e., self-energy, vertex, and cross terms), but here only the Fan-Migdal self-energy contributions are included

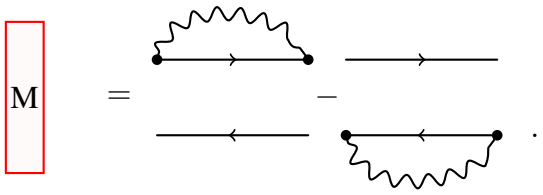

(4.44)

Omitting the wave vector index, it can be written as

$$M_{nm}(i\zeta_j) = \frac{1}{\beta}\sum_k \left[\Sigma_n(ip_k)G^0_m(i\zeta_j + ip_k) + \Sigma_m(ip_k)G^0_n(ip_k - i\zeta_j)\right] \tag{4.45}$$

or rewriting $\Sigma_n(ip_k)$ in terms of electron and phonon propagators

$$M_{nm}(i\zeta_j) = -\frac{1}{\beta}\sum_{k,l,\nu,m',n'} \Big[D^0_\nu(i\omega_l)G^0_{n'}(i\omega_l + ip_k)G^0_m(i\zeta_j + ip_k)|g^{nn'}_\nu|^2 \tag{4.46}$$

$$+D^0_\nu(i\omega_l)G^0_{m'}(i\omega_l + ip_k)G^0_n(i\zeta_j + ip_k)|g^{mm'}_\nu|^2. \tag{4.47}$$

Matsubara summation over indices k,l leads to the expression for the electron-hole self-energy

$$M_{nm}(i\zeta_j) = \sum_{\nu n'}|g^{nn'}_\nu|^2\left(\mathscr{S}_1^{nn'} + \mathscr{S}_2^{nn'}\right) + \sum_{\nu m'}|g^{mm'}_\nu|^2\left(\mathscr{S}_1^{mm'} + \mathscr{S}_2^{mm'}\right) \tag{4.48}$$

where

$$\mathscr{S}_1^{nn'} = \sum_{s=\pm 1}\frac{f^B\left(\omega_{\nu\mathbf{q}}\right) + f\left(s\varepsilon_{n'\mathbf{k}+\mathbf{q}}\right)}{i\zeta_j + \varepsilon_{n\mathbf{k}} - \varepsilon_{n'\mathbf{k}+\mathbf{q}} + s\omega_{\nu\mathbf{q}}}, \tag{4.49}$$

$$\mathscr{S}_2^{nn'} = \sum_{s=\pm 1} \frac{f^B\left(\omega_{\nu\mathbf{q}}\right) + f\left(-s\varepsilon_{n\mathbf{k}+\mathbf{q}}\right)}{i\zeta_j + \varepsilon_{n\mathbf{k}+\mathbf{q}} - \varepsilon_{n'\mathbf{k}} + s\omega_{\nu\mathbf{q}}}. \tag{4.50}$$

This expression greatly resembles the expression for the electron self-energy in Eq. (4.31), with an important difference hidden in the denominator. It might seem like a minor mathematical detail, but conceptually the single-electron energy in the denominator of Eq. (4.31) and an electron-hole energy in Eq. (4.48) mirror the single- and two-particle nature of these quantities. In analogy with the procedure done for the full electron self-energy derivation, one can obtain the electron-hole self-energy with renormalized electron and phonon propagators. Resembling the imaginary part of the electron self-energy from Eq. (4.38), the resulting expression for the imaginary part of the electron-hole self-energy is [82]

$$\begin{aligned}\frac{1}{\tau_{\mathrm{op}}(\omega,T)} = \frac{\pi}{\omega}\int_0^\infty d\Omega\alpha^2F(\Omega)\\ \int_{-\infty}^{\infty} d\varepsilon \left\{\frac{\tilde{N}(\varepsilon-\Omega,T)}{N_0} + \frac{\tilde{N}(-\varepsilon+\Omega,T)}{N_0}\right\}\\ [f_B(\Omega,T) + f(\Omega-\varepsilon,T)][f(\varepsilon-\omega,T) - f(\varepsilon+\omega,T)],\end{aligned} \tag{4.51}$$

where the dependence on temperature T is explicitly denoted. The ingredients of the imaginary parts of the electron-hole self-energy and of the electron self-energy are the same, but the former contains an additional energy integration. $1/\tau_{\mathrm{op}}(\omega)$ is an inverse of the lifetime that the electron-hole pairs have due to their interaction with phonons. The same expression is commonly used for description of higher electron-phonon scattering terms in optical conductivity formula, where $1/\tau_{\mathrm{op}}(\omega)$ is sometimes called optical electron-hole scattering rate (hence the subscript). The real part of the electron-hole self-energy can be obtained with the Kramers-Kronig transformation of $1/\tau_{\mathrm{op}}(\omega)$ and it is denoted by $\omega\lambda_{\mathrm{op}}(\omega)$.

It remains to be understood how the electron-hole scattering affects the phonons. It will now be shown where the electron-hole self-energy enters the phonon self-energy expression and exactly when it is necessary to include it.

The first-order phonon self-energy can be divided on the inter- and intra-band contributions. The former contains processes in which an electron scatters on a phonon, and with its energy it makes a transition from one band to the other. The intraband process in the first order, describes a process in which an electron stays in the same band, but changes its energy or momentum (or both). Mathematically, these two contributions can be obtained by setting $n = m$ or $n \neq m$ in the sum in Eq. (4.19). Since the first-order perturbation theory for these processes is already finite, there is no

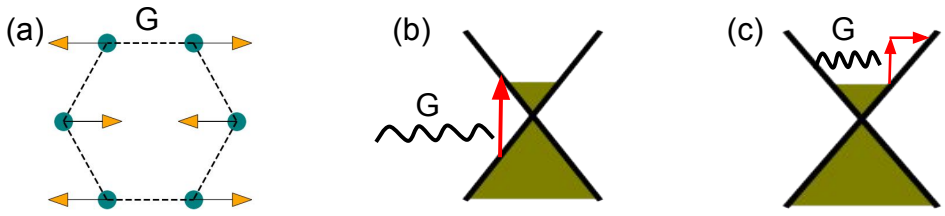

Figure 4.1: (a) Strongly-coupled optical 200 meV mode of E_{2g} symmetry (G mode) in graphene. (b) Schematics of graphene's Dirac cone with a G mode facilitated first-order interband vertical transition. (c) Schematics of an electron-hole higher order (multi-step processes) contribution to the intraband phonon self-energy.

immediate need to employ higher orders as well. However, what if we focus on the long-wavelength limit? In Fig. 4.1 we show the inter- and intra-band contributions using example of graphene. Its optical mode of E_{2g} symmetry, called the G mode, couples strongly to electrons, and assists their transitions. From the schematics 4.1 it is clear that the interband contribution remains finite in the first order, and simply counts vertical electron transitions, but a direct vertical intraband excitation seems impossible. Mathematically, taking the $\mathbf{q} \to 0$ limit, we obtain two first-order contributions to the phonon renormalization, corresponding to the adiabatic intraband

$$\Pi_{\nu}^{\text{intra},0}(\mathbf{q}=0) = \sum_{\mathbf{k}n} |g_{\nu}^{nn}(\mathbf{k},\mathbf{q}=0)|^2 \left(-\frac{\partial f_{n,\mathbf{k}}}{\partial \varepsilon_{n,\mathbf{k}}}\right) \tag{4.52}$$

and dynamical interband electron transitions:

$$\Pi_{\nu}^{\text{inter},0}(\mathbf{q}=0,\omega) = \sum_{\mathbf{k}n\neq m} |g_{\nu}^{\text{nm}}(\mathbf{k},\mathbf{q}=0)|^2 \frac{f_{\text{n}\mathbf{k}} - f_{\text{m}\mathbf{k}}}{\omega + \varepsilon_{\text{n}\mathbf{k}} - \varepsilon_{\text{m}\mathbf{k}} + i\eta}. \tag{4.53}$$

Within the first-order perturbation theory NA effects can be included only in the interband channel, since only that term has a frequency dependence. The first-order intraband term is static and it contains scattering processes within the narrow energy window, broadened by temperature. It has no imaginary part, thereby providing no EPC linewidth contribution.

In the Raman experiments, where light has a vanishing impulse, it either excites phonons directly with $\mathbf{q} \to 0$, or indirectly, through the electron-hole pair relaxation. The difference between the two processes is what the photon couples to, whether directly to phonons or via electron-hole pairs. Both of these processes, however, include a phonon. In graphene and other materials, even though these dynamical first-order intraband phonon self-energy contributions vanish in the long-wavelength

limit, Raman experiments still suggest that they in fact must somehow contribute to the linewidth. In the first order, a phonon is interacting with electrons via generation of electron-hole pairs. The processes which are disregarded in the first-order perturbation theory are the ones describing how the generated electron-hole pairs interact with phonons as well. This process results in the dynamical contribution to the intraband phonon self-energy. In conclusion, we need to include the higher-order processes in the intraband phonon self-energy term, in its long-wavelength limit, since its dynamical first-order contribution disappears.

Using a diagrammatic technique, the phonon self-energy bubble is renormalized by the diagrams describing electron-hole scattering on all the relevant phonons of the system

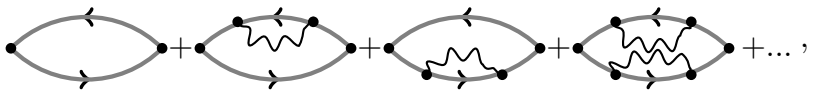

(4.54)

where the electron-hole bubbles are not bare, but are in fact interacting with phonons as well

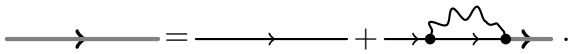

(4.55)

Here, thick grey lines are used to indicate a propagator renormalized by EPC. In this derivation, a type of diagrams that has phonons connecting the electron and hole lines inside the bubble are called vertex corrections and are omitted here.

Diagrams in Eq. (4.54) can be summed up in a Bethe-Salpeter equation for the full phonon self-energy, which can be schematically written as

$$\Pi = \Pi^0 + \Pi^0 M \Pi \tag{4.56}$$

with all the wavevector and energy subscripts omitted. In order to derive the dynamical intraband phonon self-energy expression, it is perhaps more intuitive to apply the Heisenberg equations of motion formalism on the case of electron density in one conduction band $\hat{c}^{\dagger}_{\mathbf{k}}\hat{c}_{\mathbf{k}-\mathbf{q}}$ interacting with a phonon field $u_{\nu\mathbf{q}} = \sqrt{\frac{\hbar}{2M_\nu \omega_{\nu\mathbf{q}}}}(\hat{b}_{\nu\mathbf{q}} + \hat{b}^{\dagger}_{\nu-\mathbf{q}})$. The derivation presented here is based on the seminar work from Ref. [84]. The Hamiltonian can be written as

$$\hat{H} = \hat{H}_{el} + \hat{H}_{\text{ph}} + \hat{H}_{el-ph} + \hat{H}_{ext}, \tag{4.57}$$

where the non-interacting electron term is

$$\hat{H}_e = \sum_{\mathbf{k}} \varepsilon_{\mathbf{k}} \hat{c}^\dagger_{\mathbf{k}} \hat{c}_{\mathbf{k}}, \tag{4.58}$$

and where we omitted the spin indices. Equivalently, the non-interacting phonon term is

$$\hat{H}_{ph} = \sum_{\mathbf{q}\nu} \omega_{\mathbf{q}\nu} \hat{b}^\dagger_{\mathbf{q}_\nu} \hat{b}_{\mathbf{q}\nu}. \tag{4.59}$$

Electron-phonon interaction term is familiar from Eq. (2.50). The term $\hat{H}_{ext}$ represents an external potential term

$$\hat{H}_{ext} = \alpha \sum_{\mathbf{q}} \hat{A}(-\mathbf{q}) F^{ext}(\mathbf{q}). \tag{4.60}$$

First, we will find an equation of motion for the electron density operator $\hat{c}^\dagger_{\kappa} \hat{c}_{\kappa+\mathbf{Q}}$ using the Heisenberg equation of motion

$$i \frac{\partial}{\partial t} \hat{c}^\dagger_{\kappa} \hat{c}_{\kappa+\mathbf{Q}} = [\hat{c}^\dagger_{\kappa} \hat{c}_{\kappa+\mathbf{Q}}, \hat{H}]. \tag{4.61}$$

This procedure will lead us to the expression for the EPC-induced electron-hole self-energy. We will then derive the equation of motion for the phonon field operator and obtain the expression for the phonon self-energy with the electron-hole scattering effects included. The commutators appearing on the right hand side can in fact be summarized in this form

$$\left[\hat{c}^\dagger_a \hat{c}_b, \hat{c}^\dagger_c \hat{c}_d\right] = \delta_{b,c} \hat{c}^\dagger_a \hat{c}_d - \delta_{a,d} \hat{c}^\dagger_c \hat{c}_b. \tag{4.62}$$

Explicitly, we can write

$$[\hat{c}^\dagger_{\kappa} \hat{c}_{\kappa+\mathbf{Q}}, \hat{H}_{el}] = (\varepsilon_{\kappa+\mathbf{Q}} - \varepsilon_{\kappa}) \hat{c}^\dagger_{\kappa} \hat{c}_{\kappa+\mathbf{Q}}, \tag{4.63}$$

$$[\hat{c}^\dagger_{\kappa} \hat{c}_{\kappa+\mathbf{Q}}, \hat{H}_{ph}] = 0, \tag{4.64}$$

$$[\hat{c}^\dagger_{\kappa} \hat{c}_{\kappa+\mathbf{Q}}, \hat{H}_{ext}] = \alpha \sum_{\mathbf{q}} F^{ext}(\mathbf{q}) (\hat{c}^\dagger_{\kappa} \hat{c}_{\kappa+\mathbf{Q}-\mathbf{q}} - \hat{c}^\dagger_{\kappa+\mathbf{q}} \hat{c}_{\kappa+\mathbf{Q}}), \tag{4.65}$$

$$\begin{aligned} [\hat{c}^\dagger_{\kappa} \hat{c}_{\kappa+\mathbf{Q}}, \hat{H}_{el-ph}] = \sum_{\mathbf{q}\nu} (\hat{b}_{\mathbf{q}\nu} + \hat{b}^\dagger_{-\mathbf{q}_\nu}) \\ \times \left(g_\nu(\kappa+\mathbf{Q}-\mathbf{q}, \kappa+\mathbf{Q}) \hat{c}^\dagger_{\kappa} \hat{c}_{\kappa+\mathbf{Q}-\mathbf{q}} - g_\nu(\kappa, \kappa+\mathbf{q}) \hat{c}^\dagger_{\kappa+\mathbf{q}} \hat{c}_{\kappa+\mathbf{Q}} \right). \end{aligned} \tag{4.66}$$

In order to keep only the self-consistent contributions, we need to calculate the average of the

equation of motion

$$\langle c^\dagger_\kappa c_{\kappa+\mathbf{Q}}\rangle(\omega+i\eta+\varepsilon_\kappa-\varepsilon_{\kappa+\mathbf{Q}})=\sum_{\mathbf{q}\nu} g_\nu(\kappa+\mathbf{Q}-\mathbf{q},\kappa+\mathbf{Q})\langle(\hat b_{\mathbf{q}\nu}+\hat b^\dagger_{-\mathbf{q}_\nu})\hat c^\dagger_\kappa\hat c_{\kappa+\mathbf{Q}-\mathbf{q}}\rangle- g_\nu(\kappa,\kappa+\mathbf{q})\langle(\hat b_{\mathbf{q}\nu}+\hat b^\dagger_{-\mathbf{q}_\nu})\hat c^\dagger_{\kappa+\mathbf{q}}\hat c_{\kappa+\mathbf{Q}}\rangle+\alpha F^{ext}(\mathbf{Q})(f(\varepsilon_\kappa)-f(\varepsilon_{\kappa+\mathbf{Q}})).$$

Calculating $\langle(\hat b_{\mathbf{q}\nu}+\hat b^\dagger_{-\mathbf{q}_\nu})\hat c^\dagger_\kappa\hat c_{\kappa+\mathbf{Q}-\mathbf{q}}\rangle$ and $\langle(\hat b_{\mathbf{q}\nu}+\hat b^\dagger_{-\mathbf{q}_\nu})\hat c^\dagger_{\kappa+\mathbf{q}}\hat c_{\kappa+\mathbf{Q}}\rangle$ is a bit cumbersome as it requires us to calculate their equations of motion. The general expression

$$\left[\hat b_c\hat c^\dagger_a\hat c_b,\hat H\right]=\hat b_c(\varepsilon_b-\varepsilon_a)\hat c^\dagger_a\hat c_b+\omega_c\hat c^\dagger_a\hat c_b\hat b_c+\left[\hat b_c\hat c^\dagger_a\hat c_b,\hat H_{el-ph}\right]+\hat b_c\left[\hat c^\dagger_a\hat c_b,\hat H_{ext}\right] \tag{4.67}$$

will help us with the procedure. Explicitly the last two terms can be calculated as

$$\begin{aligned}\left[\hat b_c\hat c^\dagger_a\hat c_b,\hat H_{el-ph}\right]&=g_\nu(\kappa,\mathbf{q})\left((\hat b_{\mathbf{q}\nu}+\hat b^\dagger_{-\mathbf{q}_\nu})\hat b_c\hat c^\dagger_a\hat c_k\delta_{b,\kappa+\mathbf{q}}-(\hat b_{\mathbf{q}\nu}+\hat b^\dagger_{-\mathbf{q}_\nu})\hat b_c\hat c^\dagger_{\kappa+\mathbf{q}}\hat c_b\delta_{a,\kappa}\right)\\&+g_\nu(\kappa,\mathbf{q})\left(\delta_{c,-\mathbf{q}}\delta_{b,\kappa+\mathbf{q}}\hat c^\dagger_a\hat c_k-\delta_{c,-\mathbf{q}}\delta_{a,\kappa+\mathbf{q}}\hat c^\dagger_{\kappa+\mathbf{q}}\hat c_b+\delta_{c,-\mathbf{q}}\sum_\kappa\hat c^\dagger_{\kappa+\mathbf{q}}\hat c_\kappa\hat c^\dagger_a\hat c_b\right)\end{aligned} \tag{4.68}$$

$$\hat b_c\left[\hat c^\dagger_a\hat c_b,\hat H_{ext}\right]=\alpha\hat b_c\sum_{\mathbf{q}}F^{ext}(\mathbf{q})(\hat c^\dagger_a\hat c_{b-\mathbf{q}}-\hat c^\dagger_{a+\mathbf{q}}\hat c_b). \tag{4.69}$$

The averaging procedure leaves only the first two terms of the first commutator in Eq. (4.68). To average out the terms in the second commutator in Eq. (4.69), we will use $\langle\hat b^\dagger_{-\mathbf{q}}\hat b_c\rangle=f^B(\omega_c)\delta_{c,-\mathbf{q}}$ and the mean value $\langle\sum_\kappa\hat c^\dagger_{\kappa+\mathbf{q}}\hat c_\kappa\hat c^\dagger_a\hat c_b\rangle=\delta_{\kappa,a}(1-f(\varepsilon_a))\langle\hat c^\dagger_{\kappa+\mathbf{q}}\hat c_b\rangle-\delta_{\kappa+\mathbf{q},b}f(\varepsilon_b)\langle\hat c^\dagger_a\hat c_\kappa\rangle$. From the equation of motion, we have

$$\begin{aligned}\langle\hat b_c\hat c^\dagger_a\hat c_b\rangle&=\frac{1}{\omega+i\eta+\varepsilon_a-\varepsilon_b-\omega_c}\\&\times\left(\langle\hat c^\dagger_a\hat c_{b+c}\rangle g_\nu(b+c,b)(f^B(\omega_c)+f(-\varepsilon_b)-\langle\hat c^\dagger_{a-c}\hat c_b\rangle g_\nu(a,a-c)(f^B(\omega_c)+f(\varepsilon_a))\right).\end{aligned} \tag{4.70}$$

Similarly, we can obtain

$$\begin{aligned}\langle\hat b^\dagger_c\hat c^\dagger_a\hat c_b\rangle&=\frac{1}{\omega+i\eta+\varepsilon_a-\varepsilon_b+\omega_c}\\&\times\left(\langle\hat c^\dagger_a\hat c_{b-c}\rangle g_\nu(b-c,b)(f^B(\omega_c)+1-f(\varepsilon_b))-\langle\hat c^\dagger_{a+c}\hat c_b\rangle g_\nu(a,a+c)(f^B(\omega_c)+f(\varepsilon_a))\right).\end{aligned} \tag{4.71}$$

After multiplying the Eq. (4.67) with $g_\nu(\kappa,\kappa+\mathbf{Q})$, summing over κ and manipulating the indices,

we reach the expression

$$\sum_{\kappa} g_{\nu}(\kappa,\kappa+\mathbf{Q})\langle c^{\dagger}_{\kappa}c_{\kappa+\mathbf{Q}}\rangle = \sum_{\kappa,\mathbf{k}'} \frac{g_{\nu}(\kappa,\kappa+\mathbf{Q})}{(\omega+i\eta+\varepsilon_{\kappa}-\varepsilon_{\kappa+\mathbf{Q}})}\left(\alpha F^{ext}(\mathbf{Q})(f(\varepsilon_{\kappa})-f(\varepsilon_{\kappa+\mathbf{Q}}))+\right. \tag{4.72}$$
$$\left.\langle c^{\dagger}_{\kappa}c_{\kappa+\mathbf{Q}}\rangle\left(|g_{\nu}(\mathbf{k}',\kappa)|^2[1-\frac{g_{\nu}(\mathbf{k}',\mathbf{k}'+\mathbf{Q})}{g_{\nu}(\kappa,\kappa+\mathbf{Q})}]\left(\mathscr{S}_1(\mathbf{k}',\kappa)+\mathscr{S}_2(\mathbf{k}',\kappa)\right)\right)\right.$$

where the quantities $\mathscr{S}_1$ and $\mathscr{S}_2$ have already been defined in Eq. (4.49) and Eq. (4.50), with substitution $\mathbf{q}\rightarrow\kappa-\mathbf{k}'$. The electron-hole self-energy in this case contains the vertex corrections

$$M(\kappa,\omega)=\sum_{\mathbf{k}'}|g_{\nu}(\mathbf{k}',\kappa)|^2[1-\frac{g_{\nu}(\mathbf{k}',\mathbf{k}'+\mathbf{Q})}{g_{\nu}(\kappa,\kappa+\mathbf{Q})}](\mathscr{S}_1(\mathbf{k}',\kappa)+\mathscr{S}_2(\mathbf{k}',\kappa)). \tag{4.73}$$

We need to obtain the equations of motion for the phonon field in the equaivalent manner. First, we can notice that the phonon field satisfies the relation

$$i\frac{\partial}{\partial t}u_{\nu\mathbf{q}}=i\frac{p^{\dagger}_{\nu\mathbf{q}}}{M_{\nu\mathbf{q}}} \tag{4.74}$$

where $p_{\nu\mathbf{q}}=\sqrt{\frac{\hbar M_{\nu}\omega_{\nu\mathbf{q}}}{2}}(\hat{b}_{\nu\mathbf{q}}-\hat{b}^{\dagger}_{\nu-\mathbf{q}})$. Performing another time derivative of Eq. (4.74), we reach a formula

$$(\frac{\partial^2}{\partial t^2}+\omega^2_{\nu\mathbf{q}})u_{\nu\mathbf{q}}=-\sum_{\kappa} g_{\nu}(\kappa,\kappa+\mathbf{q})\langle\hat{c}^{\dagger}_{\kappa}\hat{c}_{\kappa+\mathbf{q}}\rangle. \tag{4.75}$$

The right hand side of this expression is familiar from the aforewritten procedure

$$(\frac{\partial^2}{\partial t^2}+\omega^2_{\nu\mathbf{q}})u_{\nu\mathbf{q}}=-\sum_{\kappa}\frac{g_{\nu}(\kappa,\kappa+\mathbf{q})}{(\omega+i\eta+\varepsilon_{\kappa}-\varepsilon_{\kappa+\mathbf{q}})} \tag{4.76}$$
$$\left(\alpha F^{ext}(\mathbf{q})(f(\varepsilon_{\kappa})-f(\varepsilon_{\kappa+\mathbf{q}}))+\langle c^{\dagger}_{\kappa}c_{\kappa+\mathbf{q}}\rangle M(\kappa,\omega)\right)$$

In our case, the external potential coupling to the electron density is a phonon field, we can write

$$\alpha F^{ext}(\mathbf{q})=g_{\nu}(\kappa,\kappa+\mathbf{q})u_{\nu}(\mathbf{q}). \tag{4.77}$$

Keeping only the EPC terms u to the power of four, we reach an equation for the phonon field

$$\begin{aligned}(\frac{\partial^2}{\partial t^2}+\omega_{\nu\mathbf{q}}^2)u_{\nu\mathbf{q}} = -u_{\nu\mathbf{q}}\sum_{\kappa}|g_\nu(\kappa,\kappa+\mathbf{q})|^2\frac{f(\varepsilon_\kappa)-f(\varepsilon_{\kappa+\mathbf{q}})}{\omega+i\eta+\varepsilon_\kappa-\varepsilon_{\kappa+\mathbf{q}}}\\ -u_{\nu\mathbf{q}}\sum_{\kappa}|g_\nu(\kappa,\kappa+\mathbf{q})|^2\frac{f(\varepsilon_\kappa)-f(\varepsilon_{\kappa+\mathbf{q}})}{(\omega+i\eta+\varepsilon_\kappa-\varepsilon_{\kappa+\mathbf{q}})^2}M(\kappa,\omega).\end{aligned} \tag{4.78}$$

The first term on the right, can be recognized as the first-order phonon self-energy (4.19), while the second term includes vertex corrections and electron-hole scattering on phonons, through the electron-hole self-energy. If one decides to retain higher powers of EPC, additional terms would arise in Eq. (4.78), which can in a simplified manner be written as

$$\frac{1}{\Delta(\varepsilon,\omega)}+\frac{M(\kappa,\omega)}{\Delta(\varepsilon,\omega)^2}+\frac{M^2(\kappa,\omega)}{\Delta(\varepsilon,\omega)^3}+\frac{M^3(\kappa,\omega)}{\Delta(\varepsilon,\omega)^4}... \tag{4.79}$$

where $\Delta(\varepsilon,\omega)$ represents the quantity $\omega+i\eta+\varepsilon_\kappa-\varepsilon_{\kappa+\mathbf{q}}$. This can be recognized as a Taylor expansion and summed into

$$\frac{1}{\Delta(\varepsilon,\omega)}\frac{\Delta(\varepsilon,\omega)}{\Delta(\varepsilon,\omega)-M(\kappa,\omega)}. \tag{4.80}$$

Since we performed calculations concerned only with one band, in order to reach a dynamical intraband long-wavelength phonon self-energy, what remains is taking the limit $\mathbf{q}\to 0$. In the equation of motion for the phonon field, the first-order self-energy vanishes, and only the higher-order contributions remain. We can write the electron-hole self-energy as a sum of its real and imaginary parts, omit the wavevector index and indicate its temperature dependence

$$M(\omega,T)=\frac{i}{\tau_{\mathrm{op}}(\omega,T)}+\omega\lambda_{\mathrm{op}}(\omega,T). \tag{4.81}$$

The resulting expression for the intraband phonon self-energy is

$$\Pi_\nu^{\mathrm{intra}}(\mathbf{q}=0,\omega)=\sum_{\mathbf{k}n}|g_\nu^{nn}(\mathbf{k},\mathbf{q}=0)|^2\left(-\frac{\partial f_{n,\mathbf{k}}}{\partial\varepsilon_{n,\mathbf{k}}}\right)\cdot\frac{\omega}{\omega[1+\lambda_{\mathrm{op}}(\omega,T)]+i/\tau_{\mathrm{op}}(\omega,T)}. \tag{4.82}$$

Note that in our final calculations we perform the Fermi surface average of the above $M(\omega,T)$ [see Eq. (4.51)] assuming that the electron-phonon scatterings are not very anisotropic in momentum space, which makes the calculations more feasible. In comparison with the expression 4.52, two important things can be noticed;

1. it is dynamical and has a finite imaginary part
2. the additional factor is temperature-dependent.

The importance of this contribution to the EPC phonon self-energy is discussed thoroughly in Chapter 6.

Chapter 5

Dynamical renormalization in novel materials

In the previous chapter, a mathematical framework to go beyond the static BOA was introduced. However, the BOA is considered to be a robust approach that very rarely breaks down and it is not clear for which materials and physical regimes do we need to apply the methods that go beyond it.

In this chapter we discuss various materials for which the effects beyond the BOA can significantly modify several physical properties. The goal here is to point out the potential implications of NA effects and establish their pivotal role in computational estimations of electron-phonon properties. Apart from the expected long-wavelength NA effects, sizable NA Kohn anomalies away from the Brillouin zone center for materials with strong intervalley electron-phonon scatterings can be found. Compared to the adiabatic result, these dynamical phonon anomalies significantly modify EPC strength λ and superconducting transition temperature T_c. Further, the dynamically-induced modifications of λ have a strong impact on transport properties, where probably the most interesting is the rescaling of the low-temperature and low-frequency regime of the scattering time $1/\tau$ from about T^3 to about T^2, resembling the Fermi liquid result for electron-electron scattering.

5.1 Adiabatic or nonadiabatic?

In Chapter 1 the importance of EPC for understanding a vast number of phenomena in condensed matter physics, including resistivity, optical absorption, band gap renormalizations, structural phase transitions, CDWs, and superconductivity [4] has already been emphasized. Most of the theoretical

considerations of these properties rely on the adiabatic BOA, where electron and lattice degrees of freedom are treated separately and the dynamical effects of EPC are absent [30]. But one needs to be careful as there are certain conditions under which the adiabatic approximation fails. Specifically, provided that the electronic dampings are negligible, optical phonons around the center of the Brillouin zone (i.e., $\mathbf{q}\cdot\mathbf{v_F} < \omega$ and $1/\tau \ll \omega$) are expected to be affected by the NA corrections [85–87]. The latter was confirmed by various theoretical and experimental (e.g., Raman and inelastic x-ray scattering) works, where profound NA renormalizations of optical phonons were found, for instance, in doped bulk semiconductors [31], MgB_2 [32–36], transition metals [37, 38], graphene-based materials [39–42], hole-doped diamond [43], and doped transition metal dichalcogenides (TMDs) [44–46]. Besides these studies, where the focus is on long-wavelength optical phonons and several others where adiabatic breakdown of electron band structure renormalizations in infrared-active materials is analyzed [88–90], there are very few quantitative studies going beyond and exploring self-consistently dynamical corrections of electron-phonon properties in realistic materials, like the coupling strengths, superconductivity, and resistivity [91, 92]. The recognition of the importance of such study increased following several investigations that unveiled significant consequences of dynamic effects. It was shown that the dynamical screening of phonons, provided by the combination of molecular dynamics and real-time time-dependent-density-functional theory, can lead to significant modifications of EPC strength λ and superconductivity transition temperature T_c [91], as well as, potential energy surfaces and anharmonicity [92]. In addition, important insights were provided by the model calculations (e.g., Holstein Hamiltonian), where the influence of the dynamical phonon renormalization [93–97] and vertex corrections [98–100] on superconductivity was demonstrated. For example, it was reported that replacing the bare (adiabatic) phonon propagator with the renormalized one (i.e., including phonon self-energy corrections) in Migdal-Eliashberg equations improves considerably its accuracy [94, 95].

Accounting for the phonon self-energy corrections, damping in particular, was recognized from the calculations of the anharmonic properties and found to be instrumental for describing the superconducting dome structure in ferroelectric materials [97, 101]. Performing the anharmonicity-induced dynamical anharmonic phonon self-energy calculations was proven to be important for understanding the superconducting transition temperature in superhydrides [102]. However, these studies have not included EPC.

In an obvious need for establishing a clear role of NA effects, we will conduct a detailed *ab-initio* study on the NA phonon renormalizations and the corresponding impact on λ, T_c, as well as electron

scattering rates $1/\tau$ relevant in transport and optical absorption. Using the methods presented in Chapter 4, we will simulate NA corrections to phonon frequencies and calculate EPC-induced linewidths, which will in turn then be utilized to renormalize electron-phonon properties. We will explore whether, contrary to the common belief, the NA frequency renormalization can also be significant away from the long-wavelength $\mathbf{q} \approx 0$ region. This requires confirmation especially in the multiband and multivalley systems such as MgB_2, molybdenum disulphide (MoS_2), arsenene (As), and tungsten ditelluride (WTe_2), where strong interband or intervalley electron-phonon scatterings are possible, forming Kohn anomalies at finite $\mathbf{q}$ vectors. Then, we will introduce NA modifications of λ and T_c and quantify the strength of the dynamical effects for various superconducting two-dimensional (2D) and bulk systems. Finally, we will see how the dynamical electron-phonon effects can significantly influence, both qualitatively and quantitatively, the functional dependence of the electron-hole pair scattering rate $1/\tau_{\mathrm{op}}(\omega, T)$ and mass enhancement factor $\lambda_{\mathrm{op}}(\omega, T)$ [103, 104] on frequency ω and temperature T. For instance, the inclusion of the NA effects modifies the well-known behaviour of $1/\tau_{\mathrm{op}} \propto T^3$ to $1/\tau_{\mathrm{op}} \propto T^2$ [93, 105], resembling the Fermi liquid result for electron-electron scatterings. The latter might provide further insights into enigmatic T^2 resistivity observed in a number of complex materials [106–112].

5.2 Eliashberg spectral function

A central quantity in MBPT for describing electron dynamics due to EPC is the electron self-energy Σ, which is instrumental for understanding quasiparticle spectral features [113, 114], superconductivity properties, such as T_c [81, 104], electron scattering rates, and electron resistivity [93]. In the standard calculations of Σ based on, e.g., DFPT, the phonon propagator D is non-interacting with sharp (i.e., having infinite lifetime) adiabatic phonons [4, 30, 75], as was already mentioned several times in previous chapters. Here, we will inspect how general electron-phonon properties are modified when dynamical properties are accounted for in D via NA EPC leading to finite phonon lifetime and frequency renormalizations.

When averaged over the Fermi surface, the electron self-energy Σ is commonly expressed via the Eliashberg function [81, 93]

$$\alpha^2 F(\omega) = \frac{1}{\pi N_0} \sum_{\mathbf{q}\nu} \frac{\gamma_{\mathbf{q}\nu}}{\Omega_{\mathbf{q}\nu}} B_\nu(\mathbf{q}, \omega), \tag{5.1}$$

already introduced in Chapter 4, in Eqs. (4.35) and (4.34), with a small distinction that here the notation $\gamma_{\mathbf{q}\nu}$ for the phonon linewidths in the double-delta approximation [115] is used. The phonon spectral function $B_\nu(\mathbf{q},\omega)$ in Eq. (5.1) can be adiabatic, representing an infinitely lived DFPT set of phonons. In that case, the resulting Eliashberg spectral function is adiabatic as well, and readily available from EPW and other similar codes. The first step towards a dynamical result is if the phonon frequencies are shifted by the real part of the NA phonon self-energy. Then the phonon spectral function is again a set of delta functions, but with displaced peaks compared to the adiabatic one. The Eliashberg spectral function reflects these shifts, but since also the frequency-dependent prefactor in Eq. (5.1) includes a NA renormalization as well, the peaks in the NA Eliashberg spectral function are of renormalized height and width. The double-delta phonon linewidths $\gamma_{\mathbf{q}\nu}$ contain the EPC matrix element squared, and are therefore inversely proportional to the phonon frequency, which also needs to be renormalized. The full NA renormalization can be done if the EPC phonon broadening effects are taken into account as well. Then, the peaks in the phonon spectral function acquire finite width and the resulting, fully NA Eliashberg spectral function can look a lot different than its adiabatic counterpart. Then these possibly large renormalizations of $\alpha^2F(\omega)$ enter the electron self-energy modifying the electron spectrum, while one of the important quantities that its integral determines is the EPC constant λ

$$\lambda = 2\int_0^\infty \frac{\alpha^2F(\omega)}{\omega}d\omega, \tag{5.2}$$

which is, together with a logarithmic frequency,

$$\omega_{\log} = \exp\left[\frac{2}{\lambda}\int_0^\infty \log(\omega)\frac{\alpha^2F(\omega)}{\omega}d\omega\right], \tag{5.3}$$

a crucial quantity when calculating the superconducting T_c with the Allen-Dynes correction to the McMillan formula [116]

$$T_c = \frac{\omega_{\log}}{1.2}\exp\left[-\frac{1.04(1+\lambda)}{\lambda-\mu^*-0.62\lambda\mu^*}\right]. \tag{5.4}$$

5.3 Selected materials

In this chapter, we will investigate the NA effects in several relevant bulk and 2D systems, where conventional, phonon-mediated superconductivity was confirmed by both experiments and theory

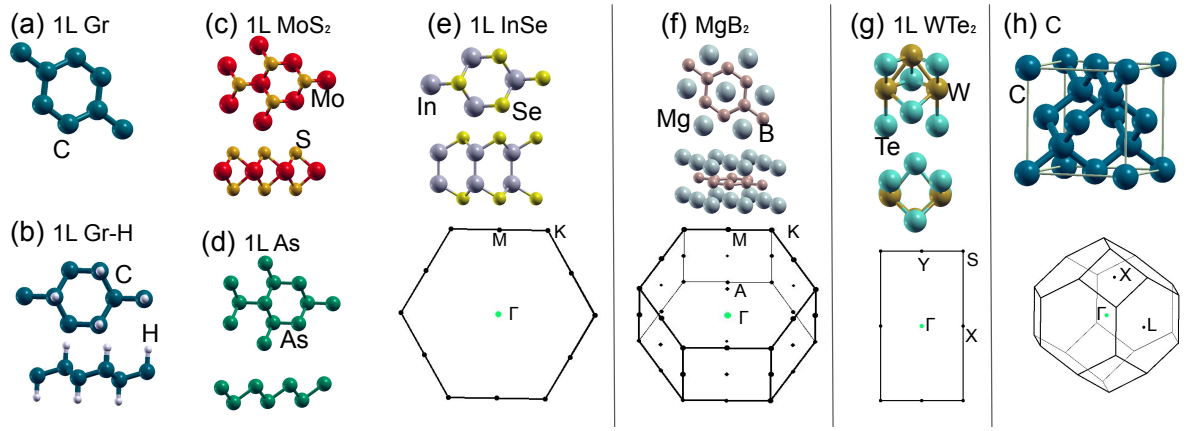

Figure 5.1: Atomic structures for various bulk and 2D systems, investigated in this chapter, and their Brillouin zones with high symmetry points. (a)-(e) simple hexagonal structures of single-layered Gr, Gr-H, MoS_2, As and InSe. Their corresponding Brillouin zone is hexagonal. Carbon atoms in Gr are all placed in one plane, while for the other materials, the side view in the bottom row reveals their out-of-hexagonal plane structure. (f) Bulk MgB_2 consists of a hexagonal B layer, sandwiched between Mg planes. (g) 1L WTe_2 has a 1T' phase symmetry. (h) A bulk structure of diamond with the corresponding Brillouin zone.

or just in theory, i.e., MgB_2 [19, 20, 80, 117–122], hole-doped diamond (C) [73, 123–126], and doped monolayers: highly electron-doped graphene (1L Gr) [127–129], hole-doped graphane (1L Gr-H) [130], electron-doped 1L MoS_2 [131–137], electron-doped 1L As [138], hole-doped 1L InSe [139, 140], and electron-doped 1L WTe_2 [141, 142].

Structures of the selected materials are shown in Fig. 5.1, as well as their corresponding Brillouin zones with marked high-symmetry points.

5.3.1 Computational details

The ground-state *ab-initio* calculations were performed by means of the QUANTUM ESPRESSO (QE) package (see Chapter 3), by applying the Perdew-Burke-Ernzerhof (PBE) functional, and optimized norm-conserving Vanderbilt pseudopotentials [143] with a plane-wave energy cutoff of 80 Ry. Isolated layers are described using a supercell geometry. Firstly, we perform the full relaxation in order to obtain the unit cell, and then we relax the out-of plane position of the atoms, while holding the in-plane positions fixed. Doping is simulated using a jellium model. The phonon and electron-phonon properties are extracted from the DFPT. The relevant electron-phonon quantities are then interpolated by means of the MLWFs, and the EPW code. In the latter calculations, the

temperature always matches the smearing value of the ground state calculations, while the broadening in the energy-conserving delta functions is set to 40 meV or less, depending on the system. Phonon self-energy was calculated within the on-the-shell approximation, where the general excitation frequencies ω in Eq. (4.19) are replaced with the adiabatic phonon frequency $\omega_{\mathbf{q}\nu}$. The Allen-Dynes version of the McMillan's formula for T_c is calculated always with $\mu^* = 0.1 - 0.15$.

The ground state calculation for highly-doped 1L Gr yields a relaxed lattice constant of 2.448 Å with the periodic images separated by 12 Å. High doping regime is achieved by the excess electron charge of 0.67 electrons per unit cell. Methfessel-Paxton smearing with 0.01 Ry combined with a $48 \times 48 \times 1$ k-point mesh is used. For the phonon calculation, a $24 \times 24 \times 1$ q-point mesh is used. MLWFs for the EPW calculation are obtained with sp^2 and p_z orbitals on the C site along with two s orbitals slightly above/below the midpoint between the two C atoms. For the interpolation, a $400 \times 400 \times 1$ and $200 \times 200 \times 1$ fine k- and q-meshes, are used respectively.

For 1L Gr-H doped with 0.1 h/u.c. the relaxed unit cell is 2.5 Å with the periodic replicas 18 Å apart. Here the Fermi-Dirac smearing with 0.01 Ry together with a $48 \times 48 \times 1$ k- and $24 \times 24 \times 1$ q-point meshes for the SCF and phonon calculations are used. MLWFs are obtained from the initial projections of sp^3 and p_z orbitals on one C atom. We again use $400 \times 400 \times 1$ and $200 \times 200 \times 1$ fine k- and q-meshes for the EPW calculation.

The self-consistent calculation details for MoS_2 include separation of periodic images by 16 Å and the relaxed lattice constant of 3.186 Å. The Fermi level crosses the K valley at 200 meV above the band minimum and just barely touches the Q valley, which is achieved by excess carrier concentration of 0.08 e/u.c. Here Gaussian smearing with 2 mRy together with $48 \times 48 \times 1$ k-point mesh is used. Phonons are calculated on a $24 \times 24 \times 1$ q-point mesh. For the Fourier interpolation, MLWFs with 5 Mo-d orbitals and 3 S-p orbitals on the two S atoms are set as initial projections. For the interpolation a $480 \times 480 \times 1$ and $160 \times 160 \times 1$ fine k- and q-meshes are used, respectively.

The relaxed unit cell constant for 1L As is 3.597 Å with periodic layers separated by 18 Å. Cells are charged with an excess charge of 0.1 e/u.c. For the SCF and phonon calculations the grids are set to a $24 \times 24 \times 1$ k-points and $12 \times 12 \times 1$ q-points, with Fermi-Dirac smearing of 0.01 Ry. Here the MLWFs are automatically generated using a selected columns of the density matrix (SCDM) approach [144] with parameters $\mu = -6$ and $\sigma = 2.5$ based on the electronic structure of arsenene. The fine k- and q-point meshes are $480 \times 480 \times 1$ and $84 \times 84 \times 1$, respectively.

For 1L InSe, we obtain the relaxed unit cell constant of 3.9 Å with the periodic layers separated by 27 Å. Hole doping is achieved by the excess charge of 0.3 h/u.c. Again the Fermi-Dirac smearing

with 0.01 Ry is used along with a $48 \times 48 \times 1$ k-point and $12 \times 12 \times 1$ q-point meshes. The EPW calculation is performed with MLWFs obtained from the initial projections of 3 Se-p orbitals. The fine k- and q-point meshes are $360 \times 360 \times 1$ and $120 \times 120 \times 1$, respectively.

As for the orthorhombic WTe_2, the relaxation yields unit cell constants $a = 3.425$ Å and $b = 6.222$ Å. The Fermi-Dirac smearing with 0.01 Ry is used in combination with a $24 \times 12 \times 1$ k-point mesh. Total negative charge per unit cell used in our calculations is 0.19. The original phonon calculations are done on a $12 \times 6 \times 1$ coarse q-point grid. For the Fourier interpolation, MLWFs with 2 W-d orbitals ($d_{x^2-y^2}$ and d_{xy}) and Te-s and Te-p orbitals as initial projections are used. q- and k-point fine meshes are for this system the same and amount to $180 \times 90 \times 1$.

For MgB_2, we obtain the relaxed unit cell determined by the lattice parameters $a = 3.083$ Å and $c = 3.521$ Å. The Fermi-Dirac smearing with 0.02 Ry is used along with a $12 \times 12 \times 12$ k-point and $12 \times 12 \times 12$ q-point meshes. The EPW calculation is performed with MLWFs obtained from the initial projections of B-pz and S orbitals. The fine k- and q-point meshes are $40 \times 40 \times 40$ and $40 \times 40 \times 40$, respectively.

For diamond, we obtain the relaxed unit cell with a lattice parameter $a = 3.49779$ Å. The Fermi-Dirac smearing with 0.02 Ry is used along with a $12 \times 12 \times 12$ k-point and $12 \times 12 \times 12$ q-point meshes, while doping is set with an excess negative charge of 0.11 per unit cell. The EPW calculation is performed with MLWFs obtained from the initial projections of 4 C-sp^3 orbitals. The fine k- and q-point meshes are $40 \times 40 \times 40$ and $50 \times 50 \times 50$, respectively.

5.4 Results

Electronic band structures along the high-symmetry lines for all the investigated systems are shown in Fig. 5.2. The electronic band structure of MgB_2 around the Fermi level consists of the hole-like σ states around the center, and π states at the edges of the Brillouin zone. The former are the most relevant for the formation of the Kohn anomalies in the phonon spectra and provide a dominating contribution to the superconducting state, because they form a tubular Fermi surface along the Γ-A direction [see Fig. 5.4 (a)]. Hole doping in diamond provides pockets around the Γ point, which will be reflected in its phonon band structure. Electron doping in graphene is set so that the Fermi level rests on the flat part of its π band, which produces a spike (Van Hove singularity) in the electronic DOS. Such a high concentration of mobile electrons will later have profound effects on the phonon dispersion. Electron doping in MoS_2 leads to 6 electron pockets between Γ and K and one pocket

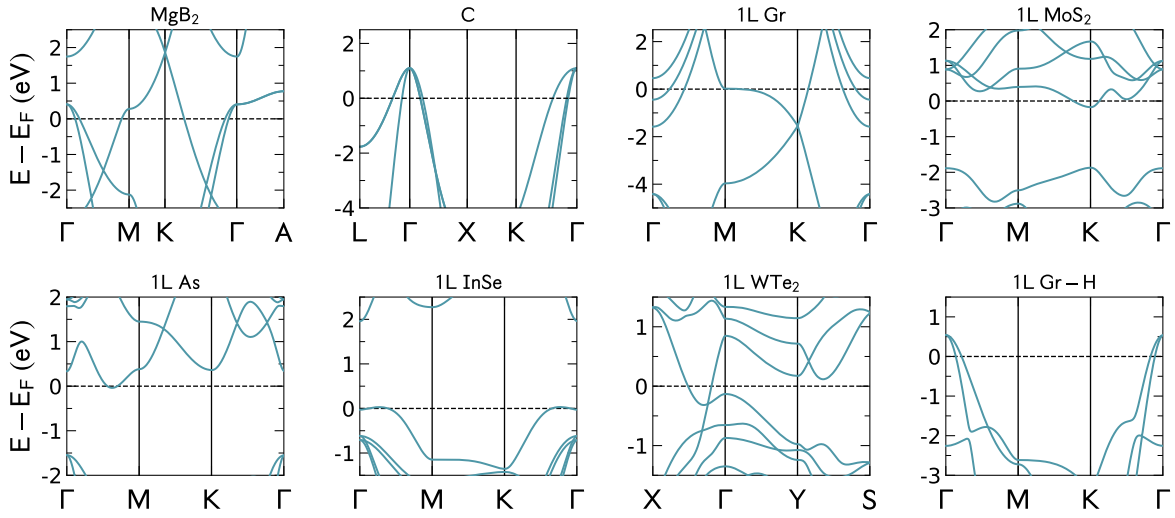

Figure 5.2: Electronic band structures for various bulk and 2D systems presented along the high-symmetry points of the first Brillouin zone (see Fig. 5.1). The results are shown for MgB_2, hole-doped diamond (C), highly electron-doped single-layer graphene (1L Gr), electron-doped single-layer molybdenum disulfide (1L MoS_2), electron-doped arsenene (1L As), hole-doped single-layer indium selenide (1L InSe), electron-doped single-layer wolfram ditelluride (1L WTe_2), and hole-doped graphane (1L Gr-H). Figure from the supplementary material of Ref. [145].

in each K point. Similarly, in 1L As there are 6 electron pockets appearing between the Γ and M points. Hole-doped InSe has a characteristic mexican-hat shaped valence band. Electron-doped WTe_2 features one electron pocket between Γ and X. Hole-doped Gr-H has σ hole pockets around the Γ point. All these states that are at the Fermi level in our calculations, are involved in the strong electron-phonon scatterings, in these cases mostly with optical phonons, and therefore make an important contribution to the total electron-phonon coupling strength λ and superconducting properties.

Familiarizing oneself with the available electron scattering phase space is important in order to better understand the Kohn anomalies that appear in the phonon band structure. Calculations of the phonon dispersions are outlined in Fig. 5.3, where standard adiabatic dispersions are compared with the ones corrected with NA frequency shifts. We can see that the Kohn anomalies appear at characteristic wavevectors, determined by the Fermi surface, while the phonon branch for which they appear is determined by the EPC matrix elements. In MgB_2, phonon softening happens along the full Γ - A direction, because in this direction, electrons can scatter with any momentum and end up

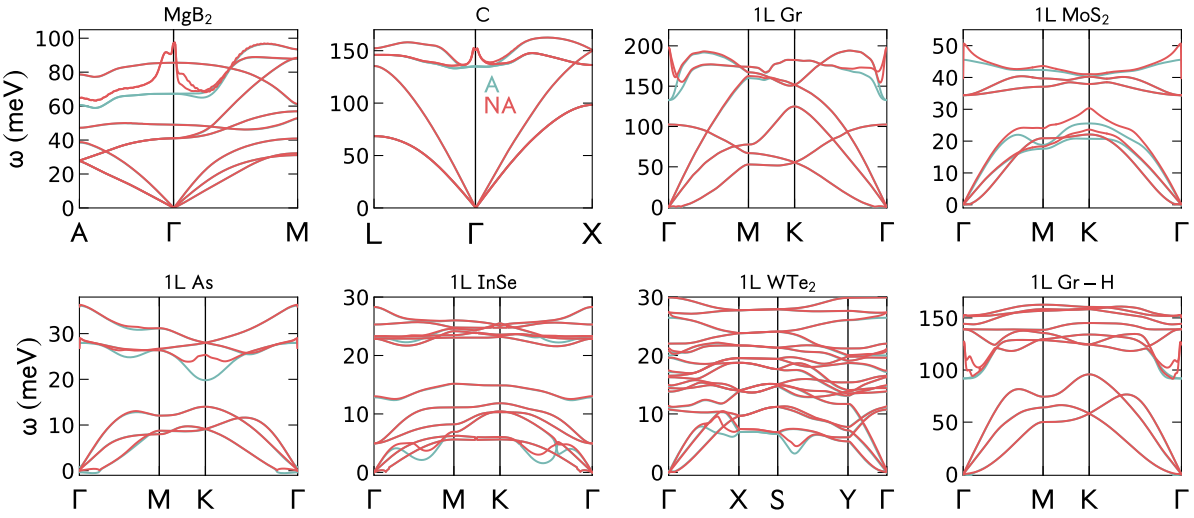

Figure 5.3: Phonon band structures of the selected materials. Adiabatic (DFPT) result is shown in blue, while the NA corrected frequencies are shown in red. Figure from the supplementary material of Ref. [145].

at some other point of the tube [see Fig. 5.4(a)]. In C and 1L Gr-H the Kohn anomalies appear in the Γ point because of the hole pocket around the Brillouin zone center in the electron band structure. 1L MoS_2, 1L InSe, 1L WTe_2 and 1L As all feature Kohn anomalies at finite wavevectors due to the fact that their Fermi level crosses multiple valleys, enabling inter-valley scattering channels. In 1L Gr, a Kohn anomaly appears in the Γ point, because the flat π band parts can be nested by vanishing $\mathbf{q}$ vectors. After locating the adiabatic Kohn anomalies, it is time to see what is the impact of NA frequency renormalization and how it shapes the dynamical Kohn anomalies. Interestingly, along with the expected NA frequency renormalizations at the Γ point for the systems with the strong EPC (1L Gr-H), there are considerable NA corrections of phonons away from the center of the Brillouin zone for MgB_2, 1L As, 1L MoS_2, 1L InSe, and 1L WTe_2. Therefore, the NA condition $\mathbf{q} \cdot \mathbf{v_F} < \omega$ [86,87] only holds for simple metals with parabolic band structure, while for the multiband systems, strong electron-phonon scatterings between same or different valleys could lead to NA Kohn anomalies at finite $\mathbf{q} = \mathbf{q_c}$, provided that the $\varepsilon_{n\mathbf{k}} - \varepsilon_{m\mathbf{k}+\mathbf{q_c}} \lesssim \omega$ condition is met. These $\mathbf{q} = \mathbf{q_c}$ dynamical transitions for MgB_2, 1L Gr-H, and 1L As represent the largest contributions to the electron-phonon scatterings and total EPC strength λ. This is visible in Fig. 5.4(b) and 5.4(c), where their dispersion with the EPC linewidth is shown, together with the corresponding Eliashberg spectral function. For instance, in cases, where intra- (C, 1L Gr-H, 1L Gr, 1L InSe) and inter-valley (1L As, 1L MoS_2, 1L WTe_2) electron-phonon scatterings happen for some wavevector

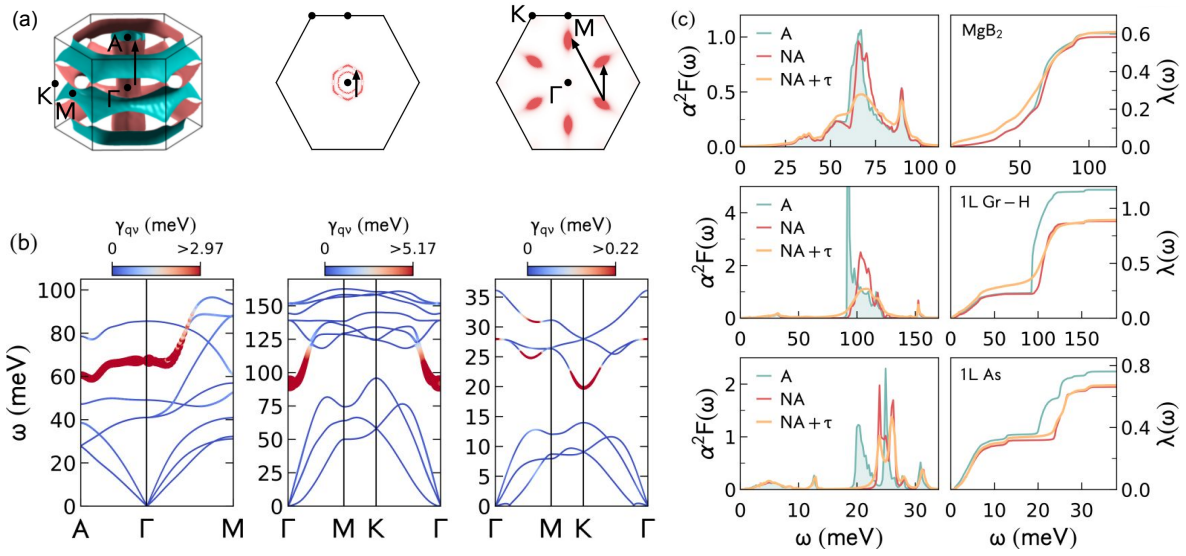

Figure 5.4: (a) Fermi surface in the first Brillouin zone for (a) MgB_2, 1L Gr-H, and As with the electron transitions causing phonon softenings denoted with a black arrow. (b) The phonon linewidths $\gamma_{\mathbf{q}\nu}$ coming from EPC. The size of the dots and colors (defined within the colorbars) represents the intensity of $\gamma_{\mathbf{q}\nu}$. (c) Eliashberg functions $\alpha^2F(\omega)$ and cumulative EPC constant $\lambda(\omega)$ obtained for MgB_2, 1L Gr-H, and 1L As. Three different results are shown: adiabatic (A), where frequencies are obtained within the adiabatic DFPT and without momentum and branch-resolved phonon broadenings $\gamma_{\mathbf{q}\nu}$ (blue), nonadiabatic (NA), where frequencies are corrected with NA effects, while the corresponding NA phonon broadening due to EPC is not included (red), and full nonadiabatic (NA+τ), where both NA frequency renormalization and NA phonon linewidth effects are taken into account (yellow). Figure adapted from Ref. [145].

$\mathbf{q_c}$ and phonon branch, it leads to strong NA renormalizations. NA renormalizations appear where the phonon linewidths $\gamma_{\mathbf{q}\nu}$ are largest and therefore create a large peak in the Eliashberg spectral function. Notice that the conditions that lead to the finite-$\mathbf{q}$ NA Kohn anomalies are similar to the criteria for the phonon-induced CDW formation [146], which include considerable nesting features of the Fermi surface or strong EPC matrix elements for $\mathbf{q} = \mathbf{q_c}$. In accordance to these results, the NA hardening of the soft phonon modes at the edges of the Brillouin zone were obtained recently also for TaS_2 [77]. Recent Raman spectroscopy measurements confirmed the importance of NA electron-phonon corrections for the zone-edge acoustic phonons in single- and double-layer WS_2 [147]. The aforementioned two NA effects are often inseparable and should be included together when calculating the Eliashberg function $\alpha^2F(\omega)$ and the total EPC strength λ.

In Fig. 5.4(c) the results of $\alpha^2F(\omega)$ and cumulative EPC constant $\lambda(\omega) = 2\int_0^\omega d\Omega\alpha^2F(\Omega)/\Omega$ for three different approaches are shown. The result in the standard adiabatic approximation, where no dynamical effects are considered in the phonon spectral function, i.e., $\Pi_\nu(\mathbf{q},\omega) \to i0$ is shown in blue, the NA approach with only dynamical frequency renormalizations included, i.e., $\Pi_\nu(\mathbf{q},\omega) \to \mathrm{Re}\Pi_\nu(\mathbf{q},\omega) + i0$, in red, and the full NA method with both frequency corrections and phonon dampings is shown in yellow. The NA frequency renormalizations are always positive [4], and since these shifts are accompanied by strong phonon damping rates, the main peaks in $\alpha^2F(\omega)$ are blueshifted and λ is reduced. For example, the NA blueshifts of the Kohn anomalies of about 33 meV and 6 meV in 1L Gr-H and 1L As, respectively, is reflected in the corresponding modifications in $\alpha^2F(\omega)$ and in a considerable reduction of λ of about 0.29 and 0.14. By including additionally the momentum- and mode-resolved broadening $\gamma_{\mathbf{q}\nu}$, the total EPC constant λ is not affected seriously, however, the spectral weight of $\alpha^2F(\omega)$ is redistributed and smoothed, so that the high-frequency main peaks contribute less, while lower frequencies contribute more to $\lambda(\omega)$. This frequency redistribution of the EPC due to NA effects has pertinent consequences on the low-temperature and low-energy behavior of electron-hole scattering rate [93], as will be shown below. Gathered results for all of the studied systems are presented in Fig. 5.5, including the dynamical corrections of the total EPC strength λ, the first moment of the phonon spectrum $\lambda\langle\omega\rangle$, logarithmic phonon frequency $\omega_{\log}$ and the superconducting transition temperature T_c. The first moment is calculated as $\lambda\langle\omega\rangle = 2\int_0^\infty d\Omega\alpha^2F(\Omega)$, and it is considered important for the McMillan's expression for T_c [116], as well as high-energy and zero-temperature estimation of the electron-hole relaxation rate $1/\tau_{\mathrm{op}}$ appearing in the optical conductivity formula [103, 104, 148, 149]. Calculations of T_c are done with the Allen-Dynes version of McMillan's formula (5.4) [150]. Considerable modifications of λ and T_c are obtained, compared to the adiabatic calculations, once the NA phonon frequency renormalizations and phonon linewidths due to EPC are taken into account. While in some cases the dynamical renormalizations of frequencies induce small relative modifications (compared to adiabatic result) of λ (MgB_2, C), there are cases where it is significantly decreased, i.e., by 19% to 42% (MoS_2, 1L InSe, 1L WTe_2, and 1L Gr-H). This is reflected in mild and considerable reduction in T_c, respectively. For example, 8-12% is obtained for MgB_2 and 70-85% for InSe (with reasonable choices of effective Coulomb repulsion μ^*). In most cases the dynamical effects on $\lambda\langle\omega\rangle$ are small (largest being for 1L Gr-H), suggesting that high-energy limits of $1/\tau_{\mathrm{op}}$ and, consequently, phonon-assisted optical absorption formula are not strongly affected by the NA renormalizations. Interestingly, the value of λ can be additionally increased by the NA phonon broadening effects, while T_c can be either increased

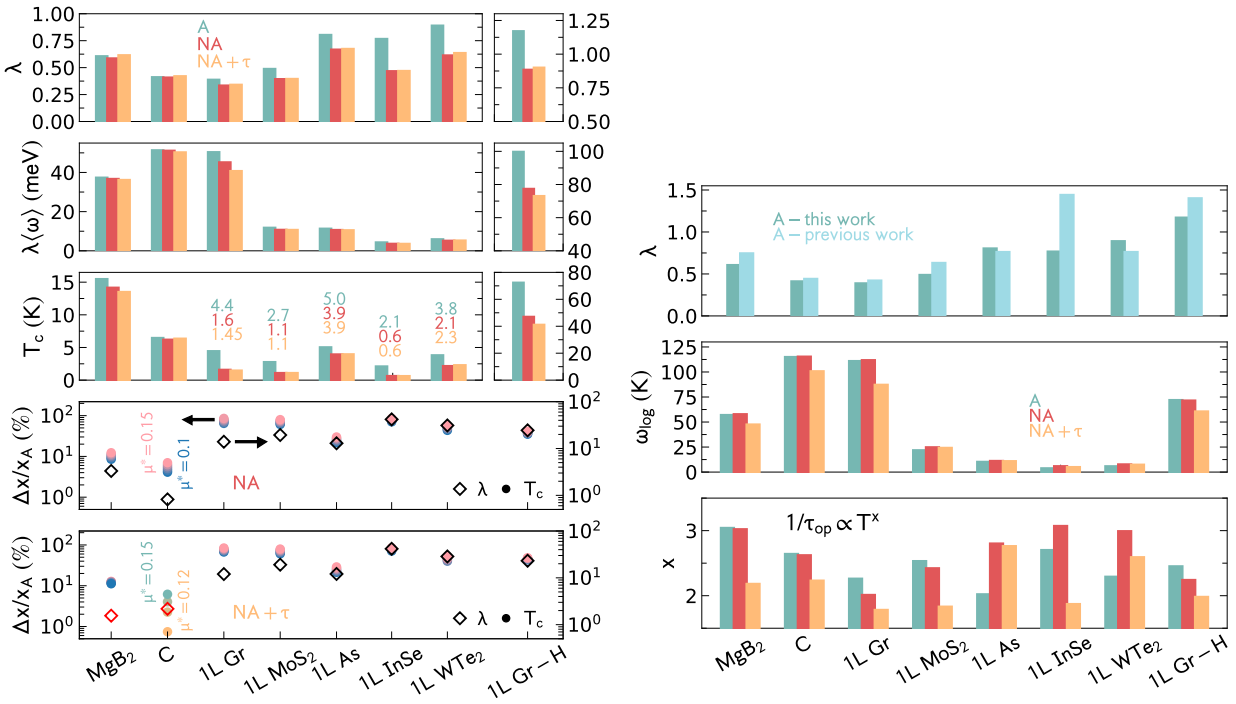

Figure 5.5: **Left panel**: total EPC strengths λ, the first moments of the phonon spectrum $\lambda\langle\omega\rangle$, and superconducting transition temperatures T_c obtained with three different approaches: adiabatic (A; within standard adiabatic DFPT methodology), nonadiabatic (NA; by including NA phonon frequency renormalizations), and fully nonadiabatic (NA+τ; by including both NA frequency renormalizations and NA phonon broadenings $\gamma_{\mathbf{q}\nu}$). Bottom panels show the corresponding relative changes $(x_{\mathrm{NA/NA+\tau}} - x_{\mathrm{A}})/x_{\mathrm{A}}$ for T_c (left axis) and λ (right axis). All relative changes are positive, except the NA+τ results of x $=\lambda$ for MgB_2 and C (red diamond signs), and of x $= T_c$ for C (green-yellow circles). **Right panel**: In the uppermost panel the comparison between our results for the adiabatic electron-phonon coupling strength λ, and previously obtained values from the literature is shown. Previous results are from: MgB_2 [122], C [124], 1L Gr [127], 1L MoS_2 [137], 1L As [138], 1L InSe [140], 1L WTe_2 [142], 1L Gr-H [130]. For doped systems, we have chosen the results from the literature that correspond to exactly the same or very similar charge carrier concentration. The difference in calculated adiabatic λ for 1L InSe probably comes from different computational details used in Ref. [140]. This difference in calculated λ is not entirely surprising considering how sensitive various properties of InSe are on the doping concentration [139, 140]. Below are the values of $\omega_{\log}$ that enter Allen-Dynes version of the McMillan's formula (5.4) as obtained with A, NA, and NA+τ approaches. In the last panel, the variations of the temperature scaling in optical relaxation rate (i.e., $1/\tau_{\mathrm{op}} = B + AT^x$) for small temperatures and frequencies as obtained with A, NA, and NA+τ approaches are shown. Figure adapted from Ref. [145].

or decreased, depending on an interplay between modifications in the position of strong peaks in $\alpha^2F(\omega)$ (via $\langle\omega\rangle$ or $\omega_{\log}$) and changes in λ. For instance, the phonon-broadening-induced reduction in $\omega_{\log}$ and increase in λ results in further decrease of T_c for MgB_2, 1L Gr, and 1L Gr-H. On the other hand, the NA phonon broadening and the accompanying redistribution of EPC in $\alpha^2F(\omega)$ induce small increase of T_c in C (e.g., around 6% for $\mu^* = 0.15$). Note also a small broadening-induced increase of T_c in the case of 1L WTe_2. The latter two examples serve as an illustration on how the NA broadening effects can be quite beneficial for obtaining higher values of T_c, and it is quite possible that these dynamical corrections could be higher and more emphasized for systems with soft phonon modes [151, 152] that are anharmonic and strongly-coupled to electrons [96, 97] (e.g., charge-density-waves materials and systems at the verge of phase transition).

Having in mind the available experimental and theoretical adiabatic results, we can notice that the NA renormalizations presented here generally improve the agreement. Namely, the theoretical first-principles estimations of T_c for MgB_2 are 50-55 K when anisotropic electron-phonon interaction and averaged Coulomb repulsion term are employed [122, 153, 154], while experimental value is $T_c = 39$ K [20] (difference of about 22-29%). As is shown here by using the isotropic Allen-Dynes solution to Eliashberg equations, the substantial part of this discrepancy could be resolved by the NA effects (inducing decrease of T_c by 8-12%). Additional improvements might be achieved by accounting for vertex corrections in the Eliashberg equations [155] and anharmonic effects [153]. Further, the *ab-initio* results of T_c for the hole-doped diamond are underestimating the experimental values [73, 124], while the present results demonstrate how the NA phonon broadening in C can enhance T_c. However, note that the obtained increase is not enough to reproduce the experiments and that the boron-related vibrational modes are instrumental for understanding the superconductivity in hole-doped diamond [125, 126]. Also, regardless of the doping concentration and the type of calculation, theoretical predictions of transition temperature in 1L MoS_2 ($T_c \gtrsim 4$ K) [132, 133, 137] are always much higher than experimental values, which are $\sim$1-2 K [134, 135]. These results suggest that the dynamical renormalizations improve this disagreement. Experimental results for WTe_2 are available as well, however, only for small electron concentrations [141, 142], where significant NA modifications are not to be expected. The previously reported adiabatic results of λ for all of the presented systems are in a good agreement with the adiabatic results from these calculations (see the right panel in Fig. 5.5).

Recently, the dynamical effects on superconducting properties via dynamical screening of EPC matrix elements were studied by means of real-time time-dependent-density-functional theory

combined with molecular dynamics [91]. The corresponding conclusion, based on the 1L Gr and 1L Gr-H cases, is that the dynamical screening that enters g^2, e.g., via the dielectric function $\varepsilon(\mathbf{q},\omega)$, can overcome the effects of the NA frequency renormalization (hardening), and leads to the enhancement of λ and T_c compared to the static-screening calculations. These results are, however, hard to compare with the present work. On the one hand, the dynamical screening of the EPC matrix elements g is unfortunately out of reach for the present many-body perturbation approach that uses phonon self-energy within DFPT [4, 79, 80, 156]. On the other hand, the approach from Ref. [91] includes the dynamically-screened g and NA frequency renromalizations, but, does not account for the NA phonon broadenings. Also, it uses a frozen-phonon scheme to account for phonon dynamics and is therefore able to include only a few modes in calculations of the total λ (i.e., the $\mathbf{q}=0$ and $\mathbf{q}=K$ optical modes for 1L Gr, and only the $\mathbf{q}=0$ optical mode for 1L Gr-H). However, the fine $\mathbf{q}$ grids are necessary to reach the numerical convergence and account for the full NA effects of the Kohn anomalies. Since the dielectric function $\varepsilon(\mathbf{q},\omega)\approx\varepsilon(\mathbf{q},0)$ for large $\mathbf{q}$ [114, 157], the dynamical screening of EPC should not play an important role in modifying the EPC properties for the materials with NA Kohn anomalies away from the Γ point, e.g., in the multivalley materials such as 1L MoS_2, 1L As, and 1L WTe_2. Nonetheless, the dynamical screening of g seems to be a quite important feature of the NA theory, and it might be a crucial (but still very demanding) extension of the present DFT-based many-body approach, e.g., to explore the impact of the strong plasmon-phonon coupling on the superconductivity and transport [158, 159].

Further, Fig. 5.6 presents the results for the optical (i.e., electron-hole pair) scattering rate $1/\tau_{\mathrm{op}}$. It enters optical conductivity formula (or current-current response tensor) and can be expressed in the following form [34, 35, 45, 93, 103, 104]

$$1/\tau_{\mathrm{op}}(\omega,T)=\frac{\pi}{\omega}\int d\Omega\alpha^2F(\Omega)\Big[2\omega\coth\frac{\Omega}{2k_BT} -(\omega+\Omega)\coth\frac{\omega+\Omega}{2k_BT}+(\omega-\Omega)\coth\frac{\omega-\Omega}{2k_BT}\Big], \tag{5.5}$$

having frequency ω and temperature T dependence. This quantity has already been introduced in Chapter 4, but here it represents a simplification of Eq. (4.51), obtained in the limit of a constant DOS. In addition, the results of the concomitant mass enhancement parameter (i.e., energy renormalization of electron-hole pairs) $\lambda_{\mathrm{op}}(\omega,T)$ are shown. The latter quantity is obtained by performing Kramers-Kronig transormation of Eq. (5.5). Both $1/\tau_{\mathrm{op}}$ and λ_{op} are essential in understanding the temperature dependence of optical conductivity [93], plasmon [149, 160] and phonon [149] damping (when

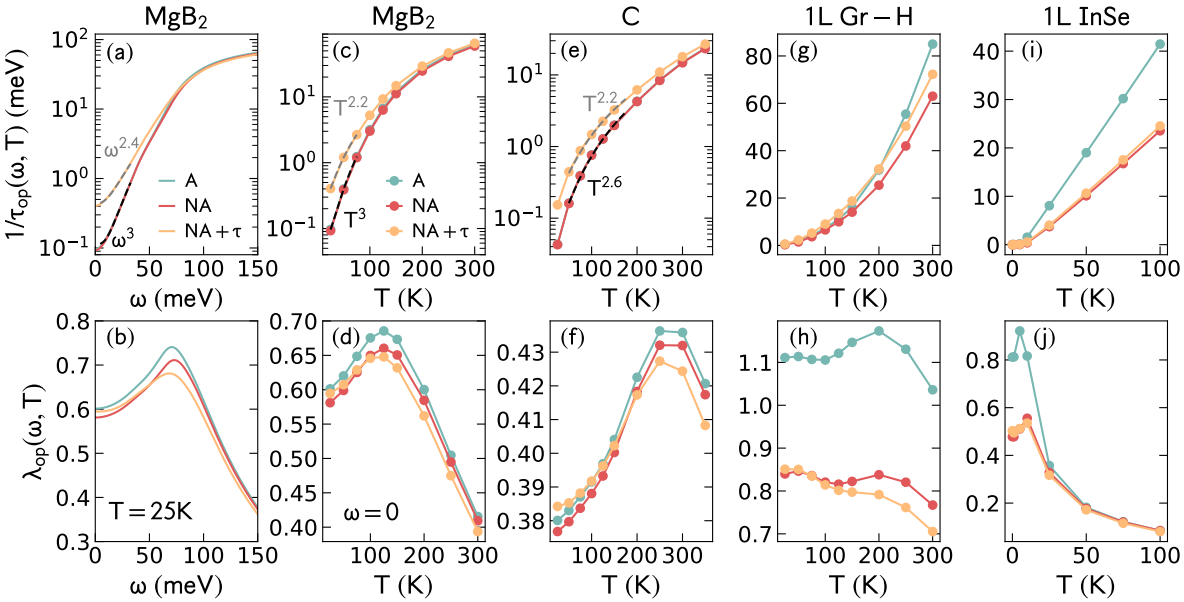

Figure 5.6: Frequency and temperature dependence of the optical (or electron-hole pair) scattering rate $1/\tau_{\rm op}(\omega,T)$ and the mass enhancement (or energy renormalization) parameter $\lambda_{\rm op}(\omega,T)$ for various bulk and 2D materials as obtained with adiabatic (A), nonadiabatic (NA), and full nonadiabatic (NA+τ) methods. Note how the scaling of the low-frequency and low-temperature regime of $1/\tau_{\rm op}$ is modified under the effect of NA phonon broadening. Figure from Ref. [145].

$\omega \neq 0$), as well as for resistivity [148, 161], band renormalization [162, 163], and specific heat [93, 162] (when $\omega = 0$). Note also that the EPC constant is $\lambda = \lambda_{\rm op}(0,0)$.

These results show intriguing modifications of the scaling law for small-ω and small-T regimes of scattering rate $1/\tau_{\rm op}$. Namely, the NA phonon broadening effects that enter the phonon spectral function can significantly decrease the exponents x and y in $1/\tau_{\rm op} \propto a\omega^x + bT^y$, generally, from about 3 to 2 (see Fig. 5.5). This NA effect is particularly emphasized for the cases where the optical phonons with large phonon linewidths are present, e.g., for MgB_2 and C. Then the large phonon linewidths extend to the low-ω part and modifies the corresponding region of $\alpha^2F(\omega)$. It is interesting to note that even though the value of the measured resistivity for MgB_2 varies between different samples, it usually shows roughly T^2 dependence at lower temperatures [164], potentially confirming our predictions.

The scaling change is even more pronounced for systems with low-ω acoustic modes at finite $\mathbf{q}$ having strong NA broadening, e.g., as it is the case for 1L MoS_2 and 1L InSe. The modification of the scaling law for $1/\tau_{\rm op}$ from the usual T^3 to T^2 that comes from the self-consistent treatment of the

NA EPC was already discussed ~ 50 years ago [93, 105], but it was never thoroughly appreciated, examined and applied to the real materials. Here it is confirmed that the T^2 and ω^2 dependence of $1/\tau_{\rm op}$ does not necessarily refer to the Fermi liquid result for the electron-electron scattering, but it can equally be a fingerprint of the strong dynamical electron-phonon scattering. One can describe the present NA effects in $1/\tau_{\rm op}$ as the effective electron-electron scatterings mediated by phonons, and thus the same phase-space arguments for the Fermi liquid result apply here. Note also the substantial modifications of $1/\tau_{\rm op}$ at higher (i.e., linear) T that come from the large modifications of EPC λ due to NA frequency renormalizations, like in the case of 1L Gr-H and 1L InSe.

The NA effects are as well reflected in functional and intensity modifications of mass enhancement parameter $\lambda_{\rm op}(\omega, T)$. Note for instance, that the ω and T scaling laws are also modified in $\lambda_{\rm op}$ for small ω and T when NA phonon broadening effects are accounted for. Large NA-induced modifications of λ, i.e., $\lambda_{\rm op}(0,0)$, are extended to finite-T region, as is evident for 1L Gr-H and 1L InSe. This should, for example, have direct implications on the electron effective mass and its temperature dependence $m^* = m_e[1+\lambda_{\rm op}(0,T)]$, i.e., the band dispersion renormalizations around the Fermi level, and its microscopic *ab-initio* explanations, which are usually rooted in the adiabatic theory [106, 165–167]. Further, finite-temperature $\lambda_{\rm op}(0,T)$ [as well as $1/\tau_{\rm op}(0,T)$], renormalized by the NA effects, which enters electron self-energy in energy-gap Eliashberg equations, can have some interesting impact on estimations of high-temperature superconductivity [168, 169] (notice that such thermal-phonon effects are absent in McMillan's formula for T_c).

5.5 Conclusion

In summary, we have thoroughly examined the influence of the NA phonon dynamics on electron-phonon properties in several theoretically and experimentally established superconductors. The effect of "slow" electrons that lag behind the "fast" moving atoms is actually quite common and it should be considered not only for understanding the dynamics of electrons [88, 90], but also for phonon dynamics and consequently for many physical phenomena that are based on the electron-phonon interaction. The results in Refs. [35, 44] show that the most dramatic dynamical modifications will occur when phonon-induced perturbations of conduction electron density in adiabatic and NA regimes are disparate as well as associated with the strong EPC. See for instance Fig. 3 in Ref. [35] for the nonadiabatic perturbation of charge density in the case of MoS_2 optical out-of-plane phonon at $\mathbf{q} = 0$. Here we show that the same applies for Kohn anomalies away from the Brillouin zone

center, with serious repercussions on the total EPC constant λ and superconducting properties.

The NA-induced modifications of EPC could after all be quite universal and an extension of the present NA treatment might be applicable and useful for explaining electron-phonon properties in a number of unusual and strongly-correlated materials hosting CDW, soft phonon modes or Kohn anomalies, phase transitions, superconducting phase, and enigmatic T^2 resistivity. For instance, the latter scaling law of resistivity was observed concomitantly in materials characterized with the high-T_c superconducting phase (e.g., cuprates [108]), Mott transition (e.g., $SrVO_3$ [111]), structural phase transition and superconductivity (e.g., $SrTiO_3$ [106, 107]), as well as in more conventional systems like Al [170] and TiS_2 [171]. Recently, the T^2 law was observed and discussed for novel graphene-based heterostructures, like graphene superlattice on hBN [172] and twisted bilayer graphene [173]. The superconductivity phase was discovered in the latter case, where the strongly-coupled and damped optical phonons might have an important contribution to the total EPC [174, 175]. In all of these cases the corresponding interpretations were typically given in terms of the Fermi liquid theory ($1/\tau_{\mathrm{FL}} \propto T^2$), i.e., electron-electron scattering, or some corresponding deviations. This work, however, confirms Allen's result [93] that T^2 scaling is not unique to the Fermi liquid result for the scattering rate, and it could also be a sign for the presence of the strongly damped phonons and enhanced EPC. Similar speculations were provided by Feton *et al.* [105], as well as by MacDonald [170].

Notice that the NA corrections might be important for precise determination of transition temperature of CDW and structural phase transition [77, 140, 176, 177], since we show that both $\mathbf{q} \approx 0$ and $\mathbf{q} > 0$ Kohn anomalies are often strongly affected by the dynamical renormalizations, as well as for the electron-phonon part of the thermal conductivity [178].

Chapter 6

Temperature-dependent Raman spectra

6.1 Raman features of graphene

The Raman active E_{2g} mode in graphene exhibits strong coupling to electrons, temperature dependence and is also considered anharmonic. We have already introduced the concept of electron-mediated phonon-phonon coupling in Chapter 4, where through taking into account higher orders of electron-phonon scattering, we actually include terms describing the process of one phonon interacting with virtual electron-hole pairs, which interact with all the other phonons in the system. The E_{2g} mode in graphene therefore represents a perfect platform to study high-order electron-phonon scattering effects due to its anharmonicity and strong EPC, which are in this way entangled.

Understanding phonons and their interactions is crucial for elucidating the role of lattice dynamics in material properties, especially when it comes to temperature and/or doping-dependent phase diagrams [140, 177]. Raman spectroscopy, a powerful and widely applicable experimental technique, plays a key role in studying temperature-dependent phonon behavior. This technique is particularly intriguing for atomically thin materials like graphene and transition metal dichalcogenides [179, 180], where it is widely used to determine the number of layers, interlayer interaction, doping concentration, as well as magnetic and structural phase transitions [181–185]. Valuable insights obtained from these experiments highlight the crucial role of EPC, particularly emphasizing how the interplay between phonons and electronic excitations significantly influences the Raman features of layered materials [186–190], especially in the case of graphene [13–15]. Raman spectroscopy was also found to be useful in probing and discussing the dynamical EPC effects, which are expected to be crucial if the phase velocity of phonons $\omega_{\nu\mathbf{q}}/\mathbf{q}$ becomes larger than the Fermi velocity of electrons

$\mathbf{v_F}$ [86, 87]. Graphene is a remarkable benchmark example of strong dynamical EPC and the failure of static BOA [39–42, 91, 92]. The E_{2g} mode is one of the most prominent features in graphene in its Raman spectra and it represents the in-plane vibrations of carbon atoms [see Fig.4.1(a)] that are strongly-coupled to electrons. In terms of Raman experiments, it is convenient to use the common terminology and for this reason, while referring to the E_{2g} mode, we will call it the G mode. While the G mode has been extensively studied with Raman spectroscopy [16, 191–204], the results are very sensitive to the experimental conditions and different groups report different linewidth and frequency temperature behaviour. However, all agree that the G-mode frequency decreases with temperature in a monotonous manner. The linewidth has a more complicated temperature dependence, but at temperatures above 1000K, it starts to increase monotonously.

One of the open questions concerns the source of the temperature dependence observed for the G mode frequency and linewidth. In addition, the origin of the two different temperature regimes in phonon linewidth is also highly debated [205, 206]. From a theoretical point of view, four-phonon anharmonicity partially explains the observed G mode temperature trends in graphene and graphite [18, 205, 207–210]. In spite of its strength, EPC is considered to have a weak contribution effect as soon as doping prohibits the long-wavelength interband electron transitions by Pauli's exclusion principle [206, 211]. This would classify highly-doped graphene to have a zero EPC linewidth contribution, in spite of strong EPC and a large concentration of electrons at the Fermi level [15, 212]. Besides, a few studies have discussed a possibility that an anomalous linewidth dependence on temperature could be a sign of EPC effects [37, 213]. Nevertheless, Raman experiments done under ultrafast laser excitation, where only the electron temperature is elevated, prove that electrons must be involved in the relaxation process in graphene [14]. It prompts us to question whether the G mode frequency decrease and linewidth increase with temperature could be a result of a shared effort between anharmonicity and EPC as it is for MgB_2 [34].

Despite the difference in their dimensionality, similarities between MgB_2 and graphene begin in their structure. Carbon atoms, arranged in a hexagonal pattern in graphene are effectively substituted with boron (B) atoms in MgB_2. Meanwhile, magnesium (Mg) atoms are positioned above the boron plane, introducing a doping mechanism within the structure. The in-plane stretching of B-B bonds gives rise to a phonon mode characterized by the E_{2g} symmetry. Due to the strong EPC, it is responsible for a superconducting transition [20, 80, 117–119, 121, 122]. Furthermore, the strong temperature dependence of Raman spectra was successfully explained outside the scope of the standard anharmonic theory by employing higher-order electron-phonon scattering within the

framework of the NA theory [32, 33, 42, 120]. Motivated by the experimental implications of optical phonon damping in transition metals being driven by the electron-hole pair decay [37], theoretical advances beyond NA theory have already been made for EPC in certain cases [34, 47, 214, 215]. It amounts to employing memory function methods usually used to calculate the intraband relaxation processes in the dynamical conductivity [82, 149, 160, 216–220], Raman response functions [221] or even exciton-phonon coupling [83]. In this way, one can account for the dynamical higher-order electron-phonon scattering (see Chapter 4), through the inclusion of phonon-induced electron-hole pair self-energy by solving the Holstein problem [222].

In Chapter 5 we have studied the strength of the NA effects in highly-doped graphene, which lowered the superconducting transition temperature from 4.4 K to 1.45 K. It was also made obvious how the majority of EPC contributions come from the zone-center G mode. Therefore, performing a thorough and detailed quantitative analysis of the NA effects in EPC in graphene holds considerable significance since EPC is regarded as the underlying mechanism of the observed superconducting transition [122, 128, 129, 223–225], just as in MgB_2. In this chapter we will systematically explore the role of the electron-mediated anharmonicity in graphene, and make a comparison with the well-known lattice-driven anharmonicity. From first principles, these EPC effects will be included through the temperature-dependent phonon-induced electron-hole pair energy renormalization and finite lifetime. This is in strong contrast to when only a phenomenological broadening is taken into account [4, 42]. These two electron-phonon quantities are expected to exhibit anharmonic-like trends and strongly impact the temperature dependence of the Raman features. We emphasize the generality of this approach, as well as the fact that it completely relies on first-principles.

6.2 Electron-mediated anharmonicity

EPC renormalizes the bare phonon frequencies and introduces a finite lifetime to otherwise infinitely sharp phonons [see Eq. (4.23) and Eq. (4.24)]. In this chapter, we will investigate the impact of EPC on the dynamics of the G mode for 4 different dopings [see Fig. 6.1(a)].

In Fig. 4.1(b), we schematically showed the vertical ($\mathbf{q} \simeq 0$) interband transitions and a 200 meV graphene's optical G mode which facilitates them. Phonon linewidth [see Fig. 6.1(b)] deriving from these contributions reduces as the doping is enhanced due to Pauli blocking. When analyzing the Raman spectra of graphene, this interband EPC contribution to the linewidth is commonly considered as the only EPC contribution [205, 207], which is why it is considered negligible at higher

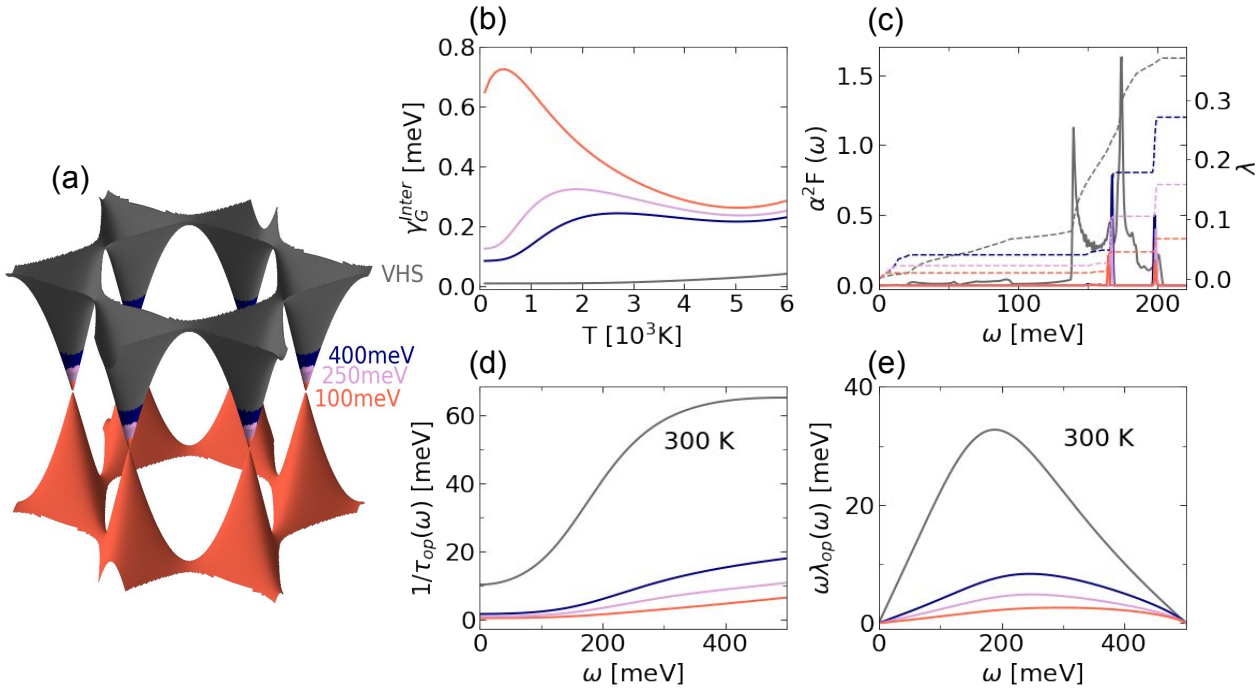

Figure 6.1: (a) Dirac cone schematics of three different chosen doping regimes in graphene with E_F set to 100 meV, 250 meV, 400 meV and 1600 meV. (b) G phonon linewidth due to coupling to interband electron transitions for different dopings, color - coded in (a). (c) Adiabatic Eliashberg spectral function for different dopings, together with a cumulative EPC constant λ showing an increase in EPC with doping. Note that the cumulative λ for 100 meV, 250 meV and 400 meV are multiplied by a factor of 10, to appear at the same scale as the largest doping. (d) Inverse lifetime of an electron-hole pair at 300 K for different dopings, induced by their interaction with phonons. (e) Energy renormalization of an electron-hole pair at 300 K for different dopings.

temperatures or dopings.

In Fig. 6.1(c) we show the adiabatic Eliashberg spectral function for different dopings in graphene, together with a cumulative EPC constant λ showing an increase in EPC with doping. The main contributions come from the G mode and A_1' mode at the K point of the Brillouin zone. The cumulative $\lambda(\omega)$ for 100 meV, 250 meV and 400 meV are multiplied by a factor of 10, so that the doping-induced increase is more evident.

Going beyond the first-order perturbation theory in order to calculate the dynamical intraband EPC contribution was motivated in Chapter 4. An example of a two-step process was schematically shown in Fig. 4.1(c). A bare phonon excites an electron-hole pair which further interacts with all the

other phonons in the system. Essentially, electrons mediate phonon-phonon interaction. In Eq. (4.82) we obtained a finite intraband contribution with an additional temperature-dependent factor deriving from the complex electron-hole self-energy. An equivalent expression can be obtained by the means of Green's functions [87, 226].

Therefore, an interacting electron-hole pair has a finite lifetime $\tau_{op}(\omega, T)$ [Fig. 6.1(d)] and interaction-induced energy shift $\omega\lambda_{op}(\omega, T)$ [Fig. 6.1(e)]. Unlike the interband linewidth contributions, these two quantities increase with the doping level, meaning that EPC effects do not reduce as the Fermi level increases. Experimentally, one can obtain the electron-hole self-energy from the optical conductivity measurements [227] and it can then be used to obtain the electron-phonon spectral function [148, 228, 229], and help understand what kind of boson is involved in the interaction. In theory, one goes in the opposite direction and first calculates the adiabatic Eliashberg spectral function, which reveals the energy of strongly-coupled phonons. A finite temperature expression for the electron-hole self-energy can be calculated from the Eliashberg spectral function as [34, 103]

$$\frac{1}{\tau_{op}(\omega)} = \frac{\pi}{\omega}\int_0^\infty d\Omega\alpha^2F(\Omega)\left[2\omega\coth\frac{\Omega}{2T_{ph}} - (\omega+\Omega)\coth\frac{\Omega+\omega}{2T} + (\omega-\Omega)\coth\frac{\omega-\Omega}{2T}\right]. \quad (6.1)$$

T_{ph} denotes the phonon temperature. However, in our work, we use a further extension to include the effects of electron band structure, what was already discussed for normal and superconducting state properties in Ref. [169, 230, 231]. Further, temperature effects can strongly alter the distribution of electronic excitations [31, 232] and the bare electron DOS can be significantly renormalized by phonons if it varies on the scale of phonon energies [217]. This subtlety is denoted in the Dyson equation (4.55) by the *dressed* electron (hole) propagator lines. The self-consistent self-energy correction leads to a non-linear EPC contribution, or 'rainbow' diagrams resembling the ones in Ref. [233]. Instead of taking into account only the bare DOS, we therefore calculate the quasi-particle DOS [Eq. (4.39)], as was mentioned in Chapter 4. It is calculated self-consistently from the set of equations for the electron spectral function [Eq. (4.40)], reachable in ARPES, and the imaginary part of the electron self-energy [Eq. (4.38)]. The energy dependence in the quasiparticle DOS, $\tilde{N}(\varepsilon)$, then affects the inverse lifetime and EPC constant [231]. The zero temperature result derived in Ref. [234] was extended to finite temperatures in Ref. [82] and the resulting expression is Eq. (4.51). The real part of the electron-hole self-energy can be obtained from the Kramers-Kronig transformations. The temperature dependence in Eq. (4.51) comes from the obvious Fermi-Dirac and Bose distribution factors, but is also hidden in the quasiparticle DOS. Note that using the quasiparticle DOS in the

calculation is equivalent to using momentum distribution functions instead of the Fermi-Dirac distribution [160].

In Fig. 6.2(a) we show the temperature variations in the imaginary part of the electron self-energy. At low temperatures, a characteristic energy dependence can be recognized resulting from the linear Dirac bands and G mode energy [235]. The resulting quasiparticle DOS [Fig. 6.2(b)], aside the temperature dependence, resembles the bare DOS in graphene. The remaining panels in Fig. 6.2, show how the three different approaches to the $1/\tau_{op}(\omega)$ calculation affect the electron-hole and phonon properties. The simplest approximation amounts to neglecting the energy dependence in the DOS. For lightly-doped graphene, it leads to negligible ω_G frequency renormalization and weak linewidth contribution. On the other hand, considering the variations of the DOS with energy leads to larger values for the electron-hole self-energy, strong G mode renormalizations and significant linewidth contribution. The characteristic rapidly increasing DOS in graphene with $E_F = 100$ meV, leads to the higher contribution coming from the ratio $\tilde{N}(\varepsilon)/N_0$ in Eq. (4.51), which is then almost always larger than one. Chemical potential in principle also depends on temperature, and should be computed self-consistently from the quasi-particle DOS. This temperature variation is left for future analysis.

It could be argued that neglecting vertex corrections introduces a degree of uncertainty, but first-principle calculations are subject to this limitation. Also, conflicting evidence in the literature regarding the validity of Migdal's theorem [85] ranges from its breakdown in the NA limit and the possibility of vertex corrections to wash out the NA effects [236–238], to its justification for EPC [87], even for large couplings [239]. Then, there is also evidence of its validity in (doped) graphene [240].

6.2.1 Conventional anharmonicity

The ionic motion is determined by the Born-Oppenheimer potential, which is usually expanded up to second order in ionic displacements, leading to a parabolic harmonic potential well. However, sometimes deviations from the harmonic model cannot be neglected, and a parabolic potential landscape can be modified in shape as well as centered around some other equilibrium position.

If anharmonicity cannot be addressed perturbatively, it becomes challenging to relinquish the benefits of treating phonons as well-defined quasiparticles. Several methods have already been developed in spite of the complexity, many of which are based on molecular dynamics [241], or path-integral molecular dynamics if quantum effects in ionic motion are included [242]. The

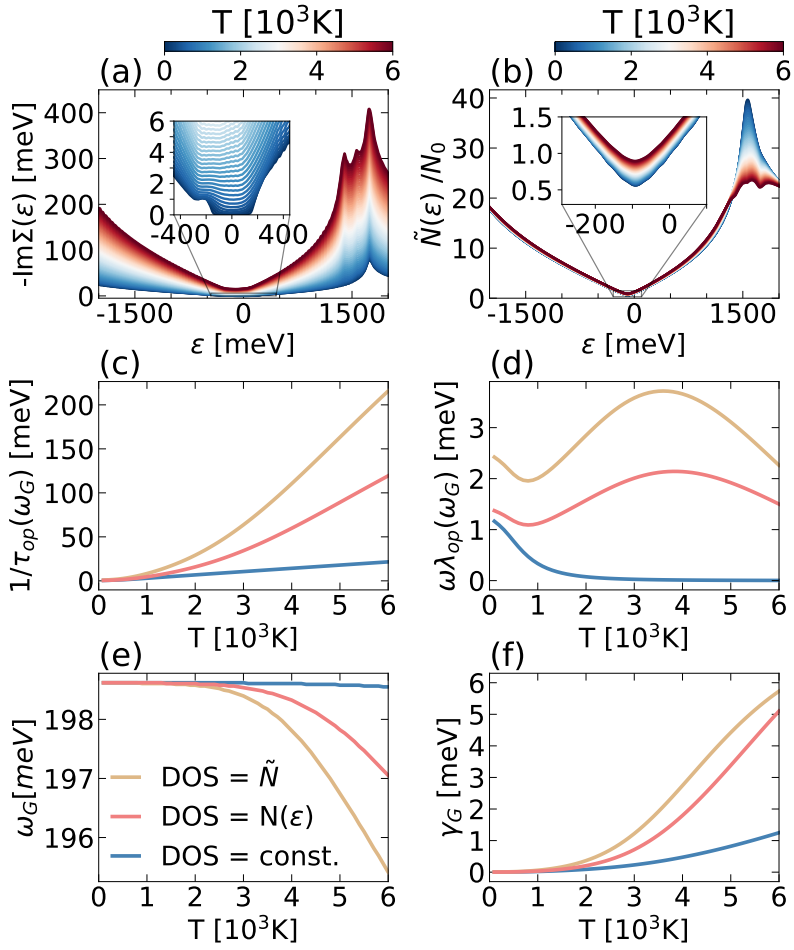

Figure 6.2: temperature-dependent one- and two- particle properties of graphene with E_F =100 meV. (a) Imaginary part of the electron self-energy. (b) Quasiparticle DOS. (c-f) Comparison of three different approaches (constant DOS, bare DOS and quasiparticle DOS) in the calculation of the temperature dependence of (c) electron-hole pair inverse finite lifetime, (d) their energy renormalization and corresponding (e) G mode frequency renormalization and (f) G mode linewidth.

stochastic self-consistent harmonic approximation (SSCHA) [243–245] is a method that correctly incorporates anharmonicity and quantum effects and it also consistently takes into account the fact that the ionic positions can be altered by both effects.

The Dyson equation describing the evolution of the interacting anharmonic phonon propagator can be written as

$$D^{\text{anh}}(\mathbf{q},\omega) = D^{0}(\mathbf{q},\omega) + D^{0}(\mathbf{q},\omega)\pi^{\text{anh}}(\mathbf{q},\omega)D^{\text{anh}}(\mathbf{q},\omega). \tag{6.2}$$

$\pi^{\text{anh}}(\mathbf{q},\omega)$ is the self-energy of the non-interacting anharmonic SCHA phonons. The Dyson equation

can be diagrammatically written as

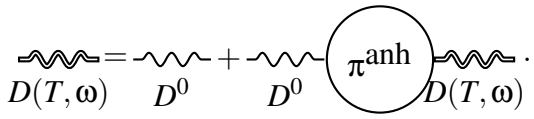

(6.3)

The single wavy line denotes a noninteracting SCHA phonon, while the double wavy line includes the effects of anharmonic interactions hidden in the anharmonic phonon self-energy. In the SSCHA code, the self-energy term is calculated within the dynamical bubble approximation [243]:

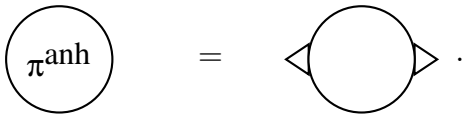

(6.4)

The triangular vertices indicate 3rd order SSCHA force constants, divided by the square root of the masses. The phonon spectral function can be obtained as the imaginary part of the phonon propagator and, in this work, we calculate it within the no-mode mixing approximation and approximate it further as a Lorentzian for each mode. We perform calculations at various temperatures and extract the zero point frequency from a linear fit. We then use this frequency as a reference and calculate the anharmonic phonon self-energy from the frequency shift that occurs with temperature.

The full anharmonic propagator containing the EPC effects is then obtained as

$$B_\nu(\mathbf{q},\omega) = -\frac{1}{\pi}\mathrm{Im}\left[\frac{2\omega^A_{\mathbf{q}\nu}}{\omega^2 - (\omega^A_{\mathbf{q}\nu})^2 - 2\omega^A_{\mathbf{q}\nu}\pi^{TOT.}_\nu(\mathbf{q},\omega)}\right] \tag{6.5}$$

where $\pi^{TOT.}_\nu(\mathbf{q},\omega)$ refers to the total phonon self-energy $\pi^{NA}_\nu(\mathbf{q},\omega)+\pi^{anh}_\nu(\mathbf{q},\omega)$. The first self-energy term $\pi^{NA}_\nu(\mathbf{q},\omega)$ is the NA EPC-induced self-energy term, obtained by adding the dynamical inter- and intra-band contributions and subtracting the static contribution, already accounted for in $\omega^A_{\mathbf{q}\nu}$. The on-shell SSCHA anharmonic phonon self-energy is denoted by $\pi^{anh}_\nu(\mathbf{q},\omega)$.

The G mode frequency is found as the position of the extremum of the calculated phonon spectral function (6.5), and depending on which self-energy contributions are contained, we obtain the interband, intraband, anharmonic, and total frequency shift with temperature.

6.3 Computational details

6.3.1 Electron-phonon contribution

From first principles we calculate electron and phonon properties with Quantum Espresso [68–70] and for EPC we use the EPW code [73–75]. We use the norm-conserving scalar pseudopotential with an energy cutoff of 100 Ry. The relaxed lattice constant is 2.448 Å and the periodic graphene planes are separated by 12 Å. We use Fermi-Dirac smearing with T = 800 K.
For the full Brillouin zone phonon calculation, needed for the Eliashberg function calculation, we use a uniform coarse 48 $\times$ 48 k grid. The phonon calculation is done on a uniform coarse 24 $\times$ 24 q grid. For the EPC calculation, we use maximally localized Wannier functions [71], with five initial projections corresponding to one sp^2 orbital and two p_z orbitals on C atom sites. The resulting Wannier functions lie on top of the two C atoms from the unit cell and on the bond centers. Smearing in the EPW calculation is set to 30 meV, while the electronic temperature in the Fermi-Dirac distributions functions of phonon self-energies is set to 800K. The fine k and q grids are 400 $\times$ 400 and 200 $\times$ 200 respectively.
For the Γ point phonon and EPC calculations, we sample the k space more densely using a 96 $\times$ 96 grid. The electronic temperature in the Fermi-Dirac distribution functions varies in our calculations. The fine k grid is set to 1000 $\times$ 1000.

6.3.2 Anharmonic contribution

In order to calculate anharmonic effects, we first perform a harmonic phonon calculation on a 12 $\times$ 12 supercell, and afterwards we run the SSCHA. The SSCHA calculation begins with initializing an ensemble of ionic configurations with the temperature and the dynamical matrix, which represent how much atoms fluctuate around the average atomic positions. Then, we perform the free energy minimization. The minimization of the variational free energy requires a large number of single-point DFT calculations, performed on supercells. These DFT calculations can become very time consuming, but lately, there has been a large amount of research put into developing machine-learned (ML) interatomic potentials. They are usually trained on a very large number of DFT data and have very good accuracy. In this work, we use the ML interatomic potential from Ref. [246] as a calculator for forces, stresses, and energies, enabling us to go to much larger supercells and numbers of configurations.

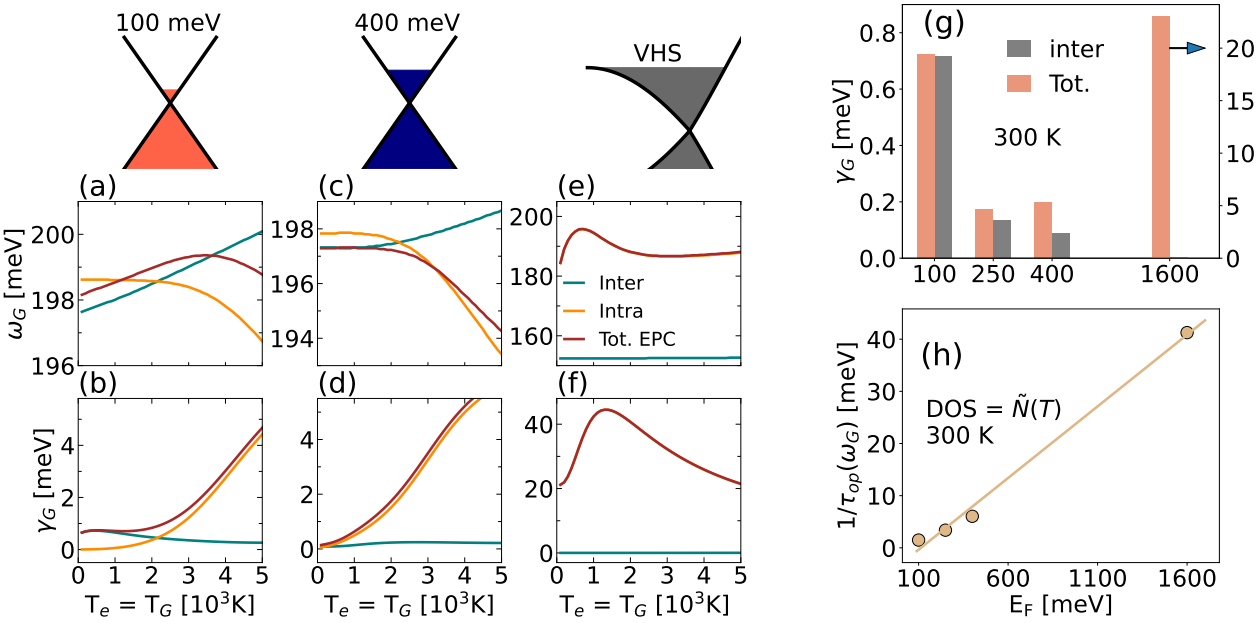

Figure 6.3: For the three doping regimes, we show the total G mode (a,c,e) frequency renormalization and (b,d,f) linewidth induced by EPC. (a) Intraband phonon self-energy contribution leads to the observed trend of frequency decrease with temperature (b) and linewidth increase with temperature. For larger doping shown in panel (c) we observe an even larger importance of the intraband contribution. For the highly-doped graphene (up to Van Hove singularity), intraband contribution is the only one possible and leads to a non-monotonic (e) frequency and (f) linewidth temperature dependence. (g) Comparison between the first-order (interband) and total contribution to the linewidth at 300 K for various dopings. (h) Doping-dependent electron-hole pair lifetime at 300 K.

Next step is the relaxation. Relaxation automatically generates the ensembles, calculates corresponding energies and forces and performs the free energy minimization. We use 1200 configurations in the ensemble and 10 as the maximum number of iterations.

After that, we compute the third order force constants (FCs). Once we have both, the third- and the second-order SSCHA FCs, we have all the ingredients to compute the spectral functions. With the SSCHA code, we can perform a static approximation calculation or a full calculation. For both, we do the summation of the anharmonic self-energy on a 120 $\times$ 120 q grid. In this work, we also use the no-mode-mixing approximation, in order to be able to assign each peak in the spectarl function to only one mode.

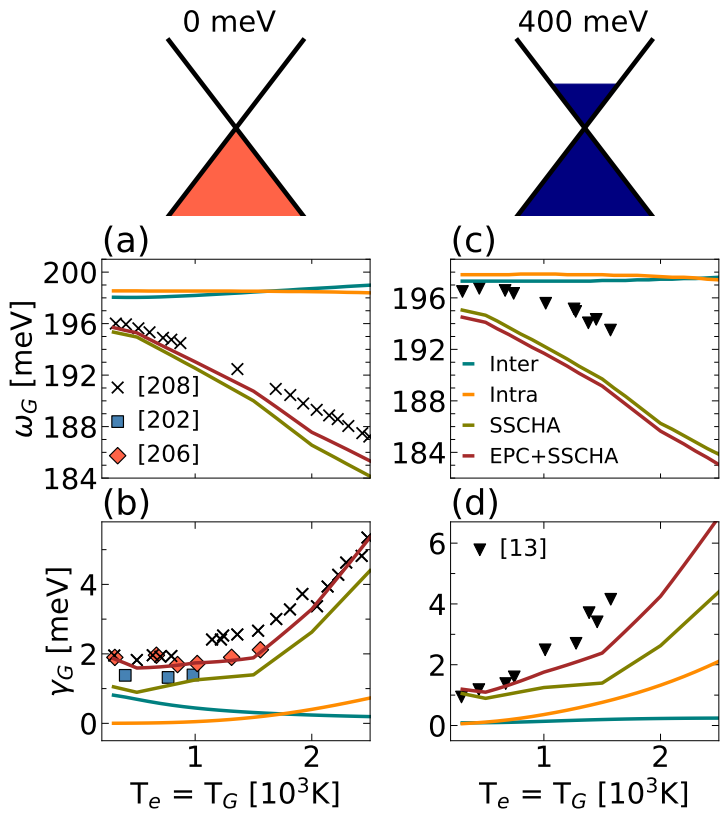

Figure 6.4: For the two different doping regimes, we show the total EPC and anharmonicity-induced G mode (a,c) frequency renormalization and (b,d) linewidth on the smaller temperature range. (a,c) Anharmonic effects have a prevailing temperature dependence at smaller temperatures shown here and determine the G mode frequency decrease with temperature observed in experiments [13, 208]. In (b,d) we show the experimental linewidth increase with temperature as reported in Refs. [13, 202, 206, 208].

6.4 Results

In Fig. 6.3 we show the resulting G mode Raman features for three different dopings. The temperature dependence is indicated as $T_e = T_G$, because the temperature of the electronic system (T_e) is in thermal equilibrium with the temperature of the G mode (T_G). If the Dirac point is at 100 meV below the Fermi level, the G mode with energy 200 meV directly facilitates the interband contribution to the EPC-induced phonon linewidth. In the second column, doping is set to 400 meV, where Pauli blocking should lead to negligible interband contributions. The third case corresponds to graphene doped up to the Van Hove singularity in the DOS. For both, the G mode frequency and linewidth temperature dependence, we explicitly distinguish between the interband and intraband contributions to the phonon self-energy.

Focusing first on the G mode frequency shift [see Figs. 6.3(a), 6.3(c), 6.3(e)] we notice how an increase in doping results in a progressively predominant influence of the intraband contribution on the overall trend. The intraband contribution also becomes more pronounced at higher temperatures

[see Fig. 5.3(a)]. The interband contribution increases the G mode frequency with temperature until, for larger dopings, its effect becomes negligible. Anharmonic effects are known to reduce the G mode frequency with an increase in temperature, especially the four-phonon contribution [18,205,207,209]. Since the intraband contribution corresponds to electron mediated phonon-phonon interaction, it mimics the anharmonic temperature trend. More striking contributions from the intraband phonon self-energy are observed for the G mode linewidth. Contrary to the common belief that the total EPC-induced linewidth derives from the interband phonon self-energy, we obtain a much larger intraband contribution, which has an opposite temperature trend. The weak initial low-temperature linewidth decrease, observed, e.g. in Refs. [202, 210] comes from the EPC interband term and is therefore present only when the Fermi level is smaller than half the G mode frequency. The intraband contribution increases with both quantities and mimics the anharmonic contribution. The anharmonic linewidth increases with temperature due to increased number of activated thermal phonons at elevated temperatures. The total EPC-induced linewidth eventually turns out to be a solely intraband effect. Therefore, overlooking the higher-order electron-phonon scattering effects, leads to an alarmingly incomplete description of the raman G mode spectral features. The obtained frequency and linewidth temperature dependence from EPC is almost entirely attributable to the commonly disregarded intraband contribution (especially in doped samples), while the complete experimental result is an outcome of its cooperative interplay with standard lattice-driven anharmonicity. It supports the conclusion drawn in Ref. [13] that anharmonicity alone is not substantially large to account for the full linewidth. In Figs. 6.3(g) and 6.3(h), we show the doping dependence of the linewidth and inverse lifetime of electron-hole pairs at 300 K. In panel (g) we give an eye opening proof of how the intraband contribution to the linewidth becomes increasingly more important with doping. The drop followed by an additional increase of linewidth as a function of doping is in agreement with experimental results reported in Ref. [212] on $FeCl_3$-doped graphene, while here we provide a convincing microscopic explanation of this behavior through interplay of interband and phonon-assisted intraband contributions to phonon linewidth. In panel Fig. 6.3(h) we show the linear dependence of the electron-hole inverse lifetime on doping. The slope of the curve amounts to 0.027, similar to the value of 0.021 reported in Ref. [212] (for intraband transitions $\mathrm{E}_{\mathbf{k}} \simeq E_F$).

After acknowledging an important role of the dynamical intraband contribution to the phonon self-energy at higher temperatures and dopings, we simulate the Raman spectrum of graphene, with both the EPC and anharmonic effects obtained with SSCHA. Results are presented in Fig. 6.4 at a smaller temperature range than in Fig. 6.3. The two chosen dopings ($E_F = 0$ and 400 meV) are

compared to Raman experiments done on graphite and lightly-doped graphene [202, 206, 208] and to graphene on SiO_2 [13]. Note that for a $E_F = 0$ doping case, the result does not need the inclusion of a chemical potential temperature shift, since due to electron-hole symmetry, this shift vanishes. Frequency dependence is largely determined by the anharmonic effects for both doping regimes, since the intraband EPC effects start contributing at larger temperatures. However, anharmonicity overestimates the frequency drop with temperature, and the EPC effects make up for it. We obtain a fairly good agreement with the temperature frequency trend observed in experiments for both cases, however, for $E_F = 400$ meV case, there seems to exist a shift between the calculation and the experiment. This is understandable, since the experiment is done on graphene with a substrate, while our simulations include only graphene.

EPC and anharmonicity cooperation is more prononunced in the G mode linewidth. For the $E_F = 0$ case, anharmonicity plays a larger role. It contributes with a monotonous temperature increase, similar to the smaller intraband EPC contribution. For a larger doping case, intraband EPC represents an important addition to the strong anharmonic effects, which, alone, underestimate the total linewidth. By comparing Fig. 6.4 with Fig. 6.3, we can notice how the intraband EPC and anharmonic effects eventually, for larger temperatures and doping, become comparable in strength. For the highest doping case investigated in this thesis, we provide further analysis in Fig. 6.5. In the first column [see panels (a) and (b)] we repeat the results already presented in Figs. 6.3(e) and 6.3(f) for clarity. In panels (c) and (d), we show the Raman spectroscopy experimental result from Ref. [247], where photo-doping is induced with lasers of high power, denoted as P_{laser}. Since in the latter experiment, the G mode spectral features are shown in terms of the P_{laser} dependence, in the uppermost panel, we provide a figure from Ref. [13], in order to show the connection between the P_{laser} and temperature, concluding that the P_{laser} in Fig. 6.5 is equivalent to large temperatures with $T_e = T_G$. In Ref. [247], at 1 mW laser power, the power density impinging on the sample is about 800 kW/cm2. The doping used in our work, differs from the one in the experiment from Ref. [247], however, the frequency and linewidth temperature dependence show similar non-monotonous trends. The only mechanism able to explain such behaviour is the higher-order EPC contribution, presented in this chapter. Similar peak in the linewidth was observed in MgB_2, and was attributed to the EPC effects [32–35].

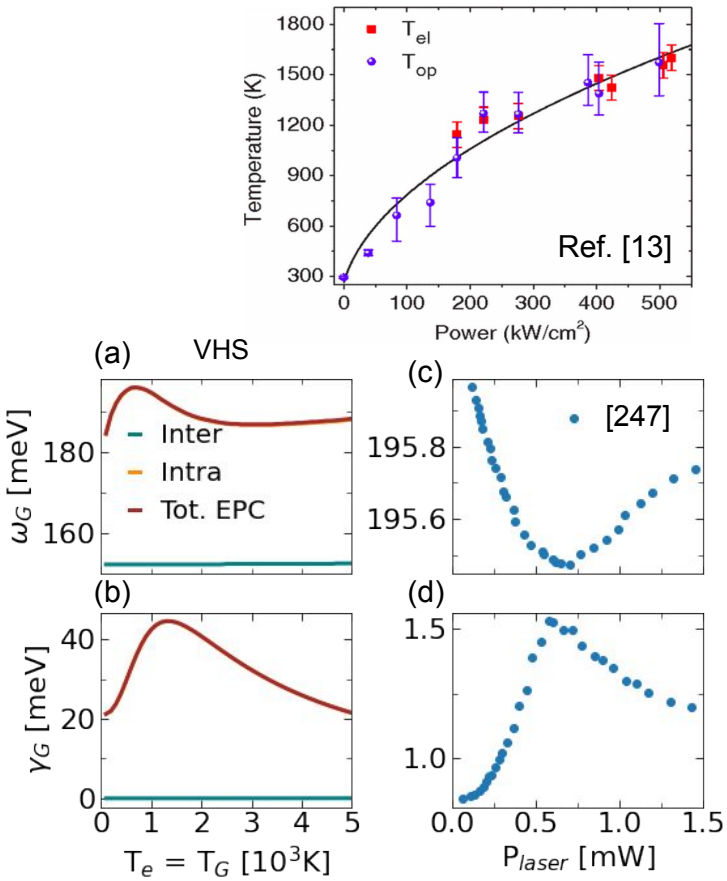

Figure 6.5: Panels (a) and (b) are repeated from Fig. 6.3(e) and 6.3(f) for clarity. In the uppermost panel on the right, we show a figure from Ref. [13], where a connection between the laser power and temperature of electrons and phonons is established. Panels (c-d) contain experimental results from Ref. [247] for the G mode frequency and linewidth, respectively.

6.4.1 Out-of-equilibrium conditions

We now turn to a slightly different scenario, achieved in ultrafast Raman experiments. The main distinction of the ultrafast regime with respect to the continuous wave measurements is that thermal equilibrium between the electron and phonon subsystems is not achieved. In one particular case, where $T_e \gg T_G$, we expect the EPC to play the leading role in the observed experimental trends as anharmonic effects are not driven by the electronic temperature. We employ the same methodology as for the equilibrium case, but only instead of setting the G mode temperature equal to the electronic one, we keep the G mode at 300 K, and vary the electronic temperature T_e. In order to simulate the experiment done in Ref. [14], we did our calculations on doped graphene with E_F =250 meV. In Fig. 6.6 we show the inverse lifetime of electron-hole pairs and their energy renormalization, calculated by progressively more complicated approaches. As for the equilibrium case, taking into account the temperature-dependent quasiparticle DOS leads to the largest contributions to

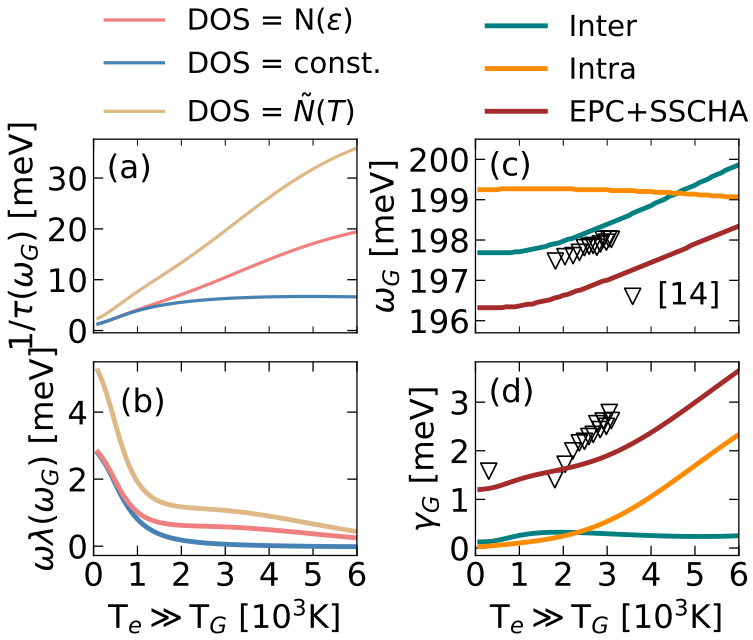

Figure 6.6: (a-b) Electron-hole pair and (c-d) G phonon mode properties for $E_F = 250$ meV in the out-of-equilibrium conditions. Phonon temperature is kept constant (300K), and the effects of changing the electronic temperature are visible in the electron-hole pair self-energy (a-b) through the temperature-dependent quasiparticle DOS. Both, (c) frequency and (d) linewidth of the G mode increase with temperature, as reported in Ref. [14].

both quantities. However, for $T_e \gg T_G$ an order of magnitude is lost in comparison with results presented in Fig. 6.2 due to the large magnitude of Bose-Einstein distribution factors for large phonon temperatures. The G mode frequency dependence in the nonequilibrium regime is now almost entirely resulting from the interband phonon self-energy. Note how the experimentally observed trend is reversed from the equilibrium one, which in our calculations corresponds to the decreased impact of the anharmonic and EPC intraband contribution. The slope of our results corresponds to the experimental one. The linewidth temperature dependence did not change qualitatively in comparison with the equilibrium case, but its magnitude is reduced. The key role belongs to the intraband contribution. We consider the EPC to be the driving mechanism behind the temperature dependence in the nonequilibrium case, making the accurate calculation of the phonon self-energy even more essential.

The theory will now be applied to the Raman-active modes of Weyl semimetals (WSMs) as the anharmonic effects are unable to describe the observed temperature behaviour [248]. In some charge density wave materials, it could be the leading mechanism behind the CDW transition [249] and it could also be important for strongly-coupled or soft phonons away from the Brillouin zone center.

6.5 Raman features of Weyl semimetals

The valence and conduction band in insulators and semiconductors are separated by an energy gap, which can be opened by spin-orbit coupling (SOC). If this mechanism of gap opening includes valence and conduction band inversion, the material is classified as a topological insulator, but if in this process, the band structure remains ungapped at a finite number of points in the Brillouin zone, it is a Dirac or a WSM [250]. A long known Dirac semimetal is graphene, while WSMs are its newly discovered three dimensional analogs. Both have linear band crossings, which leads to the observation of relativistic effects in condensed matter physics. The linear band crossing points in graphene (Dirac points) are protected by time-reversal and inversion symmetry, while in WSMs, one of these is broken [251].

Experimentally confirmed as WSMs, transition metal monopnictides, such as tantalum arsenide and phosphide (TaAs and TaP), have recently sparked interest in the scientific community due to the presence of 12 pairs of Weyl points (WPs) in their Brillouin zone. Examples of their unusual properties include surface states and Fermi arcs, visible in ARPES [251–260]. Together with topological surface states, they feature an interesting phenomenon of chiral anomaly [250, 261–267]. The two effects unambiguously identify WSMs. Chiral anomaly leads to negative magnetoresistance [263, 268, 269] and other unconventional nonlocal transport and optical features [265, 270]. Their intrinsic anomalous Hall effect [271–275], high mobility of Weyl fermions, large linear magnetoresistance [179, 276, 277] and linear frequency-dependent conductivity [278, 279] only skim the surface of these exotic materials.

Apart from these unconventional properties, the presence of Weyl cones and low-energy transitions within them affects the phonons via EPC, responsible for a plethora of transport and thermodynamic phenomena in solids. WSMs such as TaAs and TaP exhibit 24 Weyl cones in their bulk band structure, all at various energies close to the Fermi level [251–260, 279–282], in the energy window of the characteristic optical phonon frequencies [248, 282–284]. Optical spectroscopy and thermal transport measurements indeed reported EPC to be strong in WSMs [248, 282, 285–288]. When focusing on the temperature-dependent phonon linewidths and frequencies, there are discrepancies in the performed measurements, as well as their theoretical simulations [248, 282], coinciding with the disagreements of the energy positions of the WPs with respect to the Fermi level. However, all demonstrate the importance of EPC and the energy of the WPs in their phonon spectral features. The formalism of electron mediated anharmonicity has not yet been considered in the framework of WSMs even though both EPC and anharmonicity [289, 290] seem to rule their phonon spectra.

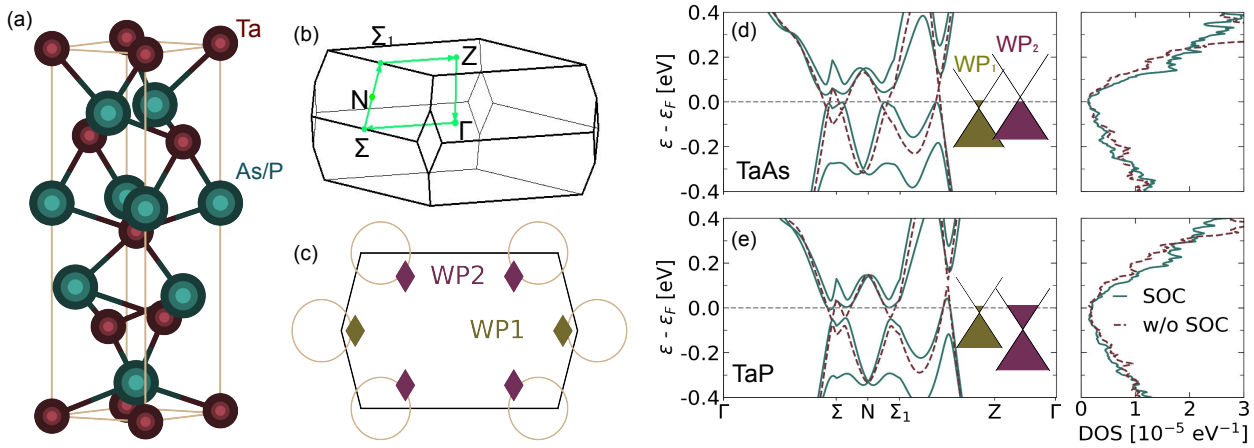

Figure 6.7: (a) Atomic structure of TaAs/TaP compound. Ta atoms are denoted in red, and As or P atoms in green. (b) Corresponding Brillouin zone with the relevant high-symmetry points marked with green points. (c) Schematics of the nodal lines in the band structure, visible if SOC is not included. With SOC, instead of nodal lines, WPs arise at the marked places. Comparison of the band structures and DOS for (d) TaAs and (e) TaP with (dashed dark-red lines) and without (green lines) the SOC effects, together with the schematic inset showing the positions of the two types of WPs in our calculations.

Considering these observations and the established role of EPC in WSMs, we investigate the impact of EPC on the temperature dependence of frequency and linewidth of Raman-active phonon modes in TaAs and TaP. We believe that consistent EPC renormalizations of both the quasiparticle DOS and phonons are crucial to obtain realistic temperature shifts of their phonon linewidth and frequency. From first principles, we will simulate the Raman spectra of two WSMs; TaAs and TaP by accounting for the dynamical higher-order electron-phonon scattering. Performing calculations with and without SOC, we will provide direct evidence of the role the WPs play in EPC and by fine-tuning the parameters, we will shed new light on the inconsistencies in the literature.

6.5.1 Basic properties of TaAs and TaP

TaAs and TaP crystallize in a body-centered tetragonal structure with space group $I4_1md$ [see Fig. 6.7(a)]. The corresponding Brillouin zone with the indicated high-symmetry and characteristic WPs can be seen in panels (b) and (c). Electron and phonon band structures are plotted along the lines connecting the symmetry points.

SOC is important in WSMs, because they consist of heavy atoms. The SOC effect originates from the relativistic interaction between spin and orbital motion of particle, which can modify atomic

energy levels and split the energy bands in crystalline materials. Comparison of band structure with and without SOC for TaAs and TaP in Figs. 6.7(d) and 6.7(e) reveals how the band degeneracy is lifted and the gap introduced at the band crossing points due to SOC. Without SOC, the valence and conduction bands touch along an unbroken closed loop, enclosing one of the high-symmetry points. These loops are called nodal lines and are shown in schematics in Fig. 6.7(c). Nodal lines exist due to the same symmetry reasons which keep the Dirac cone in graphene ungapped [250]. Since graphene is 2D and WSMs are 3D materials, the Dirac point forms a nodal line. Once SOC is turned on, valence and conduction bands are separated and displaced from the high-symmetry paths in the reciprocal space, which in turn introduces WPs as indicated in the schematics. With WP1 we denote the WP found in the z=0 plane, while WP2 denotes the WPs with a finite z coordinate. In our calculations, for TaAs we find both types of WPs within $\pm$ 5 meV with respect to the Fermi level, and for TaP, WP1 is 5 meV below it, while WP2 is 25 meV above.

Owing to the gapped band structure, the conduction electron density derives mainly from the Weyl cones and is therefore rather small. Therefore, the DOS at the Fermi level is rather low and shifting the position of the WPs with respect to the Fermi level, greatly changes the electronic DOS or the landscape of such a small Fermi surface. Consequently, the available phase space for electronic transitions modifies, which affects the phonon frequencies and linewidth and was even reported to modify the linear conductivity dependence on frequency [279]. WSMs have a sensitive Fermi level (or more precisely chemical potential) position, and the low DOS in a small energy range around the Fermi level allows for the mentioned inconsistencies regarding the WPs energies in the literature [248, 282].

The four atom unit cell of TaAs and TaP results in a total of twelve phonon modes [see Figs. 6.8(a) and 6.8(c)]. For both materials we do not observe significant SOC-induced changes in the phonon band structures. A polarized Raman study of these materials [284] identified all the optical phonon modes and determined which atoms are involved in each mode as well as the mode symmetry. The strongest EPC contribution, visible as a peak in the Eliashberg spectral function in Figs. 6.8(b) and 6.8(d) in our calculations, derives from the weakly dispersive A1, E3 and B1 optical modes sketched in Figs. 6.7(d) and 6.7(e), all at about 30 meV for TaAs and 45 meV for TaP.

The total EPC constant is quite small for TaAs even after the almost twofold SOC-induced increase (from 0.03 to 0.05). The increase derives from the large SOC-induced changes in the Fermi surface. For TaP, the SOC effect on $\alpha^2F(\omega)$ is negligible, as well as on its total EPC coupling constant, which remains similar to the one calculated for TaAs without SOC. In TaP SOC induces

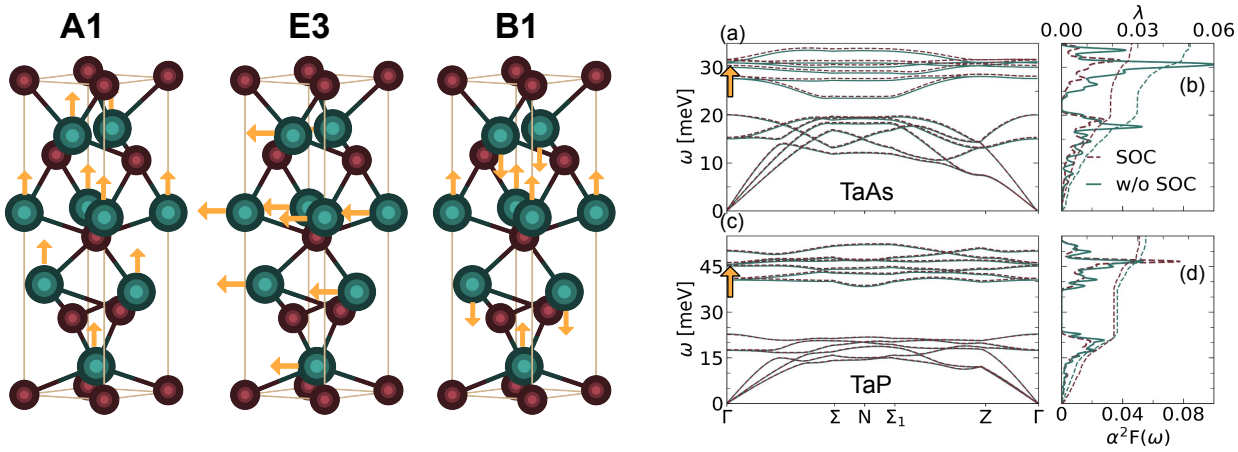

Figure 6.8: (a) Comparison of the phonon dispersions and (b) $\alpha^2F(\omega)$ together with a cumulative EPC constant $\lambda(\omega)$ for TaAs and TaP (c-d) with (dashed dark-red lines) and without (green lines) SOC effects. The three modes which contribute to the EPC the most, are shown on the left-hand side, and are also marked with the orange arrows in the phonon band structures.

large changes in the Fermi surface, but the position of the Fermi level is such that it mostly passes through the SOC-induced energy gap.

6.5.2 Temperature-dependent properties of TaAs and TaP

The main goal of Fig 6.9 is to emphasize the importance of temperature effects on the imaginary part of electron self-energy [see panel (a)] and quasiparticle DOS [see panel (b)] when calculating the electron-hole self-energy, using TaAs as the example. The ratio of the quasiparticle renormalized DOS and bare DOS at the Fermi level in the inset of panel (b) shows that the largest deviations from the bare DOS happens around the Fermi level at the energy range relevant for the phonon-assisted transitions. The importance of taking those quantities into account when calculating the electron-hole self-energy is emphasized in panels (c) and (d). In Fig. 6.9(c) it is shown how it results in a significant increase of $1/\tau_{op}(\omega, T)$, with respect to neglecting the electron DOS energy dependence altogether. Below the main panels, we show the chemical potential temperature shift (e). In doped samples, the obtained shift for TaAs indicates that at 800K the WPs end up about 50 meV above the Fermi level. Since in WSMs the temperature changes the chemical potential [264] it also greatly affects the electronic excitations distribution [31, 232]. It renders the phonon spectrum very sensitive to temperature. Essentially, the electronic DOS is varying on the energy scale of

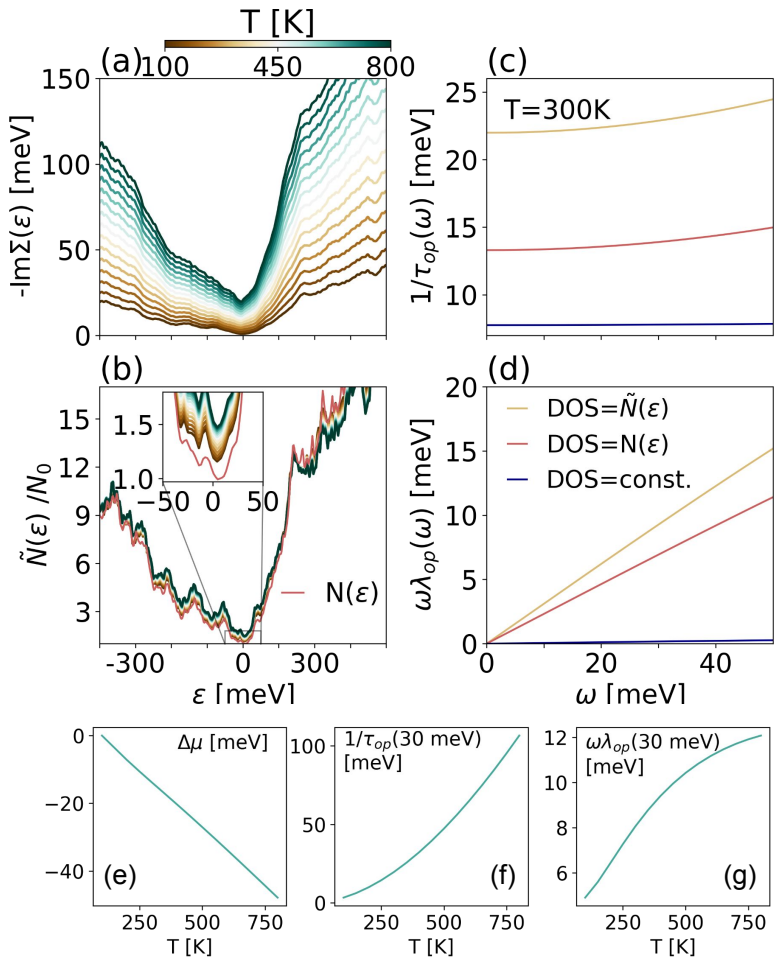

Figure 6.9: (a) Imaginary part of the electron self-energy with the color scale representing different temperatures in the range between 100K and 800K for TaAs with SOC included. (b) With the same color scale, we show the ratio between the bare DOS at the Fermi level and the renormalized quasiparticle DOS, which is a prefactor in the expression (4.51). The inset shows a close up on the energy range around the Fermi level. Energy-dependent (c) imaginary and (d) real parts of the electron-hole self-energy for 300 K, calculated with the three different expressions: Eq. (6.1) (dark blue), Eq (4.51) with $\tilde{N}(\varepsilon) \to N(\varepsilon)$ (pink) and full Eq. (4.51) (yellow). (e) Chemical potential shift due to temperature. (f) Temperature dependence of $1/\tau_{op}(30\,\text{meV})$ and (g) $\omega\lambda_{op}(30\,\text{meV})$.

phonon frequencies in TaAs and TaP, which is why bare electronic DOS renormalization can be strong [217], as well as why the temperature shifts in μ need to be taken into account when simulating the temperature-dependent phonon spectral features of WSMs. The position of μ with respect to the WPs will later be important for the interband EPC contribution to the phonon linewidth. In panels (f) and (g) we show how the real and imaginary parts of the electron-hole self-energy calculated from Eq. (4.51) depend on temperature at the energy of strongly-coupled optical phonon modes. Note that the temperature-dependent value of $1/\tau_{op}(\omega)$ or $2\text{Im}(\Sigma)$ could be used as an estimate for the broadening parameter entering the interband phonon self-energy, especially considering the small energy scales in WSMs [see Eq. (4.53)] [45, 149]. Regarding the dynamical intraband EPC contribution, it can be strongly altered by the electron-hole linewidth, $1/\tau_{op}(\omega, T)$. Regarding its temperature dependence, at the range from 100K to 800K it changes from 0 to 100 meV, which

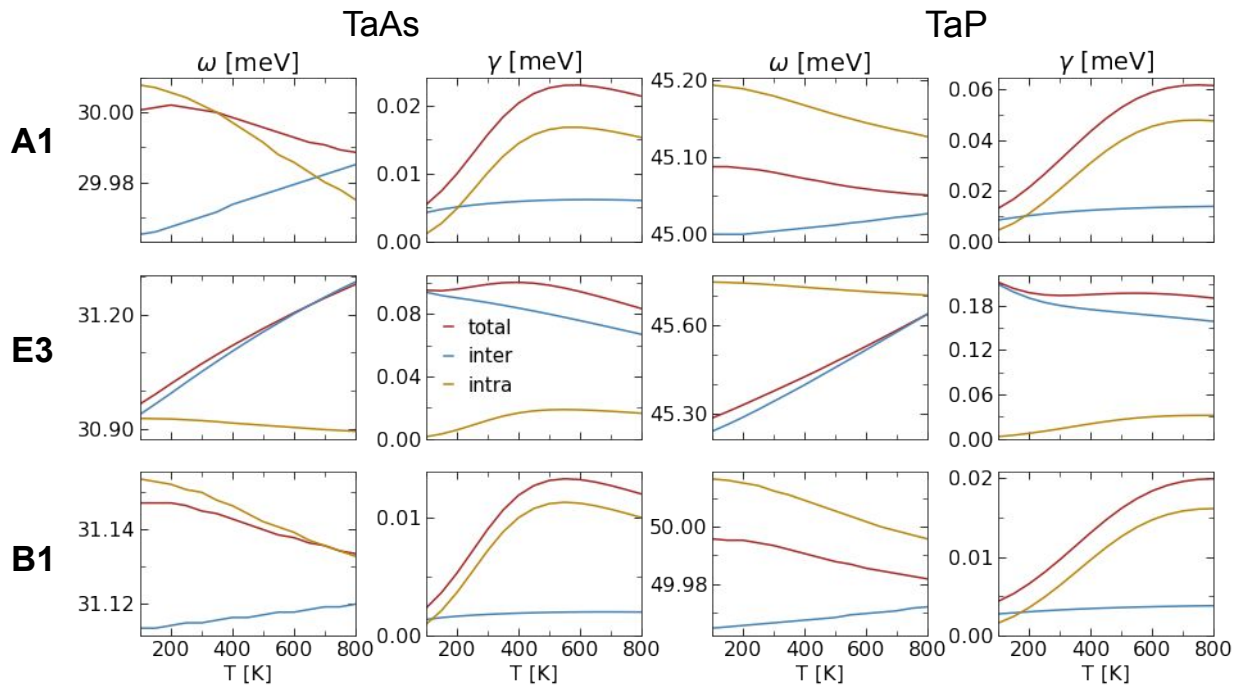

Figure 6.10: Raman features of TaAs and TaP. Each of the three rows represents one of the three modes, sketched in Fig. 6.8. In the first column, we show the temperature-dependent frequencies of the three modes in TaAs. In the second column, we show the corresponding linewidths. Similarly, in the next two columns we show temperature-dependent frequencies of the three optical modes in TaP, and their corresponding linewidths. In all the panels, we distinguish between the total EPC contribution, and its interband and intraband components.

renders the dynamical intraband contribution negligible and large, respectively. This two-particle broadening property, apart from many-body interactions, reflects also the amount of defects or irregularities in the sample. It means that its value could differ significantly from the one reported here, but it is not the case for its temperature-dependent trend.

Including all the mentioned temperature-dependent properties in the phonon self-energy calculation, we obtain the full Raman spectrum simulations for TaAs and TaP in Fig. 6.10. We investigate three optical modes coupled to electrons [see Fig. 6.8]. Modes of A1 and B1 symmetry both represent oscillations of As/P atoms along z axis, while modes of E symmetry represent orthogonal oscillations. In the Γ point E2 and E3 modes are degenerate and the Raman features look alike, so we focus just on E3.

The first two columns respectively represent the temperature-dependent frequency shifts and

linewidths for the three mentioned phonon modes for TaAs. The last two, refer to TaP in an analogous manner. For all the investigated modes, we report very weak EPC-induced frequency shift (< 0.5 meV). A1 and B1 modes exhibit similar frequency temperature dependence in TaP and TaAs, with a weak decrease owing to the intraband EPC contribution. Frequency of the E3 mode shows an opposite behaviour, following the interband EPC contribution trend. In our calculations, modes of A1 and B1 symmetries do not couple strongly to interband excitations, while modes of E symmetry do not couple to intraband electron-hole excitations.

For the linewidths of the investigated modes, we can draw similar conclusions. For the A1 and B1 linewidths, we observe an intraband EPC contribution guided increase with temperature for TaAs and TaP. At large temperatures, the linewidth reaches a plateau for TaP, while for TaAs it even seems to reverse its trend. Optical modes with symmetry A1 in TaAs are reported to be coupled to the continuum of electronic excitations confirmed by the observed temperature-tunable Fano lineshapes [282] and atypical linewidth temperature dependence [248]. Similar conclusions about the importance of phonon decay into electron-hole pairs were drawn for other WSMs [286, 291, 292]. Fano lineshape is an asymmetric phonon profile which arises as a consequence of an interference between a continuum of states and a discrete state [293] and for TaAs was interpreted as arising from coupling to the low energy continuous electron–hole pair (Weyl fermion-like) excitations [282]. The asymmetric Fano lineshape diminishes with temperature showing that EPC strength reduces. It was attributed to the Pauli blocking mechanism of the interband electron transition, but our calculations show a negligible interband contribution to the linewidth, negating this argument. On the other hand, non-monotonic linewidth temperature dependence reported in [248] resembles our result, but on a different temperature scale. Therefore, the reported A1 linewidth modifications could be a result of the intraband electron transitions and their interaction with phonons in some different $1/\tau_{op}(\omega, T)$ regime. It is also interesting to see how the interband contribution of the A1 and B1 modes shows a weak temperature-induced increase, perhaps best visible in panels (d) and (f). It is an effect of the temperature-dependent broadening and chemical potential in the interband phonon self-energy expression. Further, we observe that E3 mode is more strongly-coupled to electrons in comparison with the A1 and B1 modes, which is manifested in the obtained largest linewidth values, and it is conditioned by the interband electron transitions. It shows a weak temperature decrease, which is a result of the aforementioned Pauli blocking principle.

In Fig 6.11 we show the changes induced by SOC in TaAs. In panels (a) and (b) we show $1/\tau_{op}(\omega, T)$ and $\omega\lambda_{op}(\omega, T)$ with and without SOC effects, calculated at ω = 30 meV, which is the

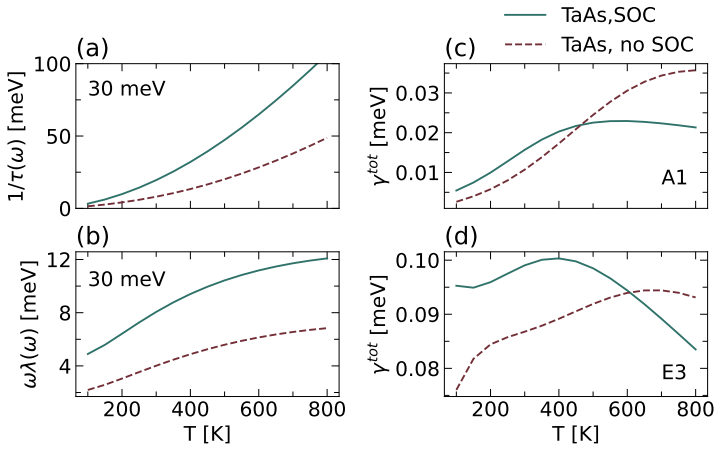

Figure 6.11: Comparison between the calculations with and without SOC for TaAs. Temperature dependence of (a) $1/\tau_{op}(\omega,T)$ and (b) $\omega\lambda_{op}(\omega,T)$ calculated at ω = 30 meV. Temperature-dependent linewidths of the (c) A1 and (d) E3 optical phonon modes with and without SOC.

energy of the three coupled phonon modes investigated in this thesis. Both of these electron-hole properties are enhanced when SOC is taken into account. In panels (c) and (d), we present the linewidth of A1 and E3 modes with and without SOC effects. The SOC-induced changes in the Fermi surface lead to a completely different temperature-dependent linewidth regime in the two cases. We believe it can be entirely attributed to the changes in the electron-scattering phase space. The B1 optical phonon mode linewidth undergoes the same non-monotonous temperature dependence with and without SOC as the A1 mode, which is why it is left out from Fig. 6.11.

In Fig 6.12 we show how the linewidth of A1 and E3 modes in TaAs can be tuned by the electron-hole relaxation time and chemical potential, respectively. Focusing first on the A1 mode, it is interesting to see how the increase of $1/\tau_{op}(\omega,T)$ decreases the temperature with the peak linewidth value and shifts the region where the linewidth of the A1 mode reverses its temperature trend. It is important to note that when multiplying the $1/\tau_{op}(\omega,T)$ with a factor written in the panels of Fig 6.12, it also affects the interband contribution via the temperature-dependent broadening in the interband phonon self-energy. This type of temperature and parameter-dependent behaviour could serve as a reconciliation of the two mentioned experiments, which are also shown in the bottom two panels in Fig 6.12, [see panels (c) and (d)]. One of them is reporting a linewidth resembling the one Fig 6.12(a) [248] and the other experiment is reporting a linewidth resembling the one in panel (b) [282]. Note also the anomalous linewidth reported for tungsten phosphide (WP_2) in Refs. [286, 291] and for niobium arsenide (NbAs) in Ref. [248], which also follow the trends obtained in our calculations. However, all these work attribute the anomalous behavior of phonon linewidth to interband transitions. The reported linewidths for TaAs exhibit temperature changes on a larger scale, than the one we observe in our calculations, with overall larger linewidths. Even though, this could

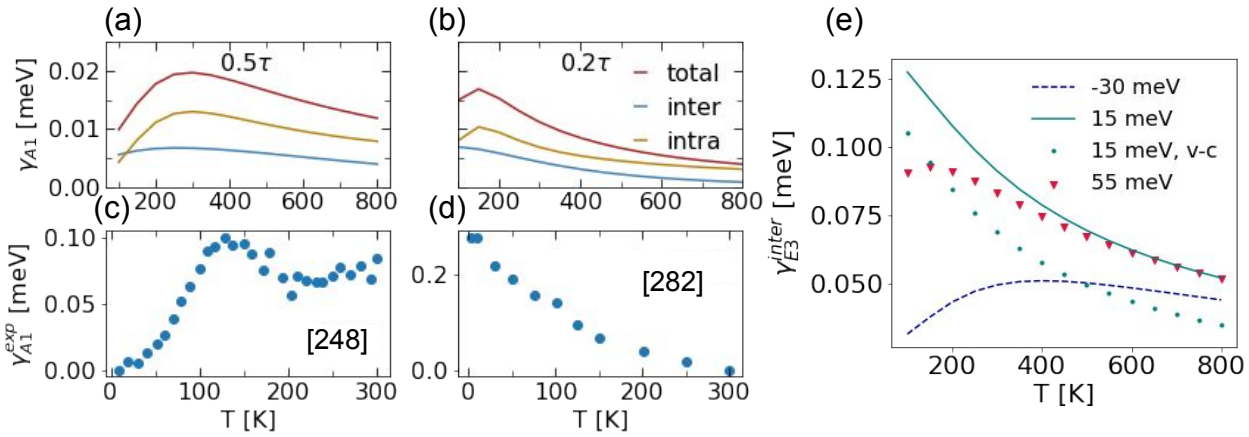

Figure 6.12: Interband, intraband and total EPC-induced A1 linewidth in TaAs when $1/\tau_{op}(\omega, T)$ is multiplied by a factor of (a) 2 (b) 5. Experimental TaAs linewidth measurements adopted from (c) Ref. [248], (d) Ref. [282], where we subtract the linewidth value at T $\rightarrow$0 and T = 300K respectively. (e) Interband EPC-induced linewidth contribution for various cases of the Fermi level position. In the legend, we denote its position with respect to the both WPs [which are in our calculations very similar in energy, see Figs. 6.7(c) and 6.7(d)]. A calculation for the Fermi level 15 meV higher than the position of the WPs, is done also by restricting the electron transitions to only the ones happening between the highest valence and lowest conduction band. This case is denoted by '15 meV, v-c'.

be an artefact of a Brillouin zone sampling, which is too coarse to capture all the relevant transitions, in our calculations also a standard anharmonic contribution and other broadening mechanisms are not included. Anharmonic contribution would be increasing with temperature, as seen for graphene in Fig. 6.4 and it could be responsible for the experimentally observed linewidth increase with temperature after about 225K. Such a trend is not visible in the other experiment, which could lead us to the conclusion that the onset of anharmonicity is shifted.

It is also worth mentioning that the overall weakness of the EPC strength that we observe in the two investigated WSMs, could derive from the PBE functional used in our calculations. Going beyond PBE, as it was shown in Refs. [294–296] for other correlated materials, could significantly enhance the EPC matrix elements and lead to the overall larger EPC effects, in better agreement with experiments.

As for the E3 mode, due to its coupling to the interband transitions, it shows sensitivity to the μ position [see Fig 6.12(e)]. We show the interband EPC contributions to the E3 mode linewidth for three different choices of the Fermi energy. The Fermi level position resulting in the linewidth

denoted by a dashed line corresponds to the case where the WPs are about 30 meV above the Fermi level. With a full line, we denote the case for which the WPs are about 15 meV below the Fermi level, while the case where the WPs are about 55 meV below the Fermi level is plotted with triangular symbols. Since this is the analysis of the Fermi level position, we keep the broadening parameter fixed at the value of 10 meV, and we do not include the chemical potential temperature shift. We find that the linewidth is the largest when the Fermi level is about 15 meV above both of the WPs. This corresponds to the case where the Weyl cones are doped until about half the E3 phonon energy. From the comparison in Fig. 6.12(e) we can confirm that the majority of contributions comes from the transitions between the valence and conduction bands, since the dotted line denotes a linewidth calculation with a sum restricted to these two bands. We also know that the valence and conduction bands in the remaining parts of the Brillouin zone are much farther apart than along the high-symmetry lines [see Fig. 6.7(c)], and even there such position of the Fermi level leads to rather small linewidth contributions. Also, in our calculations, Weyl cones are not tilted, implying that the valence and conduction bands are symmetric around WPs and graphene-like interband vertical transitions take place. This leaves the WPs to be the most significant source of the E3 linewidth contribution, even though they occupy a very small phase space volume.

Apart from the changes in the E3 linewidth value, we can notice a change in this temperature trend as the Fermi level is changed, similar to what is observed by changing the doping levels in graphene in Fig. 6.1(b). Currently, we are not familiar with the linewidth measurements performed for the modes of E symmetry, but we believe that these considerations may explain different linewidth regimes achievable by tuning the Fermi level position with respect to the WPs.

6.6 Conclusion

In this chapter, we revisited the EPC theory in graphene and WSMs, TaAs and TaP, in order to reveal its effect on the temperature-dependent properties of G in graphene and A1 mode in WSMs Raman spectral features. The EPC is screened by the first-order dynamical interband NA coupling and the dynamical intraband term, which can be viewed as electron-mediated phonon-phonon coupling. The latter effect is effectively anharmonic and shows some temperature characteristics as the standard lattice-driven anharmonicity. In graphene, in combination with conventional anharmonicity it leads the total EPC effect in the temperature dependence of G mode frequency and linewidth to support the experimental results. Our work demonstrates that for the lightly-doped graphene the

electron-mediated anharmonicity is almost equally important as standard lattice-driven one, while in highly-doped samples it dominates the phonon dynamics. In the investigated WSMs, we found that the experimentally reported unconventional linewidth of the Raman-active A1 mode does not come from the coupling to the interband electron transitions, as widely believed. In our calculations, A1 and B1 modes couple almost exclusively to intraband excitations. In fact, we manage to reproduce experimental trends by tuning the lifetime of electron-hole pairs what is completely justified as it is a quite sample-dependent feature. On the other hand, modes of E symmetry are found to couple to the interband transitions and are therefore affected by the Fermi level shifts and the position of the WPs.

We believe that the EPC-related microscopic scattering processes discussed and simulated in this chapter are crucial to describe Raman experiments for materials with significant electron coupling to Raman-active modes.

Chapter 7

Electron-phonon coupling in photoexcited systems

7.1 Photoexcitation

Photoexcitation as in pump-probe setup is a powerful tool that can track thermalization and dynamics of electron-lattice system in real time. It paves the way for effective designing and customizing of the desired functionalities of materials and for understanding the fundamental interactions in them [25, 26, 297]. Due to ultrashort duration, usually below the characteristic thermalization timescale, the corresponding laser sources are not only able to probe and disentangle the relaxation pathways of electrons, phonons, spin, and other degrees of freedom [298, 299], but can reveal new physical phenomena and phases of matter [300–306], which are sometimes unreachable in equilibrium [307]. For example, this is opening the possibility of light-induced superconductivity [308–312], controlling the temperature or dimensionality of a CDW ordered phase [300, 302, 313–316], photo-induced ferroelectricity [28, 317–322], and disorder-assisted structural transition [323].

Very often, a strongly-coupled phonon mode and considerable EPC are associated to these states of matter, and both are believed to be renormalized in a photo-excited nonequilibrium regime [324, 325]. EPC therefore plays a crucial role in the ultrafast phenomena [25, 326–328] and it is of utmost importance to master and comprehend microscopic channels ruling phonon dynamics in extreme nonequilibrium conditions. For instance, photo-induced softening of the relevant phonon mode is quite common in ultrafast dynamics [329, 330]. Nonetheless, photoexcitation can in some cases lead

to phonon hardening and consequently stabilize the structural phase [331–335]. Complementary to the time-resolved photoemission methods that provide an important access to the electron-hole thermalization process [114,298,299,336–338] and electronic structure changes [339,340], there are several ultrafast techniques, such as ultrafast electron diffraction scattering [335,341–347], coherent phonon spectroscopy [331,348–351], and time-resolved Raman spectroscopy [332,352–354], that can precisely track the phonon relaxation channels following the photoexcitation and corresponding EPC strength [348,349]. For instance, ultrafast electron diffraction had uncovered highly anisotropic non-thermal phonon relaxation in black phosphorus [345], and mapped momentum-resolved electron-phonon scattering channels and strengths in various TMDs [335,341,346,347]. Intriguingly, these methods are able to analyze photo-induced phonon frequency modifications and uncover the relevant microscopic processes, as it was done, for example, for the strongly-coupled E_{2g} optical mode in graphite with coherent phonon [331] and time-resolved Raman spectroscopies [332], as well as for the amplitude CDW mode in $TiSe_2$ by means of ultrafast electron diffraction [335]. In combination with other time-resolved spectroscopy approaches, the latter technique allowed to pinpoint the phonon modes that play an active role in unconventional superconductivity of FeSe thin films on $SrTiO_3$, and to extract the correlation-induced EPC constants [348]. Further, recent study on graphite reported dynamics of coherent vibrations for both zone-center and zone-edge phonon modes with unprecedented energy and time resolution allowed by attosecond core-level spectroscopy [350].

In order to obtain a complete insight into the ultrafast phonon dynamics and unveil the corresponding electron-phonon scattering paths, the above studies need to be complemented with microscopic theoretical methods, preferably based on quantitative description of nonequilibrium state beyond simple phenomenological approaches. In this chapter, we will examine two photo-excited 2D systems; graphene and MoS_2 and address them with a slightly different theoretical approaches. For graphene, we will first perform tight-binding model calculations of the photo-excited phonon self-energy. Then, we will employ *ab-initio* calculations and manually modify the equilibrium electronic distribution already on the DFT level, i.e., by means of cDFPT [54]. For MoS2, we will use the time-dependent Boltzmann equations (TDBE) in order to accurately simulate the time dynamics of electron distributions in the EPC calculations.

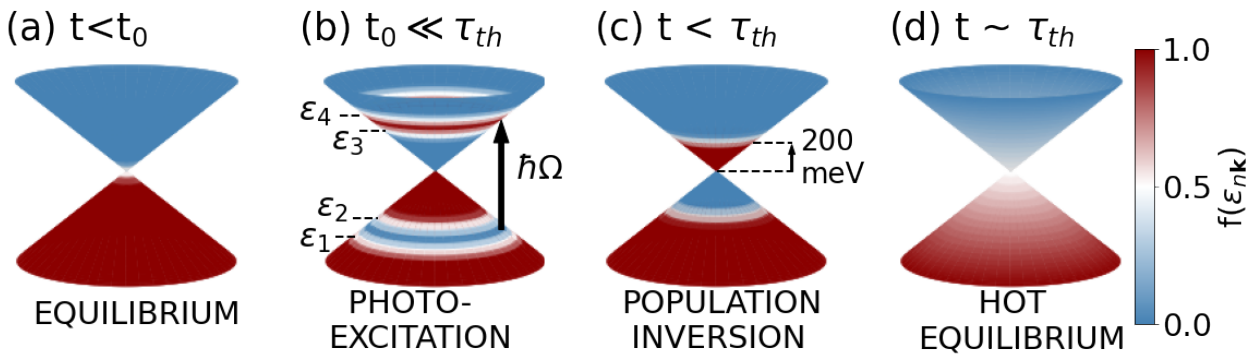

Figure 7.1: Schematic representation of different stages of electron relaxation in photo-excited graphene. (a) Dirac cone with an equilibrium Fermi-Dirac electron distribution. (b) At t_0, laser pulse excites electrons form the $[\varepsilon_1, \varepsilon_2]$ energy interval vertically upwards in the conduction band, where they fill the states in the $[\varepsilon_3, \varepsilon_4]$ range. (c) Immediately after the pulse, electrons scatter with other electrons and strongly-coupled phonons ($E_{2g} \simeq 200$ meV and $A_1' \simeq 160$ meV) until the population inversion is created. (d) When the time scale of electron thermalization (τ_{th}) is reached, electrons follow a hot Fermi-Dirac distribution, which in our calculations, amounts to 2200K. Figure adapted from Ref. [356].

7.2 Graphene

Graphene exhibits extraordinary mechanical, transport and optoelectronic properties [355], and is therefore an ideal platform to investigate the fundamentals of ultrafast electron-lattice dynamics.

7.2.1 Photo-excited carrier distribution in graphene

Photoexcitation implies promoting a certain carrier density from the valence to the conduction band, with the initial and final states separated by the energy of the laser pulse $\hbar\Omega$, which typically amounts to 1.5 eV. We will track phonon properties for various electron distributions observed inside the Dirac cone directly following the pulse application.

Experimental techniques such as time-resolved ARPES (tr-ARPES) [24, 114, 338, 357, 358], two-photon photoemission [359–361], and transient optical spectroscopy [362–364] have reveled various aspects of carrier thermalization in graphene, such as rapid electron-electron and electron-phonon recombination of highly nonequilibrium distribution towards population inversion, scattering of electrons with strongly-coupled optical phonons [362], cooling of hot carriers via acoustic phonons, as well as electron band renormalization.

In Fig. 7.1 we summarize the four relevant distinct stages of thermalization in graphene that will be later considered in our calculations. First, an equilibrium distribution [Fig. 7.1 (a)] is disrupted with a short (fs) pulse causing an occurrence of empty states below the Dirac point and filled states above it [Fig. 7.1 (b)]. Photo-generated electrons and holes establish separate distributions and begin a rapid process of thermalization and cooling through carrier-carrier and carrier-phonon scatterings. The energy transfer to the strongly-coupled optical phonons produces hot phonons, reported to exist on a femtosecond time-scale [350, 362]. Then, the photo-inverted state is established [Fig. 7.1 (c)] through the competition between phonon-induced intraband scattering and Auger recombination [365]. The formation of the population inversion has already been thoroughly explored with tr-ARPES [24, 358, 366], which reveals its relaxation time of $\sim$100 fs. After its decay electrons follow a Fermi-Dirac distribution at elevated temperatures [Fig. 7.1 (d)]. The whole process of thermalization conceptually follows the one described for graphite in Ref. [357]. Subsequent hot-carrier cooling is governed by phonon-assisted scatterings on the time scale of 1-10 ps.

We will explicitly focus on the nonequilibrium carrier distribution scattering on phonons and analyze how the different stages of transient distribution affect the EPC properties deriving from the phonon self-energy [4].

7.2.2 Phonon renormalization

Raman and coherent phonon spectroscopy have demonstrated considerable phonon hardening of the E_{2g} optical phonon mode [14, 331, 332], which was attributed to the decoupling of the non-adiabatic electron-phonon interaction in nonequilibrium. Recent attosecond core-level spectroscopy also uncovered ultrafast phonon stiffening of both zone-center E_{2g} and zone-edge A_1' phonon Kohn anomalies [350]. Our goal is to reproduce the phonon hardening and reveal the mechanism behind it. We will first analytically justify the out-of-equilibrium phonon self-energy expression and then use it with the tight-binding model.

Out-of-equilibrium phonon self-energy

By exchanging an equilibrium Fermi-Dirac distribution $f(\varepsilon)|_{\mu}^{T}$ by an arbitrary one $n(\varepsilon)$ [367–371], in Eq. (4.19), one can calculate its real Eq. (4.23) and imaginary Eq. (4.24) parts and obtain the nonequilibrium frequency renormalization and nonequilibrium phonon linewidth. Since phonon

self-energy is a linear functional of the distribution, we can write

$$\Pi[n] = \int_{-\infty}^{+\infty} d\varepsilon \Pi[\delta(\varepsilon - \varepsilon_{n,\mathbf{k}})] n(\varepsilon). \tag{7.1}$$

If we write the delta function in terms of the Fermi-Dirac distribution derivative in the zero temperature limit ($T \to 0$), the expression (7.1) becomes

$$\Pi[n] = \int_{-\infty}^{+\infty} d\varepsilon \frac{\partial \Pi|_{\mu=\varepsilon}^{T=0}}{\partial \varepsilon} n(\varepsilon) \tag{7.2}$$

since the derivative $\frac{\partial \Pi|_{\mu=\varepsilon}^{T=0}}{\partial \varepsilon} n(\varepsilon)$ refers only to the derivative of the distribution. Furthermore, we can rewrite the expression (7.2) by introducing a distribution of holes $\bar{n}(\varepsilon) = 1 - n(-\varepsilon)$ and separating the intergation over positive and negative energies

$$\begin{aligned} \Pi[n] &= \Pi|_{\mu=0}^{T=0} + \\ &\int_0^{\infty} d\varepsilon \left[\frac{\partial \Pi|_{\mu=\varepsilon}^{T=0}}{\partial \varepsilon} n(\varepsilon) + \frac{\partial \Pi|_{\mu=\varepsilon}^{T=0}}{\partial \varepsilon} \bar{n}(\varepsilon) \right] \\ &= \Pi|_{\mu=0}^{T=0} + \Pi^{(e)}[n] + \Pi^{(h)}[\bar{n}] \end{aligned} \tag{7.3}$$

where the indices 'e' and 'h' remind us that the integration is performed from 0 to ∞.

Distribution function, which would describe photo-excited graphene from Fig. 7.1 can be written as:

$$n(\varepsilon) \to f(-\varepsilon)|_{-\mu}^{T} f(\varepsilon)|_{\varepsilon_4}^{T} f(-\varepsilon)|_{-\varepsilon_3}^{T} + f(\varepsilon)|_{\mu}^{T} (1 - f(\varepsilon)|_{\varepsilon_2}^{T} f(-\varepsilon)|_{-\varepsilon_1}^{T}) \tag{7.4}$$

Energies $\varepsilon_{1,2,3,4}$ denoted in Fig. 7.1 are defined with respect to the chemical potential as:

$$\varepsilon_{1,2} = \mu - \hbar\Omega + /- \Delta/2 \tag{7.5}$$

$$\varepsilon_{3,4} = \mu + \hbar\Omega + /- \Delta/2 \tag{7.6}$$

Ω is the laser pulse energy, and Δ is the width of the energy interval, filled with photo-excited electrons. In order to calculate the photo-inverted distribution of electrons, it is enough to set $\varepsilon_2 = \varepsilon_3 = \mu$. In the zero temperature limit, all the Fermi-Dirac distributions can be exchanged by θ functions.

To carry out the calculation of the nonequilibrium phonon self-energy analytically, we can

exchange the two Fermi-Dirac distributions by θ functions:

$$n(\varepsilon) \to \theta(\varepsilon) f(\varepsilon)|_{\varepsilon_4}^{T} \theta(\varepsilon - \varepsilon_3) + \theta(-\varepsilon)(1 - f(-\varepsilon)|_{-\varepsilon_1}^{T} \theta(\varepsilon_2 - \varepsilon)) \tag{7.7}$$

This distribution can now enter expression (7.3) producing the expression

$$\begin{aligned} \Pi|_{\varepsilon_1,\varepsilon_4}^{T} = \Pi(q,\omega)|_{\mu=0}^{T=0} \\ + \sum_{\alpha=\varepsilon_1,\varepsilon_4} \theta\left(\mu_\alpha\right) \left[\Pi(q,\omega)|_{\mu_\alpha}^{T=0} - \Pi(q,\omega)|_{\mu=0}^{T=0}\right] + \Pi^{(e)}\left[\delta f|_{\varepsilon_4}^{T}\right] + \Pi^{(h)}\left[\delta f|_{-\varepsilon_1}^{T}\right] \end{aligned} \tag{7.8}$$

where

$$\delta f(\varepsilon)|_{\varepsilon_4}^{T} = f(\varepsilon)|_{\varepsilon_4}^{T} - f(\varepsilon)|_{\varepsilon_4}^{T=0}.$$

At zero temperature, only the first three terms are finite. The final self-energy expression is a combination of phonon self-energies calculated in equilibrium in the intrinsic system, electron doped wih $\mu = \varepsilon_4$ and hole doped with $\mu = \varepsilon_1$. Equipped with the out-of-equilibrium phonon self-energy expression (7.8), we can evaluate it by using the tight-binding approximation for electron energies.

Tight-binding approximation

We will now review the tight-binding model for graphene in order to use the tight-binding energies. Graphene unit cell contains two atoms, which we denote by A and B. Translation vectors which define its unit cell are

$$\begin{aligned} \mathbf{a}_1 &= a(1,0) \\ \mathbf{a}_2 &= \tfrac{a}{2}(1,\sqrt{3}). \end{aligned} \tag{7.9}$$

In order to derive the electron energies in the tight-binding approximation, we start from the Hamiltonian, which contains hopping terms between the neighboring π orbitals:

$$\hat{H} = -t \sum_{\langle ij \rangle} \left(\hat{a}_i^\dagger \hat{b}_j + \hat{b}_j^\dagger \hat{a}_i\right). \tag{7.10}$$

where *i (j)* denotes the location on one of the sublattices (A or B). Fermionic operator $\hat{a}_i^\dagger\left(\hat{a}_i\right)$ is the creation operator of a Bloch electron on atom A, while $\hat{b}_i^\dagger\left(\hat{b}_i\right)$ creates a Bloch electron on site B. Summation is performed only among the nearest neighbors. First neighbors of atom A are at a distance of δ_1, δ_2, and δ_3 from it. The same vectors can be attributed to the neighbors of the B atom,

but with a different sign. The Hamiltonian can now be written as

$$\hat{H} = -t \sum_{i \in A} \sum_{\delta=1,2,3} \left(\hat{a}_i^\dagger \hat{b}_{i+\delta} + \hat{b}_{i+\delta}^\dagger \hat{a}_i \right), \tag{7.11}$$

and converted in reciprocal space as

$$\hat{H} = -t \sum_{\delta,\mathbf{k}} \left(e^{-i\mathbf{k}\cdot\delta} \hat{a}_\mathbf{k}^\dagger \hat{b}_\mathbf{k} + e^{i\mathbf{k}\cdot\delta} \hat{b}_\mathbf{k}^\dagger \hat{a}_\mathbf{k} \right). \tag{7.12}$$

Since the hoppings happen between two sublattices, Hamiltonian contains off-diagonal terms

$$\hat{H} = -t \sum_{\mathbf{k}} \begin{pmatrix} \hat{a}_\mathbf{k}^\dagger & \hat{b}_\mathbf{k}^\dagger \end{pmatrix} \begin{pmatrix} 0 & \Delta_\mathbf{k} \\ \Delta_\mathbf{k}^* & 0 \end{pmatrix} \begin{pmatrix} \hat{a}_\mathbf{k} \\ \hat{b}_\mathbf{k} \end{pmatrix} \tag{7.13}$$

where we introduce

$$\Delta_\mathbf{k} \equiv \sum_{\delta} e^{i\mathbf{k}\cdot\delta}. \tag{7.14}$$

Vectors which connect first neighbors can now be written as

$$\begin{aligned} \delta_1 &= -\frac{a}{2}(1, 1/\sqrt{3}) \\ \delta_2 &= \frac{a}{2}(1, -1/\sqrt{3}) \\ \delta_3 &= a(0, 1/\sqrt{(3)}). \end{aligned}$$

Eigenvalues of the Hamiltonian for any $\mathbf{k}$ vector can be obtained as

$$E_\pm(\mathbf{k}) = \pm t \sqrt{1 + 4\cos\left(\frac{a}{2}k_x\right)\cos\left(\frac{\sqrt{3}}{2}k_y a\right) + 4\cos^2\left(\frac{a}{2}k_x\right)}. \tag{7.15}$$

Using the expression (7.8) with the tight-binding energies we can obtain the linewidth in the equilibrium and nonequilibrium state.

In Fig. 7.2 is the linewidth for pristine (undoped) graphene in the equilibrium state on a Γ to K path. The result is obtained with $\eta = 30$ meV, $\omega = 200$ meV and constant value for the electron-phonon matrix elements $|g|^2 = 0.036$ eV^2. Since the low energy electron dispersion around

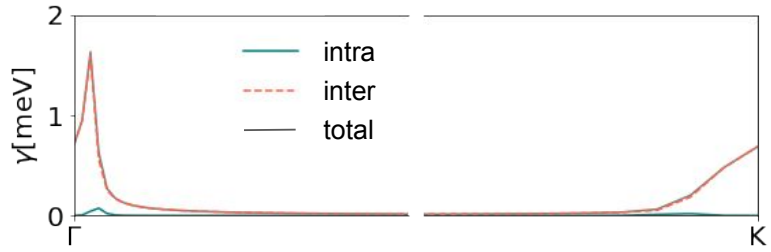

Figure 7.2: Graphene linewidth at T=200K, plotted on a Γ to K path. Interband contribution is shown with a pink dashed line, intraband with a full blue line, while the total linewidth is shown with a grey line.

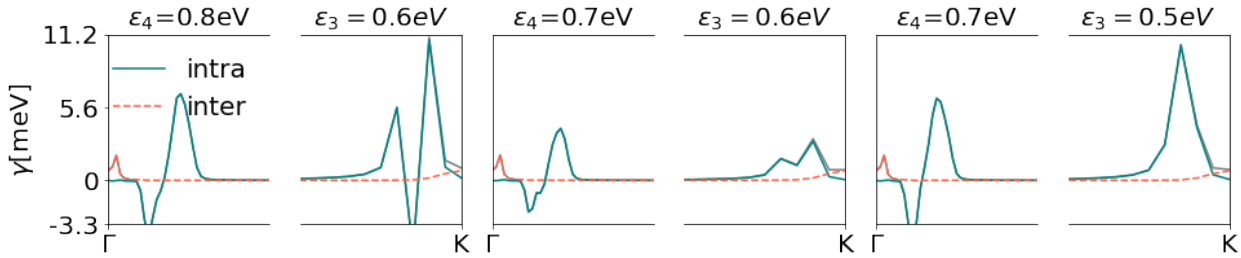

Figure 7.3: Phonon linewidth of the E_{2g} mode of photo-excited graphene for T=200K and along the Γ-K path. The interband contribution is shown with a dashed line, and intraband is shown with a full line. Results for three different choices of photo-excited energy windows (width Δ) are shown.

the Dirac point is linear, peaks in the linewidth correspond to the wavevectors $\mathbf{q}$ for which the condition $\mathbf{q}v_{\varepsilon_F} = \omega_{\mathbf{q}\nu}$ is satisfied. For pristine graphene, this happens around Γ and K points, due to electron transitions inside a Dirac cone or between the two inequivalent K points.

Calculating the linewidth in this way, provides a good way to simulate the out-of-equilibrium features arising from the photo-induced phase space changes.

Linewidth for photo-excited graphene is shown in Fig. 7.3. The photo-excited energy window is determined as $-\varepsilon_1 = \varepsilon_4$ and $-\varepsilon_2 = \varepsilon_3$. The results for a couple of different energy windows reveal how the available phase space for electron scattering greatly depends not only on the width of the photo-excited energy window, but also on its position compared to the Fermi level. In the photo-excited case, there are multiple options to achieve equality of the difference of electron energies and the phonon energy, and therefore multiple peaks arise in the linewidth. The interband peak in the vicinity of the Γ and K points is actually the unchanged equilibrium contribution. Next to it, we can see the negative linewidth contribution area coming from the intraband transitions. These

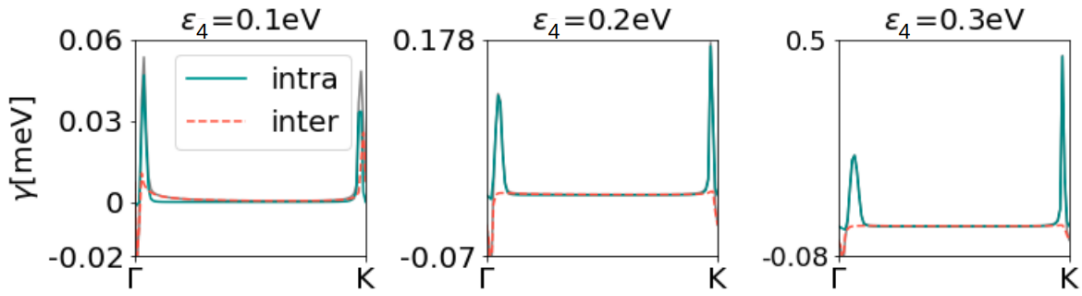

Figure 7.4: Phonon linewidth of the E_{2g} mode of photo-inverted graphene for T=200K and along the Γ-K path. The interband contribution is shown with a dashed line, and intraband is shown with a full line. Results for three different choices of photo-inverted energy windows are shown.

emerge from the electron transitions from occupied states which are higher in energy than the final unoccupied states. The largest linewidth value of 11.2 meV is achieved for a 200 meV wide energy window, but the laser energy, or the value of $\varepsilon_{3,2}$, leads to new features in proximity to the K point. This shape of the peak around the K point, greatly depends on the chosen energy interval due to the large energy dependence of the electronic DOS close to the Fermi level. The full phase space argumentation will be provided later, with the first-principles results.

Linewidth for graphene in the state of photo-inversion is shown in Fig. 7.4 with $-\varepsilon_1 = \varepsilon_4$ for a couple of different ε_4 parameter values. In comparison with the equilibrium case, the Γ and K point peaks are shifted due to the occurrence of the negative linewidth area. The negative linewidth in the photo-inverted case arises due to interband transitions from the filled states between the Dirac point and ε_4 to empty states below the Dirac point. The minimal and maximal linewidth value increases with the width of the energy window of the inverted population, however, note that phonon-assisted interband transitions are only allowed for certain configuration of electrons in photo-inverted regime. For other cases, the photo-inverted population cannot be thermalized by the E_{2g} phonon emission, which could explain why the bottleneck effect is created in the thermalization process of graphene [24, 362, 372].

First-principles results

After examining the simple tight-binding model and photo-induced linewidth of an Einstein 200 meV phonon, we can now move towards more exact calculations. In the following we calculate the phonon

dispersions and spectral functions for various stages of electron thermalization from first-principles. Since we need to manually change the electron distribution which screens the phonons and basically restrict electron transitions from a certain energy range, while allowing them in some other range, we perform calculations by means of cDFPT (see Chapter 2) and obtain statically-screened phonons with a photo-excited electron distribution. Afterwards, we perform the EPC calculations and introduce dynamical effects.

Methods and computational details

Nonequilibrium distributions from Eq. (7.4) can be implemented in the calculation of electronic-structure properties and then the renormalization of phonons is performed normally with the PHonon code in the adiabatic approximation. For the DFT calculations, we use Quantum ESPRESSO [69] and for EPC we use the EPW code [75]. We use the norm-conserving scalar pseudopotential from the PseudoDojo table [373] with an energy cutoff of 100 Ry. The relaxed lattice constant is 2.449 Å and the periodic graphene planes are separated by 12 Å. We use Fermi-Dirac smearing with $T = 800$ K. When modifying the electron distribution, we do not relax the structure, since we assume that the structure relaxation timescale is larger than the timescales we are interested in in this work. In order to capture all the relevant transitions, we densely sampled the Brillouin zone with a uniform coarse $60 \times 60 \times 1$ k-grid. The phonon calculation [30] is done on a uniform coarse $12 \times 12 \times 1$ q-grid. For the EPC calculation, the starting point is the Wannierization. We use maximally localized Wannier functions [71], with five initial projections corresponding to one sp^2 orbital and two p_z orbitals on C atom sites. The resulting Wannier functions lie on top of the two C atoms from the unit cell and on the bond centers. Smearing in the EPW calculation is set to 20 meV.

7.2.3 cDFPT details

We explicitly focus on the nonequilibrium carrier distribution scattering on phonons and analyze how the different stages of transient distribution affect the EPC properties deriving from the phonon self-energy [4]

$$\pi^c_\nu(\mathbf{q},\omega) = \sum_{\mathbf{k}nm} \left| g^{nm,c}_\nu(\mathbf{k},\mathbf{q}) \right|^2 \frac{f^c_{n\mathbf{k}} - f^c_{m\mathbf{k}+\mathbf{q}}}{\varepsilon^c_{n\mathbf{k}} - \varepsilon^c_{m\mathbf{k}+\mathbf{q}} + \omega + i\eta} \tag{7.16}$$

where with the superscript "c" we explicitly denote the quantities which are modified in cDFPT. We model the out-of-equilibrium electron distribution [see Fig. 7.1] as an equilibrium Fermi-Dirac

distribution with the addition and subtraction of Gaussian packets. Imposing an arbitrary (e.g., nonequilibrium) distribution $n(\varepsilon)$ of Dirac fermions, was already done for several 2D materials in order to investigate the linear response under non-Fermi-Dirac conditions [367, 370]. The general expression for the photo-excited distribution in our model is

$$n(\varepsilon) = f(\varepsilon)|_{E_F}^{T} - \delta_1 e^{\frac{(\frac{\varepsilon_1-\varepsilon_2}{2}-\varepsilon_1+\varepsilon)^2}{\alpha(\varepsilon_1-\varepsilon_2)}} + \delta_2 e^{\frac{(\frac{\varepsilon_3-\varepsilon_4}{2}-\varepsilon_3+\varepsilon)^2}{\alpha(\varepsilon_3-\varepsilon_4)}} \tag{7.17}$$

where all the energies are measured with respect to the Fermi energy E_F in dimensionless units (divided by the electronic temperature or the smearing value). $f(\varepsilon)|_{E_F}^{T}$ denotes the equilibrium Fermi-Dirac distribution at temperature T, i.e., $f(\varepsilon)|_{E_F}^{T} = \left(1 + e^{\frac{\varepsilon - E_F}{k_B T}}\right)^{-1}$, with k_B being the Boltzmann factor. The addition (subtraction) of the Gaussian term represents the development of the carrier (hole) population in the conduction (valence) band. Energies ε_x are marked in Fig. 7.1(b), and since the laser pulse has a vanishing momentum, we set $-\varepsilon_1 = \varepsilon_4$ and $-\varepsilon_2 = \varepsilon_3$. Factor α is present to ensure that the added (subtracted) population is confined in the desired energy interval. Factors $\delta_{1,2}$ are chosen so that the two claims hold true: (i) distribution $n(\varepsilon)$ never exceeds 1, or reduces below 0, and (ii) the total number of photo-holes and photo-electrons is preserved. The case of photo-inversion [Fig. 7.1(c)] is the limiting case of Eq. (7.17), where $\varepsilon_2 = \varepsilon_3 = 0$.

We calculate the equilibrium number of carriers N_e, characterized by the Fermi-Dirac distribution using the density of states $N(\varepsilon)$ like

$$N_e = \int_{\varepsilon_D}^{\infty} d\varepsilon N(\varepsilon) f(\varepsilon)|_{E_F}^{T_e}.$$

Then, we modify the Fermi-Dirac distribution to a photo-excited distribution $n(\varepsilon)$ and vary it in order to conserve the number of carriers. In other words, the condition

$$N_e = \int_{\varepsilon_D}^{\infty} d\varepsilon N(\varepsilon) n(\varepsilon)$$

needs to be satisfied. Note that as the free parameters we consider either ε_1 and ε_2 or their equivalent above the Dirac point ($\varepsilon_{3,4}$), but not both. The carrier number conservation is finally ensured with the factors $\delta_{1,2}$ from the expression (7.17). In the case of a hot electron distribution, the same logic applies. The number of photo-excited carriers becomes the number of carriers above the Dirac point described by a hot Fermi-Dirac distribution with a corresponding electron temperature. For our set

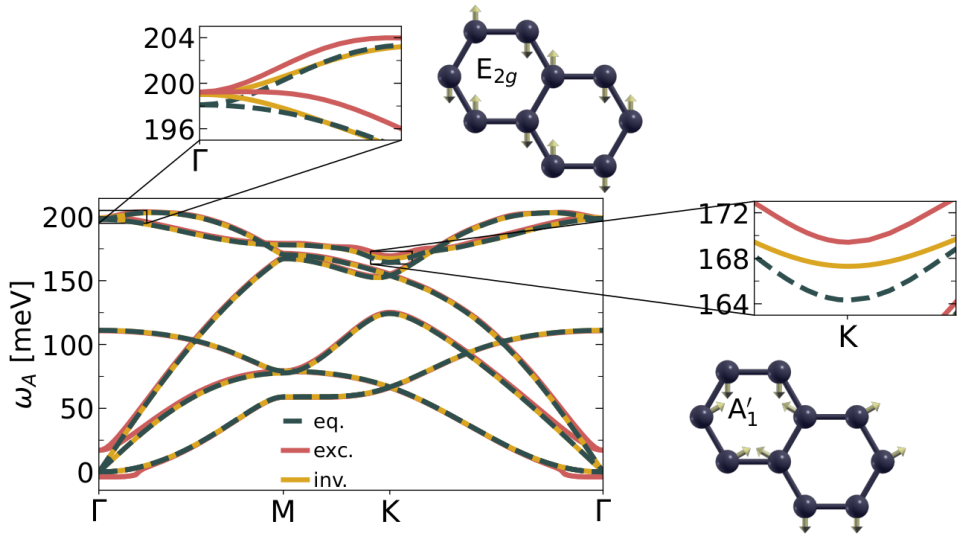

Figure 7.5: Adiabatic DFPT phonon dispersion in the presence of a photo-excited (red line) and photo-inverted (yellow line) electron distribution in comparison with an equilibrium result (dark-grey dashed line). Two insets are a zoom in region around high-symmetry points (Γ and K), showing the hardening of strongly-coupled optical modes (E_{2g} and A_1') along with a schematics of the corresponding atomic motions. Figure adapted from Ref. [356].

of parameters, the electronic temperature for which the number of carriers remains consistent is 2200 K. In the case of a photo-excited and photo-inverted calculation we manually change the Fermi-Dirac distribution in the self-consistent DFT calculation. The modified distribution then enters the DFPT calculation. The adiabatic phonon frequencies and EPC matrix elements are therefore obtained by constraining the occupation functions in DFT and DFPT calculations, while the corresponding nonadiabatic results is obtained by imposing a constrain of occupations on Eq. (7.16). Note that the reference phonon results for equilibrium as presented in Fig.7.1(a) of the main text are adiabatic harmonic DFPT results calculated at electronic temperature of $T = 800\,\mathrm{K}$, without inclusion of phonon entropy and phonon-phonon corrections.

7.2.4 Photo-induced static effects in the phonon spectrum

The cDFPT phonon dispersions are shown in Fig. 7.5. We compare the phonon dispersion for the case of photo-excited electron population as in Fig. 7.1(a) and photo-inverted distribution Fig. 7.1(b) with the equilibrium adiabatic case (DFPT). The largest effects of the nonequilibrium electron distribution happen for the strongly-coupled optical modes E_{2g} and A_1' around Γ and K points, respectively. We

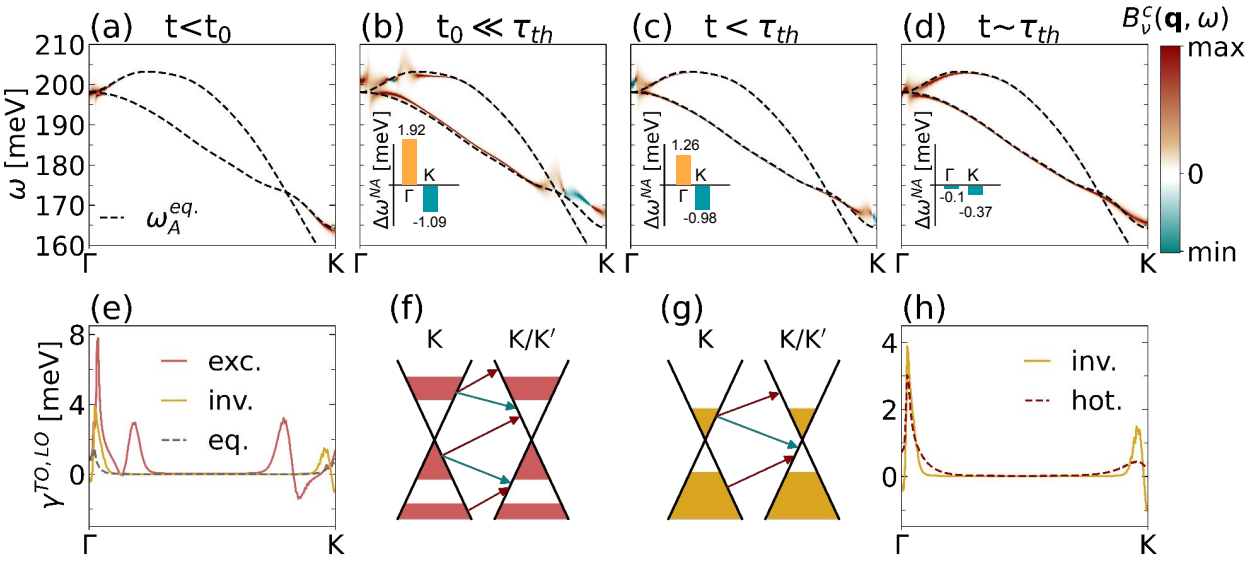

Figure 7.6: Dynamical phonon spectral functions at different stages of electron relaxation in comparison with the adiabatic equilibrium DFPT result (dark-grey dashed line), i.e., for: (a) equilibrium regime, (b) far nonequilibrium following the laser excitation, (c) population inversion, (d) hot equilibrium distribution. Note the strong renormalizations occurring near the two strongly-coupled optical modes (E_{2g} and A_1'). Also, the negative linewidth contribution to spectral function is shown in teal. The histograms in the insets of (b)-(d) show the nonadiabatic corrections to the E_{2g} and A_1' modes ($\Delta^{\mathrm{NA}} = \omega^{\mathrm{NA}} - \omega^{\mathrm{A}}$). (e) Phonon linewidth on Γ to K path of LO/TO optical modes, due to EPC. Color-coding is the same as in Fig. 7.5. (f-g) Intra- and inter-valley (i.e., K → K and K → K′) electron transitions which contribute to the phonon self-energy. The color-coded arrows reveal positive (brown) and negative (teal) contributions to the linewidth. (h) Same as in (e) but for the photo-inverted (yellow) and hot electron distributions (dark red). Figure from Ref. [356].

can observe phonon hardening for both phonons, and it ranges from $\simeq 1$ meV for the E_{2g} mode and $4-6$ meV for the A_1' mode. Our results are in very good agreement with Refs. [14, 331, 332] and especially with Ref. [350] where the attosecond core-level spectroscopy demonstrated that the Raman-inactive A_1' mode is the dominating channel for dissipation of electronic coherence due to stronger coupling to electrons [374]. Note also that in our calculations the acoustic sum rule is not fully fulfilled because we inhibit the long-wavelength dipole-allowed transitions [63, 77] by filling the states above the Fermi energy.

7.2.5 Photo-induced dynamical effects in the phonon spectrum

In Fig. 7.6 we present the results of the nonequilibrium EPC calculations. They contain the phonon spectral function, which incorporates nonadiabatic renormalization effects and transverse and longitudinal optical phonon linewidth along the $\Gamma - \mathrm{K}$ path. The first row represents four spectral functions corresponding to the four distinct electron distributions from Fig. 7.1, together with the equilibrium adiabatic result for comparison (dark-grey dashed lines). Spectral function is calculated using the expression

$$B^c_\nu(\mathbf{q},\omega) = -\frac{1}{\pi}\mathrm{Im}\left\{\frac{2\omega^c_{\mathbf{q}\nu}}{\omega^2 - (\omega^c_{\mathbf{q}\nu})^2 - 2\omega^c_{\mathbf{q}\nu}[\Pi^c_\nu(\mathbf{q},\omega) - \Pi^c_\nu(\mathbf{q})]}\right\} \tag{7.18}$$

where superscripts 'c' denote the quantities renormalized in cDFPT. We subtract the adiabatic phonon self-energy on a coarse mesh, used in the PHonon calculation.

The photo-excited electron distribution opens up new scattering possibilities, which are schematically shown with arrows in Fig. 7.6(f). Besides the significant modifications of the well-known nonadiabatic Kohn anomalies [11, 39] at the Γ and K points coming from the nonequilibrium population, the spectral function shows additional new anomalies further away from the Γ and K points. These photo-induced dynamical phonon anomalies come from the electron transitions away from the Dirac point, at the photo-doped regions.

Compared to the equilibrium adiabatic dispersions, a 4 meV renormalization is visible directly in the Γ point for the E_{2g} mode, and away from it, the highest optical branch is renormalized by 5 meV. For the A'_1 mode, we observe a 5 meV hardening and a 6 meV modification at the intersection of the two optical branches. We note that these sharp transient frequency modifications are quite large and are comparable to the nonadiabatic frequency shifts of the E_{2g} mode in highly-doped graphene [39]. In the case of population inversion, the nonequilibrium electron distribution is condensed in the vicinity of the Dirac point, bringing the nonequilibrium spectral features closer to the Γ and K points. We again observe phonon hardening for the E_{2g} and A'_1 modes of about 2 meV for both. Interestingly, for the strong nonequilibrium and population inversion we observe additional phonon hardening (softening) for E_{2g} (A'_1) when the nonadiabatic effects are taken into account [hystograms in insets of Figs. 7.6(b) and 7.6(c)]. In fact, significant increase of the nonadiabatic correction is obtained for the strong nonequilibrium, while it is reduced for the population inversion and almost diminished for the hot equilibrium case. Note that this is contrary to the conclusions drawn in Ref. [331], where the decrease of the nonadiabaticity is suggested.

The corresponding contributions to the linewidth [Figs. 7.6(e) and 7.6(h)] show that values at the Γ and K points are unaltered, while slightly away from these points it is significantly enhanced compared to its value at equilibrium. Equilibrium graphene linewidth contributions for the E_{2g} and A_1' modes come from the vertical interband electron scattering inside the Dirac cone ($q \simeq \Gamma$) or between the two neighboring ones ($q \simeq$ K), as already announced from the tight-binding model. These features around Γ and K points appear symmetrically. For a highly nonequilibrium case, additional notable phonon broadening arises displaced from the high-symmetry points, at momenta where the new dynamical anomalies appear.

A crucial thing to notice is that in the photo-excited state, electrons can scatter from the filled states at higher energies to the low-energy empty states [see Fig. 7.6 (f-g), downwards pointing teal arrows], causing a negative linewidth contribution. This phonon gain, happens in the immediate vicinity of the dynamical anomalies. For the population inversion, the phonon-gain contributions are located directly at the Γ and K high-symmetry points.

A remarkable fact that the propagation of light pulses in some semiconductors coincides with the presence of vigorous coherent THz lattice vibrations, captivated the attention of the research community three decades ago [375–386]. Theoretically it was approached by considering a quasi-equilibrium electron distribution [387]. Specifically, in graphene, acoustic phonon generation was experimentally achieved [388] and theoretically explained [389].

A conceptually similar phenomenon has recently been widely explored in graphene, namely the photo-induced plasmon amplification with a high potential for the development of novel optoelectronic devices [370, 371, 390–397]. Our observation of phonon gain is in agreement with the observation of the negative plasmon linewidth and negative conductivity in the photo-inverted state, and it simply means that hot phonons are emitted in the nonequilibrium regime. In particular, the results show that far nonequilibrium state supports the generation of incoherent hot phonons with momenta slightly away from the high-symmetry points (i.e., phonon displacement pattern is shifted in phase between neighboring unit cells), while the population inversion supports coherent phonon generation of hot E_{2g} and A_1' (i.e., phonon displacement pattern is repeated between neighboring unit cells). This could explain, on the one hand, the reduction of the phonon dephasing rate of E_{2g} mode as reported in Ref. [331], and, on the other hand, the non-displacive mechanism for the generation of both E_{2g} and A_1' hot coherent phonons as obtained in attosecond core-level spectroscopy [350].

As for the hot electron distribution, we calculated the number of carriers located above the Dirac point in the state of photo-inversion and found the temperature for which a Fermi-Dirac distribution

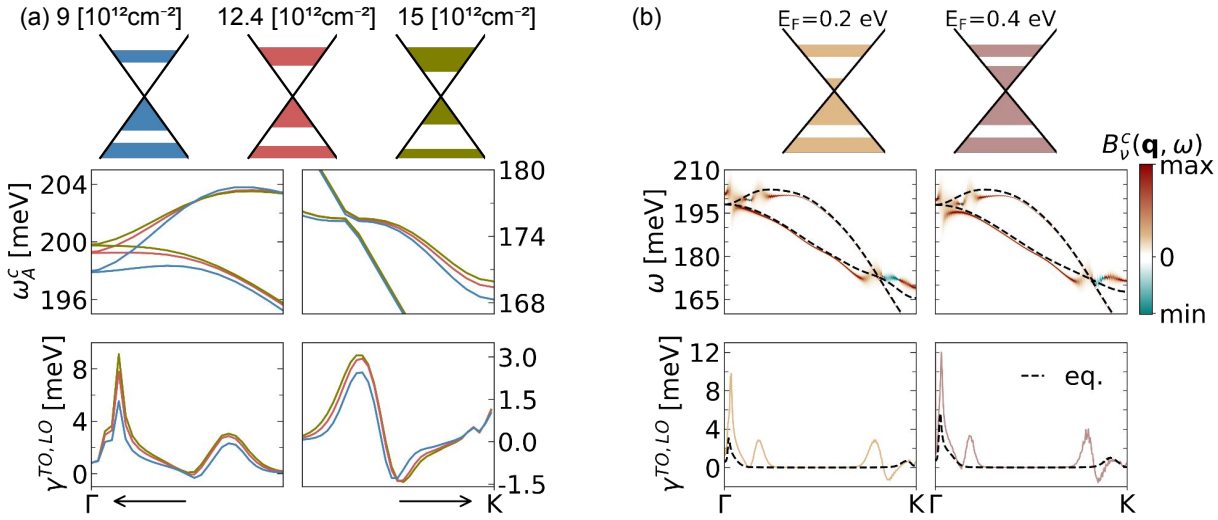

Figure 7.7: (a) nonequilibrium phonon renormalization for different densities of excited electrons. In the first row, we show the corresponding adiabatic DFPT dispersions in the vicinity of Γ and K points and observe phonon-hardening increase with photo-excited electron density. The second row contains the corresponding EPC induced linewidths. (b) Two cases of electron-doped photo-excited graphene (i.e., for $E_F = 0.2\,\text{eV}$ and $E_F = 0.4\,\text{eV}$). In the first row, we show the corresponding dynamical spectral functions. The second row shows the linewidths for the two doping regimes. We observe the same features as in Fig. 7.6(e) with significant increase in the linewidth close to the Γ point. It derives from the larger electron density at the Fermi level. Again, note the negative linewidth occurrence and dynamical anomalies. Figure from Ref. [356].

produces the same number of carriers in the conduction band. We show the spectral function for the hot equilibrium electron distribution at $T = 2200\,\text{K}$. The E_{2g} and A_1' modes are slightly hardened, and here one can clearly see also the edge of the electron-hole pair excitation continuum. The linewidth resembles the one obtained for the photo-inverted population, only without the negative contributions.

In experiments, it is possible to change the laser fluence. In our simulations, it would correspond to changing the excited carrier density (Fig. 7.7). Effective carrier density is denoted in Fig. 7.7(a) above the Dirac cones, and is calculated as the summed density of photo-excited electrons and holes. As expected, we observe larger phonon stiffening in the DFPT calculation for a larger carrier density. Here we show only the adiabatic dispersions to focus solely on the increased phonon stiffening in the Γ and K points. The E_{2g} phonon hardening increases by 2 meV as the photo-excited density increases by $6 \times 10^{12}\,\text{cm}^{-1}$. Further, we observe larger phonon linewidths deriving from the modified phase

space with increasing carrier density. Directly in the Γ point the linewidth remains at its equilibrium value, while slight differences in the position of the peaks away from the high-symmetry points are visible.

Furthermore, since in experiments graphene is frequently placed on a substrate, we also provide results for doped graphene, specifically for $E_F = 200$ and 400 meV (see Fig. 7.7). We compare the photo-doped spectral function with the adiabatic DFPT equilibrium calculation for the corresponding Fermi energy (dashed black lines). Again, we notice larger phonon hardening around the K point (5 meV for both dopings) then around the Γ point (4 meV for $E_F = 200$ meV and 1 meV for $E_F = 400$ meV). We observe dynamical anomalies at the same positions as they occur in the pristine photo-doped case. We notice how with increased doping, the dynamical phonon dispersion softens and the effects of photo-induced phonon hardening are less pronounced. Largest softening is observed around the dynamical anomalies. In general, for doped graphene, the intrinsic linewidths of the two highest optical modes are larger than for pristine graphene. When doped graphene is photo-excited, linewidth behaves in the same fashion as in the pristine photo-doped case, with the strong dynamical anomalies occurring in the vicinity of the high-symmetry points.

Phase space effects vs. decoupling

In order to emphasize the importance of photo-induced phase space in phonon spectral features, we will conduct the analysis of the adiabatic phonon self-energy as calculated in cDFPT [45, 398]

$$\Pi^c_\nu(\mathbf{q}) = \sum_{\mathbf{k}nm} \left|g^{nm,c}_\nu(\mathbf{k},\mathbf{q})\right|^2 \frac{f^c_{n\mathbf{k}} - f^c_{m\mathbf{k}+\mathbf{q}}}{\varepsilon^c_{n\mathbf{k}} - \varepsilon^c_{m\mathbf{k}+\mathbf{q}}}. \tag{7.19}$$

Averaging out the electronic degrees of freedom deriving from the EPC matrix elements, leads to $|g^{nm,c}_\nu(\mathbf{k},\mathbf{q})| \hookrightarrow |g^c_\nu(\mathbf{q})|$ and the self-energy expression (7.19) can be approximately written as $\Pi^c_\nu(\mathbf{q}) = |g^c_\nu(\mathbf{q})|^2 \chi^c_0(\mathbf{q})$ where $\chi^c_0(\mathbf{q})$ denotes the bare susceptibility function

$$\chi^c_0(\mathbf{q}) = \sum_{\mathbf{k}nm} \frac{f^c_{n\mathbf{k}} - f^c_{m\mathbf{k}+\mathbf{q}}}{\varepsilon^c_{n\mathbf{k}} - \varepsilon^c_{m\mathbf{k}+\mathbf{q}}}. \tag{7.20}$$

In this way, we can separate the nonequilibrium effects that come from the modifications in screened EPC matrix elements $|g^c_\nu(\mathbf{q})|$ and the photo-induced changes in the available phase space via $\chi^c_0(\mathbf{k})$.

In Fig. 7.8 we show the analysis for the conduction band, but the results for the valence band are the same due to the electron-hole symmetry in graphene. In the first two columns,

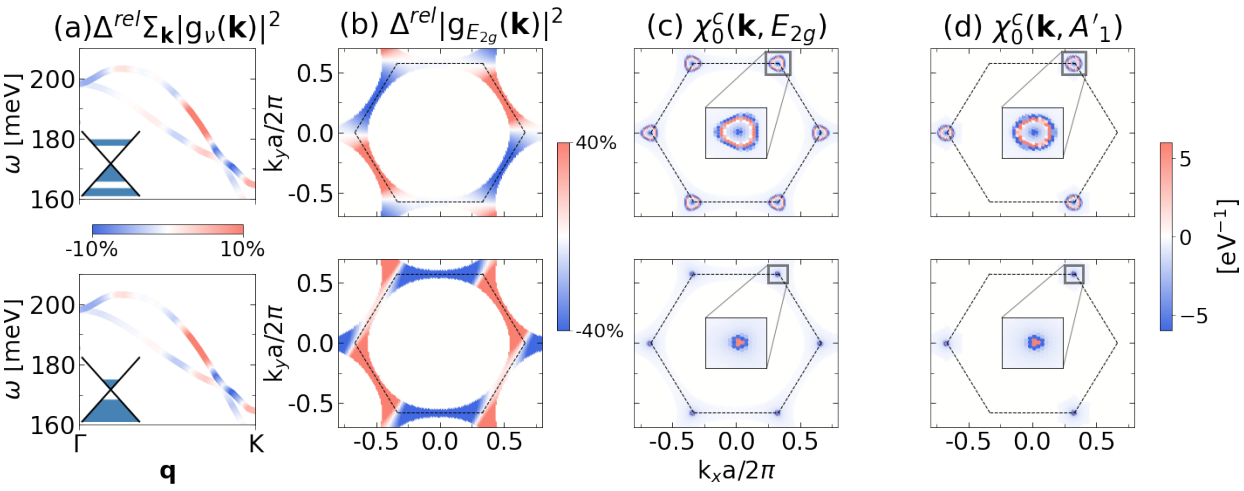

Figure 7.8: The analysis of static phonon self-energies, revealing the electronic processes behind phonon anomalies in the case of photo-excited (first row) and photo-inverted (second row) electron distributions. (a) Relative change in the **k**-summed EPC matrix elements $\Delta^{rel}\sum_{\mathbf{k}}|g_\nu(\mathbf{k})|^2$ for the two highest optical modes and along the $\Gamma-$K q-path. (b) $\Delta^{rel}|g_{E_{2g}}(\mathbf{k})|^2$ resolved in **k** space. (c),(d) **k**-resolved static susceptibility $\chi_0^c(\mathbf{k})$ for the E_{2g} and A_1' modes, respectively. The positive (negative) contributions to both $\Delta^{rel}|g_{E_{2g}}(\mathbf{k})|^2$ and $\chi_0^c(\mathbf{k})$ are shown with red (blue). Figure from Ref. [356].

we can see the relative difference between the EPC matrix elements in the photo-excited and photo-inverted graphene with respect to the pristine equilibrium case for the E_{2g} and A_1' modes $\Delta^{rel}|g_\nu(\mathbf{k})|^2 = (|g_\nu^c(\mathbf{k})|^2 - |g_\nu^{eq}(\mathbf{k})|^2)/|g_\nu^{eq}(\mathbf{k})|^2$. In the first column, the relative differences are calculated after the electron-phonon matrix elements were summed throughout the whole Brillouin zone for a chosen **q** point on the $\Gamma-$K path and for each one of the two highest optical modes. The largest value of the relative change is only $\pm 10\%$ and it appears for those wavevectors **q** for which the electronic transitions are forbidden by the specific electronic structure of graphene and for which the EPC strength is weak at equilibrium (i.e., away from the Γ and K points). More dramatic changes occur if $\Delta^{rel}|g_{E_{2g}}(\mathbf{k})|^2$ is resolved in the k_x-k_y plane [column (b) in Fig. 7.8]. Here we explicitly show the result for $\mathbf{q}=\Gamma$ for which we found the largest values of $\Delta^{rel}|g_{E_{2g}}(\mathbf{k})|^2$. For both the photo-excited and photo-inverted electron distribution case, our calculations show that $\Delta^{rel}|g_{E_{2g}}(\mathbf{k})|^2$ reaches values of $\pm$ 40% in certain regions of k_x-k_y space for the E_{2g} mode. We observe a symmetrical pattern of positive and negative contributions to $\Delta^{rel}|g_{E_{2g}}(\mathbf{k})|^2$. Due to phase space restrictions, only a small region around the K points is picked out when doing a self-energy calculation, or multiplying $|g_\nu^c(\mathbf{q})|^2$ and $\chi_0^c(\mathbf{q})$. In other words, as shown in columns (c) and (d)

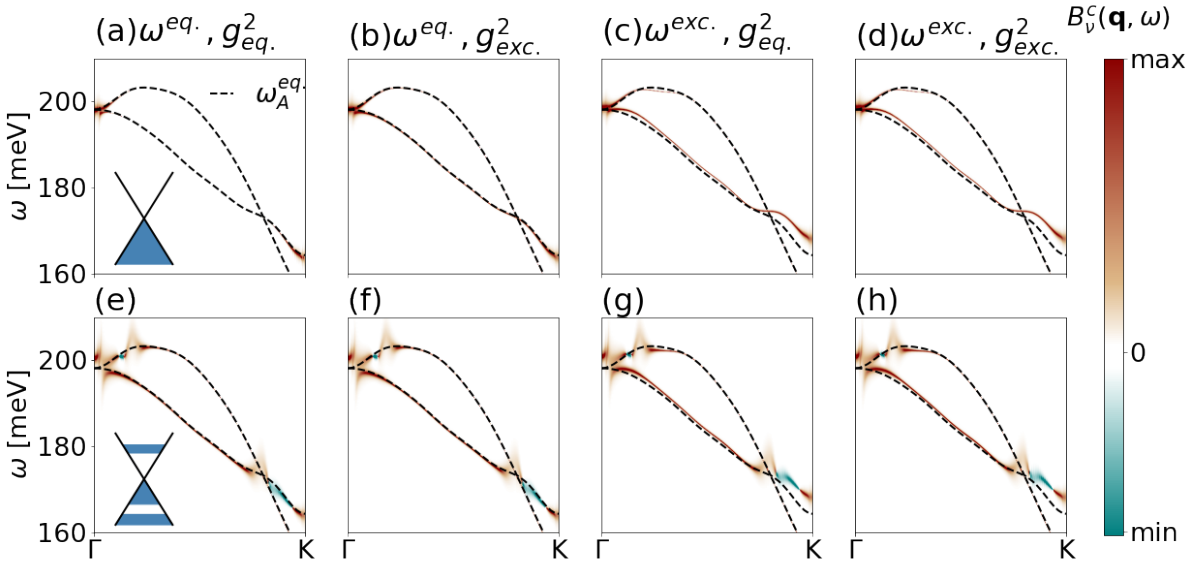

Figure 7.9: Spectral functions obtained by combining all possible combinations of the equilibrium and photo-excited values for the electron distribution, adiabatic DFPT frequencies and electron-phonon matrix elements. The inset in the first panel means that the whole first row is obtained with the equilibrium electron distribution, and the second row with the photo-excited one. The chosen values of the adiabatic phonon frequencies and electron-phonon matrix elements are written above each column. Figure from the supplementary material of Ref. [356].

of Fig. 7.8, $\chi_0^c(\mathbf{k})$ is finite around the Dirac points also in a symmetric pattern. In this way, when calculating the phonon self-energy and summing over the whole Brillouin zone, the net effect of the large relative changes $\Delta^{rel}|g_{E_{2g}}(\mathbf{k})|^2$ cancels out as equal amounts of positive and negative values are picked out by the $\chi_0^c(\mathbf{k})$ factor. We performed this type of analysis along the Γ to K path and the largest relative changes we observed happen in the Γ point, which is why we present that result.

In Fig. 7.9 we further analyze the role of electron phase-space modifications and changes in the electron-phonon matrix elements in the observed renormalizations of the phonon band structure. There we gradually move from a completely equilibrium calculation to the completely photo-excited calculation, in each of the panels changing either the equilibrium DFPT phonon frequency to the photo-excited one, the equilibrium electron-phonon matrix elements to photo-excited ones or the equilibrium electron-distribution to the photo-excited one. Firstly we will focus on the first panel (a). For this calculation we use an equilibrium Fermi-Dirac distribution schematically shown in the inset.

We do a DFPT calculation and obtain equilibrium phonon frequencies $\omega_\nu^{eq}(\mathbf{q})$, coupled to electrons in equilibrium via $|g_\nu^{nm}(\mathbf{k},\mathbf{q})|^2$. Then we proceed with an electron-phonon calculation and obtain a shown phonon spectral function. Now, we will shift our focus on the last panel (h), where we use a photo-excited distribution schematically shown in the inset. We do a cDFPT calculation and obtain nonequilibrium phonon frequencies $\omega_\nu^{exc}(\mathbf{q})$, coupled to photo-excited electrons via $|g_\nu^{nm,c}(\mathbf{k},\mathbf{q})|^2$. In all the panels in between, we take all the possible combinations of equilibrium and photo-excited distributions, DFPT phonon frequencies and electron-phonon matrix elements. In the whole first row, the electron distribution is fixed to the equilibrium one (Fermi-Dirac), while in the second, it is fixed to the photo-excited distribution from Eq. (7.17).

Moving from panel (a) to (b) [or from (e) to (f)], the electron-phonon matrix elements are changed from their equilibrium values to their photo-excited values, while the phonon frequencies are the ones obtained from an equilibrium DFPT calculation. We do not observe any significant difference between these two panels, when $|g_\nu^{nm}(\mathbf{k},\mathbf{q})|^2$ are exchanged by $|g_\nu^{nm,c}(\mathbf{k},\mathbf{q})|^2$. The same applies to the two other pairs of panels [i.e., (c-d) and (g-h)], calculated with a photo-excited phonon frequency. We observe phonon hardening around the K point which clearly derives from the adiabatic cDFPT photo-excited frequencies and again, we do not observe any additional changes deriving from the photo-induced electron-phonon matrix elements.

Eventually, the effects of photo-induced changes of the electron-phonon matrix elements are small, and it turns out that the phonon hardening and decrease of the dephasing rate observed in Ref. [331], along with other nonequilibrium phenomena presented here, come dominantly from the photo-induced changes in the carrier scattering phase space $\chi_0^c(\mathbf{k})$. Therefore, optically-induced phonon blueshifts are not necessarily a sign of the suppressed coupling and it could come from the pure electronic origin, as was shown for instance in the case of photo-excited $TiSe_2$ [335]. This resolves the debate on whether the EPC strength is suppressed [331] or enhanced [325] in the nonequilibrium graphene.

Now we will thoroughly inspect the color-coded contributions to the bare electron susceptibility $\chi_0^c(\mathbf{k})$. The features for $\mathbf{q} = \mathrm{K}$ and $\mathbf{q} = \Gamma$ are in essence the same, so the discussion is applicable to both. In the equilibrium case where the Fermi surface is almost a point, the only contribution comes from the Dirac point. Since the electrons can only scatter from the filled states below the Fermi energy to the empty states above it, expression (7.20) leads to the negative $\chi^0(\mathbf{k})$. Focusing now on the photo-excited case (Fig. 7.8, first row), we first notice the mentioned equilibrium contribution (red dots) positioned directly in the Dirac points. Photo-excited electrons fill the states visible

here as an additional triangle around each Dirac point. Each triangle consists of positive and negative susceptibility contributions. Electrons from the positive $\chi_0^c(\mathbf{k})$ portion are responsible for the negative linewidth contribution, as they contribute by scattering from the higher energy filled states to the lower energy empty ones. Due to finite temperature, this is in principle also possible within an equilibrium distribution, but those contributions are then suppressed by the much larger negative $\chi_0(\mathbf{k})$ contribution. The electrons from the negative $\chi_0^c(\mathbf{k})$ section make standard transitions to higher energy empty states. In the EPC calculations, we used a dynamical susceptibility term [see Eq. (4.19)], which, together with varying the wavevector $\mathbf{q}$, leads to the competition between these two contributions and, hence, to the net negative linewidth regions visible in Fig. 7.6. The obvious difference between susceptibility contribution shape in the Γ and K points, is the result of trigonal warping [399], which is reversed in the neighboring K points. Setting $\mathbf{q} = \mathrm{K}$ leads to the superposition of two relatively rotated triangles, making the A_1' susceptibility look circular.

$\chi_0^c(\mathbf{k})$ for the photo-inverted distribution, consists of two circular contributions, as the filled/empty states are in the energy range of a linear electron distribution. Color-coding again suggests that the electrons closer to the Dirac point rather scatter to the empty states below the Fermi level, while the higher energy electrons do the opposite and contribute positively to the phonon linewidth. In this case, varying the wavevector $\mathbf{q}$ in the dynamical susceptibility calculation reduces the phase space for the electrons in the negative section, as a number of vertical transitions is restricted. It confines the phonon gain to be placed directly in the high-symmetry points. In this discussion we rely on the explanations involving only the nonequilibrium electron distribution, when in fact also the electron energies $\varepsilon_{n\mathbf{k}}^c$ renormalize. These effects are also consistently taken into account, but we did not observe a difference in $\varepsilon_{n\mathbf{k}}^c$ values in- and out- of equilibrium larger than 0.1%, even when calculating the band structure with the displaced atoms in the direction of the strongly-coupled E_{2g} and A_1' modes. As the atoms move along these phonon modes, the gap opens, but we did not find significant photo-induced renormalizations of the gap value. It further confirms our finding that the statically-screened EPC matrix elements remain similar to their equilibrium value.

Note in the end that the present analysis on phonon dynamics based on cDFPT is not only restricted to the nonequilibrium induced by laser pulses, but it could be utilized to study phonon renormalization in any out-of-equilibrium conditions. For instance, impact of the static electric fields and the corresponding nonequilibrium electrons on phonons in current-carrying materials is still not well understood despite its importance for comprehending various transport properties [369,400,401].

7.3 Molybdenum disulphide

The cDFT and cDFPT approaches are time independent and lack information on carrier population dynamics and its temporal evolution towards thermal equilibrium caused by various scattering events. There are a few other theoretical descriptions of electron-lattice energy flow. Probably the most famous one is the two temperature model (TTM) and its extensions [24, 402–407], where it is assumed that electron and lattice subsystems are already thermalized. It is commonly used in its phenomenological form to supplement the experimental observations of the heat transfer [24, 403, 404, 408], and was further useful to address the hot phonon dynamics and phonon bottleneck in materials with highly anisotropic EPC, such as graphene [24, 407, 409], graphite [410], MgB_2 [35, 36], MoS_2 [411], and lead halid perovskites [412]. It was also used as a basis to study laser-induced energy renormalization of hot phonons in MgB_2 as a function of time [35].

However, the TTM is likely to fail in describing femtosecond lattice dynamics below the electron thermalization time, where full information of energy-momentum phase space in nonequilibrium state is required [407].

An alternative *ab-initio* method to track carrier dynamics upon laser excitation is based on real-time time-dependent density functional theory (rt-TDDFT) and Ehrenfest dynamics, and along the EPC allows to include many-body electron-electron and electron-hole interactions [325, 413–418]. In combination with molecular dynamics and real-space lattice distortions, the latter method can account for time-resolved self-consistent renormalization of phonon energies and EPC strengths [325, 417], providing a microscopic information on laser-induced structural transitions [418] and enhanced superconducting properties [325, 417]. However, since it relies on real-space distortions and supercell approaches to account for electron-lattice interactions, it is numerically challenging for the rt-TDDFT to provide full momentum-resolved analysis on phonon dynamics and, in practice, usually considers only very few coherent optical phonons, such as zone-center E_{2g} and zone-edge A_1' modes in graphene [325], and zone-center A_{1g} mode in MoS_2 [417].

A considerable improvement in describing nonequilibrium scattering events is met with TDBE, especially with their first-principles implementations [345, 347, 419–422]. When both electron-phonon and phonon-phonon scattering channels are included, the TDBE can accurately describe energy-, momentum-, and time-dependent modifications to electron and phonon population in both sub-picosecond and picosecond regimes [43]. In order to obtain first-principles information on the time-dependent phonon renormalization process and electron-phonon scattering channels following laser excitation with a full momentum and frequency resolution, for MoS_2 we will combine the

TDBE and many-body phonon self-energy calculations. With this methodology we will investigate a photo-excited MoS_2 monolayer, a prototypical 2D semiconductor with exceptional electronic [423] and optoelectronic [339, 340, 424–427] properties for which vibrational, electronic, valley, spin, and other degrees of freedom play an active and important role.

By means of TDBE, one can obtain thermalization of carrier distribution function with band and momentum resolution $f^{el}_{n\mathbf{k}}$ as a function of time, with electron-phonon and phonon-phonon scatterings taken into account [347, 407, 421]. The acquired distribution functions $f^{el}_{n\mathbf{k}}$ can then be utilized to construct the time-resolved phonon self-energy $\Pi_{\mathbf{q}\nu}(\omega;t)$ and the full nonadiabatic phonon spectral functions $B_{\mathbf{q}\nu}(\omega;t)$. This enables the analysis of photo-induced phonon frequency and linewidth (i.e., relaxation rate) modifications.

Importantly, in this chapter we will examine the potential increase of the overall phonon scattering rate in nonequilibrium. This is important as it opens a possibility for enhancing the total EPC strength, making photo-induced nonequilibrium state a promising route for tailoring vibrational properties of quantum matter. This is especially important for MoS_2 where phonons play a primary role in the emergence of novel quantum phenomena, such as in exciton dynamics [428–431] as well as formation of Holstein polaron [432], CDW [433] and superconductivity [134–136, 434].

7.3.1 Theory

At thermal equilibrium, fermion and boson distribution functions are time independent and they coincide with the Fermi-Dirac and the Bose-Einstein occupations $f_{n\mathbf{k}}$ and $f^{B}_{\mathbf{q}\nu}$. A nonequilibrium regime, implies that at least one distribution function differs from its equilibrium counterpart. The dynamics of a non-thermal electron-lattice system in the time-dependent Boltzmann equations formalism, is captured by time-dependent modifications of electron and phonon occupation functions $f^{el}_{n\mathbf{k}}(t)$ and $f^{ph}_{\mathbf{q}\nu}(t)$, while electron and phonon energies, as well as the corresponding coupling functions are unaltered and fixed to their equilibrium values. TDBE can be written as [407, 421, 422]

$$\partial_t f^{el}_{n\mathbf{k}}(t) = \Gamma_{n\mathbf{k}}(t) \tag{7.21}$$

$$\partial_t f^{ph}_{\mathbf{q}\nu}(t) = \Gamma_{\mathbf{q}\nu}(t) \tag{7.22}$$

where ∂_t denotes the partial temporal derivative $\partial/\partial t$. $\Gamma_{n\mathbf{k}}$ and $\Gamma_{\mathbf{q}\nu}$ are the various scattering mechanisms leading to a temporal change in the distribution functions. They are called the collision integrals for electrons and phonons and they can include electron-phonon, phonon-phonon

interactions, electron-electron, scattering on impurities and interaction with external fields. If we focus solely on the first two contributions, the Hamiltonian has four terms:

$$\hat{H} = \hat{H}_{el} + \hat{H}_{ph} + \hat{H}_{el-ph} + \hat{H}_{ph-ph}. \tag{7.23}$$

In the second quantization formalism, the electronic Hamiltonian is

$$\hat{H}_{el} = \sum_{n\mathbf{k}} \varepsilon_{n\mathbf{k}} \hat{c}^{\dagger}_{\mathbf{k}n} \hat{c}_{\mathbf{k}n}$$

and the harmonic phonon part is

$$\hat{H}_{ph} = \sum_{\nu\mathbf{q}} \omega_{\nu\mathbf{q}} \left(\hat{b}_{\mathbf{q}\nu} \hat{b}^{\dagger}_{\mathbf{q}\nu} + \frac{1}{2} \right).$$

The EPC part,

$$\hat{H}_{el-ph} = \sum_{\mathbf{k}\mathbf{q}\nu mn} g_{\nu} \left(\mathbf{k}n, \mathbf{k}+\mathbf{q}m \right) \hat{c}^{\dagger}_{\mathbf{k}+\mathbf{q}m} \hat{c}_{\mathbf{k}n} (\hat{b}_{\mathbf{q}\nu} + \hat{b}^{\dagger}_{-\mathbf{q}\nu}),$$

has already been introduced in (2.50). The three-phonon anharmonic part can be written as [407]

$$\hat{H}_{ph-ph} = \frac{1}{3!} \sum_{\nu\nu'\nu''} \sum_{\mathbf{q}\mathbf{q}'\mathbf{q}''} A_{\mathbf{q}\mathbf{q}'\mathbf{q}''\nu\nu'\nu''} (\hat{b}_{\mathbf{q}\nu} + \hat{b}^{\dagger}_{-\mathbf{q}\nu})(\hat{b}_{\mathbf{q}'\nu'} + \hat{b}^{\dagger}_{-\mathbf{q}'\nu'})(\hat{b}_{\mathbf{q}''\nu''} + \hat{b}^{\dagger}_{-\mathbf{q}''\nu''})$$

where $A_{\mathbf{q}\mathbf{q}'\mathbf{q}''\nu\nu'\nu''}$ are the phonon-phonon scattering matrix elements. If electron-phonon and phonon-phonon terms are small, they can be treated perturbatively. It also means that the initial and final states the system assumes before and after the scattering mechanisms kick in, are well defined. Within the BOA, the Hamiltonian can be solved by a separation of the wavefunction on the electronic and harmonic phonon part (see Chapter 2), so for the initial and final states we can use this type of a wavefunction: $|i/f\rangle = \chi_{i/f}(\mathbf{r}^{\mathbf{n}}_{\mathbf{k}}) \psi^{\mathbf{r}^{\mathbf{n}}_{\mathbf{k}}}_{i/f}(\mathbf{r}^{\mathbf{e}}_{\mathbf{l}})$. We have laid the foundation for the application of Fermi golden rule, which gives the probability per unit of time of evolution from the initial state $|i\rangle$ to the final state $|f\rangle$ under the action of a perturbing Hamiltonian applied to the system. In our case, the perturbing Hamiltonian is the sum of electron-phonon and phonon-phonon terms, and the transition probability per unit time can be written as

$$\Gamma_{i\to f} = 2\pi |\langle f | \hat{H}_{el-ph} + \hat{H}_{ph-ph} | i \rangle|^2 \delta(E_f - E_i). \tag{7.24}$$

In the case of electron-phonon interaction, the difference in the initial and final energies in the energy conserving delta functions can be written as $\varepsilon_{m\mathbf{k}+\mathbf{q}} \pm \omega_{\nu\mathbf{q}} - \varepsilon_{n\mathbf{k}}$, while in the case of phonon-phonon interaction $\omega_{\nu''\mathbf{q}''} \pm \omega_{\nu'\mathbf{q}'} - \omega_{\nu\mathbf{q}}$ where the sign of the phonon energy determines whether phonon absorption or phonon emission occurred. Sandwiching the second quantization annihilation and creation operators between the initial and final Born-Oppenheimer states yield terms such as

$$\langle \psi_f | \hat{c}^{\dagger}_{\mathbf{k}+\mathbf{q}m} \hat{c}_{\mathbf{k}n} | \psi_i \rangle$$

or

$$\langle \chi_f | \hat{b}^{\dagger}_{\nu-\mathbf{q}} \hat{b}_{\nu\mathbf{q}} | \chi_i \rangle$$

and

$$\langle \chi_f | \hat{b}^{(\dagger)}_{\nu\mathbf{q}} | \chi_i \rangle .$$

In order to calculate the electronic collision integral $\Gamma_{n\mathbf{k}}$ one needs to sum over all initial and final phonon states determined by the wavevector $\mathbf{q}$ and phonon branch ν. For the phonon collision integral, initial and final states need to be summed over all $\mathbf{k}$ vectors and electronic bands *n,m*. The total rate of change in the distribution functions due to EPC, is a result of phonon assisted processes in which an electron scatters from $\varepsilon_{n\mathbf{k}}$ to $\varepsilon_{m\mathbf{k}+\mathbf{q}}$ or vice versa by either emission or absorption of a phonon. Even though both collision integrals, describe the same processes, summation over different indices leads to different expressions. If we focus first on the electronic collision integral, these terms can be different from zero only if the initial state is occupied and the final state is empty leading to terms

$$\sqrt{f^{el}_{n\mathbf{k}}(1 - f^{el}_{m\mathbf{k}+\mathbf{q}})}$$

or vice versa

$$\sqrt{f^{el}_{m\mathbf{k}+\mathbf{q}}(1 - f^{el}_{n\mathbf{k}})}.$$

Terms containing one boson operator, yield phonon occupation factors

$$\langle \chi_f | \hat{b}^{\dagger}_{\mathbf{q}\nu} | \chi_i \rangle = \sqrt{f^{ph}_{\mathbf{q}\nu}}$$

and

$$\langle \chi_f | \hat{b}_{\mathbf{q}\nu} | \chi_i \rangle = \sqrt{1 + f^{ph}_{\mathbf{q}\nu}}.$$

The resulting electronic collision integral from EPC is

$$\Gamma^{el-ph}_{n\mathbf{k}}(t) = \frac{2\pi}{\hbar}\sum_{m\mathbf{q}\nu}|g^{nm}_{\nu}(\mathbf{k},\mathbf{q})|^2 \tag{7.25}$$
$$\times\Big[(1-f^{el}_{n\mathbf{k}})f^{el}_{m\mathbf{k}+\mathbf{q}}[\delta(\varepsilon_{m\mathbf{k}+\mathbf{q}}-\omega_{\nu\mathbf{q}}-\varepsilon_{n\mathbf{k}})f^{ph}_{\mathbf{q}\nu}+\delta(\varepsilon_{m\mathbf{k}+\mathbf{q}}+\omega_{\nu\mathbf{q}}-\varepsilon_{n\mathbf{k}})(1+f^{ph}_{\mathbf{q}\nu})]$$
$$-f^{el}_{n\mathbf{k}}(1-f^{el}_{m\mathbf{k}+\mathbf{q}})[\delta(\varepsilon_{m\mathbf{k}+\mathbf{q}}+\omega_{\nu\mathbf{q}}-\varepsilon_{n\mathbf{k}})f^{ph}_{\mathbf{q}\nu}+\delta(\varepsilon_{m\mathbf{k}+\mathbf{q}}-\omega_{\nu\mathbf{q}}-\varepsilon_{n\mathbf{k}})(1+f^{ph}_{\mathbf{q}\nu})].$$

The EPC contribution to the phonon collision integral derives from the difference between phonon absorption and phonon emission processes, both of which change the phonon distribution

$$\Gamma^{ph-el}_{\mathbf{q}\nu}(t) = \frac{4\pi}{\hbar}\sum_{mn\mathbf{k}}|g^{nm}_{\nu}(\mathbf{k},\mathbf{q})|^2\Big[(1-f^{el}_{n\mathbf{k}})f^{el}_{m\mathbf{k}+\mathbf{q}} \tag{7.26}$$
$$\times\Big[\delta(\varepsilon_{m\mathbf{k}+\mathbf{q}}+\omega_{\nu q}-\varepsilon_{n\mathbf{k}})f^{ph}_{\mathbf{q}\nu}+\delta(\varepsilon_{m\mathbf{k}+\mathbf{q}}-\omega_{\nu\mathbf{q}}-\varepsilon_{n\mathbf{k}})(1+f^{ph}_{\mathbf{q}\nu})\Big].$$

Phonon collision integral has a phonon-phonon contribution, which can be written as

$$\Gamma^{ph-ph}_{\mathbf{q}\nu}(t) = \frac{2\pi}{\hbar}\sum_{\nu'\nu''}\int\frac{d\mathbf{q}}{\Omega_{BZ}}|A_{\mathbf{q}\mathbf{q}'\mathbf{q}''\nu\nu'\nu''}|^2 \tag{7.27}$$
$$\times\Big[(1+f^{ph}_{\mathbf{q}\nu})(1+f^{ph}_{\mathbf{q}'\nu'})f^{ph}_{\mathbf{q}''\nu''}-f^{ph}_{\mathbf{q}\nu}f^{ph}_{\mathbf{q}\nu'}(1+f^{ph}_{\mathbf{q}''\nu''})\delta(\omega_{\mathbf{q}\nu}+\omega_{\mathbf{q}'\nu^{+\prime}}-\omega_{\mathbf{q}''\nu^{+\prime\prime}})\delta^{G}_{\mathbf{q}\mathbf{q}'-\mathbf{q}''}$$
$$+\frac{1}{2}\Big[(1+f^{ph}_{\mathbf{q}\nu})f^{ph}_{\mathbf{q}''\nu''}f^{ph}_{\mathbf{q}\nu'}-(1+f^{ph}_{\mathbf{q}'\nu'})f^{ph}_{\mathbf{q}\nu}f^{ph}_{\mathbf{q}\nu''+1}\delta(\omega_{\mathbf{q}\nu}-\omega_{\mathbf{q}'\nu^{+\prime}}-\omega_{\mathbf{q}''\nu^{+\prime\prime}})\delta^{G}_{\mathbf{q}-\mathbf{q}'-\mathbf{q}''}\Big].$$

The Kronecker deltas are finite only for terms with $\mathbf{q}=0$ or $\mathbf{q}=\mathbf{G}$, where $\mathbf{G}$ are reciprocal lattice vectors. The latter term accounts for Umklapp processes. The derivation carried out here, can be found in Refs. [347, 407, 421]. The time evolution of $f^{el}_{n\mathbf{k}}(t)$ and $f^{ph}_{\mathbf{q}\nu}(t)$, dictated by electron-phonon and phonon-phonon scattering processes can then be described with the following coupled integro-differential equations [407, 421]:

$$\partial_t f^{el}_{n\mathbf{k}}(t) = \Gamma^{el-ph}_{n\mathbf{k}}[f^{el}_{n\mathbf{k}}(t), f^{ph}_{\mathbf{q}\nu}(t)], \tag{7.28}$$
$$\partial_t f^{ph}_{\mathbf{q}\nu}(t) = \Gamma^{ph-el}_{\mathbf{q}\nu}[f^{el}_{n\mathbf{k}}(t), f^{ph}_{\mathbf{q}\nu}(t)] + \Gamma^{ph-ph}_{\mathbf{q}\nu}[f^{ph}_{\mathbf{q}\nu}(t)]. \tag{7.29}$$

In our calculations, the time dependence of the collision integrals is explicitly accounted for in the calculations by reevaluating $\Gamma^{el-ph}_{n\mathbf{k}}$ and $\Gamma^{ph-el}_{\mathbf{q}\nu}$ at each time step of the time propagation with new occupation functions. The phonon-phonon collision integral is treated within the relaxation-time

approximation and calculated with shengBTE code. Electron-electron scattering channel governs the thermalization of photo-excited carriers when $f^{el}_{n\mathbf{k}}(t)$ deviates significantly from the equilibrium distribution. Here we will consider exclusively electronic excited state characterized by a weak deviation from a Fermi-Dirac function. In this regime, electron-electron scattering plays only a minor role in the carrier dynamics and it is therefore neglected. The calculations of electronic distribution functions from TDBE shown and used in this chapter, are done by Prof. Fabio Caruso (Christian-Albrechts-Universität zu Kiel).

The initial photo-excited concentration of electrons is taken to be $n = 10^{14}\,\mathrm{cm}^{-2}$. The corresponding initial photo-holes and photo-electrons are defined with two separate chemical potentials and high carrier temperature, while keeping in mind the conservation of carrier number. Namely, we define $f^{el}_{n\mathbf{k}}(t=0) = f_{n\mathbf{k}}(\mu_{\mathrm{e/h}}, T^0_e)$, with μ_{e} (μ_{h}) being the electron (hole) chemical potential, $T^0_{\mathrm{e}} = 2000\,\mathrm{K}$, while phonon temperature is set to $T^0_{\mathrm{p}} = 100\,\mathrm{K}$. Equations (7.28) and (7.29) are solved by time-stepping the derivatives with small time step of 1 fs up to 40 ps.

In order to have a full time-dependent information of electron-phonon dynamics, an important step forward is to update the phonon frequencies coming from the modified electron occupation functions $f^{el}_{n\mathbf{k}}(t)$. This can be calculated by means of the time-resolved phonon spectral function defined as

$$B_{\mathbf{q}\nu}(\omega;t) = -\frac{1}{\pi}\mathrm{Im}\left[\frac{2\omega_{\mathbf{q}\nu}}{\omega^2 - \omega^2_{\mathbf{q}\nu} - 2\omega_{\mathbf{q}\nu}\Pi_{\mathbf{q}\nu}(\omega;t)}\right]. \tag{7.30}$$

The crucial ingredient to the above expression is the time-resolved NA phonon self-energy [4] defined as $\Pi^{\mathrm{NA}}_{\mathbf{q}\nu}(\omega;t) = \Pi_{\mathbf{q}\nu}(\omega;t) - \Pi_{\mathbf{q}\nu}(0)$, where the adiabatic part at $t \to -\infty$, i.e., $\Pi_{\mathbf{q}\nu}(0)$, is subtracted, and where the time dependence is hidden in the electronic distribution functions

$$\Pi_{\mathbf{q}\nu}(\omega;t) = \sum_{\mathbf{k}nm} |g^{nm}_{\nu}(\mathbf{k},\mathbf{q})|^2 \frac{f^{el}_{n\mathbf{k}}(t) - f^{el}_{m\mathbf{k}+\mathbf{q}}(t)}{\omega + \varepsilon_{n\mathbf{k}} - \varepsilon_{m\mathbf{k}+\mathbf{q}} + i\eta}. \tag{7.31}$$

In our approach, the electron occupation functions $f^{el}_{n\mathbf{k}}(t)$ entering the phonon spectral function (7.30) and phonon self-energy (7.31) are no longer Fermi-Dirac distributions as in the standard thermal case [4], but are extracted from TDBE Eq. (7.28) and, therefore, represent nonequilibrium occupations and redistribution of charge carriers at each time instant after the laser excitation.

The corresponding photo-induced renormalization of phonon frequency and modifications to the phonon linewidth (relaxation rate) can be tracked as a function of time by means of the following

expressions [4]

$$\Omega^2_{\mathbf{q}\nu}(t) = \omega^2_{\mathbf{q}\nu} + 2\omega_{\mathbf{q}\nu}\mathrm{Re}\,\Pi_{\mathbf{q}\nu}(\Omega_{\mathbf{q}\nu}(t);t), \tag{7.32}$$

$$\gamma_{\mathbf{q}\nu}(t) = -\mathrm{Im}\,\Pi_{\mathbf{q}\nu}(\Omega_{\mathbf{q}\nu}(t);t). \tag{7.33}$$

A similar idea was adopted recently in Refs. [345, 347] where occupation functions as obtained from TDBE were introduced into dynamic structure factors to complement ultrafast electron diffraction experiments.

We also define the spectral representation of the phonon scattering rate $\gamma F(\omega)$ in order to quantify the modifications to the electron-phonon scattering channels relevant for phonon dynamics and to discuss possible enhancements to the total EPC strength upon the laser excitation

$$\gamma F(\omega;t) = \sum_{\mathbf{q}\nu} \gamma_{\mathbf{q}\nu}(t)\delta\left(\omega - \Omega_{\mathbf{q}\nu}(t)\right), \tag{7.34}$$

where $\delta(x)$ is the Dirac delta function. Note that the above spectral function is defined in a similar manner as the Eliashberg function $\alpha^2F(\omega)$ [93]. The cumulative scattering rate of phonons can then be written as

$$\gamma(\omega;t) = \int_0^\omega d\omega' \gamma F(\omega';t), \tag{7.35}$$

while the total phonon scattering rate is $\gamma(\omega \to \infty;t)$.

All of the above equations and the corresponding input parameters are calculated in this work by means of DFPT [30, 68] and Wannier interpolation [435] of EPC matrix elements g^{nm}_ν [75].

7.3.2 Computational details

We use Quantum ESPRESSO [68–70] for the DFT calculations, and for EPC we use the EPW code [73–75]. All calculations are performed with the norm-conserving Perdew-Burke-Ernzerhof pseudopotential with a kinetic energy cutoff of 120 Ry. The lattice constant is set to the value of 3.188 Å, while the neighboring MoS_2 sheets are separated by 12.7 Å. The self-consistent electron density calculation is done on a $20 \times 20 \times 1$ k-point grid and the phonon calculation on a $6 \times 6 \times 1$ q-point grid. Both are done with the equilibrium electron occupation functions for pristine MoS_2, with the valence band occupied and the conduction band unoccupied. To interpolate electron-phonon

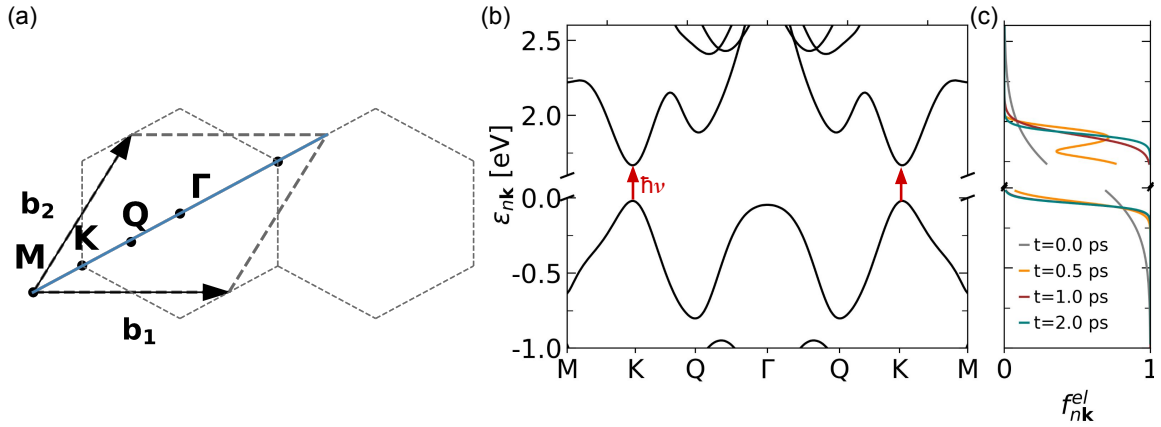

Figure 7.10: (a) Brillouin zone and high-symmetry points of single layer MoS_2. (b) Electronic band structure of MoS_2 with (c) time evolution of the photo-excited occupation functions as obtained from the TDBE. Figure adapted from Ref. [436].

quantities, we use 11 maximally localized Wannier functions [71] with the initial projections of d-orbitals on the Mo sites and p-orbitals on the S atom sites. All electronic structure parameters for the self-consistent cycle and the Wannierization match the ones used to solve the TDBE. The fine sampling of the Brillouin zone for the electron-phonon interpolation is done on a $200 \times 200 \times 1$ grid. The fine q-point grid is always extracted among these 40000 points, whether it is a path in q-space or a full Brillouin zone calculation. Smearing in the EPW calculation is set to 40 meV.

7.3.3 Results and discussion

Fig. 7.10 depicts the Brillouin zone of single-layer MoS_2 and the electronic band structure along high-symmetry points. MoS_2 is a semiconducting TMD with a direct band gap at the K point of the Brillouin zone, and interesting multi-valley topology of valence and conduction bands. The latter is considered to be instrumental for various physical phenomena in MoS_2, such as enhanced EPC of the A_{1g} phonon mode as observed with Raman spectroscopy [44], exciton-phonon coupling [430, 431], anisotropic electron-phonon scattering following laser excitation [347], and multi-valley superconductivity [134–136, 434]. Additionally, in Fig. 7.10(c) we show occupation functions $f^{el}_{n\mathbf{k}}(t)$ for several time instants up to $t = 2$ ps as obtained from the solution of the TDBE Eqs. (7.28) and (7.29). Initial hot distribution of photo-holes and photo-electrons (grey lines) thermalizes to smaller effective electron temperatures (about 180 K) with different time scales.

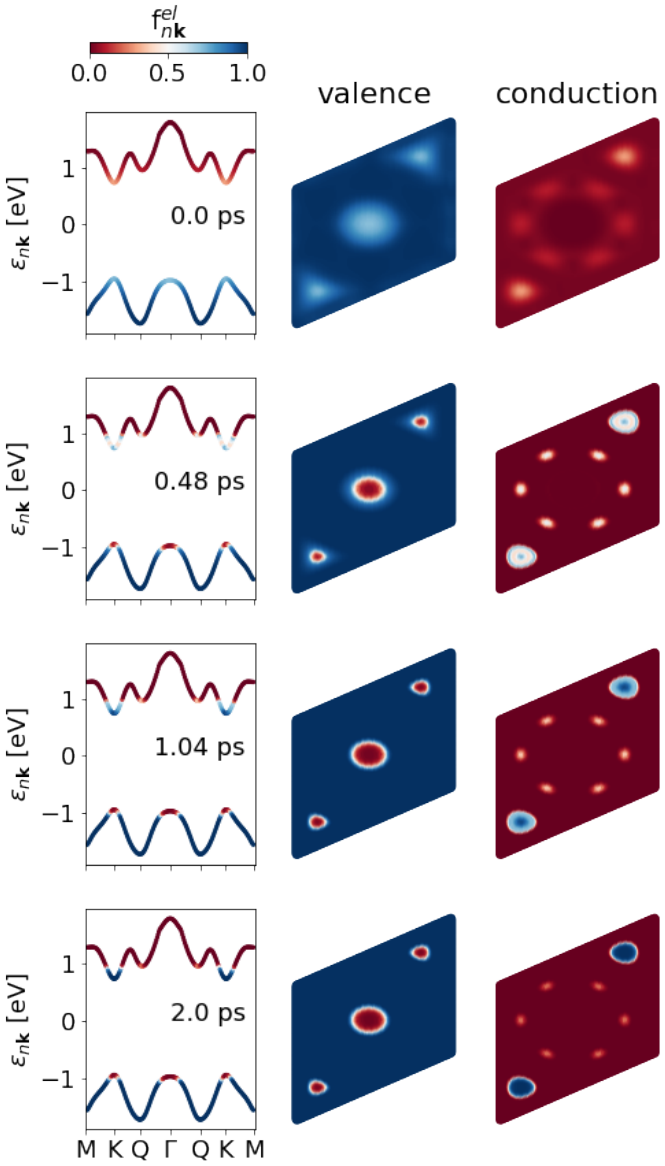

Figure 7.11: Time evolution of electron distribution in the valence and conduction bands. In the first column, electron dispersion with a color scale which determines the occupation is shown. The dispersion is plotted across the M-K- Q-Γ-Q-K-M path denoted by a blue line in Fig. 7.10(a). The annotation in the middle of each panel denotes the time instant after photoexcitation. In the second and third column, electron distribution is shown in the valence and conduction band across the Brillouin zone, bounded by vectors $\mathbf{b_1}$ and $\mathbf{b_2}$ in Fig. 7.10(a).

Namely, holes are almost thermalized at $t = 0.5$ ps, while it takes around 2 ps for excited electrons to equilibrate. This is perhaps more obvious in Fig. 7.11, where the colorscale indicates the **k**-resolved occupations. The reason for this is the difference in the phase space of valence and conduction bands, where the Q valley acts as a sort of bottleneck for electron-phonon scattering in the conduction band and slows down the process. In Fig. 7.10(c), this is reflected by the accumulated charge for $t = 0.5$ ps that forms a non-Fermi-Dirac distribution. In Fig. 7.11 one can explicitly trace how the Q valleys fill with electrons and gradually become empty again. The impact of the nonequilibrium electron and

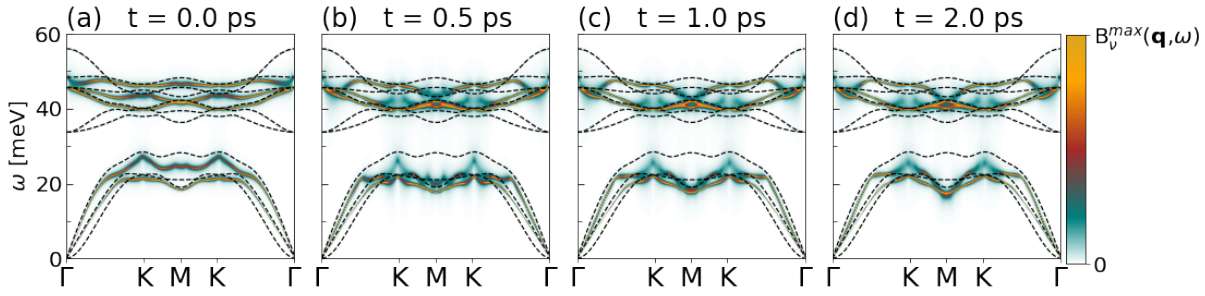

Figure 7.12: Phonon spectral functions $B_\nu(\mathbf{q},\omega)$ of photo-excited MoS_2 shown along high-symmetry points in the first Brillouin zone and for several time frames after excitation: (a) $t = 0$ ps, (b) $t = 0.5$ ps, (c) $t = 1$ ps, and (d) $t = 2$ ps. The dashed lines are phonon dispersions for pristine equilibrium MoS_2 as obtained from the adiabatic DFPT. Significant photo-induced phonon broadening enhancements and dynamical Kohn anomalies can be observed around the high-symmetry points both for optical and acoustic branches. Figure from Ref. [436].

hole distributions on phonons is shown in Fig. 7.12 where we report the full phonon spectral functions for several time delays. Considerable and time-varying nonequilibrium phonon renormalizations are observed for both acoustic and optical branches, especially around the high-symmetry points of the Brillouin zone. In addition, these renormalizations are accompanied by a remarkable enhancement of the phonon broadenings. Characteristic multi-valley landscape of MoS_2 electronic states in momentum space, the Γ and K valleys in the valence band and the K and Q valleys in the conduction band, permits only selective population dynamics and anisotropic electron-phonon scatterings. Photo-holes in $\mathbf{k} = \Gamma$ and $\mathbf{k} = \mathrm{K}$ valence valleys promote specifically $\mathbf{q} = \Gamma$ and $\mathbf{q} = \mathrm{K}$, while photo-electrons in $\mathbf{k} = \mathrm{K}$ and $\mathbf{k} = \mathrm{Q}$ conduction valleys promote dominantly $\mathbf{q} = \Gamma$ and $\mathbf{q} = \mathrm{M}$ electron-phonon scatterings of optical and acoustic phonons. This in turn influences considerably phonon frequency and linewidths, and results in remarkable anisotropic nonequilibrium phonon softening and dynamical Kohn anomalies at aforesaid phonon momenta. For instance, particularly strong modifications of phonon frequency is observed close to $\mathbf{q} = \Gamma$, where large dynamical Kohn anomaly of the A_{1g} optical mode appears, surpassing the strength of the corresponding phonon anomaly in equilibrium state of doped MoS_2 samples [44–46]. Also, sizeable phonon softening is induced for the longitudinal acoustic (LA) phonon at $\mathbf{q} = \mathrm{M}$, which is considered relevant for the appearance of the superconductivity [135] and CDW [433] in doped MoS_2.

As already discussed, Kohn anomalies are distinct softenings of phonon dispersion coming from singularities in static phonon self-energy $\Pi_{\mathbf{q}\nu}(0)$, which in turn come from highly anisotropic

electron-phonon matrix elements $g^{nm}_{\nu}(\mathbf{k},\mathbf{q})$ as well as from the intense and anisotropic density of states of electron-hole pair excitations [4]. If the Kohn anomaly calculated in the nonadiabatic regime [i.e., with $\Pi_{\mathbf{q}\nu}(\omega)$] is different from the static one, it is usually dubbed dynamical. The examples of dynamical Kohn anomalies are shown in Chapter 5. Here we illustrate to which extent a photo-excited carrier distribution can provide a route to trigger and control the emergence of Kohn anomalies over transient timescales. The A_{1g} mode was shown to be significantly coupled to electrons once multiple valleys are occupied [44], as it is the case here for photo-excited MoS_2. The same phonon mode is as well quite affected at the M point, while energetically lower E_{2g} optical mode is softened and broadened at the K point. Also, both longitudinal and transverse acoustic modes are modified, especially around the M and K points. Softening of the LA mode at M point particularly stands out, where at time $t = 2$ ps its frequency is decreased by about 10 meV compared to the equilibrium value. Since the LA mode at $\mathbf{q} = \mathrm{M}$ is instrumental for phonon-mediated superconductivity [135] as well as the CDW formation [433], these results suggest a possibility to tune these ordered states by laser excitations.

In the following, we will study the phase space arguments and analyze the electron-phonon scattering events out-of-equilibrium that lead to these remarkable phonon renormalizations and phonon linewidth enhancements. In the top panels of Figs. 7.13(a) and 7.13(b) we show the momentum-resolved occupation functions $f^{el}_{n\mathbf{k}}(t)$ of valence and conduction bands for $t = 0$ and 2 ps, respectively. The corresponding bottom panels show the contributions to the phonon dispersions and linewidths coming only from the electron-phonon scatterings in the valence and conduction bands. Both time frames are characterized by the similar phase space for the valence and conduction bands, i.e., depopulated $\mathbf{k} = \Gamma$ and $\mathbf{k} = \mathrm{K}$ valleys in the valence band and populated $\mathbf{k} = \mathrm{K}$ and $\mathbf{k} = \mathrm{Q}$ valleys in the conduction band. Such occupation promote $\mathbf{q} = \Gamma$ and $\mathbf{q} = \mathrm{K}$ electron-phonon scatterings in the former, while $\mathbf{q} = \Gamma$, $\mathbf{q} = \mathrm{K}$ and $\mathbf{q} = \mathrm{M}$ electron-phonon scatterings within the latter band. Consequently, these intra- and inter-valley scatterings in the valence band lead to nonequilibrium renormalization of the optical A_{1g} and E_{2g} phonons at Γ and K points, respectively, as well as of the LA mode at the K point. Similarly, the scattering channels in the conduction band produce phonon softenings of the optical A_{1g} phonon at Γ and M points, and the LA mode at the K and M points. As the initially hot distribution of electrons and holes at $t = 0$ ps is distributed into more sharp occupations at the top and bottom of valence and conduction bands at $t = 2$ ps, some alterations of the phonon bands and broadenings become more pronounced while others are reduced. For instance, as the K valley becomes more populated, while the occupation in the Q valley is reduced in the

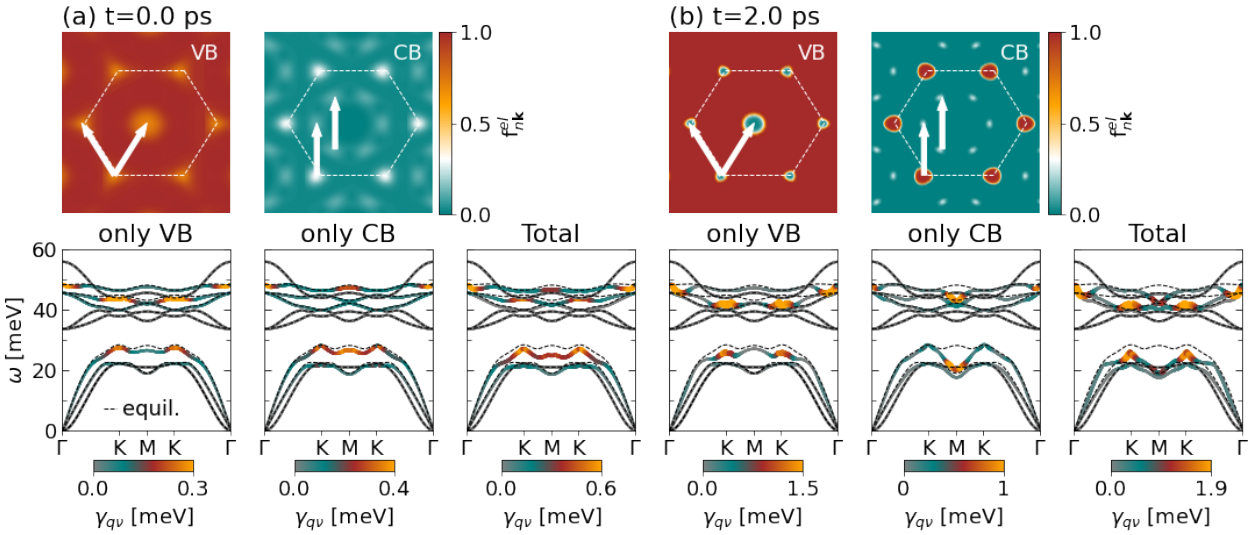

Figure 7.13: Nonequilibrium electron-phonon scattering channels coming from valence- (VB) and conduction-band (CB) distributions. The VB- and CB-resolved contributions are presented for two time instants (a) $t = 0$ ps and (b) $t = 2$ ps. Upper panels depict the momentum-resolved occupation functions $f^{el}_{n\mathbf{k}}(t)$ for the CB and VB within the first Brillouin zone. White arrows represent the dominating inter-valley scatterings channels. The lower panels show the VB- and CB-resolved contributions to the phonon dispersion and linewidth $\gamma_{\mathbf{q}\nu}$. In addition, the overall result of dynamical phonon renormalization, coming from both VB and CB nonequilibrium channels, is shown. The dashed lines again show the phonon dispersions for pristine equilibrium MoS_2 as obtained from the adiabatic DFPT. Figure from Ref. [436].

conduction band, the corresponding modifications of the $\mathbf{q} = \mathrm{K}$ ($\mathbf{q} = \mathrm{M}$) phonons coming only from conduction-band scatterings are reduced (enhanced).

Femtosecond electron diffraction experiment revealed that scatterings in multi-layer $MoTe_2$ are dominated by the zone-center A_{1g} and E_{2g} optical phonons, as well as by the LA phonons at the M point of the BZ [346]. Momentum-resolved picture of the energy transfer between excited electrons and phonons in thin bulk-like films of WSe_2 reveals importance of inter-valley scattering between two Q points followed by emission of the acoustic M-point phonons [341, 426]. On the other hand, coherent phonon dynamics extracted from femtosecond pump-probe spectroscopy had shown that ultrafast intervalley scattering in monolayer $MoSe_2$ is dictated dominantly by the LA phonons, but at K point of the Brilouin zone [351]. Multi-layer films of $MoTe_2$ and WSe_2 are indirect-band-gap semiconductors, and are therefore characterized by different scattering phase space for excited carriers compared to monolayer $MoSe_2$, which has a direct band gap at the K point. Consequently,

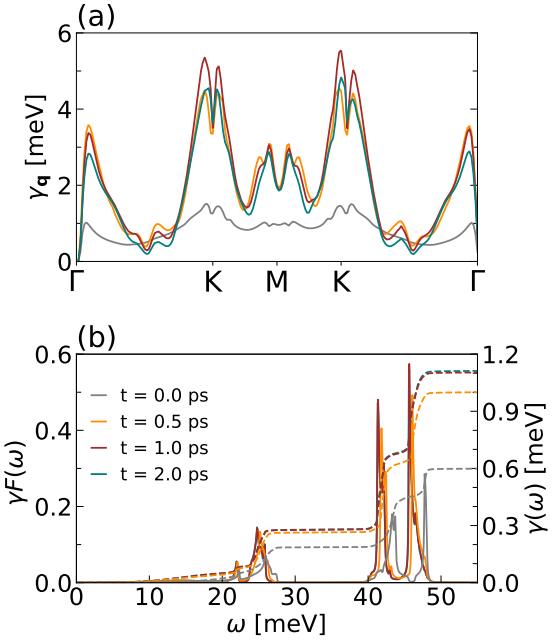

Figure 7.14: (a) Total phonon scattering rate (summed over all branches) along the high-symmetry points and as a function of time. (b) Spectral representation of phonon scattering rates $\gamma F(\omega)$ (phonon density of states weighted with phonon linewidth contributions) as a function of frequency ω shown for several time delays. Right axis shows the cumulative scattering rate $\gamma(\omega)$. Figure from Ref. [436].

monolayer and thin films of TMDs have distinct ultrafast phonon dynamics, coming from different shapes of conduction and valence valleys. For instance, in bulk-like semiconducting TMDs the Q conduction valley has lower energy than the K valley, and therefore the Q $\leftrightarrow$ Q$'$ inter-valley scatterings are dominant with emission of the $\mathbf{q} = \mathrm{M}$ phonons. For corresponding single layers the situation is different, where the K conduction valley has the lowest energy, and more dominant are the K $\leftrightarrow$ K$'$ scatterings (actually in the both conduction and valence bands) and the concomitant $\mathbf{q} = \mathrm{K}$ phonon emission. This opens many possibilities to tailor ultrafast phonon scatterings, e.g., by strain, pressure, doping, and other techniques that can significantly alter the energy positions of valleys [437].

To further demonstrate the implications of nonequilibrium carrier distribution on phonon dynamics, we show in Fig. 7.14 the total phonon scattering rate (summed over all branches) as a function of time along the high-symmetry points and spectral representation of phonon scattering rates $\gamma F(\omega)$ with the corresponding cumulative scattering rate $\gamma(\omega)$ [see Eqs. (7.34) and (7.35)]. The momentum resolved scattering rate $\gamma_{\mathbf{q}}$ reveals important role of the $\mathbf{q} = \Gamma$ and $\mathbf{q} = \mathrm{K}$ phonons and their dominance in the overall phonon relaxation dynamics. Importance of these specific phonon modes are in line with the ultrafast coherent phonon dynamics in single-layer $MoSe_2$ [351], while anisotropic phonon response is in accordance with recent results obtained with ultrafast electron

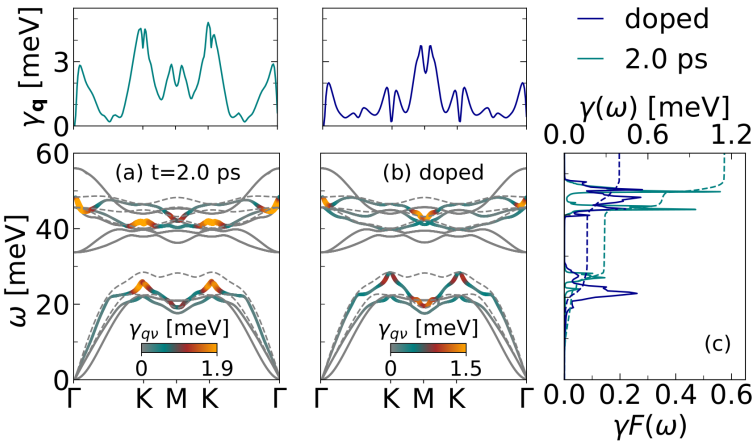

Figure 7.15: (a) Total and mode-resolved nonequilibrium phonon scattering rates along the high-symmetry points for $t = 2$ ps. (b) Same as (a) but for the case of electron-doped equilibrium MoS_2 for the effective carrier concentration $n_{\text{eff}} = 2 \times 10^{14}$ cm^{-2} that matches the photo-excited carrier (i.e., both photo-hole and photo-electron) density at $t = 2$ ps. (c) Spectral representation of phonon scattering rates $\gamma F(\omega)$ as a function of frequency ω and the cumulative scattering rate $\gamma(\omega)$ for the photo-doped and doped cases presented in (a) and (b) panels. Figure from Ref. [436].

diffraction spectroscopy in MoS_2 monolayer [347]. Certain discrepancies in timescales between experiments and theoretical results obtained here could be attributed to the screening of the matrix element induced by the substrate [347].

The obtained relaxation rates around Γ, K, as well as M points are also significantly increased in time, where values at $t = 2$ ps are $4-5$ times larger compared to the corresponding values at the initial time. The frequency-resolved scattering rate is presented in Fig. 7.14(b) via $\gamma F(\omega)$, where it shown that nonequilibrium phonon scattering rates is larger for optical modes above 40 meV. The results for cumulative rate $\gamma(\omega)$ confirms the gradual increase of the total rate as a function of time. Note that the recent theoretical study based on nonequilibrium Green's functions also obtained that the Γ- and K-point phonons are dominantly involved in nonequilibrium carrier dynamics in monolayer MoS_2 [438]. Interestingly, they also show that the optical phonons participate more in the relaxation dynamics compared to the acoustic modes.

In addition, we want to explore the difference in phonon dynamics between the photo-doped (i.e., photo-excited) scenario investigated here and the standard case of the electron-doped material via field-effect techniques or atom adsorption (i.e., via dopants). Fig. 7.15 compares the total and mode-resolved phonon scattering rates along the high-symmetry points for photo-excited MoS_2 at $t = 2$ ps [panel (a)] and MoS_2 doped with electron carrier concentration of $n_{\text{eff}} = 2 \times 10^{14}$ cm^{-2}, which corresponds to the effective photo-induced carrier (both electron and hole) density at $t = 2$ ps [panel (b)]. For the electron-doped case, the active phase space for electron-phonon scatterings

consists only of the K and Q valleys in the conduction band. This in turn promotes dominantly intra-valley $\mathbf{q} = \Gamma$ and inter-valley $\mathbf{q} = \mathrm{M}$ scatterings and consequently phonon renormalizations and broadening around these symmetry points. Furthermore, in Fig. 7.15(c) we show spectral representation of phonon scattering rates $\gamma F(\omega)$ and the cumulative scattering rate $\gamma(\omega)$ for these two cases, where it is clear that photo-doping induces larger and richer phonon-electron scatterings, since the corresponding scattering phase space includes both photo-holes and photo-electrons, i.e., both valence and conduction valleys.

Overall, the present results clearly demonstrate a notable increase of phonon-electron scattering rate with photoexcitation, which points to the potential of enhancing the total EPC strength out-of-equilibrium [417] as well as inducing and modifying the concomitant superconducting properties. Note that in order to have a more conclusive answer to the intriguing physical problem of photo-induced superconductivity, one would need to go beyond the present consideration and adopt more rigorous time-dependent methodology of superconductivity, such as nonequilibrium Green's function techniques [25, 327, 439–441].

7.4 Conclusion

Understanding the mechanisms behind the out-of-equilibrium EPC provides valuable insights into the fundamental physics of graphene and MoS_2 and helps unravel the complex interplay between charge carriers and lattice vibrations. We investigated the coupling of the high-energy optical phonon modes with the photo-excited electron distribution by means of cDFPT in graphene and we explored the phonon relaxation pathways and the ensuing nonequilibrium phonon renormalization in the photo-excited MoS_2 monolayer by combining the *ab-initio* time-dependent Boltzmann equation and the phonon self-energy calculations.

In graphene, we observed hardening of the well-known Kohn anomalies at the center and edge of the Brillouin zone, while for MoS_2, our findings show how population and depopulation of conduction and valence valleys promote anisotropic electron-phonon scatterings and trigger strong Kohn anomalies and softenings.

We obtained complex nonadiabatic EPC features that emerge in both the dispersion and linewidth, and mostly originate from the new scattering channels opened in nonequilibrium. For instance, sharp dynamical phonon anomalies away from the high-symmetry points and the overall increase of the phonon scattering rate have been observed for graphene. Also, we showed incoherent phonon gain at

finite wavevectors irrespective of the doping level or the concentration of the photo-excited carriers, while coherent phonon generation is expected in the state of population inversion and is within the scope of typical experiments. In MoS_2 nonequilibrium of electronic energy levels induces strong Kohn anomaly of the E_{2g} mode close to the center and edge of the Brillouin zone, and strongly softens the longitudinal acoustic phonon at the M point. In accordance to the recent ultrafast experiments, our momentum-resolved analysis demonstrates that the $\mathbf{q} = \Gamma$ and $\mathbf{q} = \mathrm{K}$ phonon modes play a key role in intra- and inter-valley scattering channels and they are thus characterized by large relaxation rates. It is also shown that as the effective electron temperature decreases, i.e., as the photo-holes and photo-electrons are scattered towards the top and bottom of valence and conduction valleys, the overall phonon relaxation rate is significantly enhanced. The richness of the phase space for the photo-carriers and the corresponding impact on phonon dynamics was further demonstrated in comparison to the electron-doped MoS_2 in equilibrium, where, instead of K-point, M-point modes are ruling the phonon relaxation and renormalization, and where phonon relaxation rates have less intensity.

Present results and methodology might be instrumental for gaining crucial microscopic insights of photo-excited states in multi-valley systems, such as TMDs, as well as discovering new photo-induced ordered phases (e.g., superconductivity and charge density waves) and structural transformations in condensed matter. We believe our work offers crucial information on the nature of EPC, justifies the known nonequilibrium features and sheds new light on the understanding of the underlying ultrafast vibrational relaxation mechanisms.

Chapter 8

Thesis summary and outlook

The main objective of this doctoral thesis is to conduct a comprehensive first-principles investigation of the dynamical electron-phonon coupling (EPC) and the corresponding role it has in various bulk and quasi-2D materials. Under both equilibrium and non-equilibrium conditions, the thesis addresses the question of the consequences the dynamical EPC has on phonons.

The research relies on density functional theory (DFT) and is supplemented with appropriate theoretical extensions not a priori considered in first-principles calculations. DFT has proven to be a powerful tool for calculating EPC from first principles. The purpose of this research is to enhance this method by combining DFT with many-body perturbation theory (MBPT), programs for calculating anharmonic effects, and Boltzmann transport equations.

DFT relies on the adiabatic approximation, which is why the first topic of this doctoral research deals with nonadiabatic correction of the phonon spectrum of various 2D materials. Deepening the understanding of dynamical EPC, which is inaccessible within the framework of available first-principles calculations, is of great importance and can greatly alter adiabatically predicted phonon properties. This significantly contributes to understanding the dynamical effects of EPC and their far-reaching implications in the superconducting and transport properties of various materials. We propose a method for correcting phonon spectra and EPC and demonstrate its consequences on the calculation of superconducting and transport properties. We have shown that in eight representative systems, dynamical corrections mitigate statically obtained Kohn anomalies in the phonon spectrum and, in turn, drastically reduce the strength of EPC.

In addition to dynamical effects, DFT does not account for higher-order effects in MBPT when calculating the phonon self-energy. This thesis demonstrates that higher-order MBPT brings

significant anharmonic contributions mediated by electrons. Such research aids in understanding temperature-dependent Raman spectra of systems with strong electron-phonon interaction. It is shown that in graphene and Weyl semimetals, despite common beliefs, EPC represents a significant mechanism for temperature-dependent phonon frequency changes and linewidths.

New interesting phases can be induced in materials through photoexcitation, which is of great significance for applications yet largely unexplored. We present two new methods for simulating nonequilibrium electron distributions and their consequences on the dynamics of phonons, electrons, and EPC. In photoinduced graphene, we simulated nonequilibrium carrier distributions in several relaxation phases and calculated the dynamical spectral function of phonons. We discovered phonon stiffening and general broadening of phonon lines due to electron binding out-of-equilibrium. EPC calculations in photoexcited MoS_2 revealed transient phonon anomalies and phonon linewidth broadening during electron thermalization. This approach is suitable for studying ultrafast phenomena where dynamical phonon renormalization plays a crucial role. This research provides a foundation for studying systems where photoexcitation can induce phase transitions or ordered states.

This dissertation outlines several theoretical methods that complement the shortcomings of first-principles calculations and can be applied to a wide range of materials and physical problems. The dissertation is closely linked to experimental work, while the technological application of such research extends from finding optimal materials for various devices to tailoring their desired properties and applying them in various branches of industry.

Curriculum vitae

Nina Girotto was born on the 28th of July 1996, in Rijeka, Croatia. She graduated from "Prva Sušačka Hrvatska Gimnazija in 2015, and enrolled in the graduate program, Master of Science in Physics, at the Department of Physics, Faculty of Science, University of Zagreb. In 2020, she graduated with the topic of "Nonadiabatic renormalization of optical phonons in highly-doped graphene", under the mentorship of Dr. Dino Novko. The same year she began her doctoral studies in condensed matter theory at the Department of Physics, Faculty of Science, University of Zagreb. Until now, she has been working as a research assistant at the Institute of Physics in Zagreb, under the supervision of Dr. Dino Novko. She is a part of the Surfaces, interfaces and 2D materials research group group led by Dr. Marko Kralj. During her PhD studies, she published 5 papers and is the first author of 4 of them.

Refereed publications

Published

1 **Girotto, N.**, Novko, D., *Dynamical renormalization of electron-phonon coupling in conventional superconductors,* Phys. Rev. B 107, 064310 (2023).

2 **Girotto, N.**, Caruso, F., Novko, D., *Ultrafast Nonadiabatic Phonon Renormalization in Photoexcited Single-Layer MoS2,* J. Phys. Chem. C, 127, 33, 16515–16524(2023).

3 **Girotto, N.**, Novko, D., *Dynamical Phonons Following Electron Relaxation Stages in Photoexcited Graphene,* J. Phys. Chem. Lett., 14, 39, 8709–8716 (2023).

4 Berges, J., **Girotto**, N., Wehling, T., Marzari, N. and Poncé, S., *Phonon Self-Energy Corrections: To Screen, or Not to Screen,* Phys. Rev. X 13, 041009 (2023).

5 **Girotto, N.**, Linhart, L., Libisch, F., *Coupled phonons in twisted bilayer graphene,* Phys. Rev. B 108, 155415 (2023).

Supervisor information

Dino Novko received his Master degree in Physics from University of Zagreb (Croatia) in 2013, and Doctoral degree in Physics and Materials Science from University of Basque Country (Spain) in 2017. From 2017 to 2018, he was a Postdoctoral researcher at Freie Universität Berlin (Germany), while next year he got a Postdoctoral position at the Institute of Physics, Zagreb. In 2019 he was employed as a Research Associate at the Institute of Physics, Zagreb, and promoted to Senior Research Associate in 2023. His research focuses on energy dissipation of vibrating molecules on metal surfaces, collective electron dynamics (such as plasmons and excitons) in 2D materials, dynamical electron-phonon coupling, with recent focus on hot-electron and hot-phonon generation and ultrafast aspects of matter. So far, he published more than 50 scientific papers in renowned journals (with 1150 citations according to Google Scholar), presented 8 invited talks at major conferences and 6 invited seminars at renowned international institutions, as well as co-organized 3 international conferences.

References

[1] Neil W. Ashcroft and N. David Mermin. *Solid State Physics*, page 826. Saunders College Publishing, 1976.

[2] Gerald D. Mahan. *Physics of Solids and Liquids*, page 785. Springer New York, NY, 2013.

[3] Göran Grimvall. *Selected Topics in Solid State Physics*, page 304. North Holland Publishing Company, Amsterdam, 1981.

[4] Feliciano Giustino. Electron-phonon interactions from first principles. *Rev. Mod. Phys.*, 89:015003, 2017.

[5] Feliciano Giustino, Steven G. Louie, and Marvin L. Cohen. Electron-phonon renormalization of the direct band gap of diamond. *Phys. Rev. Lett.*, 105:265501, Dec 2010.

[6] T. Valla, A. V. Fedorov, P. D. Johnson, and S. L. Hulbert. Many-body effects in angle-resolved photoemission: Quasiparticle energy and lifetime of a mo(110) surface state. *Phys. Rev. Lett.*, 83:2085–2088, Sep 1999.

[7] S. Moser, L. Moreschini, J. Jaćimović, O. S. Barišić, H. Berger, A. Magrez, Y. J. Chang, K. S. Kim, A. Bostwick, E. Rotenberg, L. Forró, and M. Grioni. Tunable polaronic conduction in anatase tio_2. *Phys. Rev. Lett.*, 110:196403, May 2013.

[8] Chaoyu Chen, José Ávila, Emmanouil Frantzeskakis, Anna Levy, and Maria Asensio. Observation of a two-dimensional liquid of fröhlich polarons at the bare srtio3 surface. *Nature Communications*, 6:8585, 10 2015.

[9] Claudia Cancellieri, A. Mishchenko, U. Aschauer, Alessio Filippetti, Carina Faber, Osor Barišić, Victor Rogalev, Thorsten Schmitt, N. Nagaosa, and V. Strocov. Polaronic metal state at the laalo3/srtio3 interface. *Nature Communications*, 7, 07 2015.

[10] W. Kohn. Image of the fermi surface in the vibration spectrum of a metal. *Phys. Rev. Lett.*, 2:393–394, May 1959.

[11] S. Piscanec, M. Lazzeri, Francesco Mauri, A. C. Ferrari, and J. Robertson. Kohn anomalies and electron-phonon interactions in graphite. *Phys. Rev. Lett.*, 93:185503, Oct 2004.

[12] S. Pisana, Michele Lazzeri, Cinzia Casiraghi, Kostya Novoselov, Andre Geim, Andrea Ferrari, and Francesco Mauri. Breakdown of the adiabatic born-oppenheimer approximation in graphene. *Nature materials*, 6:198–201, 04 2007.

[13] Stéphane Berciaud, Melinda Y. Han, Kin Fai Mak, Louis E. Brus, Philip Kim, and Tony F. Heinz. Electron and optical phonon temperatures in electrically biased graphene. *Phys. Rev. Lett.*, 104:227401, Jun 2010.

[14] Carino Ferrante, Alessandra Virga, Lara Benfatto, Miles Martinati, D. Fazio, U. Sassi, Claudia Fasolato, A. Ott, Paolo Postorino, Dobae Yoon, G. Cerullo, F. Mauri, A. Ferrari, and Tullio Scopigno. Raman spectroscopy of graphene under ultrafast laser excitation. *Nature Communications*, 9, 01 2018.

[15] C. A. Howard, M. P. M. Dean, and F. Withers. Phonons in potassium-doped graphene: The effects of electron-phonon interactions, dimensionality, and adatom ordering. *Phys. Rev. B*, 84:241404, Dec 2011.

[16] Cinzia Casiraghi. Probing disorder and charged impurities in graphene by raman spectroscopy. *physica status solidi (RRL) - Rapid Research Letters*, 3:175 – 177, 09 2009.

[17] F. Weber, S. Rosenkranz, J.-P. Castellan, R. Osborn, R. Hott, R. Heid, K.-P. Bohnen, T. Egami, A. H. Said, and D. Reznik. Extended phonon collapse and the origin of the charge-density wave in $2h-\mathrm{nbse}_2$. *Phys. Rev. Lett.*, 107:107403, Sep 2011.

[18] Jingjing Lin, Liwei Guo, Qingsong Huang, Yuping Jia, Kang Li, Xiaofang Lai, and Xiaolong Chen. Anharmonic phonon effects in raman spectra of unsupported vertical graphene sheets. *Phys. Rev. B*, 83:125430, Mar 2011.

[19] Jun Nagamatsu, Norimasa Nakagawa, Takahiro Muranaka, Yuji Zenitani, and Jun Akimitsu. Superconductivity at 39 k in magnesium diboride. *Nature*, 410(6824):63, Mar 2001.

[20] Hyoung Joon Choi, David Roundy, Hong Sun, Marvin L. Cohen, and Steven G. Louie. The origin of the anomalous superconducting properties of mgb2. *Nature*, 418(6899):758, Aug 2002.

[21] A. P. Drozdov, M. I. Eremets, I. A. Troyan, V. Ksenofontov, and S. I. Shylin. Conventional superconductivity at 203 kelvin at high pressures in the sulfur hydride system. *Nature*, 525(7567):73–76, August 2015.

[22] Ion Errea, Matteo Calandra, Chris J. Pickard, Joseph Nelson, Richard J. Needs, Yinwei Li, Hanyu Liu, Yunwei Zhang, Yanming Ma, and Francesco Mauri. High-pressure hydrogen sulfide from first principles: A strongly anharmonic phonon-mediated superconductor. *Phys. Rev. Lett.*, 114:157004, Apr 2015.

[23] J. Bardeen, L. N. Cooper, and J. R. Schrieffer. Theory of superconductivity. *Phys. Rev.*, 108:1175, Dec 1957.

[24] Jens Christian Johannsen, Søren Ulstrup, Federico Cilento, Alberto Crepaldi, Michele Zacchigna, Cephise Cacho, I. C. Edmond Turcu, Emma Springate, Felix Fromm, Christian Raidel, Thomas Seyller, Fulvio Parmigiani, Marco Grioni, and Philip Hofmann. Direct view of hot carrier dynamics in graphene. *Phys. Rev. Lett.*, 111:027403, Jul 2013.

[25] Claudio Giannetti, Massimo Capone, Daniele Fausti, Michele Fabrizio, Fulvio Parmigiani, and Dragan Mihailovic. Ultrafast optical spectroscopy of strongly correlated materials and high-temperature superconductors: a non-equilibrium approach. *Advances in Physics*, 65(2):58, 2016.

[26] Alberto de la Torre, Dante M. Kennes, Martin Claassen, Simon Gerber, James W. McIver, and Michael A. Sentef. Colloquium: Nonthermal pathways to ultrafast control in quantum materials. *Rev. Mod. Phys.*, 93:041002, Oct 2021.

[27] Charles J. Sayers, Armando Genco, Chiara Trovatello, Stefano Dal Conte, Vladislav O. Khaustov, Jorge Cervantes-Villanueva, Davide Sangalli, Alejandro Molina-Sanchez, Camilla Coletti, Christoph Gadermaier, and Giulio Cerullo. Strong coupling of coherent phonons to excitons in semiconducting monolayer mote2. *Nano Letters*, 23(20):9235–9242, September 2023.

[28] Xian Li, Tian Qiu, Jiahao Zhang, Edoardo Baldini, Jian Lu, Andrew M. Rappe, and Keith A. Nelson. Terahertz field-induced ferroelectricity in quantum paraelectric srtio$_3$. *Science*, 364(6445):1079, 2019.

[29] A. S. Disa, J. Curtis, M. Fechner, A. Liu, A. von Hoegen, M. Först, T. F. Nova, P. Narang, A. Maljuk, A. V. Boris, and et al. Photo-induced high-temperature ferromagnetism in $YTiO_3$. *Nature*, 617(7959):73, may 2023.

[30] Stefano Baroni, Stefano de Gironcoli, Andrea Dal Corso, and Paolo Giannozzi. Phonons and related crystal properties from density-functional perturbation theory. *Rev. Mod. Phys.*, 73:515, 2001.

[31] Fernando Cerdeira and Manuel Cardona. Effect of carrier concentration on the raman frequencies of si and ge. *Phys. Rev. B*, 5:1440, Feb 1972.

[32] E. Cappelluti. Electron-phonon effects on the raman spectrum in Mgb_2. *Phys. Rev. B*, 73:140505, Apr 2006.

[33] Yu. S. Ponosov and S. V. Streltsov. Raman-active E_{2g} phonon in mgb_2: Electron-phonon interaction and anharmonicity. *Phys. Rev. B*, 96:214503, Dec 2017.

[34] Dino Novko. Nonadiabatic coupling effects in mgb_2 reexamined. *Physical Review B*, 98(4):041112, 2018.

[35] Dino Novko, Fabio Caruso, Claudia Draxl, and Emmanuele Cappelluti. Ultrafast hot phonon dynamics in mgb_2 driven by anisotropic electron-phonon coupling. *Phys. Rev. Lett.*, 124:077001, Feb 2020.

[36] Emmanuele Cappelluti, Fabio Caruso, and Dino Novko. Properties and challenges of hot-phonon physics in metals: Mgb_2 and other compounds. *Progress in Surface Science*, 97(3):100664, 2022.

[37] Yu. S. Ponosov, G. A. Bolotin, C. Thomsen, and M. Cardona. Raman scattering in os: Nonadiabatic renormalization of the optical phonon self-energies. *physica status solidi (b)*, 208(1):257, 1998.

[38] Yu. S. Ponosov and S. V. Streltsov. Raman evidence for nonadiabatic effects in optical phonon self-energies of transition metals. *Phys. Rev. B*, 94:214302, Dec 2016.

[39] Michele Lazzeri and Francesco Mauri. Nonadiabatic kohn anomaly in a doped graphene monolayer. *Phys. Rev. Lett.*, 97:266407, Dec 2006.

[40] Simone Pisana, Michele Lazzeri, Cinzia Casiraghi, Kostya S. Novoselov, A. K. Geim, Andrea C. Ferrari, and Francesco Mauri. Breakdown of the adiabatic born–oppenheimer approximation in graphene. *Nature Materials*, 6(3):198, Mar 2007.

[41] Stefano Piscanec, Michele Lazzeri, J. Robertson, Andrea C. Ferrari, and Francesco Mauri. Optical phonons in carbon nanotubes: Kohn anomalies, peierls distortions, and dynamic effects. *Phys. Rev. B*, 75:035427, Jan 2007.

[42] A. Marco Saitta, Michele Lazzeri, Matteo Calandra, and Francesco Mauri. Giant nonadiabatic effects in layer metals: Raman spectra of intercalated graphite explained. *Phys. Rev. Lett.*, 100:226401, Jun 2008.

[43] Fabio Caruso, Moritz Hoesch, Philipp Achatz, Jorge Serrano, Michael Krisch, Etienne Bustarret, and Feliciano Giustino. Nonadiabatic kohn anomaly in heavily boron-doped diamond. *Phys. Rev. Lett.*, 119:017001, Jul 2017.

[44] Thibault Sohier, Evgeniy Ponomarev, Marco Gibertini, Helmuth Berger, Nicola Marzari, Nicolas Ubrig, and Alberto F. Morpurgo. Enhanced electron-phonon interaction in multivalley materials. *Phys. Rev. X*, 9:031019, Aug 2019.

[45] Dino Novko. Broken adiabaticity induced by lifshitz transition in mos_2 and ws_2 single layers. *Communications Physics*, 3(1):1, 2020.

[46] Peio Garcia-Goiricelaya, Jon Lafuente-Bartolome, Idoia G. Gurtubay, and Asier Eiguren. Emergence of large nonadiabatic effects induced by the electron-phonon interaction on the complex vibrational quasiparticle spectrum of doped monolayer mos_2. *Phys. Rev. B*, 101:054304, Feb 2020.

[47] D. Novko, M. Alducin, and J. I. Juaristi. Electron-mediated phonon-phonon coupling drives the vibrational relaxation of co on cu(100). *Phys. Rev. Lett.*, 120:156804, Apr 2018.

[48] M. Born and R. Oppenheimer. Zur quantentheorie der molekeln. *Annalen der Physik*, 389(20):457–484, 1927.

[49] P. Hohenberg and W. Kohn. Inhomogeneous electron gas. *Phys. Rev.*, 136:B864, 1964.

[50] W. Kohn and L. J. Sham. Self-consistent equations including exchange and correlation effects. *Phys. Rev.*, 140:A1133, 1965.

[51] J. P. Perdew and Alex Zunger. Self-interaction correction to density-functional approximations for many-electron systems. *Phys. Rev. B*, 23:5048–5079, May 1981.

[52] John P. Perdew, Kieron Burke, and Matthias Ernzerhof. Generalized gradient approximation made simple. *Phys. Rev. Lett.*, 77:3865–3868, Oct 1996.

[53] É. D. Murray, S. Fahy, D. Prendergast, T. Ogitsu, D. M. Fritz, and D. A. Reis. Phonon dispersion relations and softening in photoexcited bismuth from first principles. *Phys. Rev. B*, 75:184301, May 2007.

[54] Yusuke Nomura and Ryotaro Arita. Ab initio downfolding for electron-phonon-coupled systems: Constrained density-functional perturbation theory. *Phys. Rev. B*, 92:245108, 2015.

[55] Kun Liu, Sheng Mao, Shunhong Zhang, and Jian Zhou. Photoinduced rippling of two-dimensional hexagonal nitride monolayers. *Nano Letters*, 22(22):9006–9012, 2022. PMID: 36342788.

[56] P. Tangney and S. Fahy. Density-functional theory approach to ultrafast laser excitation of semiconductors: Application to the A_1 phonon in tellurium. *Phys. Rev. B*, 65:054302, Jan 2002.

[57] É. D. Murray, D. M. Fritz, J. K. Wahlstrand, S. Fahy, and D. A. Reis. Effect of lattice anharmonicity on high-amplitude phonon dynamics in photoexcited bismuth. *Phys. Rev. B*, 72:060301, Aug 2005.

[58] Charles Paillard, Engin Torun, Ludger Wirtz, Jorge Íñiguez, and Laurent Bellaiche. Photoinduced phase transitions in ferroelectrics. *Phys. Rev. Lett.*, 123:087601, Aug 2019.

[59] Giovanni Marini and Matteo Calandra. Lattice dynamics of photoexcited insulators from constrained density-functional perturbation theory. *Phys. Rev. B*, 104:144103, Oct 2021.

[60] Andreas Görling. Density-functional theory beyond the hohenberg-kohn theorem. *Phys. Rev. A*, 59:3359–3374, May 1999.

[61] Anders Hellman, Behrooz Razaznejad, and Bengt Lundqvist. Potential-energy surfaces for excited states in extended systems. *The Journal of chemical physics*, 120:4593–602, 04 2004.

[62] F. Aryasetiawan, M. Imada, A. Georges, G. Kotliar, S. Biermann, and A. I. Lichtenstein. Frequency-dependent local interactions and low-energy effective models from electronic structure calculations. *Phys. Rev. B*, 70:195104, 2004.

[63] Erik G. C. P. van Loon, Jan Berges, and Tim O. Wehling. Downfolding approaches to electron-ion coupling: Constrained density-functional perturbation theory for molecules. *Phys. Rev. B*, 103:205103, 2021.

[64] Erik G. C. P. van Loon, Malte Rösner, Mikhail I. Katsnelson, and Tim O. Wehling. Random phase approximation for gapped systems: Role of vertex corrections and applicability of the constrained random phase approximation. *Phys. Rev. B*, 104:045134, 2021.

[65] Masatoshi Imada and Takashi Miyake. Electronic structure calculation by first principles for strongly correlated electron systems. *J. Phys. Soc. Jpn.*, 79:112001, 2010.

[66] Gregory H. Wannier. The structure of electronic excitation levels in insulating crystals. *Phys. Rev.*, 52:191–197, Aug 1937.

[67] Nicola Marzari and David Vanderbilt. Maximally localized generalized wannier functions for composite energy bands. *Phys. Rev. B*, 56:12847–12865, Nov 1997.

[68] Paolo Giannozzi, Stefano Baroni, Nicola Bonini, Matteo Calandra, Roberto Car, Carlo Cavazzoni, Davide Ceresoli, Guido L. Chiarotti, Matteo Cococcioni, Ismaila Dabo, Andrea Dal Corso, Stefano de Gironcoli, Stefano Fabris, Guido Fratesi, Ralph Gebauer, Uwe Gerstmann, Christos Gougoussis, Anton Kokalj, Michele Lazzeri, Layla Martin-Samos, Nicola Marzari, Francesco Mauri, Riccardo Mazzarello, Stefano Paolini, Alfredo Pasquarello, Lorenzo Paulatto, Carlo Sbraccia, Sandro Scandolo, Gabriele Sclauzero, Ari P. Seitsonen, Alexander Smogunov, Paolo Umari, and Renata M. Wentzcovitch. Quantum ESPRESSO: A modular and open-source software project for quantum simulations of materials. *J. Phys. Condens. Matter*, 21:395502, 2009.

[69] P. Giannozzi, O. Andreussi, T. Brumme, O. Bunau, M. Buongiorno Nardelli, M. Calandra, R. Car, C. Cavazzoni, D. Ceresoli, M. Cococcioni, N. Colonna, I. Carnimeo, A. Dal Corso, S. de Gironcoli, P. Delugas, R. A. DiStasio, A. Ferretti, A. Floris, G. Fratesi, G. Fugallo, R. Gebauer, U. Gerstmann, F. Giustino, T. Gorni, J. Jia, M. Kawamura, H.-Y. Ko, A. Kokalj, E. Küçükbenli, M. Lazzeri, M. Marsili, N. Marzari, F. Mauri, N. L. Nguyen, H.-V. Nguyen, A. Otero-de-la-Roza, L. Paulatto, S. Poncé, D. Rocca, R. Sabatini, B. Santra, M. Schlipf, A. P. Seitsonen, A. Smogunov, I. Timrov, T. Thonhauser, P. Umari, N. Vast, X. Wu, and S. Baroni. Advanced capabilities for materials modelling with Quantum ESPRESSO. *J. Phys. Condens. Matter*, 29:465901, 2017.

[70] Paolo Giannozzi, Oscar Baseggio, Pietro Bonfà, Davide Brunato, Roberto Car, Ivan Carnimeo, Carlo Cavazzoni, Stefano de Gironcoli, Pietro Delugas, Fabrizio Ferrari Ruffino, Andrea Ferretti, Nicola Marzari, Iurii Timrov, Andrea Urru, and Stefano Baroni. Quantum ESPRESSO toward the exascale. *J. Chem. Phys.*, 152:154105, 2020.

[71] Nicola Marzari, Arash A. Mostofi, Jonathan R. Yates, Ivo Souza, and David Vanderbilt. Maximally localized Wannier functions: Theory and applications. *Rev. Mod. Phys.*, 84:1419, 2012.

[72] Ivo Souza, Nicola Marzari, and David Vanderbilt. Maximally localized wannier functions for entangled energy bands. *Phys. Rev. B*, 65:035109, Dec 2001.

[73] Feliciano Giustino, Marvin L. Cohen, and Steven G. Louie. Electron-phonon interaction using wannier functions. *Phys. Rev. B*, 76:165108, Oct 2007.

[74] Jesse Noffsinger, Feliciano Giustino, Brad D. Malone, Cheol-Hwan Park, Steven G. Louie, and Marvin L. Cohen. EPW: A program for calculating the electron–phonon coupling using maximally localized Wannier functions. *Comput. Phys. Commun.*, 181:2140, 2010.

[75] S. Poncé, E.R. Margine, C. Verdi, and F. Giustino. EPW: Electron–phonon coupling, transport and superconducting properties using maximally localized Wannier functions. *Comput. Phys. Commun.*, 209:116, 2016.

[76] Xuetao Zhu, Yanwei Cao, Jiandi Zhang, E. W. Plummer, and Jiandong Guo. Classification of charge density waves based on their nature. *Proceedings of the National Academy of Sciences*, 112(8):2367–2371, February 2015.

[77] Jan Berges, Nina Girotto, Tim Wehling, Nicola Marzari, and Samuel Poncé. Phonon self-energy corrections: To screen, or not to screen. *Phys. Rev. X*, 13:041009, Oct 2023.

[78] P. N. Keating. Dielectric screening and the phonon spectra of metallic and nonmetallic crystals. *Phys. Rev.*, 175:1171–1180, Nov 1968.

[79] Andrea Marini. Equilibrium and out-of-equilibrium realistic phonon self-energy free from overscreening. *Phys. Rev. B*, 107:024305, Jan 2023.

[80] Matteo Calandra, Gianni Profeta, and Francesco Mauri. Adiabatic and nonadiabatic phonon dispersion in a wannier function approach. *Phys. Rev. B*, 82:165111, Oct 2010.

[81] Philip B. Allen and Božidar Mitrović. Theory of superconducting tc. volume 37 of *Solid State Physics*, page 1. Academic Press, 1983.

[82] S. G. Sharapov and J. P. Carbotte. Effects of energy dependence in the quasiparticle density of states on far-infrared absorption in the pseudogap state. *Phys. Rev. B*, 72:134506, Oct 2005.

[83] Gabriel Antonius and Steven G. Louie. Theory of exciton-phonon coupling. *Phys. Rev. B*, 105:085111, Feb 2022.

[84] Nina Girotto. Vlastita energija fonona. *seminar iz kolegija 'Visokotemperaturna supravodljivost'*, 2022.

[85] A. B. Migdal. Interaction between electrons and lattice vibrations in a normal metal. *Sov. Phys. JETP*, 7(6):996, 1958.

[86] S. Engelsberg and J. R. Schrieffer. Coupled electron-phonon system. *Phys. Rev.*, 131:993, 1963.

[87] E.G Maksimov and S.V Shulga. Nonadiabatic effects in optical phonon self-energy. *Solid State Communications*, 97(7):553, 1996.

[88] S. Poncé, Y. Gillet, J. Laflamme Janssen, A. Marini, M. Verstraete, and X. Gonze. Temperature dependence of the electronic structure of semiconductors and insulators. *The Journal of Chemical Physics*, 143(10):102813, 2015.

[89] Philip B. Allen and Jean Paul Nery. Low-temperature semiconductor band-gap thermal shifts: T^4 shifts from ordinary acoustic and T^2 from piezoacoustic coupling. *Phys. Rev. B*, 95:035211, Jan 2017.

[90] Anna Miglio, Véronique Brousseau-Couture, Emile Godbout, Gabriel Antonius, Yang-Hao Chan, Steven G. Louie, Michel Côté, Matteo Giantomassi, and Xavier Gonze. Predominance of non-adiabatic effects in zero-point renormalization of the electronic band gap. *npj Computational Materials*, 6(1):167, 2020.

[91] Shi-Qi Hu, Xin-Bao Liu, Da-Qiang Chen, Chao Lian, En-Ge Wang, and Sheng Meng. Nonadiabatic electron-phonon coupling and its effects on superconductivity. *Phys. Rev. B*, 105:224311, Jun 2022.

[92] Shi-Qi Hu, Da-Qiang Chen, Sheng-Jie Zhang, Xin-Bao Liu, and Sheng Meng. Probing precise interatomic potentials by nonadiabatic nonlinear phonons. *Materials Today Physics*, 27:100790, 2022.

[93] Philip B. Allen and Richard Silberglitt. Some effects of phonon dynamics on electron lifetime, mass renormalization, and superconducting transition temperature. *Phys. Rev. B*, 9:4733, Jun 1974.

[94] F. Marsiglio. Pairing and charge-density-wave correlations in the holstein model at half-filling. *Phys. Rev. B*, 42:2416–2424, Aug 1990.

[95] Benjamin Nosarzewski, Michael Schüler, and Thomas P. Devereaux. Spectral properties and enhanced superconductivity in renormalized migdal-eliashberg theory. *Phys. Rev. B*, 103:024520, Jan 2021.

[96] Chandan Setty, Matteo Baggioli, and Alessio Zaccone. Anharmonic phonon damping enhances the T_c of bcs-type superconductors. *Phys. Rev. B*, 102:174506, Nov 2020.

[97] Chandan Setty, Matteo Baggioli, and Alessio Zaccone. Superconducting dome in ferroelectric-type materials from soft mode instability. *Phys. Rev. B*, 105:L020506, Jan 2022.

[98] C. Grimaldi, L. Pietronero, and S. Strässler. Nonadiabatic superconductivity: Electron-phonon interaction beyond migdal's theorem. *Phys. Rev. Lett.*, 75:1158, Aug 1995.

[99] E. Cappelluti, C. Grimaldi, L. Pietronero, and S. Strässler. Nonadiabatic channels in the superconducting pairing of fullerides. *Phys. Rev. Lett.*, 85:4771, Nov 2000.

[100] Lev P. Gor'kov. Superconducting transition temperature: Interacting fermi gas and phonon mechanisms in the nonadiabatic regime. *Phys. Rev. B*, 93:054517, Feb 2016.

[101] Chandan Setty, Matteo Baggioli, and Alessio Zaccone. Anharmonic theory of superconductivity and its applications to emerging quantum materials. *Journal of Physics: Condensed Matter*, 36(17):173002, feb 2024.

[102] DJordje Dangi'c, Lorenzo Monacelli, Raffaello Bianco, Francesco Mauri, and Ion Errea. Large impact of phonon lineshapes on the superconductivity of solid hydrogen. 2023.

[103] S.V. Shulga, O.V. Dolgov, and E.G. Maksimov. Electronic states and optical spectra of htsc with electron-phonon coupling. *Physica C: Superconductivity*, 178(4):266–274, 1991.

[104] F. Marsiglio and J. P. Carbotte. *Electron-Phonon Superconductivity*, page 73. Springer Berlin Heidelberg, Berlin, Heidelberg, 2008.

[105] E. W. Fenton, J. P. Jan, Å. Karlsson, and R. Singer. Ideal resistivity of bismuth-antimony alloys and the electron-electron interaction. *Phys. Rev.*, 184:663–667, Aug 1969.

[106] D. van der Marel, J. L. M. van Mechelen, and I. I. Mazin. Common fermi-liquid origin of T^2 resistivity and superconductivity in n-type $srtio_3$. *Phys. Rev. B*, 84:205111, Nov 2011.

[107] Xiao Lin, Benoît Fauqué, and Kamran Behnia. Scalable t² resistivity in a small single-component fermi surface. *Science*, 349(6251):945, 2015.

[108] Neven Barišić, Mun K. Chan, Yuan Li, Guichuan Yu, Xudong Zhao, Martin Dressel, Ana Smontara, and Martin Greven. Universal sheet resistance and revised phase diagram of the cuprate high-temperature superconductors. *Proceedings of the National Academy of Sciences*, 110(30):12235, 2013.

[109] Susanne Stemmer and S James Allen. Non-fermi liquids in oxide heterostructures. *Reports on Progress in Physics*, 81(6):062502, 2018.

[110] Jialu Wang, Jing Wu, Tao Wang, Zhuokai Xu, Jifeng Wu, Wanghua Hu, Zhi Ren, Shi Liu, Kamran Behnia, and Xiao Lin. T-square resistivity without umklapp scattering in dilute metallic bi2o2se. *Nature Communications*, 11(1):3846, 2020.

[111] Mathieu Mirjolet, Francisco Rivadulla, Premysl Marsik, Vladislav Borisov, Roser Valentí, and Josep Fontcuberta. Electron–phonon coupling and electron–phonon scattering in srvo3. *Advanced Science*, 8(15):2004207, 2021.

[112] Kamran Behnia. On the origin and the amplitude of t-square resistivity in fermi liquids. *Annalen der Physik*, 534(5):2100588, 2022.

[113] Andrea Damascelli, Zahid Hussain, and Zhi-Xun Shen. Angle-resolved photoemission studies of the cuprate superconductors. *Rev. Mod. Phys.*, 75:473–541, Apr 2003.

[114] Marten Düvel, Marco Merboldt, Jan Philipp Bange, Hannah Strauch, Michael Stellbrink, Klaus Pierz, Hans Werner Schumacher, Davood Momeni, Daniel Steil, G. S. Matthijs Jansen, Sabine Steil, Dino Novko, Stefan Mathias, and Marcel Reutzel. Far-from-equilibrium electron–phonon interactions in optically excited graphene. *Nano Letters*, 22(12):4897, 2022.

[115] Philip B. Allen. Neutron spectroscopy of superconductors. *Phys. Rev. B*, 6:2577, Oct 1972.

[116] W. L. McMillan. Transition temperature of strong-coupled superconductors. *Phys. Rev.*, 167:331–344, Mar 1968.

[117] K.-P. Bohnen, R. Heid, and B. Renker. Phonon dispersion and electron-phonon coupling in mgb_2 and alb_2. *Phys. Rev. Lett.*, 86:5771–5774, Jun 2001.

[118] J. Kortus, I. I. Mazin, K. D. Belashchenko, V. P. Antropov, and L. L. Boyer. Superconductivity of metallic boron in mgb_2. *Phys. Rev. Lett.*, 86:4656–4659, May 2001.

[119] Amy Y. Liu, I. I. Mazin, and Jens Kortus. Beyond eliashberg superconductivity in mgb_2: Anharmonicity, two-phonon scattering, and multiple gaps. *Phys. Rev. Lett.*, 87:087005, Aug 2001.

[120] T. Yildirim, O. Gülseren, J. W. Lynn, C. M. Brown, T. J. Udovic, Q. Huang, N. Rogado, K. A. Regan, M. A. Hayward, J. S. Slusky, T. He, M. K. Haas, P. Khalifah, K. Inumaru, and R. J. Cava. Giant anharmonicity and nonlinear electron-phonon coupling in mgb_2: A combined first-principles calculation and neutron scattering study. *Phys. Rev. Lett.*, 87:037001, Jun 2001.

[121] Asier Eiguren and Claudia Ambrosch-Draxl. Wannier interpolation scheme for phonon-induced potentials: Application to bulk mgb_2, w, and the (1×1) h-covered w(110) surface. *Phys. Rev. B*, 78:045124, Jul 2008.

[122] E. R. Margine and F. Giustino. Anisotropic migdal-eliashberg theory using wannier functions. *Phys. Rev. B*, 87:024505, Jan 2013.

[123] E. A. Ekimov, V. A. Sidorov, E. D. Bauer, N. N. Mel'nik, N. J. Curro, J. D. Thompson, and S. M. Stishov. Superconductivity in diamond. *Nature*, 428(6982):542, Apr 2004.

[124] Lilia Boeri, Jens Kortus, and O. K. Andersen. Three-dimensional mgb_2-type superconductivity in hole-doped diamond. *Phys. Rev. Lett.*, 93:237002, Nov 2004.

[125] H. J. Xiang, Zhenyu Li, Jinlong Yang, J. G. Hou, and Qingshi Zhu. Electron-phonon coupling in a boron-doped diamond superconductor. *Phys. Rev. B*, 70:212504, Dec 2004.

[126] Feliciano Giustino, Jonathan R. Yates, Ivo Souza, Marvin L. Cohen, and Steven G. Louie. Electron-phonon interaction via electronic and lattice wannier functions: Superconductivity in boron-doped diamond reexamined. *Phys. Rev. Lett.*, 98:047005, Jan 2007.

[127] E. R. Margine and Feliciano Giustino. Two-gap superconductivity in heavily *n*-doped graphene: Ab initio migdal-eliashberg theory. *Phys. Rev. B*, 90:014518, Jul 2014.

[128] B. M. Ludbrook, G. Levy, P. Nigge, M. Zonno, M. Schneider, D. J. Dvorak, C. N. Veenstra, S. Zhdanovich, D. Wong, P. Dosanjh, C. Straßer, A. Stöhr, S. Forti, C. R. Ast, U. Starke, and A. Damascelli. Evidence for superconductivity in li-decorated monolayer graphene. *Proceedings of the National Academy of Sciences*, 112(38):11795, 2015.

[129] Satoru Ichinokura, Katsuaki Sugawara, Akari Takayama, Takashi Takahashi, and Shuji Hasegawa. Superconducting calcium-intercalated bilayer graphene. *ACS Nano*, 10(2):2761, 2016.

[130] G. Savini, A. C. Ferrari, and Feliciano Giustino. First-principles prediction of doped graphane as a high-temperature electron-phonon superconductor. *Phys. Rev. Lett.*, 105:037002, Jul 2010.

[131] J. T. Ye, Y. J. Zhang, R. Akashi, M. S. Bahramy, R. Arita, and Y. Iwasa. Superconducting dome in a gate-tuned band insulator. *Science*, 338(6111):1193, 2012.

[132] Yizhi Ge and Amy Y. Liu. Phonon-mediated superconductivity in electron-doped single-layer mos_2: A first-principles prediction. *Phys. Rev. B*, 87:241408, Jun 2013.

[133] M. Rösner, S. Haas, and T. O. Wehling. Phase diagram of electron-doped dichalcogenides. *Phys. Rev. B*, 90:245105, Dec 2014.

[134] Davide Costanzo, Sanghyun Jo, Helmuth Berger, and Alberto F. Morpurgo. Gate-induced superconductivity in atomically thin mos2 crystals. *Nature Nanotechnology*, 11(4):339, Apr 2016.

[135] Yajun Fu, Erfu Liu, Hongtao Yuan, Peizhe Tang, Biao Lian, Gang Xu, Junwen Zeng, Zhuoyu Chen, Yaojia Wang, Wei Zhou, Kang Xu, Anyuan Gao, Chen Pan, Miao Wang, Baigeng Wang, Shou-Cheng Zhang, Yi Cui, Harold Y. Hwang, and Feng Miao. Gated tuned superconductivity and phonon softening in monolayer and bilayer mos2. *npj Quantum Materials*, 2(1):52, Sep 2017.

[136] Erik Piatti, Domenico De Fazio, Dario Daghero, Srinivasa Reddy Tamalampudi, Duhee Yoon, Andrea C. Ferrari, and Renato S. Gonnelli. Multi-valley superconductivity in ion-gated mos_2 layers. *Nano Letters*, 18(8):4821, 2018.

[137] Peio Garcia-Goiricelaya, Jon Lafuente-Bartolome, Idoia G. Gurtubay, and Asier Eiguren. Long-living carriers in a strong electron–phonon interacting two-dimensional doped semiconductor. *Communications Physics*, 2(1):81, Jul 2019.

[138] Xin Kong, Miao Gao, Xun-Wang Yan, Zhong-Yi Lu, and Tao Xiang. Superconductivity in electron-doped arsenene. *Chinese Physics B*, 27(4):046301, apr 2018.

[139] A. V. Lugovskoi, M. I. Katsnelson, and A. N. Rudenko. Strong electron-phonon coupling and its influence on the transport and optical properties of hole-doped single-layer inse. *Phys. Rev. Lett.*, 123:176401, Oct 2019.

[140] Mohammad Alidoosti, Davoud Nasr Esfahani, and Reza Asgari. Charge density wave and superconducting phase in monolayer inse. *Phys. Rev. B*, 103:035411, Jan 2021.

[141] Ebrahim Sajadi, Tauno Palomaki, Zaiyao Fei, Wenjin Zhao, Philip Bement, Christian Olsen, Silvia Luescher, Xiaodong Xu, Joshua A. Folk, and David H. Cobden. Gate-induced superconductivity in a monolayer topological insulator. *Science*, 362(6417):922, 2018.

[142] Wei Yang, Chong-Jie Mo, Shi-Bin Fu, Yu Yang, Fa-Wei Zheng, Xiao-Hui Wang, Yuan-An Liu, Ning Hao, and Ping Zhang. Soft-mode-phonon-mediated unconventional superconductivity in monolayer $1t^{'}-wte_2$. *Phys. Rev. Lett.*, 125:237006, Dec 2020.

[143] D. R. Hamann. Optimized norm-conserving vanderbilt pseudopotentials. *Phys. Rev. B*, 88:085117, Aug 2013.

[144] Valerio Vitale, Giovanni Pizzi, Antimo Marrazzo, Jonathan R. Yates, Nicola Marzari, and Arash A. Mostofi. Automated high-throughput wannierisation. *npj Computational Materials*, 6(1):66, 2020.

[145] Nina Girotto and Dino Novko. Dynamical renormalization of electron-phonon coupling in conventional superconductors. *Phys. Rev. B*, 107:064310, Feb 2023.

[146] M. D. Johannes, I. I. Mazin, and C. A. Howells. Fermi-surface nesting and the origin of the charge-density wave in $Nbse_2$. *Phys. Rev. B*, 73:205102, May 2006.

[147] Qixing Wang, Yu Li Huang, Qi Zhang, Jiayu Ma, Xin Luo, and Yun-Mei Li. Self-energy corrections to zone-edge acoustic phonons in monolayer and bilayer ws_2. *Phys. Rev. B*, 109:L121202, Mar 2024.

[148] P. B. Allen. Electron-phonon effects in the infrared properties of metals. *Phys. Rev. B*, 3:305, Jan 1971.

[149] Dino Novko. Dopant-induced plasmon decay in graphene. *Nano Letters*, 17(11):6991, 2017.

[150] P. B. Allen and R. C. Dynes. Transition temperature of strong-coupled superconductors reanalyzed. *Phys. Rev. B*, 12:905, Aug 1975.

[151] Yoshikuni Kaga, Philipp Werner, and Shintaro Hoshino. Eliashberg theory of the jahn-teller-hubbard model. *Phys. Rev. B*, 105:214516, Jun 2022.

[152] Cunyuan Jiang, Enrico Beneduce, Matteo Baggioli, Chandan Setty, and Alessio Zaccone. Sharp kohn-like phonon anomalies due to charge order can strongly enhance the superconducting t_c. *arXiv*, 2022.

[153] Hyoung Joon Choi, David Roundy, Hong Sun, Marvin L. Cohen, and Steven G. Louie. First-principles calculation of the superconducting transition in mgb_2 within the anisotropic eliashberg formalism. *Phys. Rev. B*, 66:020513, Jul 2002.

[154] A. Floris, G. Profeta, N. N. Lathiotakis, M. Lüders, M. A. L. Marques, C. Franchini, E. K. U. Gross, A. Continenza, and S. Massidda. Superconducting properties of mgb_2 from first principles. *Phys. Rev. Lett.*, 94:037004, Jan 2005.

[155] E. Cappelluti, S. Ciuchi, C. Grimaldi, L. Pietronero, and S. Strässler. High T_c superconductivity in mgb_2 by nonadiabatic pairing. *Phys. Rev. Lett.*, 88:117003, Mar 2002.

[156] Ville J. Härkönen, Robert van Leeuwen, and E. K. U. Gross. Many-body green's function theory of electrons and nuclei beyond the born-oppenheimer approximation. *Phys. Rev. B*, 101:235153, Jun 2020.

[157] Carla Verdi, Fabio Caruso, and Feliciano Giustino. Origin of the crossover from polarons to fermi liquids in transition metal oxides. *Nature Communications*, 8(1), jun 2017.

[158] Thomas Bauer and Claus Falter. Impact of dynamical screening on the phonon dynamics of metallic la_2cuo_4. *Phys. Rev. B*, 80:094525, Sep 2009.

[159] J. Krsnik and O. S. Barišić. Importance of coupling strength in shaping electron energy loss and phonon spectra of phonon-plasmon systems. *Phys. Rev. B*, 106:075207, Aug 2022.

[160] I. Kupčić. General theory of intraband relaxation processes in heavily doped graphene. *Phys. Rev. B*, 91:205428, May 2015.

[161] B. Chakraborty, W. E. Pickett, and P. B. Allen. Density of states, optical mass, and dc electrical resistance of ta, w, nb, and mo using slater-koster interpolation. *Phys. Rev. B*, 14:3227, Oct 1976.

[162] Göran Grimvall. New aspects on the electron-phonon system at finite temperatures with an application on lead and mercury. *Physik der Kondensierten Materie*, 9(3):283, jul 1969.

[163] Philip B. Allen and Marvin L. Cohen. Calculation of the temperature dependence of the electron-phonon mass enhancement. *Phys. Rev. B*, 1:1329–1336, Feb 1970.

[164] John M Rowell. The widely variable resistivity of mgb2 samples. *Superconductor Science and Technology*, 16(6):R17, apr 2003.

[165] S. James Allen, Bharat Jalan, SungBin Lee, Daniel G. Ouellette, Guru Khalsa, Jan Jaroszynski, Susanne Stemmer, and Allan H. MacDonald. Conduction-band edge and shubnikov–de haas effect in low-electron-density $srtio_3$. *Phys. Rev. B*, 88:045114, Jul 2013.

[166] J. L. M. van Mechelen, D. van der Marel, C. Grimaldi, A. B. Kuzmenko, N. P. Armitage, N. Reyren, H. Hagemann, and I. I. Mazin. Electron-phonon interaction and charge carrier mass enhancement in $srtio_3$. *Phys. Rev. Lett.*, 100:226403, Jun 2008.

[167] Marios Zacharias, Matthias Scheffler, and Christian Carbogno. Fully anharmonic nonperturbative theory of vibronically renormalized electronic band structures. *Phys. Rev. B*, 102:045126, Jul 2020.

[168] J. Appel. Role of thermal phonons in high-temperature superconductivity. *Phys. Rev. Lett.*, 21:1164, Oct 1968.

[169] Warren E. Pickett. Effect of a varying density of states on superconductivity. *Phys. Rev. B*, 21:3897–3901, May 1980.

[170] A. H. MacDonald. Electron-phonon enhancement of electron-electron scattering in al. *Phys. Rev. Lett.*, 44:489–493, Feb 1980.

[171] A. H. Thompson. Electron-electron scattering in tis_2. *Phys. Rev. Lett.*, 35:1786, Dec 1975.

[172] J. R. Wallbank, R. Krishna Kumar, M. Holwill, Z. Wang, G. H. Auton, J. Birkbeck, A. Mishchenko, L. A. Ponomarenko, K. Watanabe, T. Taniguchi, K. S. Novoselov, I. L. Aleiner, A. K. Geim, and V. I. Fal'ko. Excess resistivity in graphene superlattices caused by umklapp electron–electron scattering. *Nature Physics*, 15(1):32–36, oct 2018.

[173] Alexandre Jaoui, Ipsita Das, Giorgio Di Battista, Jaime Díez-Mérida, Xiaobo Lu, Kenji Watanabe, Takashi Taniguchi, Hiroaki Ishizuka, Leonid Levitov, and Dmitri K. Efetov. Quantum critical behaviour in magic-angle twisted bilayer graphene. *Nature Physics*, 18(6):633, 2022.

[174] Young Woo Choi and Hyoung Joon Choi. Strong electron-phonon coupling, electron-hole asymmetry, and nonadiabaticity in magic-angle twisted bilayer graphene. *Phys. Rev. B*, 98:241412, Dec 2018.

[175] Young Woo Choi and Hyoung Joon Choi. Dichotomy of electron-phonon coupling in graphene moiré flat bands. *Phys. Rev. Lett.*, 127:167001, Oct 2021.

[176] Mohammad Alidoosti, Davoud Nasr Esfahani, and Reza Asgari. Superconducting properties of doped blue phosphorene: effects of non-adiabatic approach. *2D Materials*, 9(4):045029, sep 2022.

[177] Dino Novko, Zahra Torbatian, and Ivor Lončarić. Electron correlations rule the phonon-driven instability in single-layer $tise_2$. *Phys. Rev. B*, 106:245108, Dec 2022.

[178] Tae Yun Kim, Cheol-Hwan Park, and Nicola Marzari. The electronic thermal conductivity of graphene. *Nano Letters*, 16(4):2439, 2016.

[179] Chenglong Zhang, Zhujun Yuan, Su-Yang Xu, Ziquan Lin, Bingbing Tong, M. Zahid Hasan, Junfeng Wang, Chi Zhang, and Shuang Jia. Tantalum monoarsenide: an exotic compensated semimetal. 02 2015.

[180] Xin Lu, Xin Luo, Jun Zhang, Su Quek, and Qihua Xiong. Lattice vibrations and raman scattering in two-dimensional layered materials beyond graphene. *Nano Research*, 9, 09 2016.

[181] P. H. Tan, W. P. Han, W. J. Zhao, Z. H. Wu, K. Chang, H. Wang, Y. F. Wang, N. Bonini, N. Marzari, N. Pugno, G. Savini, A. Lombardo, and A. C. Ferrari. The shear mode of multilayer graphene. *Nature Materials*, 11(4):294–300, February 2012.

[182] Yanyuan Zhao, Xin Luo, Hai Li, Jun Zhang, Paulo Araujo, C. Gan, Jumiati Wu, Hua Zhang, Su Quek, Mildred Dresselhaus, and Qihua Xiong. Inter layer breathing and shear modes in few-trilayer mos2 and wse2. *Nano letters*, 13, 03 2013.

[183] Andrea Ferrari and Denis Basko. Raman spectroscopy as a versatile tool for studying the properties of graphene. *Nature nanotechnology*, 8:235–46, 04 2013.

[184] Cong Xin, Liu Xuelu, Miao-Ling Lin, and Ping-Heng Tan. Application of raman spectroscopy to probe fundamental properties of two-dimensional materials. *npj 2D Materials and Applications*, 4, 12 2020.

[185] A Das, S. Pisana, Biswanath Chakraborty, S Piscanec, S Saha, Umesh Waghmare, K Novoselov, H. Krishnamurthy, A.K. Geim, A.C. Ferrari, and A. Sood. Monitoring dopants by raman scattering in an electrochemically top-gated graphene transistor. *Nature nanotechnology*, 3:210–5, 04 2008.

[186] P.M Rafailov, M Dworzak, and C Thomsen. Luminescence and raman spectroscopy on mgb2. *Solid State Communications*, 122(7):455–458, 2002.

[187] Duhee Yoon, Dongchan Jeong, Hu-Jong Lee, Riichiro Saito, Young-Woo Son, Hyun Cheol Lee, and Hyeonsik Cheong. Fano resonance in raman scattering of graphene. *Carbon*, 61:373–378, 2013.

[188] Qing-Hai Tan, Yu-Jia Sun, Xue-Lu Liu, Yanyuan Zhao, Qihua Xiong, Ping-Heng Tan, and Jun Zhang. Observation of forbidden phonons, fano resonance and dark excitons by resonance raman scattering in few-layer ws2. *2D Materials*, 4(3):031007, jul 2017.

[189] D. Chen, Y.-L. Jia, T.-T. Zhang, Z. Fang, K. Jin, P. Richard, and H. Ding. Raman study of electron-phonon coupling in thin films of the spinel oxide superconductor $liti_2o_4$. *Phys. Rev. B*, 96:094501, Sep 2017.

[190] Suvodeep Paul, Saheb Karak, Annie Mathew, Ankita Ram, and Surajit Saha. Electron-phonon and phonon-phonon anharmonic interactions in $2h-\mathrm{Mo}X_2$ ($x = \mathrm{S}, \mathrm{Te}$): A comprehensive resonant raman study. *Phys. Rev. B*, 104:075418, Aug 2021.

[191] S. Linas, Y. Magnin, B. Poinsot, O. Boisron, G. D. Förster, V. Martinez, R. Fulcrand, F. Tournus, V. Dupuis, F. Rabilloud, L. Bardotti, Z. Han, D. Kalita, V. Bouchiat, and F. Calvo. Interplay between raman shift and thermal expansion in graphene: Temperature-dependent measurements and analysis of substrate corrections. *Phys. Rev. B*, 91:075426, Feb 2015.

[192] I Calizo, Alexander Balandin, Wenzhong Bao, Feng Miao, and Jeanie Lau. Temperature dependence of the raman spectra of graphene and graphene multilayers. *Nano letters*, 7:2645–9, 10 2007.

[193] P R Shaina, Lijin George, Vani Yadav, and Manu Jaiswal. Estimating the thermal expansion coefficient of graphene: the role of graphene–substrate interactions. *Journal of Physics: Condensed Matter*, 28(8):085301, jan 2016.

[194] Duhee Yoon, Young-Woo Son, and Hyeonsik Cheong. Negative thermal expansion coefficient of graphene measured by raman spectroscopy. *Nano letters*, 11:3227–31, 08 2011.

[195] Shibing Tian, Yang Yang, Zhe Liu, Chao Wang, Ruhao Pan, Changzhi Gu, and Junjie Li. Temperature-dependent raman investigation on suspended graphene: Contribution from thermal expansion coefficient mismatch between graphene and substrate. *Carbon*, 104:27–32, 2016.

[196] Ya-Rong Lee, Jianbing Huang, J.-C. Lin, and Jia-Ren Lee. Study of the substrate-induced strain of the as-grown graphene on cu(100) using temperature-dependent raman spectroscopy: Estimating the mode-gruneisen parameter with temperature. *Journal of Physical Chemistry C*, 121:27427–27436, 2017.

[197] A. C. Ferrari, J. C. Meyer, V. Scardaci, C. Casiraghi, M. Lazzeri, F. Mauri, S. Piscanec, D. Jiang, K. S. Novoselov, S. Roth, and A. K. Geim. Raman spectrum of graphene and graphene layers. *Phys. Rev. Lett.*, 97:187401, Oct 2006.

[198] F. Tuinstra and J. L. Koenig. Raman spectrum of graphite. *J. Chem. Phys*, 53:1126–1130, 1970.

[199] N.J Everall, J Lumsdon, and D.J Christopher. The effect of laser-induced heating upon the vibrational raman spectra of graphites and carbon fibres. *Carbon*, 29(2):133–137, 1991.

[200] PingHeng Tan, YuanMing Deng, Qian Zhao, and WenChao Cheng. The intrinsic temperature effect of the raman spectra of graphite. *Appl. Phys. Lett.*, 74:1818–1820, 1999.

[201] J. Sonntag, K. Watanabe, T. Taniguchi, B. Beschoten, and C. Stampfer. Charge carrier density dependent raman spectra of graphene encapsulated in hexagonal boron nitride. *Phys. Rev. B*, 107:075420, Feb 2023.

[202] H.-N. Liu, X. Cong, M.-L. Lin, and P.-H. Tan. The intrinsic temperature-dependent raman spectra of graphite in the temperature range from 4k to 1000k. *Carbon*, 152:451–458, 2019.

[203] J. Hlinka, I. Gregora, J. Pokorny, C. Hérold, N. Emery, J. F. Marêché, and P. Lagrange. Lattice dynamics of cac_6 by raman spectroscopy. *Phys. Rev. B*, 76:144512, Oct 2007.

[204] J. C. Chacón-Torres, A. Y. Ganin, M. J. Rosseinsky, and T. Pichler. Raman response of stage-1 graphite intercalation compounds revisited. *Phys. Rev. B*, 86:075406, Aug 2012.

[205] Zherui Han, Xiaolong Yang, Sean E. Sullivan, Tianli Feng, Li Shi, Wu Li, and Xiulin Ruan. Raman linewidth contributions from four-phonon and electron-phonon interactions in graphene. *Phys. Rev. Lett.*, 128:045901, Jan 2022.

[206] Dong-Hun Chae, Benjamin Krauss, Klaus Klitzing, and Jurgen Smet. Hot phonons in an electrically biased graphene constriction. *Nano letters*, 10:466–71, 02 2010.

[207] Nicola Bonini, Michele Lazzeri, Nicola Marzari, and Francesco Mauri. Phonon anharmonicities in graphite and graphene. *Phys. Rev. Lett.*, 99:176802, Oct 2007.

[208] G. Montagnac, R. Caracas, E. Bobocioiu, F. Vittoz, and B. Reynard. Anharmonicity of graphite from uv raman spectroscopy to 2700k. *Carbon*, 54:68–75, 2013.

[209] X. Chen, M.-L. Lin, X. Cong, Y.-C. Leng, X. Zhang, and P.-H. Tan. Intrinsic phonon anharmonicity in heavily doped graphene probed by raman spectroscopy. *Carbon*, 185:282–288, 2021.

[210] P. Giura, N. Bonini, G. Creff, J. B. Brubach, P. Roy, and M. Lazzeri. Temperature evolution of infrared- and raman-active phonons in graphite. *Phys. Rev. B*, 86:121404, Sep 2012.

[211] Tsuneya Ando. Anomaly of optical phonon in monolayer graphene. *Journal of the Physical Society of Japan*, 75(12):124701, 2006.

[212] Xue Chen, Sven Reichardt, Miao-Ling Lin, Yu-Chen Leng, Yan Lu, Heng Wu, Rui Mei, Ludger Wirtz, Xin Zhang, Andrea C. Ferrari, and Ping-Heng Tan. Control of raman scattering quantum interference pathways in graphene. *ACS Nano*, 17(6):5956–5962, 2023. PMID: 36897053.

[213] Yu. S. Ponosov, I. Loa, V. E. Mogilenskikh, and K. Syassen. Raman scattering in osmium under pressure. *Phys. Rev. B*, 71:220301, Jun 2005.

[214] D. Novko, M. Alducin, M. Blanco-Rey, and J. I. Juaristi. Effects of electronic relaxation processes on vibrational linewidths of adsorbates on surfaces: The case of co/cu(100). *Phys. Rev. B*, 94:224306, Dec 2016.

[215] Raúl Bombín, A. S. Muzas, Dino Novko, J. Iñaki Juaristi, and Maite Alducin. Anomalous transient blueshift in the internal stretch mode of co/pd(111). *Phys. Rev. B*, 107:L121404, Mar 2023.

[216] Ivan Kupić and Slaven Barǐsić. Optical properties of the q1d multiband models – the transverse equation of motion approach. *arXiv: Strongly Correlated Electrons*, 2005.

[217] Anton N. Knigavko, Jules P. Carbotte, and Frank Marsiglio. Observation of phonon structure in electron density of states of a normal metal. *EPL*, 71:776–782, 2005.

[218] I. Kupčić. Intraband memory function and memory-function conductivity formula in doped graphene. *Phys. Rev. B*, 95:035403, Jan 2017.

[219] Philip B. Allen. Electron self-energy and generalized drude formula for infrared conductivity of metals. *Phys. Rev. B*, 92:054305, Aug 2015.

[220] B. Chakraborty and P. B. Allen. Solids with thermal or static disorder. ii. optical properties. *Phys. Rev. B*, 18:5225–5235, Nov 1978.

[221] Ivan Kupčić. Raman spectroscopy of collective modes in charge-density-wave systems: The mean-field microscopic theory. *Journal of Raman Spectroscopy*, 40:442 – 452, 11 2008.

[222] T. Holstein. Theory of transport phenomena in an electron-phonon gas. *Annals of Physics*, 29(3):410–535, 1964.

[223] Gianni Profeta, Matteo Calandra, and Francesco Mauri. Phonon-mediated superconductivity in graphene by lithium deposition. *Nature Physics*, 8(2):131, Feb 2012.

[224] Thomas E. Weller, Mark Ellerby, Siddharth S. Saxena, Robert P. Smith, and Neal T. Skipper. Superconductivity in the intercalated graphite compounds c6yb and c6ca. *Nature Physics*, 1(1):39, Oct 2005.

[225] Matteo Calandra and Francesco Mauri. Theoretical explanation of superconductivity in c_6Ca. *Phys. Rev. Lett.*, 95:237002, Nov 2005.

[226] F. Marsiglio, R. Akis, and J. P. Carbotte. Phonon self-energy effects due to superconductivity: A real-axis formulation. *Phys. Rev. B*, 45:9865–9871, May 1992.

[227] A V Puchkov, D N Basov, and T Timusk. The pseudogap state in high- superconductors: an infrared study. *Journal of Physics: Condensed Matter*, 8(48):10049, nov 1996.

[228] J Carbotte, E. Schachinger, and D Basov. Coupling strength of charge carriers to spin fluctuations in high-temperature superconductors. *Nature*, 401:354–6, 10 1999.

[229] F. Marsiglio, T. Startseva, and J.P. Carbotte. Inversion of k3c60 reflectance data. *Physics Letters A*, 245(1):172–176, 1998.

[230] Warren E. Pickett. Generalization of the theory of the electron-phonon interaction: Thermodynamic formulation of superconducting- and normal-state properties. *Phys. Rev. B*, 26:1186–1207, Aug 1982.

[231] Boidar Mitrović and Jules P. Carbotte. Effects of energy dependence in the electronic density of states on some normal state properties. *Canadian Journal of Physics*, 61:758–783, 1983.

[232] Yu.S. Ponosov, C. Thomsen, and M. Cardona. Electronic raman scattering and phonon self-energy effects in osmium. *Physica C: Superconductivity*, 235-240:1153–1154, 1994.

[233] Raffaello Bianco and Ion Errea. Non-perturbative theory of the electron-phonon coupling and its first-principles implementation. 2023.

[234] B. Mitrović and M. A. Fiorucci. Effects of energy dependence in the electronic density of states on the far-infrared absorption in superconductors. *Phys. Rev. B*, 31:2694–2699, Mar 1985.

[235] J. P. Carbotte, E. J. Nicol, and S. G. Sharapov. Effect of electron-phonon interaction on spectroscopies in graphene. *Phys. Rev. B*, 81:045419, Jan 2010.

[236] L. Pietronero, S. Strässler, and C. Grimaldi. Nonadiabatic superconductivity. i. vertex corrections for the electron-phonon interactions. *Phys. Rev. B*, 52:10516–10529, Oct 1995.

[237] E. Cappelluti and L. Pietronero. Nonadiabatic superconductivity: The role of van hove singularities. *Phys. Rev. B*, 53:932–944, Jan 1996.

[238] K. Itai. Theory of raman scattering in coupled electron-phonon systems. *Phys. Rev. B*, 45:707–717, Jan 1992.

[239] Johannes Bauer, Jong E. Han, and Olle Gunnarsson. Quantitative reliability study of the migdal-eliashberg theory for strong electron-phonon coupling in superconductors. *Phys. Rev. B*, 84:184531, Nov 2011.

[240] Bitan Roy, Jay D. Sau, and S. Das Sarma. Migdal's theorem and electron-phonon vertex corrections in dirac materials. *Phys. Rev. B*, 89:165119, Apr 2014.

[241] R. Car and M. Parrinello. Unified approach for molecular dynamics and density-functional theory. *Phys. Rev. Lett.*, 55:2471–2474, Nov 1985.

[242] D. M. Ceperley. Path integrals in the theory of condensed helium. *Rev. Mod. Phys.*, 67:279–355, Apr 1995.

[243] Lorenzo Monacelli, Raffaello Bianco, Marco Cherubini, Matteo Calandra, Ion Errea, and Francesco Mauri. The stochastic self-consistent harmonic approximation: calculating vibrational properties of materials with full quantum and anharmonic effects. *Journal of Physics: Condensed Matter*, 33(36):363001, jul 2021.

[244] Ion Errea, Matteo Calandra, and Francesco Mauri. Anharmonic free energies and phonon dispersions from the stochastic self-consistent harmonic approximation: Application to platinum and palladium hydrides. *Phys. Rev. B*, 89:064302, Feb 2014.

[245] Raffaello Bianco, Ion Errea, Lorenzo Paulatto, Matteo Calandra, and Francesco Mauri. Second-order structural phase transitions, free energy curvature, and temperature-dependent anharmonic phonons in the self-consistent harmonic approximation: Theory and stochastic implementation. *Phys. Rev. B*, 96:014111, Jul 2017.

[246] Patrick Rowe, Gábor Csányi, Dario Alfè, and Angelos Michaelides. Development of a machine learning potential for graphene. *Phys. Rev. B*, 97:054303, Feb 2018.

[247] Antoine Tiberj, Miguel Rubio-Roy, Matthieu Paillet, Jean Roch Huntzinger, Périne Landois, Mirko Mikolasek, Sylvie Contreras, Jean Louis Sauvajol, Erik Dujardin, and Ahmed Azmi Zahab. Reversible optical doping of graphene. *Scientific Reports*, 3, 2013.

[248] Jennifer Coulter, Gavin B. Osterhoudt, Christina A. C. Garcia, Yiping Wang, Vincent M. Plisson, Bing Shen, Ni Ni, Kenneth S. Burch, and Prineha Narang. Uncovering electron-phonon scattering and phonon dynamics in type-i weyl semimetals. *Phys. Rev. B*, 100:220301, Dec 2019.

[249] C. M. Varma and A. L. Simons. Strong-coupling theory of charge-density-wave transitions. *Phys. Rev. Lett.*, 51:138, Jul 1983.

[250] N. P. Armitage, E. J. Mele, and Ashvin Vishwanath. Weyl and dirac semimetals in three-dimensional solids. *Rev. Mod. Phys.*, 90:015001, Jan 2018.

[251] Xiangang Wan, Ari M. Turner, Ashvin Vishwanath, and Sergey Y. Savrasov. Topological semimetal and fermi-arc surface states in the electronic structure of pyrochlore iridates. *Phys. Rev. B*, 83:205101, May 2011.

[252] Hongming Weng, Chen Fang, Zhong Fang, B. Andrei Bernevig, and Xi Dai. Weyl semimetal phase in noncentrosymmetric transition-metal monophosphides. *Phys. Rev. X*, 5:011029, Mar 2015.

[253] N. Xu, Hongming Weng, B. Lv, Christian Matt, J. Park, Federico Bisti, V. Strocov, Dariusz Gawryluk, Ekaterina Pomjakushina, K. Conder, Nicholas Plumb, Milan Radovic, Gabriel Autès, Oleg Yazyev, Zanxi Fang, Xianzhu Dai, Tan Qian, J. Mesot, Hanjie Ding, and Ming Shi. Observation of weyl nodes and fermi arcs in tantalum phosphide. *Nature Communications*, 7:11006, 03 2016.

[254] Su-Yang Xu, Ilya Belopolski, Daniel S. Sanchez, Chenglong Zhang, Guoqing Chang, Cheng Guo, Guang Bian, Zhujun Yuan, Hong Lu, Tay-Rong Chang, Pavel P. Shibayev, Mykhailo L. Prokopovych, Nasser Alidoust, Hao Zheng, Chi-Cheng Lee, Shin-Ming Huang, Raman Sankar, Fangcheng Chou, Chuang-Han Hsu, Horng-Tay Jeng, Arun Bansil, Titus Neupert, Vladimir N. Strocov, Hsin Lin, Shuang Jia, and M. Zahid Hasan. Experimental discovery of a topological weyl semimetal state in tap. *Science Advances*, 1(10):e1501092, 2015.

[255] Shin-Ming Huang, Su-Yang Xu, Ilya Belopolski, Chi-Cheng Lee, Guoqing Chang, Baokai Wang, Nasser Alidoust, Guang Bian, Madhab Neupane, Chenglong Zhang, Shuang Jia, Arun Bansil, Hsin Lin, and M. Zahid Hasan. A weyl fermion semimetal with surface fermi arcs in the transition metal monopnictide taas class. *Nature Communications*, 6:7373, 06 2015.

[256] Baiqing Lv, Baiqing Lv, Nan Xu, Nan Xu, Hongming Weng, Junzhang Ma, Junzhang Ma, Pierre Richard, Xiaochun Huang, Lingxiao Zhao, Genfu Chen, Christian E. Matt, Federico Bisti, Vladimir N. Strocov, Joël Mésot, Joël Mésot, Joël Mésot, Zhong Fang, Xi Dai, Tian Qian, Ming Shi, and Hong Ding. Observation of weyl nodes in taas. *Nature Physics*, 11:724 – 727, 2015.

[257] Su-Yang Xu, Ilya Belopolski, Nasser Alidoust, Madhab Neupane, Guang Bian, Chenglong Zhang, Raman Sankar, Guoqing Chang, Zhujun Yuan, Chi-Cheng Lee, Shin-Ming Huang, Hao Zheng, Jie Ma, Daniel S. Sanchez, BaoKai Wang, Arun Bansil, Fangcheng Chou, Pavel P. Shibayev, Hsin Lin, Shuang Jia, and M. Zahid Hasan. Discovery of a weyl fermion semimetal and topological fermi arcs. *Science*, 349(6248):613–617, 2015.

[258] B. Q. Lv, H. M. Weng, B. B. Fu, X. P. Wang, H. Miao, J. Ma, P. Richard, X. C. Huang, L. X. Zhao, G. F. Chen, Z. Fang, X. Dai, T. Qian, and H. Ding. Experimental discovery of weyl semimetal taas. *Phys. Rev. X*, 5:031013, Jul 2015.

[259] L. Yang, Z. Liu, Yan Sun, Han Peng, YANG Haifeng, Tao Zhang, Beatrice Zhou, Yi Zhang, Yanfeng Guo, Marein Rahn, D. Prabhakaran, Zahid Hussain, Sung-Kwan Mo, Claudia Felser, Binghai Yan, and Y. Chen. Weyl semimetal phase in the non-centrosymmetric compound taas. *Nature Physics*, 11, 09 2015.

[260] Su-Yang Xu, Nasser Alidoust, Ilya Belopolski, Zhujun Yuan, Guang Bian, Tay-Rong Chang, Hao Zheng, Vladimir Strocov, Daniel Sanchez, Guoqing Chang, Chenglong Zhang, Daixiang Mou, Yun Wu, Lunan Huang, Chi-Cheng Lee, Shin-Ming Huang, Baokai Wang, Arun Bansil, Horng-Tay Jeng, and M. Zahid Hasan. Discovery of a weyl fermion state with fermi arcs in niobium arsenide. *Nature Physics*, 11:748–754, 08 2015.

[261] Vivek Aji. Adler-bell-jackiw anomaly in weyl semimetals: Application to pyrochlore iridates. *Phys. Rev. B*, 85:241101, Jun 2012.

[262] Anton A. Burkov. Chiral anomaly and transport in weyl metals. *Journal of Physics: Condensed Matter*, 27, 2015.

[263] D. T. Son and B. Z. Spivak. Chiral anomaly and classical negative magnetoresistance of weyl metals. *Phys. Rev. B*, 88:104412, Sep 2013.

[264] Phillip E. C. Ashby and J. P. Carbotte. Chiral anomaly and optical absorption in weyl semimetals. *Phys. Rev. B*, 89:245121, Jun 2014.

[265] S. A. Parameswaran, T. Grover, D. A. Abanin, D. A. Pesin, and A. Vishwanath. Probing the chiral anomaly with nonlocal transport in three-dimensional topological semimetals. *Phys. Rev. X*, 4:031035, Sep 2014.

[266] P. Rinkel, P. L. S. Lopes, and Ion Garate. Signatures of the chiral anomaly in phonon dynamics. *Phys. Rev. Lett.*, 119:107401, Sep 2017.

[267] Zhida Song, Jimin Zhao, Zhong Fang, and Xi Dai. Detecting the chiral magnetic effect by lattice dynamics in weyl semimetals. *Phys. Rev. B*, 94:214306, Dec 2016.

[268] Yupeng Li, Zhen Wang, Pengshan Li, Xiaojun Yang, Zhixuan Shen, Feng Sheng, Xiaodong Li, Yunhao Lu, Yi Zheng, and an Zhu. Negative magnetoresistance in weyl semimetals nbas and nbp: Intrinsic chiral anomaly and extrinsic effects. *Frontiers of Physics*, 12, 12 2016.

[269] F. Arnold, M. Naumann, S.-C. Wu, Y. Sun, M. Schmidt, H. Borrmann, C. Felser, B. Yan, and E. Hassinger. Chiral weyl pockets and fermi surface topology of the weyl semimetal taas. *Phys. Rev. Lett.*, 117:146401, Sep 2016.

[270] Yuval Baum, Erez Berg, S. A. Parameswaran, and Ady Stern. Current at a distance and resonant transparency in weyl semimetals. *Phys. Rev. X*, 5:041046, Dec 2015.

[271] Zhong Fang, Naoto Nagaosa, Kei S. Takahashi, Atsushi Asamitsu, Roland Mathieu, Takeshi Ogasawara, Hiroyuki Yamada, Masashi Kawasaki, Yoshinori Tokura, and Kiyoyuki Terakura. The anomalous hall effect and magnetic monopoles in momentum space. *Science*, 302(5642):92–95, 2003.

[272] Di Xiao, Ming-Che Chang, and Qian Niu. Berry phase effects on electronic properties. *Rev. Mod. Phys.*, 82:1959–2007, Jul 2010.

[273] Kai-Yu Yang, Yuan-Ming Lu, and Ying Ran. Quantum hall effects in a weyl semimetal: Possible application in pyrochlore iridates. *Phys. Rev. B*, 84:075129, Aug 2011.

[274] A. A. Burkov and Leon Balents. Weyl semimetal in a topological insulator multilayer. *Phys. Rev. Lett.*, 107:127205, Sep 2011.

[275] A. A. Burkov. Anomalous hall effect in weyl metals. *Phys. Rev. Lett.*, 113:187202, Oct 2014.

[276] Chenglong Zhang, Cheng Guo, Hong Lu, Xiao Zhang, Zhujun Yuan, Ziquan Lin, Junfeng Wang, and Shuang Jia. Large magnetoresistance over an extended temperature regime in monophosphides of tantalum and niobium. *Phys. Rev. B*, 92:041203, Jul 2015.

[277] Chandra Shekhar, Ajaya Nayak, Yan Sun, Marcus Schmidt, M. Nicklas, Inge Leermakers, U. Zeitler, Walter Schnelle, Juri Grin, Claudia Felser, and Binghai Yan. Extremely large magnetoresistance and ultrahigh mobility in the topological weyl semimetal nbp. *Nature Physics*, 11, 02 2015.

[278] B. Xu, Y. M. Dai, L. X. Zhao, K. Wang, R. Yang, W. Zhang, J. Y. Liu, H. Xiao, G. F. Chen, A. J. Taylor, D. A. Yarotski, R. P. Prasankumar, and X. G. Qiu. Optical spectroscopy of the weyl semimetal taas. *Phys. Rev. B*, 93:121110, Mar 2016.

[279] Christina A. C. Garcia, Jennifer Coulter, and Prineha Narang. Optoelectronic response of the type-i weyl semimetals taas and nbas from first principles. *Phys. Rev. Res.*, 2:013073, Jan 2020.

[280] Davide Grassano, Olivia Pulci, Adriano Conte, and Friedhelm Bechstedt. Validity of weyl fermion picture for transition metals monopnictides taas, tap, nbas, and nbp from ab initio studies. *Scientific Reports*, 8, 02 2018.

[281] Chi-Cheng Lee, Su-Yang Xu, Shin-Ming Huang, Daniel S. Sanchez, Ilya Belopolski, Guoqing Chang, Guang Bian, Nasser Alidoust, Hao Zheng, Madhab Neupane, Baokai Wang, Arun Bansil, M. Zahid Hasan, and Hsin Lin. Fermi surface interconnectivity and topology in weyl fermion semimetals taas, tap, nbas, and nbp. *Phys. Rev. B*, 92:235104, Dec 2015.

[282] B. Xu, Yaomin Dai, L. Zhao, K. Wang, Run Yang, Wolke Zhang, J. Liu, Hong Xiao, G. Chen, S. Trugman, Jian-Xin Zhu, A. Taylor, Dzmitry Yarotski, Rohit Prasankumar, and X. Qiu. Temperature-tunable fano resonance induced by strong coupling between weyl fermions and phonons in taas. *Nature Communications*, 8:14933, 04 2017.

[283] H. W. Liu, P. Richard, Z. D. Song, L. X. Zhao, Z. Fang, G.-F. Chen, and H. Ding. Raman study of lattice dynamics in the weyl semimetal taas. *Phys. Rev. B*, 92:064302, Aug 2015.

[284] H W Liu, P Richard, L X Zhao, G-F Chen, and H Ding. Comparative raman study of weyl semimetals taas, nbas, tap and nbp. *Journal of Physics: Condensed Matter*, 28(29):295401, jun 2016.

[285] Shihao Han, Qinghang Tang, Hongmei Yuan, Yufeng Luo, and Huijun Liu. Effects of electron-phonon coupling on the phonon transport properties of the weyl semimetals nbas and taas: A comparative study. *Journal of Materiomics*, 9(3):520–526, 2023.

[286] Gavin B. Osterhoudt, Yaxian Wang, Christina A. C. Garcia, Vincent M. Plisson, Johannes Gooth, Claudia Felser, Prineha Narang, and Kenneth S. Burch. Evidence for dominant phonon-electron scattering in weyl semimetal wp_2. *Phys. Rev. X*, 11:011017, Jan 2021.

[287] A. Sharafeev, V. Gnezdilov, R. Sankar, F. C. Chou, and P. Lemmens. Optical phonon dynamics and electronic fluctuations in the dirac semimetal Cd_3As_2. *Phys. Rev. B*, 95:235148, Jun 2017.

[288] Anmin Zhang, Xiaoli Ma, Changle Liu, Rui Lou, Yimeng Wang, Qiaohe Yu, Yiyan Wang, Tian-long Xia, Shancai Wang, Lei Zhang, Xiaoqun Wang, Changfeng Chen, and Qingming Zhang. Topological phase transition between distinct weyl semimetal states in $mote_2$. *Phys. Rev. B*, 100:201107, Nov 2019.

[289] Guoliang Wan, Wei Yao, Kenan Zhang, Changhua Bao, Hongyun Zhang, Haijun Zhang, Yang Wu, and Shuyun Zhou. Ultrafast electronic dynamics of a weyl semimetal mote$_2$ revealed by time and angle resolved photoemission spectroscopy. *arXiv: Materials Science*, 2017.

[290] Ouyang Tao, Huaping Xiao, Chao Tang, Ming Hu, and Jianxin Zhong. Anisotropic thermal transport in weyl semimetal taas: a first principles calculation. *Physical chemistry chemical physics : PCCP*, 18 25:16709–14, 2016.

[291] Junhong Yu, Jianzhou Zhao, Yangyang Lv, Yadong Han, Zhang Hang, Jinlong Xu, and Jianbo Hu. Anomalous nonequilibrium phonon scattering in the weyl semimetal Wp_2. *Phys. Rev. Res.*, 5:023137, May 2023.

[292] Hung-Yu Yang, Xiaohan Yao, Vincent Plisson, Shirin Mozaffari, Jan P. Scheifers, Aikaterini Flessa Savvidou, Eun Sang Choi, Gregory T. McCandless, Mathieu F. Padlewski, Carsten Putzke, Philip J. W. Moll, Julia Y. Chan, Luis Balicas, Kenneth S. Burch, and Fazel Tafti. Evidence of a coupled electron-phonon liquid in nbge2. *Nature Communications*, 12(1), September 2021.

[293] U. Fano. Effects of configuration interaction on intensities and phase shifts. *Phys. Rev.*, 124:1866–1878, Dec 1961.

[294] Zhenglu Li, Gabriel Antonius, Meng Wu, Felipe H. da Jornada, and Steven G. Louie. Electron-phonon coupling from ab initio linear-response theory within the *gw* method: Correlation-enhanced interactions and superconductivity in $ba_{1-x}k_xbio_3$. *Phys. Rev. Lett.*, 122:186402, May 2019.

[295] Z. P. Yin, A. Kutepov, and G. Kotliar. Correlation-enhanced electron-phonon coupling: Applications of *gw* and screened hybrid functional to bismuthates, chloronitrides, and other high-T_c superconductors. *Phys. Rev. X*, 3:021011, May 2013.

[296] Jin-Jian Zhou, Jinsoo Park, Iurii Timrov, Andrea Floris, Matteo Cococcioni, Nicola Marzari, and Marco Bernardi. Ab initio electron-phonon interactions in correlated electron systems. *Phys. Rev. Lett.*, 127:126404, Sep 2021.

[297] Michael Först, Cristian Manzoni, Stefan Kaiser, Yasuhide Tomioka, Yoshinori Tokura, Roberto Merlin, and Andrea Cavalleri. Nonlinear phononics: A new ultrafast route to lattice control. *Nature Physics*, 7, 01 2011.

[298] H. Petek and S. Ogawa. Femtosecond time-resolved two-photon photoemission studies of electron dynamics in metals. *Progress in Surface Science*, 56(4):239, 1997.

[299] M. Bauer, A. Marienfeld, and M. Aeschlimann. Hot electron lifetimes in metals probed by time-resolved two-photon photoemission. *Progress in Surface Science*, 90(3):319, 2015.

[300] L. Stojchevska, I. Vaskivskyi, T. Mertelj, P. Kusar, D. Svetin, S. Brazovskii, and D. Mihailovic. Ultrafast switching to a stable hidden quantum state in an electronic crystal. *Science*, 344(6180):177, 2014.

[301] Kerstin Haupt, Maximilian Eichberger, Nicolas Erasmus, Andrea Rohwer, Jure Demsar, Kai Rossnagel, and Heinrich Schwoerer. Ultrafast metamorphosis of a complex charge-density wave. *Phys. Rev. Lett.*, 116:016402, Jan 2016.

[302] Anshul Kogar, Alfred Zong, Pavel E. Dolgirev, Xiaozhe Shen, Joshua Straquadine, Ya-Qing Bie, Xirui Wang, Timm Rohwer, I-Cheng Tung, Yafang Yang, Renkai Li, Jie Yang, Stephen Weathersby, Suji Park, Michael E. Kozina, Edbert J. Sie, Haidan Wen, Pablo Jarillo-Herrero, Ian R. Fisher, Xijie Wang, and Nuh Gedik. Light-induced charge density wave in LaTe3. *Nature Physics*, 16(2):159, nov 2020.

[303] Q. M. Liu, D. Wu, Z. A. Li, L. Y. Shi, Z. X. Wang, S. J. Zhang, T. Lin, T. C. Hu, H. F. Tian, J. Q. Li, and et al. Photoinduced multistage phase transitions in ta2nise5. *Nature Communications*, 12(1):2050, apr 2021.

[304] J. Maklar, Y. W. Windsor, C. W. Nicholson, M. Puppin, P. Walmsley, V. Esposito, M. Porer, J. Rittmann, D. Leuenberger, M. Kubli, and et al. Nonequilibrium charge-density-wave order beyond the thermal limit. *Nature Communications*, 12(1):2499, may 2021.

[305] Yingchao Zhang, Xun Shi, Mengxue Guan, Wenjing You, Yigui Zhong, Tika R. Kafle, Yaobo Huang, Hong Ding, Michael Bauer, Kai Rossnagel, and et al. Creation of a novel inverted charge density wave state. *Structural Dynamics*, 9(1):014501, 01 2022.

[306] Yijing Huang, Shan Yang, Samuel Teitelbaum, Gilberto De la Peña, Takahiro Sato, Matthieu Chollet, Diling Zhu, Jennifer L. Niedziela, Dipanshu Bansal, Andrew F. May, and et al. Observation of a novel lattice instability in ultrafast photoexcited snse. *Phys. Rev. X*, 12:011029, Feb 2022.

[307] D. Basov, R. Averitt, and D. Hsieh. Towards properties on demand in quantum materials. *Nature Materials*, 16:1077–1088, 11 2017.

[308] D. Fausti, R. I. Tobey, N. Dean, S. Kaiser, A. Dienst, M. C. Hoffmann, S. Pyon, T. Takayama, H. Takagi, and A. Cavalleri. Light-induced superconductivity in a stripe-ordered cuprate. *Science*, 331(6014):189, 2011.

[309] Wentao Zhang, Choongyu Hwang, Christopher L. Smallwood, Tristan L. Miller, Gregory Affeldt, Koshi Kurashima, Chris Jozwiak, Hiroshi Eisaki, Tadashi Adachi, Yoji Koike, Dung-Hai Lee, and Alessandra Lanzara. Ultrafast quenching of electron–boson interaction and superconducting gap in a cuprate superconductor. *Nature Communications*, 5(1):4959, 2014.

[310] M. Mitrano, A. Cantaluppi, D. Nicoletti, S. Kaiser, A. Perucchi, S. Lupi, P. Di Pietro, D. Pontiroli, M. Riccò, S. R. Clark, D. Jaksch, and A. Cavalleri. Possible light-induced superconductivity in k3c60 at high temperature. *Nature*, 530(7591):461, feb 2016.

[311] Dante M. Kennes, Eli Y. Wilner, David R. Reichman, and Andrew J. Millis. Transient superconductivity from electronic squeezing of optically pumped phonons. *Nature Physics*, 13(5):479, jan 2017.

[312] F. Giusti, A. Marciniak, F. Randi, G. Sparapassi, F. Boschini, H. Eisaki, M. Greven, A. Damascelli, A. Avella, and D. Fausti. Signatures of enhanced superconducting phase coherence in optimally doped $bi_2sr_2y_{0.08}ca_{0.92}cu_2o_{8+\delta}$ driven by midinfrared pulse excitations. *Phys. Rev. Lett.*, 122:067002, Feb 2019.

[313] F. Schmitt, P. S. Kirchmann, U. Bovensiepen, R. G. Moore, L. Rettig, M. Krenz, J.-H. Chu, N. Ru, L. Perfetti, D. H. Lu, and et al. Transient electronic structure and melting of a charge density wave in tbte₃. *Science*, 321(5896):1649, 2008.

[314] Timm Rohwer, Stefan Hellmann, Martin Wiesenmayer, Christian Sohrt, Ankatrin Stange, Bartosz Slomski, Adra Carr, Yanwei Liu, Luis Miaja Avila, Matthias Kalläne, and et al. Collapse of long-range charge order tracked by time-resolved photoemission at high momenta. *Nature*, 471(7339):490, mar 2011.

[315] Shaofeng Duan, Yun Cheng, Wei Xia, Yuanyuan Yang, Chengyang Xu, Fengfeng Qi, Chaozhi Huang, Tianwei Tang, Yanfeng Guo, Weidong Luo, and et al. Optical manipulation of electronic dimensionality in a quantum material. *Nature*, 595(7866):239–244, jul 2021.

[316] Yun Cheng, Alfred Zong, Jun Li, Wei Xia, Shaofeng Duan, Wenxuan Zhao, Yidian Li, Fengfeng Qi, Jun Wu, Lingrong Zhao, and et al. Light-induced dimension crossover dictated by excitonic correlations. *Nature Communications*, 13(1):963, feb 2022.

[317] R. Mankowsky, A. von Hoegen, M. Först, and A. Cavalleri. Ultrafast reversal of the ferroelectric polarization. *Phys. Rev. Lett.*, 118:197601, May 2017.

[318] T. F. Nova, A. S. Disa, M. Fechner, and A. Cavalleri. Metastable ferroelectricity in optically strained srtio3. *Science*, 364(6445):1075, 2019.

[319] Dongbin Shin, Simone Latini, Christian Schäfer, Shunsuke A. Sato, Edoardo Baldini, Umberto De Giovannini, Hannes Hübener, and Angel Rubio. Simulating terahertz field-induced ferroelectricity in quantum paraelectric $srtio_3$. *Phys. Rev. Lett.*, 129:167401, Oct 2022.

[320] Viktor Krapivin, Mingqiang Gu, D. Hickox-Young, S. W. Teitelbaum, Y. Huang, G. de la Peña, D. Zhu, N. Sirica, M.-C. Lee, R. P. Prasankumar, and et al. Ultrafast suppression of the ferroelectric instability in $ktao_3$. *Phys. Rev. Lett.*, 129:127601, Sep 2022.

[321] Chenchen Song, Qing Yang, Xinbao Liu, Hui Zhao, Cui Zhang, and Sheng Meng. Electronic origin of laser-induced ferroelectricity in srtio3. *The Journal of Physical Chemistry Letters*, 14(2):576, 2023.

[322] M. Fechner, M. Först, G. Orenstein, V. Krapivin, A. S. Disa, M. Buzzi, A. von Hoegen, G. de la Pena, Q. L Nguyen, R. Mankowsky, and et al. Quenched lattice fluctuations in optically driven $srtio_3$. *arXiv:2301.08703*, 2023.

[323] Simon E. Wall, Shan Yang, Luciana Vidas, Matthieu Chollet, James M. Glownia, Michael E Kozina, Tetsuo Katayama, Thomas Henighan, Mason P. Jiang, Timothy A. Miller, David A. Reis, Lynn A. Boatner, Olivier Delaire, and Mariano Trigo. Ultrafast disordering of vanadium dimers in photoexcited vo2. *Science*, 362:572 – 576, 2018.

[324] E. Pomarico, M. Mitrano, H. Bromberger, M. A. Sentef, A. Al-Temimy, C. Coletti, A. Stöhr, S. Link, U. Starke, C. Cacho, and et al. Enhanced electron-phonon coupling in graphene with periodically distorted lattice. *Phys. Rev. B*, 95:024304, Jan 2017.

[325] Shi-Qi Hu, Hui Zhao, Chao Lian, Xin-Bao Liu, Meng-Xue Guan, and Sheng Meng. Tracking photocarrier-enhanced electron-phonon coupling in nonequilibrium. *npj Quantum Materials*, 7(1):14, jan 2022.

[326] Fabrizio Carbone, Ding-Shyue Yang, Enrico Giannini, and Ahmed H. Zewail. Direct role of structural dynamics in electron-lattice coupling of superconducting cuprates. *Proceedings of the National Academy of Sciences*, 105(51):20161, 2008.

[327] A. F. Kemper, M. A. Sentef, B. Moritz, T. P. Devereaux, and J. K. Freericks. Review of the theoretical description of time-resolved angle-resolved photoemission spectroscopy in electron-phonon mediated superconductors. *Annalen der Physik*, 529(9):1600235, 2017.

[328] Edoardo Baldini, Michael A. Sentef, Swagata Acharya, Thomas Brumme, Evgeniia Sheveleva, Fryderyk Lyzwa, Ekaterina Pomjakushina, Christian Bernhard, Mark van Schilfgaarde, Fabrizio Carbone, and et al. Electron–phonon-driven three-dimensional metallicity in an insulating cuprate. *Proceedings of the National Academy of Sciences*, 117(12):6409, 2020.

[329] Muneaki Hase, Masahiro Kitajima, Shin-ichi Nakashima, and Kohji Mizoguchi. Dynamics of coherent anharmonic phonons in bismuth using high density photoexcitation. *Phys. Rev. Lett.*, 88:067401, Jan 2002.

[330] F. Thiemann, G. Sciaini, A. Kassen, U. Hagemann, F. Meyer zu Heringdorf, and M. Horn-von Hoegen. Ultrafast transport-mediated homogenization of photoexcited electrons governs the softening of the A_{1g} phonon in bismuth. *Phys. Rev. B*, 106:014315, Jul 2022.

[331] Kunie Ishioka, Muneaki Hase, Masahiro Kitajima, Ludger Wirtz, Angel Rubio, and Hrvoje Petek. Ultrafast electron-phonon decoupling in graphite. *Phys. Rev. B*, 77:121402, Mar 2008.

[332] Hugen Yan, Daohua Song, Kin Fai Mak, Ioannis Chatzakis, Janina Maultzsch, and Tony F. Heinz. Time-resolved raman spectroscopy of optical phonons in graphite: Phonon anharmonic coupling and anomalous stiffening. *Phys. Rev. B*, 80:121403, Sep 2009.

[333] Viktor Krapivin, Mingqiang Gu, D. Hickox-Young, S. W. Teitelbaum, Y. Huang, G. de la Peña, D. Zhu, N. Sirica, M.-C. Lee, R. P. Prasankumar, A. A. Maznev, K. A. Nelson, M. Chollet, James M. Rondinelli, D. A. Reis, and M. Trigo. Ultrafast suppression of the ferroelectric instability in $ktao_3$. *Phys. Rev. Lett.*, 129:127601, Sep 2022.

[334] Mason P. Jiang, Mariano Trigo, Ivana Savić, S. Fahy, E. D. Murray, C. Bray, J. N. Clark, Thomas Henighan, Michael E Kozina, Matthieu Chollet, James M. Glownia, Matthias C. Hoffmann, D. Zhu, Olivier Delaire, Andrew F. May, Brian C. Sales, Aaron M. Lindenberg, Peter Zalden, T. Sato, Roberto Merlin, and David A. Reis. The origin of incipient ferroelectricity in lead telluride. *Nature Communications*, 7, 2016.

[335] Martin R. Otto, Jan-Hendrik Pöhls, Laurent P. René de Cotret, Mark J. Stern, Mark Sutton, and Bradley J. Siwick. Mechanisms of electron-phonon coupling unraveled in momentum and time: The case of soft phonons in $tise_2$. *Science Advances*, 7(20):eabf2810, 2021.

[336] Antonija Grubišić Čabo, Jill A. Miwa, Signe S. Grønborg, Jonathon M. Riley, Jens C. Johannsen, Cephise Cacho, Oliver Alexander, Richard T. Chapman, Emma Springate, Marco Grioni, and et al. Observation of ultrafast free carrier dynamics in single layer mos2. *Nano Letters*, 15(9):5883, 2015.

[337] H. Beyer, G. Rohde, A. Grubišić Čabo, A. Stange, T. Jacobsen, L. Bignardi, D. Lizzit, P. Lacovig, C. E. Sanders, S. Lizzit, and et al. 80% valley polarization of free carriers in singly oriented single-layer ws_2 on au(111). *Phys. Rev. Lett.*, 123:236802, Dec 2019.

[338] M. X. Na, A. K. Mills, F. Boschini, M. Michiardi, B. Nosarzewski, R. P. Day, E. Razzoli, A. Sheyerman, M. Schneider, G. Levy, S. Zhdanovich, T. P. Devereaux, A. F. Kemper, D. J. Jones, and A. Damascelli. Direct determination of mode-projected electron-phonon coupling in the time domain. *Science*, 366(6470):1231, 2019.

[339] Eva A. A. Pogna, Margherita Marsili, Domenico De Fazio, Stefano Dal Conte, Cristian Manzoni, Davide Sangalli, Duhee Yoon, Antonio Lombardo, Andrea C. Ferrari, Andrea Marini, and et al. Photo-induced bandgap renormalization governs the ultrafast response of single-layer mos2. *ACS Nano*, 10(1):1182, 2016.

[340] Ryan E. Wood, Lawson T. Lloyd, Fauzia Mujid, Lili Wang, Marco A. Allodi, Hui Gao, Richard Mazuski, Po-Chieh Ting, Saien Xie, Jiwoong Park, and et al. Evidence for the dominance of carrier-induced band gap renormalization over biexciton formation in cryogenic ultrafast experiments on mos2 monolayers. *The Journal of Physical Chemistry Letters*, 11(7):2658, 2020.

[341] L. Waldecker, R. Bertoni, H. Hübener, T. Brumme, T. Vasileiadis, D. Zahn, A. Rubio, and R. Ernstorfer. Momentum-resolved view of electron-phonon coupling in multilayer wse$_2$. *Phys. Rev. Lett.*, 119:036803, Jul 2017.

[342] Ming-Fu Lin, Vidya Kochat, Aravind Krishnamoorthy, Lindsay Bassman, Clemens Weninger, Qiang Zheng, Xiang Zhang, Amey Apte, Chandra Sekhar Tiwary, Xiaozhe Shen, and et al. Ultrafast non-radiative dynamics of atomically thin MoSe2. *Nature Communications*, 8(1):1745, nov 2017.

[343] Mark J. Stern, Laurent P. René de Cotret, Martin R. Otto, Robert P. Chatelain, Jean-Philippe Boisvert, Mark Sutton, and Bradley J. Siwick. Mapping momentum-dependent electron-phonon coupling and nonequilibrium phonon dynamics with ultrafast electron diffuse scattering. *Phys. Rev. B*, 97:165416, Apr 2018.

[344] P. Maldonado, T. Chase, A. H. Reid, X. Shen, R. K. Li, K. Carva, T. Payer, M. Horn von Hoegen, K. Sokolowski-Tinten, X. J. Wang, and et al. Tracking the ultrafast nonequilibrium energy flow between electronic and lattice degrees of freedom in crystalline nickel. *Phys. Rev. B*, 101:100302, Mar 2020.

[345] Hélène Seiler, Daniela Zahn, Marios Zacharias, Patrick-Nigel Hildebrandt, Thomas Vasileiadis, Yoav William Windsor, Yingpeng Qi, Christian Carbogno, Claudia Draxl, Ralph Ernstorfer, and et al. Accessing the anisotropic nonthermal phonon populations in black phosphorus. *Nano Letters*, 21(14):6171, 2021.

[346] Aravind Krishnamoorthy, Ming-Fu Lin, Xiang Zhang, Clemens Weninger, Ruru Ma, Alexander Britz, Chandra Sekhar Tiwary, Vidya Kochat, Amey Apte, Jie Yang, and et al. Optical control of non-equilibrium phonon dynamics. *Nano Letters*, 19(8):4981, 2019.

[347] Tristan L. Britt, Qiuyang Li, Laurent P. René de Cotret, Nicholas Olsen, Martin Otto, Syed Ali Hassan, Marios Zacharias, Fabio Caruso, Xiaoyang Zhu, and Bradley J. Siwick. Direct view of phonon dynamics in atomically thin mos2. *Nano Letters*, 22(12):4718, 2022.

[348] S. Gerber, S.-L. Yang, D. Zhu, H. Soifer, J. A. Sobota, S. Rebec, J. J. Lee, T. Jia, B. Moritz, C. Jia, and et al. Femtosecond electron-phonon lock-in by photoemission and x-ray free-electron laser. *Science*, 357(6346):71, 2017.

[349] Petra Hein, Stephan Jauernik, Hermann Erk, Lexian Yang, Yanpeng Qi, Yan Sun, Claudia Felser, and Michael Bauer. Mode-resolved reciprocal space mapping of electron-phonon interaction in the weyl semimetal candidate t_d-WTe$_2$. *Nature Communications*, 11(1):2613, may 2020.

[350] T. P. H. Sidiropoulos, N. Di Palo, D. E. Rivas, S. Severino, M. Reduzzi, B. Nandy, B. Bauerhenne, S. Krylow, T. Vasileiadis, T. Danz, P. Elliott, S. Sharma, K. Dewhurst, C. Ropers, Y. Joly, M. E. Garcia, M. Wolf, R. Ernstorfer, and J. Biegert. Probing the energy conversion pathways between light, carriers, and lattice in real time with attosecond core-level spectroscopy. *Phys. Rev. X*, 11:041060, Dec 2021.

[351] Soungmin Bae, Kana Matsumoto, Hannes Raebiger, Ken ichi Shudo, Yong-Hoon Kim, Ørjan Sele Handegård, Tadaaki Nagao, Masahiro Kitajima, Yuji Sakai, Xiang Zhang, and et al. K-point longitudinal acoustic phonons are responsible for ultrafast intervalley scattering in monolayer MoSe$_2$. *Nature Communications*, 13(1):4279, jul 2022.

[352] Shiwei Wu, Wei-Tao Liu, Xiaogan Liang, P. James Schuck, Feng Wang, Y. Ron Shen, and Miquel Salmeron. Hot phonon dynamics in graphene. *Nano Letters*, 12(11):5495, 2012.

[353] Stavros Katsiaounis, Andrey V. Sharkov, Eugeniy V. Khoroshilov, Georgios Paterakis, John Parthenios, and Konstantinos Papagelis. Time-resolved raman scattering in exfoliated and cvd graphene crystals. *The Journal of Physical Chemistry C*, 125(38):21003, 2021.

[354] Carino Ferrante, Giorgio Di Battista, Luis E. Parra López, Giovanni Batignani, Etienne Lorchat, Alessandra Virga, Stéphane Berciaud, and Tullio Scopigno. Picosecond energy transfer in a transition metal dichalcogenide–graphene heterostructure revealed by transient raman spectroscopy. *Proceedings of the National Academy of Sciences*, 119(15):e2119726119, 2022.

[355] D. N. Basov, M. M. Fogler, A. Lanzara, Feng Wang, and Yuanbo Zhang. Colloquium: Graphene spectroscopy. *Rev. Mod. Phys.*, 86:959–994, Jul 2014.

[356] Nina Girotto and Dino Novko. Dynamical phonons following electron relaxation stages in photoexcited graphene. *The Journal of Physical Chemistry Letters*, 14(39):8709–8716, 2023. PMID: 37735110.

[357] G. Rohde, A. Stange, A. Müller, M. Behrendt, L.-P. Oloff, K. Hanff, T. J. Albert, P. Hein, K. Rossnagel, and M. Bauer. Ultrafast formation of a fermi-dirac distributed electron gas. *Phys. Rev. Lett.*, 121:256401, Dec 2018.

[358] Isabella Gierz, Jesse C Petersen, Matteo Mitrano, Cephise Cacho, I C Edmond Turcu, Emma Springate, Alexander Stöhr, Axel Köhler, Ulrich Starke, and Andrea Cavalleri. Snapshots of non-equilibrium dirac carrier distributions in graphene. *Nature Materials*, 12(12):1119–1124, Dec 2013.

[359] S. Xu, J. Cao, C. C. Miller, D. A. Mantell, R. J. D. Miller, and Y. Gao. Energy dependence of electron lifetime in graphite observed with femtosecond photoemission spectroscopy. *Phys. Rev. Lett.*, 76:483–486, Jan 1996.

[360] Gunnar Moos, Cornelius Gahl, Roman Fasel, Martin Wolf, and Tobias Hertel. Anisotropy of quasiparticle lifetimes and the role of disorder in graphite from ultrafast time-resolved photoemission spectroscopy. *Phys. Rev. Lett.*, 87:267402, Dec 2001.

[361] Shijing Tan, Adam Argondizzo, Cong Wang, Xuefeng Cui, and Hrvoje Petek. Ultrafast multiphoton thermionic photoemission from graphite. *Phys. Rev. X*, 7:011004, Jan 2017.

[362] Tobias Kampfrath, Luca Perfetti, Florian Schapper, Christian Frischkorn, and Martin Wolf. Strongly coupled optical phonons in the ultrafast dynamics of the electronic energy and current relaxation in graphite. *Phys. Rev. Lett.*, 95:187403, Oct 2005.

[363] Markus Breusing, Claus Ropers, and Thomas Elsaesser. Ultrafast carrier dynamics in graphite. *Phys. Rev. Lett.*, 102:086809, Feb 2009.

[364] S. Pagliara, G. Galimberti, S. Mor, M. Montagnese, G. Ferrini, M. S. Grandi, P. Galinetto, and F. Parmigiani. Photoinduced π-π^* band gap renormalization in graphite. *Journal of the American Chemical Society*, 133(16):6318, 2011.

[365] Torben Winzer, Ermin Malić, and Andreas Knorr. Microscopic mechanism for transient population inversion and optical gain in graphene. *Phys. Rev. B*, 87:165413, Apr 2013.

[366] Isabella Gierz, Matteo Mitrano, Jesse C Petersen, Cephise Cacho, I C Edmond Turcu, Emma Springate, Alexander Stöhr, Axel Köhler, Ulrich Starke, and Andrea Cavalleri. Population inversion in monolayer and bilayer graphene. *Journal of Physics: Condensed Matter*, 27(16):164204, apr 2015.

[367] A. Freddie Page, Fouad Ballout, Ortwin Hess, and Joachim M. Hamm. Nonequilibrium plasmons with gain in graphene. *Phys. Rev. B*, 91:075404, Feb 2015.

[368] Christian Tanguy and Monique Combescot. Absorption-edge singularities for a nonequilibrium fermi sea. ii. second-order diagrammatic expansion. *Phys. Rev. B*, 50:11499–11507, Oct 1994.

[369] Mohsen Sabbaghi, Tobias Stauber, Hyun-Woo Lee, J. Sebastian Gomez-Diaz, and George W. Hanson. In-plane optical phonon modes of current-carrying graphene. *Phys. Rev. B*, 105:235405, Jun 2022.

[370] Sang Park, Michael Sammon, Eugene Mele, and Tony Low. Plasmonic gain in current biased tilted dirac nodes. *Nature Communications*, 13:7667, 12 2022.

[371] Tony Low, Pai-Yen Chen, and D. N. Basov. Superluminal plasmons with resonant gain in population inverted bilayer graphene. *Phys. Rev. B*, 98:041403, Jul 2018.

[372] Eva A. A. Pogna, Xiaoyu Jia, Alessandro Principi, Alexander Block, Luca Banszerus, Jincan Zhang, Xiaoting Liu, Thibault Sohier, Stiven Forti, Karuppasamy Soundarapandian, Bernat Terrés, Jake D. Mehew, Chiara Trovatello, Camilla Coletti, Frank H. L. Koppens, Mischa Bonn, Hai I. Wang, Niek van Hulst, Matthieu J. Verstraete, Hailin Peng, Zhongfan Liu, Christoph Stampfer, Giulio Cerullo, and Klaas-Jan Tielrooij. Hot-carrier cooling in high-quality graphene is intrinsically limited by optical phonons. *ACS Nano*, 15(7):11285–11295, 2021. PMID: 34139125.

[373] M. J. van Setten, M. Giantomassi, E. Bousquet, M. J. Verstraete, D. R. Hamann, X. Gonze, and G. M. Rignanese. The PseudoDojo: Training and grading a 85 element optimized norm-conserving pseudopotential table. *Comput. Phys. Commun.*, 226:39, 2018.

[374] Sergej Krylow, Felipe Valencia Hernandez, Bernd Bauerhenne, and Martin E. Garcia. Ultrafast structural relaxation dynamics of laser-excited graphene: Ab initio molecular dynamics simulations including electron-phonon interactions. *Phys. Rev. B*, 101:205428, May 2020.

[375] R. Merlin. Generating coherent thz phonons with light pulses. *Solid State Communications*, 102(2):207–220, 1997. Highlights in Condensed Matter Physics and Materials Science.

[376] T. K. Cheng; S. D. Brorson; A. S. Kazeroonian; J. S. Moodera; G. Dresselhaus; M. S. Dresselhaus; E. P. Ippen. Impulsive excitation of coherent phonons observed in reflection in bismuth and antimony. *Appl. Phys. Lett.*, 57:1004–1006, 1990.

[377] G. C. Cho, W. Kütt, and H. Kurz. Subpicosecond time-resolved coherent-phonon oscillations in gaas. *Phys. Rev. Lett.*, 65:764–766, Aug 1990.

[378] J. M. Chwalek; C. Uher; J. F. Whitaker; G. A. Mourou; J. A. Agostinelli. Subpicosecond time-resolved studies of coherent phonon oscillations in thin-film $yba_2cu_3o_{6+x}$ (x<0.4). *Appl. Phys. Lett.*, 58:980–982, 1991.

[379] T. K. Cheng; J. Vidal; H. J. Zeiger; G. Dresselhaus; M. S. Dresselhaus; E. P. Ippen. Mechanism for displacive excitation of coherent phonons in sb, bi, te, and ti_2o_3. *Appl. Phys. Lett.*, 59:1923–1925, 1991.

[380] W. Albrecht, Th. Kruse, and H. Kurz. Time-resolved observation of coherent phonons in superconducting $yba_2cu_3o_{7-ffi}$ thin films. *Phys. Rev. Lett.*, 69:1451–1454, Aug 1992.

[381] T. Pfeifer, W. Kütt, H. Kurz, and R. Scholz. Generation and detection of coherent optical phonons in germanium. *Phys. Rev. Lett.*, 69:3248–3251, Nov 1992.

[382] S. Hunsche, K. Wienecke, T. Dekorsy, and H. Kurz. Impulsive softening of coherent phonons in tellurium. *Phys. Rev. Lett.*, 75:1815–1818, Aug 1995.

[383] T. Dekorsy, H. Auer, C. Waschke, H. J. Bakker, H. G. Roskos, H. Kurz, V. Wagner, and P. Grosse. Emission of submillimeter electromagnetic waves by coherent phonons. *Phys. Rev. Lett.*, 74:738–741, Jan 1995.

[384] T. Dekorsy, H. Auer, H. J. Bakker, H. G. Roskos, and H. Kurz. Thz electromagnetic emission by coherent infrared-active phonons. *Phys. Rev. B*, 53:4005–4014, Feb 1996.

[385] G. C. Cho, W. Kütt, and H. Kurz. Subpicosecond time-resolved coherent-phonon oscillations in gaas. *Phys. Rev. Lett.*, 65:764–766, Aug 1990.

[386] T. Pfeifer, W. Kütt, H. Kurz, and R. Scholz. Generation and detection of coherent optical phonons in germanium. *Phys. Rev. Lett.*, 69:3248–3251, Nov 1992.

[387] H. J. Zeiger, J. Vidal, T. K. Cheng, E. P. Ippen, G. Dresselhaus, and M. S. Dresselhaus. Theory for displacive excitation of coherent phonons. *Phys. Rev. B*, 45:768–778, Jan 1992.

[388] Trond Andersen, Bo Dwyer, Javier Sanchez-Yamagishi, Joaquin Rodriguez-Nieva, Kartiek Agarwal, Kenji Watanabe, Takashi Taniguchi, Eugene Demler, Philip Kim, Hongkun Park, and M.D. Lukin. Electron-phonon instability in graphene revealed by global and local noise probes. *Science*, 364:154–157, 04 2019.

[389] C. Zhao, W. Xu, and François M. Peeters. Cerenkov emission of terahertz acoustic-phonons from graphene. *Applied Physics Letters*, 102:222101, 2013.

[390] Mohsen Sabbaghi, Hyun-Woo Lee, Tobias Stauber, and Kwang S. Kim. Drift-induced modifications to the dynamical polarization of graphene. *Phys. Rev. B*, 92:195429, Nov 2015.

[391] Tiago A. Morgado and Mário G. Silveirinha. Directional dependence of the plasmonic gain and nonreciprocity in drift-current biased graphene. *Nanophotonics*, 11(21):4929, 2022.

[392] Victor Ryzhii, Maxim Ryzhii, and Taiichi Otsuji. Negative dynamic conductivity of graphene with optical pumping. *Journal of Applied Physics*, 101:083114 – 083114, 04 2007.

[393] S. A. Mikhailov, N. A. Savostianova, and A. S. Moskalenko. Negative dynamic conductivity of a current-driven array of graphene nanoribbons. *Phys. Rev. B*, 94:035439, Jul 2016.

[394] René Petersen, Thomas Garm Pedersen, and F. Javier García de Abajo. Nonlocal plasmonic response of doped and optically pumped graphene, mos_2, and black phosphorus. *Phys. Rev. B*, 96:205430, Nov 2017.

[395] Tiago A. Morgado and Mário G. Silveirinha. Negative landau damping in bilayer graphene. *Phys. Rev. Lett.*, 119:133901, Sep 2017.

[396] Stephane Boubanga-Tombet, Wojciech Knap, Deepika Yadav, Akira Satou, Dmytro B. But, Vyacheslav V. Popov, Ilya V. Gorbenko, Valentin Kachorovskii, and Taiichi Otsuji. Room-temperature amplification of terahertz radiation by grating-gate graphene structures. *Phys. Rev. X*, 10:031004, Jul 2020.

[397] Ben Van Duppen, Andrea Tomadin, Alexander N Grigorenko, and Marco Polini. Current-induced birefringent absorption and non-reciprocal plasmons in graphene. *2D Materials*, 3(1):015011, feb 2016.

[398] Jan Berges, Erik G. C. P. van Loon, Arne Schobert, Malte Rösner, and Tim O. Wehling. Ab initio phonon self-energies and fluctuation diagnostics of phonon anomalies: Lattice instabilities from dirac pseudospin physics in transition metal dichalcogenides. *Phys. Rev. B*, 101:155107, Apr 2020.

[399] G. Dresselhaus. Graphite landau levels in the presence of trigonal warping. *Phys. Rev. B*, 10:3602–3609, Oct 1974.

[400] Wen-Hao Mao, Man-Yu Shang, and Jing-Tao Lü. Hot and cold phonons in electrically biased graphene. *Phys. Rev. B*, 106:125406, Sep 2022.

[401] Wen-Hao Mao, Man-Yu Shang, and Jing-Tao Lü. Current-driven collective dynamics of non-hermitian edge vibrations in armchair graphene nanoribbons. *Phys. Rev. B*, 107:085419, Feb 2023.

[402] Philip B. Allen. Theory of thermal relaxation of electrons in metals. *Phys. Rev. Lett.*, 59:1460, Sep 1987.

[403] L. Perfetti, P. A. Loukakos, M. Lisowski, U. Bovensiepen, H. Eisaki, and M. Wolf. Ultrafast electron relaxation in superconducting $bi_2sr_2cacu_2o_{8+\delta}$ by time-resolved photoelectron spectroscopy. *Phys. Rev. Lett.*, 99:197001, Nov 2007.

[404] B. Koopmans, G. Malinowski, F. Dalla Longa, D. Steiauf, M. Fähnle, T. Roth, M. Cinchetti, and M. Aeschlimann. Explaining the paradoxical diversity of ultrafast laser-induced demagnetization. *Nature Materials*, 9(3):259, dec 2009.

[405] Lutz Waldecker, Roman Bertoni, Ralph Ernstorfer, and Jan Vorberger. Electron-phonon coupling and energy flow in a simple metal beyond the two-temperature approximation. *Phys. Rev. X*, 6:021003, Apr 2016.

[406] Pablo Maldonado, Karel Carva, Martina Flammer, and Peter M. Oppeneer. Theory of out-of-equilibrium ultrafast relaxation dynamics in metals. *Phys. Rev. B*, 96:174439, Nov 2017.

[407] Fabio Caruso and Dino Novko. Ultrafast dynamics of electrons and phonons: from the two-temperature model to the time-dependent boltzmann equation. *Advances in Physics: X*, 7(1):2095925, 2022.

[408] Paulina Majchrzak, Sahar Pakdel, Deepnarayan Biswas, Alfred J. H. Jones, Klara Volckaert, Igor Marković, Federico Andreatta, Raman Sankar, Chris Jozwiak, Eli Rotenberg, and et al. Switching of the electron-phonon interaction in $1t-vse_2$ assisted by hot carriers. *Phys. Rev. B*, 103:L241108, Jun 2021.

[409] Fabio Caruso, Dino Novko, and Claudia Draxl. Photoemission signatures of nonequilibrium carrier dynamics from first principles. *Phys. Rev. B*, 101:035128, Jan 2020.

[410] Y. Ishida, T. Togashi, K. Yamamoto, M. Tanaka, T. Taniuchi, T. Kiss, M. Nakajima, T. Suemoto, and S. Shin. Non-thermal hot electrons ultrafastly generating hot optical phonons in graphite. *Scientific Reports*, 1(1):64, aug 2011.

[411] Zherui Han, Peter Sokalski, Li Shi, and Xiulin Ruan. Prediction of hot zone-center optical phonons in laser-irradiated molybdenum disulfide with a semiconductor multitemperature model. *Phys. Rev. B*, 107:L041407, Jan 2023.

[412] Christopher C. S. Chan, Kezhou Fan, Han Wang, Zhanfeng Huang, Dino Novko, Keyou Yan, Jianbin Xu, Wallace C. H. Choy, Ivor Lončarić, and Kam Sing Wong. Uncovering the electron-phonon interplay and dynamical energy-dissipation mechanisms of hot carriers in hybrid lead halide perovskites. *Advanced Energy Materials*, 11(9):2003071, 2021.

[413] Alexey V. Akimov and Oleg V. Prezhdo. The pyxaid program for non-adiabatic molecular dynamics in condensed matter systems. *Journal of Chemical Theory and Computation*, 9(11):4959, 2013.

[414] Alexey V. Akimov and Oleg V. Prezhdo. Advanced capabilities of the pyxaid program: Integration schemes, decoherence effects, multiexcitonic states, and field-matter interaction. *Journal of Chemical Theory and Computation*, 10(2):789, 2014.

[415] Zhaogang Nie, Run Long, Linfeng Sun, Chung-Che Huang, Jun Zhang, Qihua Xiong, Daniel W. Hewak, Zexiang Shen, Oleg V. Prezhdo, and Zhi-Heng Loh. Ultrafast carrier thermalization and cooling dynamics in few-layer mos2. *ACS Nano*, 8(10):10931–10940, 2014.

[416] Qijing Zheng, Weibin Chu, Chuanyu Zhao, Lili Zhang, Hongli Guo, Yanan Wang, Xiang Jiang, and Jin Zhao. Ab initio nonadiabatic molecular dynamics investigations on the excited carriers in condensed matter systems. *WIREs Computational Molecular Science*, 9(6):e1411, 2019.

[417] Xin-Bao Liu, Shi-Qi Hu, Daqiang Chen, Mengxue Guan, Qing Chen, and Sheng Meng. Calibrating out-of-equilibrium electron–phonon couplings in photoexcited mos2. *Nano Letters*, 22(12):4800, 2022.

[418] Meng-Xue Guan, Xin-Bao Liu, Da-Qiang Chen, Xuan-Yi Li, Ying-Peng Qi, Qing Yang, Pei-Wei You, and Sheng Meng. Optical control of multistage phase transition via phonon coupling in $mote_2$. *Phys. Rev. Lett.*, 128:015702, Jan 2022.

[419] Vatsal A. Jhalani, Jin-Jian Zhou, and Marco Bernardi. Ultrafast hot carrier dynamics in gan and its impact on the efficiency droop. *Nano Letters*, 17(8):5012, 2017.

[420] Sridhar Sadasivam, Maria K. Y. Chan, and Pierre Darancet. Theory of thermal relaxation of electrons in semiconductors. *Phys. Rev. Lett.*, 119:136602, Sep 2017.

[421] Fabio Caruso. Nonequilibrium lattice dynamics in monolayer mos_2. *The Journal of Physical Chemistry Letters*, 12(6):1734, 2021.

[422] Xiao Tong and Marco Bernardi. Toward precise simulations of the coupled ultrafast dynamics of electrons and atomic vibrations in materials. *Phys. Rev. Res.*, 3:023072, Apr 2021.

[423] Lutz Waldecker, Archana Raja, Malte Rösner, Christina Steinke, Aaron Bostwick, Roland J. Koch, Chris Jozwiak, Takashi Taniguchi, Kenji Watanabe, Eli Rotenberg, and et al. Rigid band shifts in two-dimensional semiconductors through external dielectric screening. *Phys. Rev. Lett.*, 123:206403, Nov 2019.

[424] Diana Y. Qiu, Felipe H. da Jornada, and Steven G. Louie. Optical spectrum of mos_2: Many-body effects and diversity of exciton states. *Phys. Rev. Lett.*, 111:216805, Nov 2013.

[425] Alejandro Molina-Sánchez, Davide Sangalli, Kerstin Hummer, Andrea Marini, and Ludger Wirtz. Effect of spin-orbit interaction on the optical spectra of single-layer, double-layer, and bulk mos_2. *Phys. Rev. B*, 88:045412, Jul 2013.

[426] R. Bertoni, C. W. Nicholson, L. Waldecker, H. Hübener, C. Monney, U. De Giovannini, M. Puppin, M. Hoesch, E. Springate, R. T. Chapman, and et al. Generation and evolution of spin-, valley-, and layer-polarized excited carriers in inversion-symmetric wse_2. *Phys. Rev. Lett.*, 117:277201, Dec 2016.

[427] Thomas Mueller and Ermin Malic. Exciton physics and device application of two-dimensional transition metal dichalcogenide semiconductors. *npj 2D Materials and Applications*, 2(1):29, sep 2018.

[428] Bruno R. Carvalho, Leandro M. Malard, Juliana M. Alves, Cristiano Fantini, and Marcos A. Pimenta. Symmetry-dependent exciton-phonon coupling in 2d and bulk mos_2 observed by resonance raman scattering. *Phys. Rev. Lett.*, 114:136403, Apr 2015.

[429] Sven Reichardt and Ludger Wirtz. Nonadiabatic exciton-phonon coupling in raman spectroscopy of layered materials. *Science Advances*, 6(32):eabb5915, 2020.

[430] Yang-hao Chan, Jonah B. Haber, Mit H. Naik, Jeffrey B. Neaton, Diana Y. Qiu, Felipe H. da Jornada, and Steven G. Louie. Exciton lifetime and optical line width profile via exciton–phonon interactions: Theory and first-principles calculations for monolayer mos_2. *Nano Letters*, 23(9):3971, 2023.

[431] Jan Philipp Bange, Paul Werner, David Schmitt, Wiebke Bennecke, Giuseppe Meneghini, AbdulAziz AlMutairi, Marco Merboldt, Kenji Watanabe, Takashi Taniguchi, Sabine Steil, and et al. Ultrafast dynamics of bright and dark excitons in monolayer wse_2 and heterobilayer wse_2/mos_2. *2D Materials*, 10(3):035039, jul 2023.

[432] Mingu Kang, Sung Won Jung, Woo Jong Shin, Yeongsup Sohn, Sae Hee Ryu, Timur K. Kim, Moritz Hoesch, and Keun Su Kim. Holstein polaron in a valley-degenerate two-dimensional semiconductor. *Nature Materials*, 17(8):676, may 2018.

[433] Mohammed K. Bin Subhan, Asif Suleman, Gareth Moore, Peter Phu, Moritz Hoesch, Hidekazu Kurebayashi, Christopher A. Howard, and Steven R. Schofield. Charge density waves in electron-doped molybdenum disulfide. *Nano Letters*, 21(13):5516, 2021.

[434] J. M. Lu, O. Zheliuk, I. Leermakers, N. F. Q. Yuan, U. Zeitler, K. T. Law, and J. T. Ye. Evidence for two-dimensional ising superconductivity in gated mos_2. *Science*, 350(6266):1353, 2015.

[435] Arash A. Mostofi, Jonathan R. Yates, Young-Su Lee, Ivo Souza, David Vanderbilt, and Nicola Marzari. wannier90: A tool for obtaining maximally-localised wannier functions. *Computer Physics Communications*, 178(9):685, 2008.

[436] Nina Girotto, Fabio Caruso, and Dino Novko. Ultrafast nonadiabatic phonon renormalization in photoexcited single-layer mos2. *The Journal of Physical Chemistry C*, 127(33):16515–16524, 2023.

[437] E. Blundo, E. Cappelluti, M. Felici, G. Pettinari, and A. Polimeni. Strain-tuning of the electronic, optical, and vibrational properties of two-dimensional crystals. *Applied Physics Reviews*, 8(2):021318, 06 2021.

[438] Enrico Perfetto and Gianluca Stefanucci. Real-time gw-ehrenfest-fan-migdal method for nonequilibrium 2d materials. *Nano Letters*, 0(0):null, 0.

[439] M. A. Sentef, A. F. Kemper, A. Georges, and C. Kollath. Theory of light-enhanced phonon-mediated superconductivity. *Phys. Rev. B*, 93:144506, Apr 2016.

[440] Yuta Murakami, Naoto Tsuji, Martin Eckstein, and Philipp Werner. Nonequilibrium steady states and transient dynamics of conventional superconductors under phonon driving. *Phys. Rev. B*, 96:045125, Jul 2017.

[441] M. A. Sentef. Light-enhanced electron-phonon coupling from nonlinear electron-phonon coupling. *Phys. Rev. B*, 95:205111, May 2017.